Pressure and Temperature Interference for Geothermal Projects in Dense Production Areas

A Case Study for the Delft Area

P.L. Reinhard

MSc Graduation Thesis
Delft University of Technology

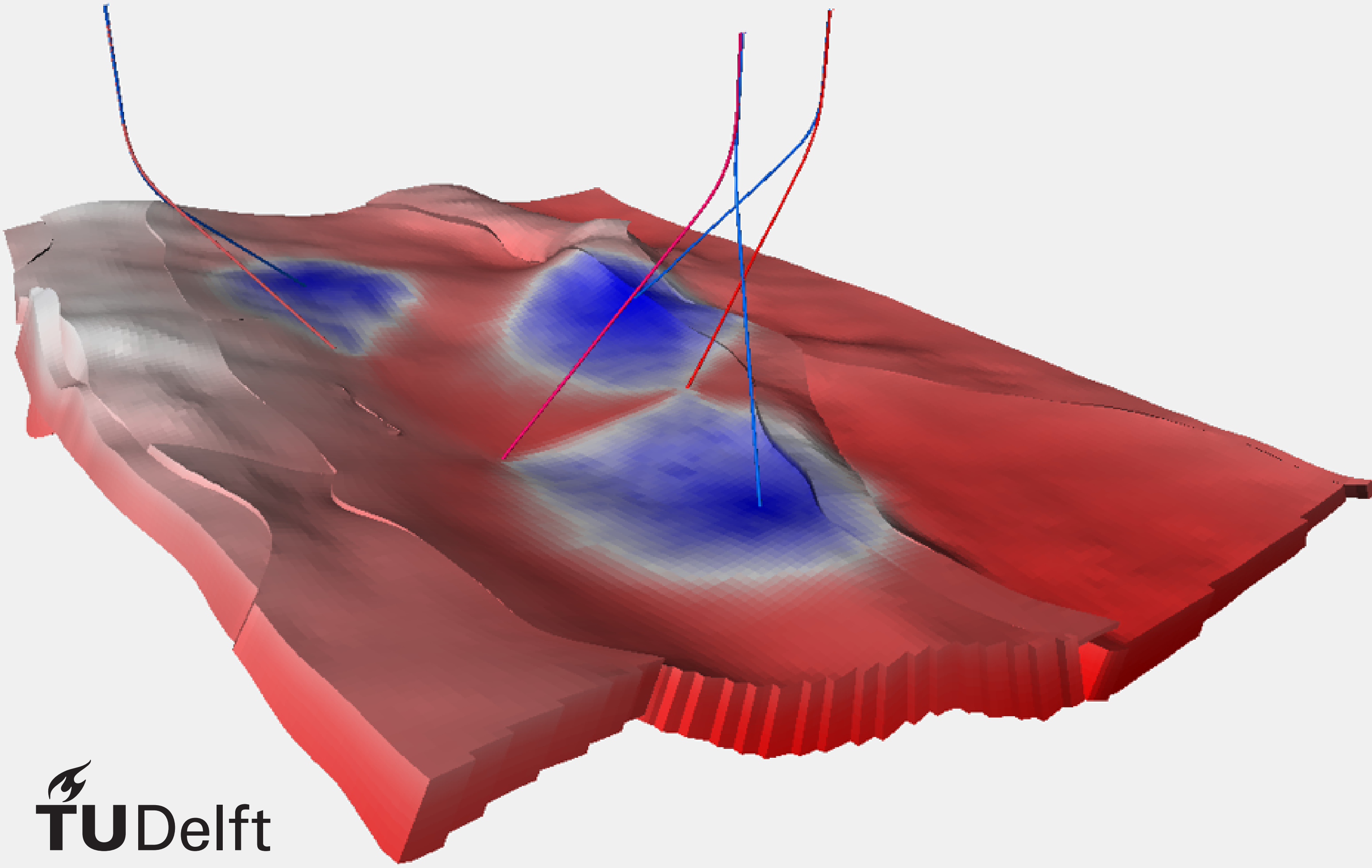

TUDelft

Pressure and Temperature Interference for Geothermal Projects in Dense Production Areas

A Case Study for the Delft Area

Graduation thesis as a Double Degree

Delft, September 13th 2019

By:

P.L. Reinhard

Master of Science
in Petroleum Engineering & Geosciences,
at the faculty of Civil Engineering & Geosciences

Master of Science
in Sustainable Energy Technology,
at the faculty of Electrical Engineering, Mathematics and Computer Science

to be defended publicly at the Delft University of Technology,
on 13 September, 2019 at 11:00.

Student number:	4186818	
Project duration:	15 October, 2018 – 13 September, 2019	
Graduation committee PE&G:	Dr. Ir. F. Vossepoel,	TU Delft, committee chair
	Dr. A. Barnhoorn	TU Delft
	Dr. Ir. R. Godderij	EBN B.V., supervisor
	Dr. A. Daniilidis,	TU Delft
Graduation committee SET:	Dr. Ir. F. Vossepoel,	TU Delft, committee chair
	Dr. A. Correljé,	TU Delft
	Dr. Ir. R. Godderij	EBN B.V., supervisor

This thesis is confidential and cannot be made public until October 1, 2019.

Abstract

The main objective of this study is to quantify interference effects between production and injection wells for geothermal projects that operate within the same reservoir. The secondary objective is to study the time it takes for the reservoir unit to thermally recharge after production has stopped. Two reservoir simulators are benchmarked to decide which one to use for reaching these objectives. The Ammerlaan, Duijvestijn and DAP doublets, all targeting the the Delft Sandstone Member in the West Netherlands Basin, serve as a case study. A literature review is presented to gain a better understanding of the geological history and the structural setting. A box-model of the study area is created and used to benchmark the two reservoir simulators. A static reservoir model is developed in Petrel through seismic interpretation, structural modelling, facies modelling and petrophysical modelling. Populating this static model with dynamic properties allows us to perform reservoir simulations in Eclipse100 and study the propagation of pressure and temperature. A discrete parameter analysis aims to capture the uncertainties that are associated with reservoir modelling and simulation. In this study, data is used from seismic surveys, wireline logs, core studies, a cuttings study and the monthly production volumes of the Ammerlaan and Duijvestijn doublets. It is shown that interference on temperature has a long term (20-30 years) effect on the Duijvestijn (positively) and the Ammerlaan and DAP doublets (negatively). The combined total energy production of the three doublets over 100 years is small with a decrease of 3% due to temperature interference, compared to when running the doublets in stand-alone configuration. Interference on pressure has a short term (days) effect on the achieved flow rate when the injection well cannot reach its target injection rate and is constraint on the maximum allowable pressure at which it is allowed to inject. This occurs under the low permeability scenarios and can be observed when the pressure wave arrives at the neighbouring injector. The Duijvestijn, Ammerlaan and DAP doublets all benefit from this through a combined increase in energy production of 8% over 100 years of production, averaged over all scenarios. During thermal recharge after production, the average reservoir temperature increases asymptotically. Temperature recharges to 96.1% to 97.4% of the initial reservoir temperature after 1000 years of recharging under different thickness and conductivity scenarios. The absence of a thermal influx at the bottom of the reservoir model is limiting the capacity of the reservoir to recharge to its initial average temperature. Interviews are conducted to investigate the implications that the findings of this research have on the policy measures for geothermal projects. Suggestions for changes in policy are made to optimize the recovery of heat in the subsurface.

Preface

This thesis marks the end of my studies at Delft University of Technology. There are several people that I would like to thank that have been involved with this project and my studies. First and foremost, my supervisors Femke Vossepoel and Raymond Godderij. Femke has given me superb guidance throughout the project and was always available to challenge my ideas and push me in the right direction. Secondly, I want to show great gratitude towards Raymond, who has been so engaged despite his busy schedule. He has added great value to this project by sharing his in-depth knowledge of reservoir engineering and putting me in touch with the right people. I would also like to thank my committee members Aad Correljé, Auke Barnhoorn and Alex Daniilidis for giving me valuable feedback and guidance.

Then I would like to thank EBN B.V. for having me as their intern. Big thanks to all its colleagues and in particular Dominique who has helped me on several technical topics. Also, my fellow interns at EBN who have made the tough times bearable. I hope to see them back in my future career. I would like to express my gratitude to Barbara Cox, Jan-Dirk Jansen, Rien Herber, Berend Scheffers and Harmen Mijnlieff for letting me interview them on the implications of the findings of this thesis.

Obtaining an MSc degree would not have been possible without my parents. They raised me and enabled me to study at a prestigious university, for which I am very grateful. They have been very supportive over the years and making them proud has given me a lot of positive energy. Delft University of Technology has kept me on a steep learning curve while also giving me space to broaden my horizon and dive into new subjects. Facilitating an exchange semester at ETH Zurich and allowing me to combine two MSc degrees has boosted my personal development. The former was not possible without the Climate-KIC institution. Climate-KIC provided me with financial support and let me on a transformational journey through Europe where I learned a lot about climate change and entrepreneurship.

Even though it is a bit of a long read, I sincerely hope that this work will contribute to the development of the geothermal industry. Exploiting this energy source successfully can significantly reduce the carbon footprint of heating and cooling and get us closer to reaching the goals of the Paris Agreement.

P.L. Reinhard
Delft, September 2019

Contents

List of Figures

List of Tables

Abbreviations

AD-GPRS	Automatic Differentiation General Purpose Research Simulator
AMM	Ammerlaan well
BH	Bottomhole
BHP	Bottom-hole pressure
CPU	Central processing unit
COP	Coefficient of Performance
DAGO	Dutch Association for Geothermal Operators
DAP	Delft Aardwarmte Project
DARTS	Delft Advanced Research Terra Simulator
DEL	Delft
DSSM	Delft Sandstone Member
DUV	Duijvestijn well
E&P	Exploration and production
EBN B.V.	Energie Beheer Nederland B.V.
Eq.	Equation
ESP	Electric submersible pump
EZK	Economische Zaken & Klimaat
FBHP	Flowing bottom-hole pressure
Fm.	Formation
GR	Gamma ray
Grp.	Group
GUI	Graphical user interface
HON	Honselersdijk
Mbr.	Member
MKP	Moerkappelle
NA	Not available
N/G	Net-to-gross
NLOG	Nederlands Olie en Gas Portaal
OB	Overburden
OBL	Operator based linearization
PNA	Pijnacker
PRN	Pernis
RWK	Rijswijk
SDE	Stimulering Duurzame Energieproductie
SEG	Society of Exploration Geophysicists
SodM	Staatstoezicht op de Mijnen
SP	Spontaneous potential
TM	Transmissibility Multiplier
TNO-AGE	Toegepast Natuurwetenschappelijk Onderzoek - Advisory Group for Economic Affairs
TVD	True vertical depth
TVT	True vertical thickness
THP	Tubing head pressure
VDB	Van den Bosch
UB	Underburden
WAG	Water-alternating-gas
WNB	West Netherlands Basin

1

Introduction

1.1. Problem Statement

Geothermal energy is a promising alternative for heating as it is suitable for industrial and domestic applications. In 2017, The Netherlands produced 3 PJ of geothermal energy. A consortium of Dutch companies and institutions has high expectations of geothermal energy and expects to reach a yearly production of 50 PJ in 2030 and 200 PJ in 2050 (Schoof, 2018). There are 12 geothermal doublets located in the West Netherlands Basin and with 20 approved exploration licenses there is an expected increasing use of geothermal heating (TNO, 2019). Knowledge of the subsurface in this area has been gained through earlier exploration by the oil and gas industry. The subsurface also has favorable permeabilities and geothermal gradient.

Within the Delft area, two geothermal doublets are being operated by the greenhouse companies Ammerlaan and Duijvestijn. The Delft Aardwarmte Project (DAP) is a third doublet that is planned to be drilled in the vicinity of the existing doublets (Figure 1.1.1). The Ammerlaan doublet is planning to drill two new big-bore wells with expected pumping rates to increase from 150 m^3/h to 350 m^3/h. It raises concerns of optimal recovery of the subsurface heat within the area. It is possible that in time, the cold water that is re-injected at a higher pumping rate will reach the neighbouring production wells in a shorter time. This can lead to an earlier thermal breakthrough and shorten the lifetime of the doublet. The neighbouring doublets are expected to communicate through pressure build-up and draw-down. To quantify the thermal power, lifetime and interference of the neighbouring doublets, pressure and temperature differences over time need to be studied through reservoir simulation.

By doing this, technical risks such as limited thermal power and early cold water breakthrough can be assessed. These technical risks translate to lower revenues over the lifetime of a project. Therefore, a quantitative study should incorporate the geological and operational uncertainties that can have an impact on the performance of these doublets. A systematic approach to reservoir characterization and simulation can enable companies to better assess the technical and economic risks of an investment. For a maturing industry that is relying on subsidies, such as the Dutch geothermal industry, it is of uttermost importance that economic and technical risks are properly assessed so that successful projects are delivered. A sequence of consecutive failing projects can lead to the government to move away from geothermal energy, ceasing its development. This can also imply that the way geothermal licensing is currently carried out has to be revised and more coordination between, and supervision of, the license holders is necessary. This is also highlighted in the letter of the Inspector-General of Mines to the Minister of Economic Affairs and Climate wherein the Inspector advocates for area-oriented licensing and putting strict requirements on the expertise of the parties operating geothermal projects in The Netherlands (SodM, 2017).

In a future scenario wherein the geothermal industry develops successfully, and more and more projects are delivered, the problem of thermal recharge arises. This can be described as follows: As geothermal energy is produced, and cold water is re-injected, a cold waterfront propagates from the injector, cooling down the reservoir. The potential of geothermal energy in The Netherlands on the long-term (~100-1000 years) is dependent on the ability of the subsurface to thermally recharge the reservoir by heat transfer. This will ultimately determine if this application of geothermal energy as a source for supplying heat for households and industry in The Netherlands can be defined as renewable.

Reservoir simulation has developed over the decades by activities in hydrocarbon exploration and production. It entails modelling the hydrocarbons in multiple compositions and phases, which requires advanced and comprehensive reservoir simulators. Low-enthalpy geothermal reservoir simulation in The Netherlands deals with, in the absence of significant volumes of residual hydrocarbons, only one-phase (liquid) and one-component (water). Hence it does not require the extensive functionalities that an expensive commercial simulator from the oil and gas industry has. Because economical margins in the Dutch geothermal industry are low compared to the E&P industry, it needs an affordable alternative that incorporates all and only the processes and variables that are important in geothermal reservoir simulation. For the development of an industry-standard simulator, the relevant processes that need to be incorporated must be identified. Incorporating the relevant processes increases the modelling performance and its attempt to approximate reality. Uncertainty quantification in reservoir simulation is often done by running an ensemble of simulations. Increasing the computational performance of a reservoir simulator can drastically decrease the simulation time when such an ensemble consists of hundreds of different scenarios. Available reservoir simulators can be benchmarked to determine the computational and modelling performance of the simulators.

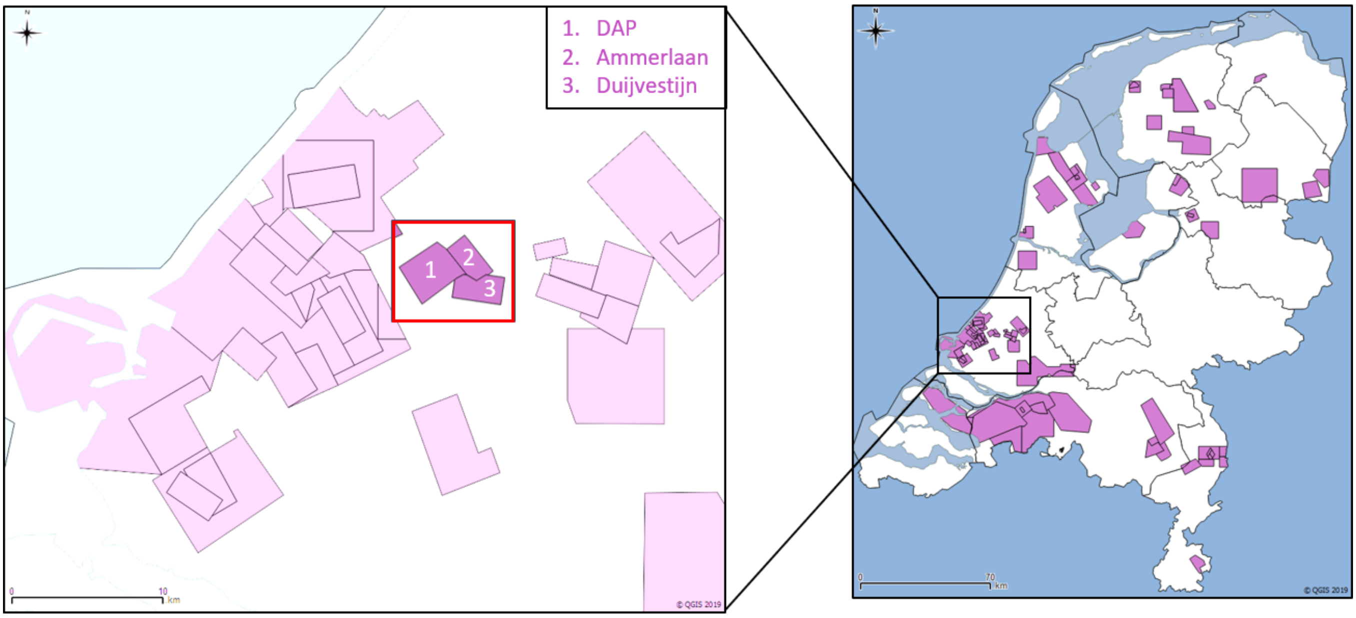

Figure 1.1.1: Overview of the geothermal licenses that have been applied for or approved in The Netherlands. The study area, with the licenses for the Ammerlaan, Duijvestijn and DAP concessions, is indicated in red (TNO, 2019).

1.2. Research Questions

The following research questions aim to address the three above mentioned problems:

- How large is the interference on pressure and temperature over time between the Ammerlaan, Duijvestijn and DAP doublets and how will this affect their own and combined heat production?
- What are the implications that interference has on the policy measures for geothermal projects operating in dense production areas?
- How large is the effect of thermal conductivity of the fluid and rock on the thermal recharge rate of the Delft Sandstone Member reservoir zone?
- How does the computational and modelling performance of Eclipse100 compare to that of DARTS for the case of a simplified 3D box-model of the reservoir?

1.3. Previous Work

Within the oil and gas industry, pressure interference effects are often examined by pressure response tests in the field (Mueller et al., 1965) while flow interference effects are studied by simulating and analysing streamlines from the injector(s) to the producer(s) (Dehdari et al., 2008). This type of analysis can be applied to water flooding and water-alternating-gas (WAG) injection, where the displacement of oil or gas is dependent on the optimal well placement and property distribution in the reservoir. Interference effects for geothermal doublets have been investigated by comparing hypothetical well placement configurations (Willems et al., 2017a). This study was performed on a 2D-box model, aiming to optimize well placement. In our case study, 3D reservoir boundaries are established through seismic interpretation and the proposed wells are based on existing or planned well trajectories. We quantify temperature interference with thermal power output instead of the lifetime of a doublet. Lifetime can be a useful performance indicator but is not very robust for making comparisons. It is dependent on the assumed minimum production temperature, which is very sensitive for the heating application and the development strategy (e.g. supporting heat production with extra heat pumps).

In The Netherlands, the current policy for determining license boundaries has been formulated by TNO-AGE after consultation with the Economic Ministry of Affairs Mijnlieff and van Wees (2009); TNO-AGE (2014). It prescribes that production of the doublet should not induce a temperature difference of 1 degree Celsius and pressure difference of 1 bar within the granted lifetime of the doublet. The oil and gas industry applies self-enforcing provisions through unitization agreements. In such an agreement, multiple firms allocate the rights to produce a subset of the expected reserves of a reservoir unit. Libecap and Wiggins (1985) has shown that these kind of agreements can fail due to information asymmetries among operators. The study suggests that such agreements can be more successful when they are made earlier, before information advantages are created.

Thermal recharge analysis was performed on sedimentary geothermal prospects for a structural model that targeted a hypothetical reservoir on top of a salt layer sequence (Daniilidis et al., 2016). The structural modelling approach incorporates salt intrusions, underlying the geothermal prospect. Salt is highly conductive compared to shale and we therefore expect that the thermal rate of recharge found in this study is small compared to that found by Daniilidis et al. (2016). Another study on thermal recharge of geothermal reservoirs focused on a hypothetical box model with properties that represented the geological setting in Copenhagen area (Denmark), targeting the Triassic Buntersandstone (Poulsen et al., 2015). The hypothetical model incorporates a heat influx at the lower boundary of the reservoir, representing the heat flow from the Earth's interior. This heat flow provides the underburden and the reservoir with heat through conduction, increasing the thermal rate of recharge. Different overburden and underburden thicknesses are used in geothermal modelling. They range from 200m, (Willems, 2012), 400m (Shetty, 2018) to 500m (Poulsen et al., 2015). In some cases overburden and underburden were not incorporated (Willems et al., 2017a) or the thicknesses have not been reported (Daniilidis and Herber, 2017; Saeid et al., 2015).

There are currently numerous commercial and academic reservoir simulators on the market, both commercial and open-source. Geothermal reservoir simulation studies were performed in COMSOL (Saeid et al., 2015; Smits, 2008; Watanabe et al., 2010; Willems et al., 2017a,b), Eclipse100 (Aramburo, 2017; Gilding, 2010; Groot, 2014; Reith, 2018), FEFLOW (Cacace et al., 2010; Ondrak et al., 1998), AD-GPRS (Shetty, 2018; Wang et al., 2019; Wong et al., 2015), PyTOUGH (Daniilidis and Herber, 2017) or TOUGH2 (Daniilidis et al., 2016). DARTS is a newly developed simulator and has been benchmarked against TOUGH2 and AD-GPRS (Wang et al., 2019). Wang et al. (2019) has shown that DARTS achieves results that have good matches with the simulators AD-GPRS and TOUGH2, while simulation time was significantly reduced. In this study, DARTS is benchmarked against Eclipse100, a simulator developed by Schlumberger with over 30 years of development.

1.4. Research Approach

The approach to this research is described in this section. To benchmark the two simulators, a homogeneous 3D box-model of the reservoir is created in Petrel. To have a fair comparison between the two simulators, equal target time steps, grid properties, operational constraints and central processing unit (CPU) are used. After benchmarking, one of the two simulators is chosen for studying doublet performance and the thermal recharge of the reservoir.

To study interference effects as a case study, a real-world reservoir wherein multiple geothermal doublets are operating is required. In an ideal scenario, the study area has high-resolution seismic coverage, petrophysical data and production data (pressure, flow rates and temperature) available. The Ammerlaan, Duijvestijn and DAP concession lies in the West Netherlands Basin (WNB) and targets the Delft Sandstone Member, in the Lower Cretaceous Nieuwerkerk Formation. This concession only partially fulfills the requirements described above since it has a limited resolution on the production data publicly available (monthly volumes published on NLOG).

The implications, that the quantified interference effects can have on the policy measures for geothermal projects, are investigated. Interviews are conducted to gain knowledge on the stakeholder landscape and the interaction between the different stakeholders. Policy documents are reviewed to determine the current policy measures, which are then tested to the study case.

Geological literature and petrophysical studies are reviewed and then seismic interpretation is performed. A static reservoir model is developed that approximates the geological setting and petrophysical properties of the relevant stratigraphic units. Dynamic properties are populated in the grid to provide the numerical model with initial conditions (e.g. pressure, temperature and viscosity) and determine their values over time. Schlumberger's Petrel Suite is used for the development of a static and dynamic reservoir model. The integrated Eclipse100 reservoir simulator allows us to perform dynamic reservoir simulations. The static and dynamic reservoir model contains various uncertainties due to the lack of data coverage and the limited resolution of the measurements. A discrete parameter analysis is performed, evaluating the full factorial design of the discrete values that we assume for the identified uncertain parameters.

The thermal recharge of the reservoir model is assessed by shutting in the wells in the Eclipse100 reservoir simulator and measuring the time it takes for the reservoir to recharge to 99 % of its initial temperature. The over- and underburden layer thicknesses are increased and the layering method is varied to see how that affects the rate of thermal recharge.

1.5. Thesis Outline

The literature study, performed to better understand the geological history and current geological setting, is summarized in Chapter 2. The used data and description of the geothermal physics can be found in Chapter 3. The steps to develop the static reservoir model are described in Chapter 5. The development of the dynamic model is described in Chapter 6. The methodology and results of analysing the doublets performance is described in 7. The implications of the findings presented in that chapter on policy measures are investigated in Chapter 8. Chapter 9 describes the thermal recharge analysis. The limitations of reservoir modelling related to this study are discussed in Chapter 10. Chapter 11 presents the conclusions taken from the results. Chapter 12 finalizes this thesis by giving recommendations for future studies.

2

Geological Setting

The target reservoir unit in this study is the Delft Sandstone Member (DSSM). This member consists of a fluvial succession that was deposited during the Late-Cretaceous as infill of the West Netherlands Basin (WNB). Section 2.1 will describe the formation of this basin and Section 2.2 will describe the relevant stratigraphic units that are included in the reservoir model. A complete stratigraphic overview of the studied area can be found in Figure 2.1.1. Section 2.3 will elaborate on the present structural setting in more detail.

2.1. Formation of the West Netherlands Basin

The WNB is a 60 km wide trans-tensional basin in the southwest of the Netherlands (Figure 2.1.2). It is structurally bounded to the north by the Zandvoort Ridge and the Central Netherlands Basin, to the offshore by the IJmuiden High (Van Adrichem Boogaert and Kouwe, 1993; Wong et al., 2007), to the south by the London-Brabant Massif and the southeast by the Roer Valley Graben. The thicknesses of this infill can reach up to 3000 m. The basin highs have been targeted for hydrocarbon exploration and production since 1954, reaching its peak production around the 1980s (Donselaar et al., 2015). The formation of the WNB can be subdivided in a pre-, syn- and post-rifting phase, which will be described below.

2.1.1. Pre-rift phase: Late Permian – Middle Jurassic

The WNB comprised one stable block before the pre-rift phase. The pre-rift phase was initiated by a rift pulse during the Late Permian that caused the basin to be uplifted followed by regional thermal subsidence in the Early Triassic (Wong et al., 2007). Then the Early Kimmerian tectonic phase (241 Ma), which was controlled by the major faulting zone towards the northeast, resulted in a simple large-scale half-graben structure. The Triassic deposits in this area are composed of lacustrine claystones, sandstones of aeolian and fluvial origin, carbonates and evaporites (Vondrak et al., 2018). The occurrence of volcanic rocks and intrusive sills show evidence of igneous activity during the pre-rift phase (Wong et al., 2007).

2.1.2. Syn-rift phase: Late Jurassic – Early Cretaceous

After relatively weak rifting during the pre-rift phase, several stronger rifting pulses occurred within a short time-span (Kimmeridgian 155 Ma - Hauterivian 135 Ma) that caused the breaking up of the basin while it was filled with fluvial syn-rift deposits (Wong et al., 2007). Erosion proceeded on the adjacent platforms and highs (Vondrak et al., 2018). Differential subsidence continued during the Valanginian and the basin transitioned from a coastal to a shallow marine environment, lowering the sedimentation rates (Vondrak et al., 2018). The intensity of the rifting decreased from the Hauterivian onwards (Donselaar et al., 2015) and ceased during the Aptian-Albian (Van Adrichem Boogaert and Kouwe, 1993).

2.1.3. Post-rift phase: Late Cretaceous – Quaternary

Subsidence became the dominant mechanism into the Late Cretaceous due to the relaxation of thermal anomalies, introduced by the intense rifting of the previous phase (Vondrak et al., 2018). The Late Cretaceous Laramide phase created a regional compressional stress field that caused the inversion of several basins in the Netherlands, among which the WNB (Figure 2.1.2).

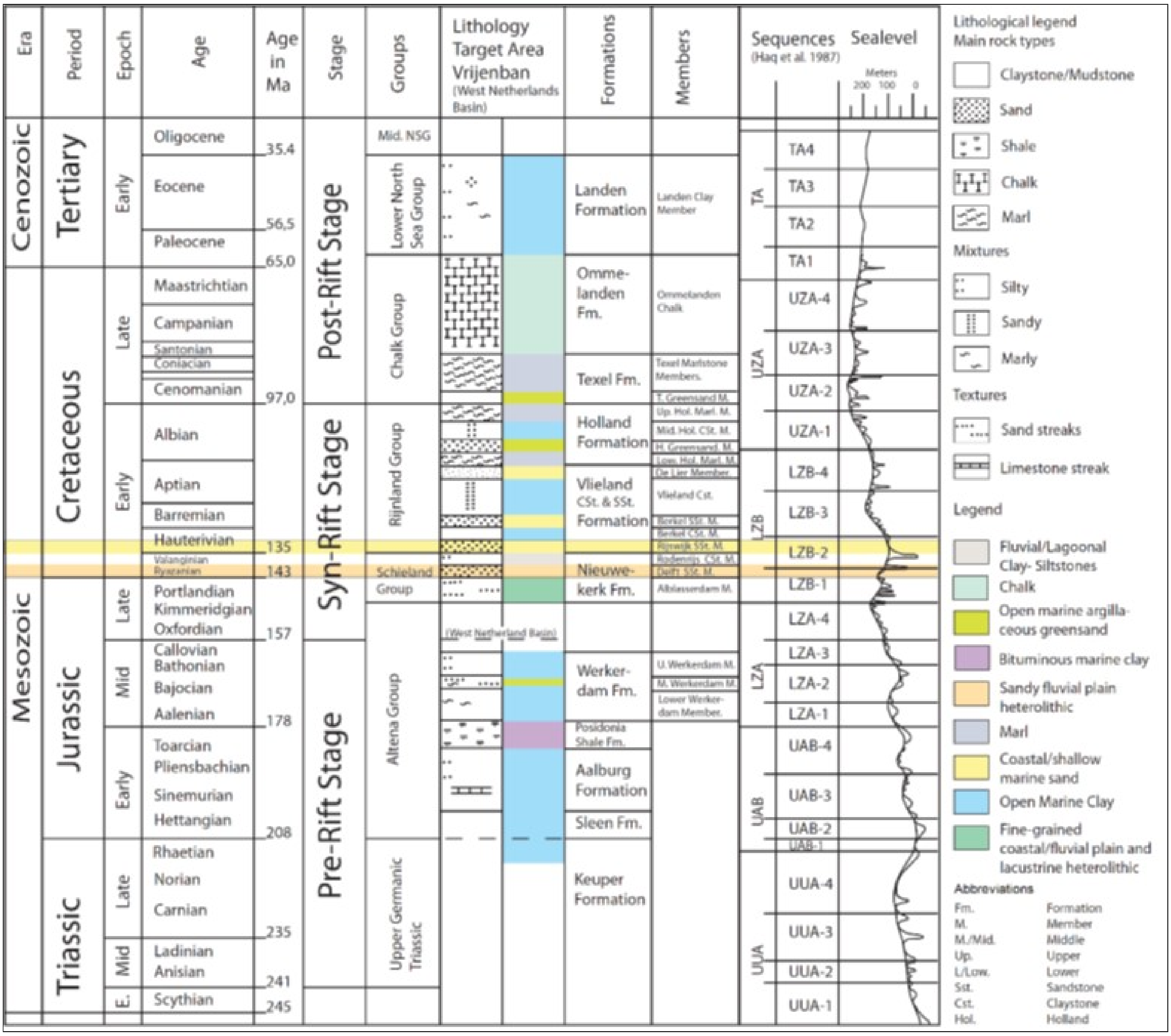

Figure 2.1.1: Regional stratigraphy of the study area. Lithology based on wells DEL-3, DEL-8, PNA-13, PNA-15 and RWK-1. Delft Sandstone Member is highlighted in brown and the Rijswijk Member in yellow (Donselaar et al., 2015).

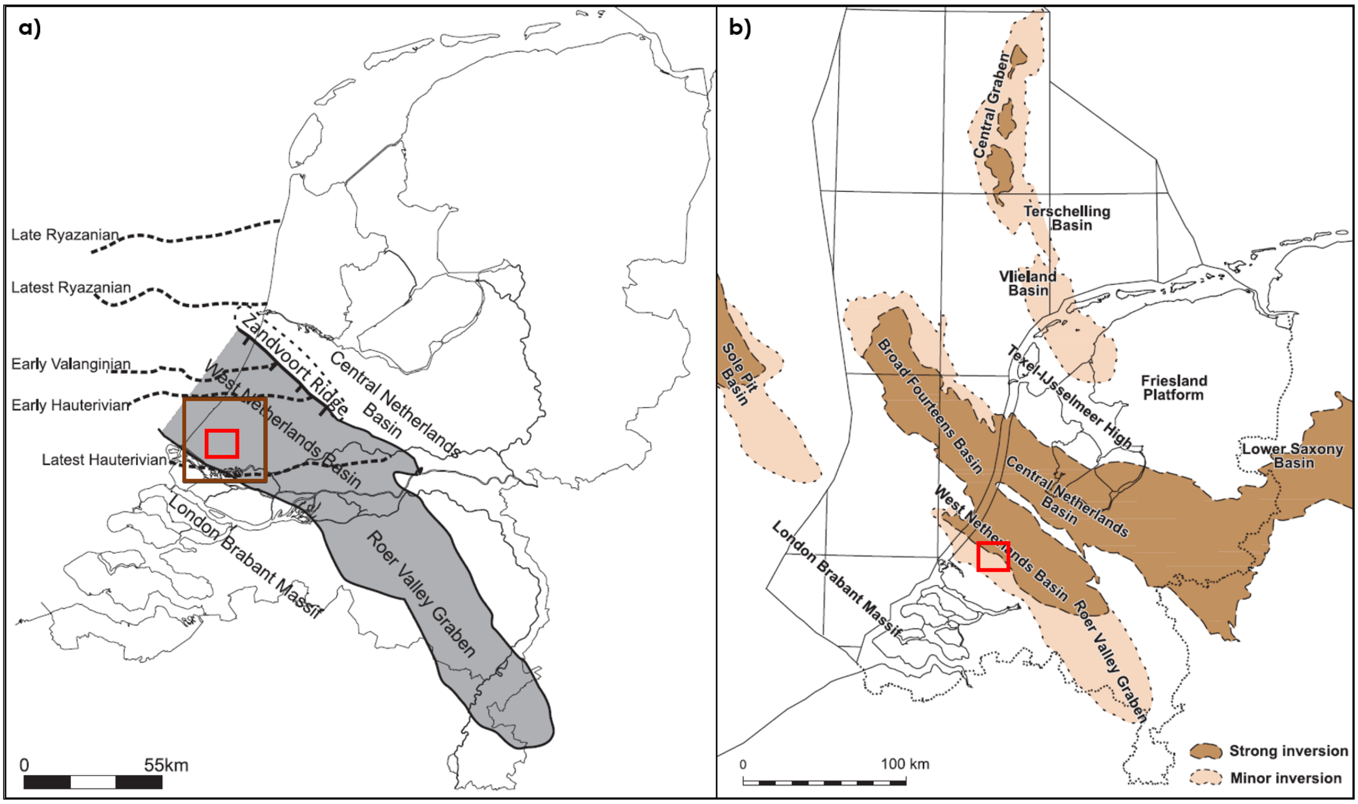

Figure 2.1.2: a) Geological setting of the WNB during the Cretaceous. According to Jeremiah et al., the shoreline moved into the WNB indicated by the timelines. The studied area of Vondrak et al. (2018) is indicated by the brown and area of the simulation wells is indicated in red. b) Post-rift inversion of basins in The Netherlands evidenced by the missing Chalk Group due to erosion during inversion. The WNB was among the basins that was exposed to minor and strong inversion, indicated in respectively light-brown and dark-brown) (Wong et al., 2007). The area of the simulation wells is indicated in red.

2.2. Regional Stratigraphy

Deposits ranging from the Upper Jurassic to the Lower Cretaceous belong to the Schieland Group in which the Delfland Subgroup is present. This Subgroup contains the Dutch continental strata lying south of the Vlieland High, among which the Nieuwerkerk Formation. This formation, deposited in syn-rift conditions as described in Section 2.1.2, is subdivided from base to top into the Alblasserdam Member, the DSSM, and the Rodenrijs Member (Van Adrichem Boogaert and Kouwe, 1993). Biostratigraphy, chemostratigraphy, marker beds, wire-line logs (SP and GR) and seismic data have been used to correlate the members within the Nieuwerkerk Fm. (Den Hartog Jager, 1996; DeVault and Jeremiah, 2002; Donselaar et al., 2015; Vondrak et al., 2018; Willems et al., 2017c). The following section describes these members and the work that has been done for the analysis and correlation of the members.

2.2.1. Alblasserdam Member

The Alblasserdam Member unconformably overlies the Middle-Jurassic shallow-marine limestones and shelf-mudstones of the Brabant and Werkendam Formation (Vondrak et al., 2018). The member is found throughout the WNB with a thickness ranging from 100-1300 m (Donselaar et al., 2015). Van Adrichem Boogaert and Kouwe (1993) and Den Hartog Jager (1996) used it for all fluviatile deposits that showed no indication of marine influences. This is supported by sporomorph assemblage analysis done by DeVault and Jeremiah (2002). The deposits within this member contain clay- and siltstones, fine to medium-grained sandstones and coarse-grained sandstones (Wiggers, 2009). Thickness ranges cannot be accurately determined because most wells do not penetrate the full interval of the member.

2.2.2. Delft Sandstone Member

The DSSM conformably overlies the Alblasserdam Member and consists of meandering river deposits and associated floodplain fines, deposited in a lower coastal-plain setting. This is evidenced in the core data by the lack of marine expressions, the presence of erosive surfaces, paleosols, in-situ coal beds and channel sands (Den Hartog Jager, 1996). Channel sands are distinguished by sedimentological characteristics such as trough, cross- and laminar bedding (Donselaar and Overeem, 2008). The DSSM was interpreted to originate from the Valanginian age (139-134 Ma) based on sporomorphic analysis (Van Adrichem Boogaert and Kouwe, 1993). However, analysis done with newly-acquired palynological data contradicts this and shows that the DSSM consists of a complex reservoir architecture of thick sandstone packages originating from two (Willems et al., 2017c) or three (Vondrak et al., 2018) different phases during the Ryazanian and Valanginan age. Another contradiction in previous studies is related to the lateral (dis-)continuity of the DSSM. According to (Van Adrichem Boogaert and Kouwe, 1993), the DSSM can be interpreted as one continuous interval across the WNB. In the works of Gilding (2010),Groot (2014) and Donselaar et al. (2015), the DSSM is interpreted as a discontinuous interval of fluvial deposits that vary greatly in thickness from 0 to 130 m across the WNB. They distinguish three different units within the DSSM based on net-to-gross (N/G) found in the wireline logs. DeVault and Jeremiah (2002) and Vondrak et al. (2018) argue that the DSSM is rather a consortium of discontinuous deposits that is found throughout the Nieuwerkerk Fm. and is therefore not necessarily seen as a separate member. Vondrak et al. (2018) showed by biostratigraphical correlation that the distribution of the sands is bound by the sub-basins trending NW–SE but are not continuous throughout the WNB. The channel activity gradually shifted from NE to SW due to tectonic activity in combination with ceasing fault movement (Figure 2.2.2).

2.2.3. Rodenrijs Claystone Member

The Rodenrijs Claystone Member conformably overlies the DSSM and originates from the Late Valanginian to Early Hauterivian (Van Adrichem Boogaert and Kouwe, 1993). The member was identified in all wells in the WNB that were drilled beyond the Cretaceous with thicknesses ranging from 30 m to over 100 m (Gilding, 2010). Marine influences increased during the transgressive sequence of these times until the Barremian, where the fluvial deposits were completely replaced by marine strata (Den Hartog Jager, 1996). Horizontal organic bands indicate a low energetic depositional environment. The deposits do not contain the sporomorphs that were present in the underlying members (Vondrak et al., 2018) and thin coal layers are present in the core data that are difficult to correlate from one well to the next (DeVault and Jeremiah, 2002). These findings indicate that this member was deposited in a lagoonal environment. Due to the sea connection, the stacking of channel/overbank deposits was closely bound to the eustatic sea-level rise (DeVault and Jeremiah, 2002).

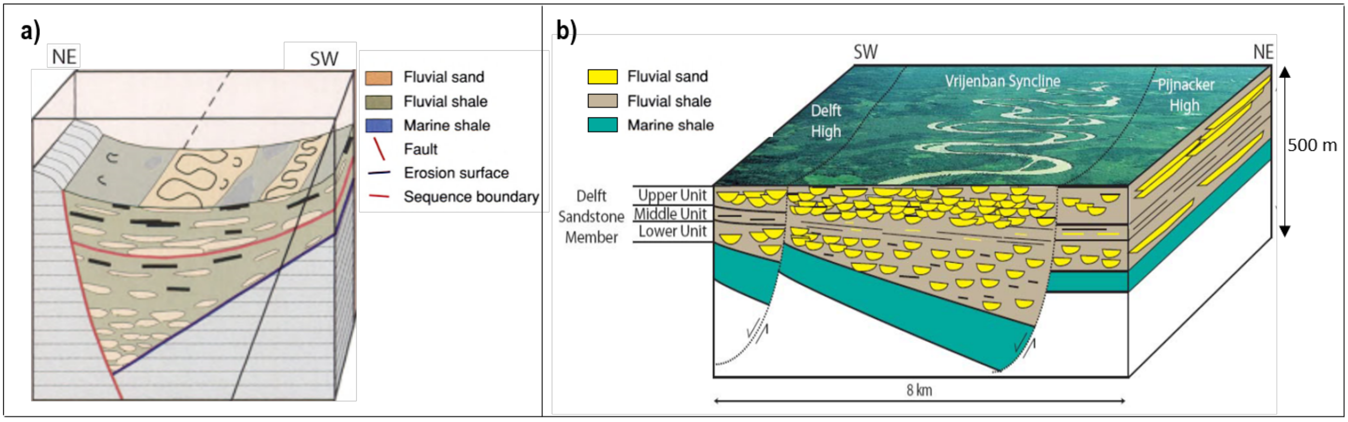

Figure 2.2.1: Depositional models of the DSSM where three units have been distinguished with varying N/G (note the reversed looking direction). a) Accommodation space decreases towards the east according to Den Hartog Jager (1996). b) Accommodation space increases towards the east according to Gilding (2010) and Donselaar et al. (2015).

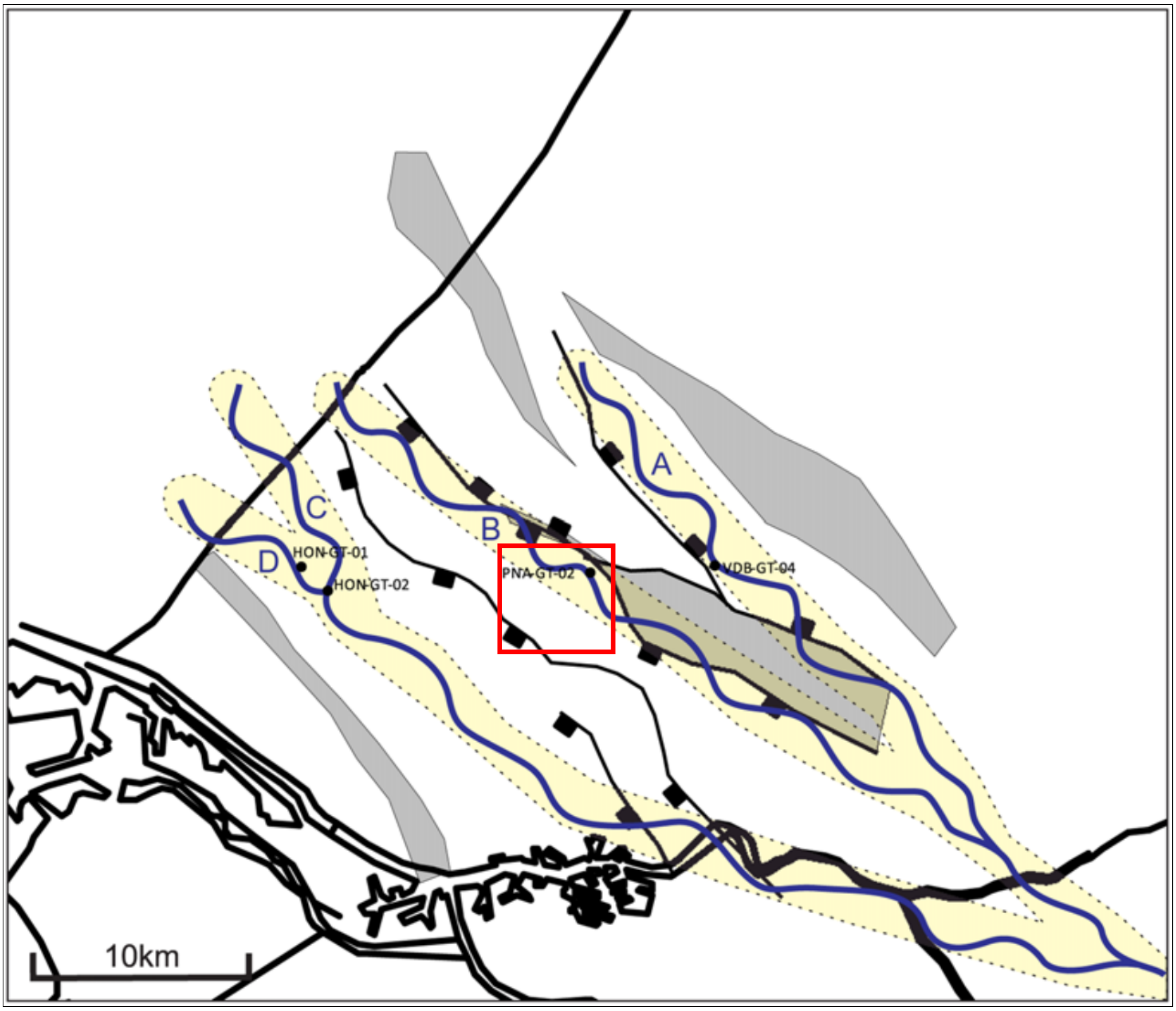

Figure 2.2.2: Map view of the reservoir architecture of the Nieuwerkerk Fm. in the WNB with the study area indicated in red. Channel belts widths are interpreted to be ~2km. Channel belts A and B were active during the Late Ryazanian. Channel belts B, C and D were active during the Valanginian. Channel B partially covers our study area, suggesting that part the western part of the area contains fewer sand deposits (modified from Vondrak et al. (2018)).

2.3. Structural Setting

The WNB has a geological history with extensive extensional and compressional faulting that caused large variations in thicknesses. It is therefore important for the reservoir model, and future geothermal reservoir models of the WNB, to describe the structural setting in more detail. The main structures can be classified in the Delft High, Pijnacker High and Vrijenban Syncline, as shown in Figure 2.3.1. The trapping mechanisms for hydrocarbons are pop-up structures, also called flower-structures, that were formed during the inversion phase. The North Sea Group overlies the Upper Rijnland Group on these structures due to the erosion of the Chalk Group. Two pop-up structures are predominant within the study area. Towards the Southwest lies the Delft High, also sometimes referred to as the Rijswijk structure. In the Northeast of the study area lies the Pijnacker high.

2.3.1. The Delft High

The dimensions of the Delft High were determined through seismics and had an approximate length of 10 km and a varying width from 0.2 to 1 km. It extends beyond the study area to the Berkel, IJsselmonde, Rijskwijk and Oude Leede-fields. Multiple exploration wells have been drilled to produce the hydrocarbons in this structure. The Delft (DEL) field encountered oil and gas accumulations in the Rijswijk Member (part of the Upper Rijnland Group) but not in the DSSM (Weerd, 2016). A cuttings analysis of DEL-03 showed that there was also no residual bitumen present in this formation (Drost, 2009). Because the Rijswijk Member overlies the Nieuwerkerk Formation, oil has likely has migrated through the DSSM along the faults. So even though no oil was encountered, there is still a possibility that the DSSM might contain residual hydrocarbons that could be encountered in the proposed wells for the DAP doublet.

2.3.2. The Pijnacker High

The Pijnacker High is a relatively smaller structure compared to the Delft High. It does not extend laterally as far as the Delft high. Within the study area, it has a length of approximately 12 km and a varying width from 0.3 to 2 km. It consists of a pop-up structure and a horst-graben. The pop-up structure was formed by an inverted normal fault and a reverse fault system. The former Pijnacker oil field lies in this structure. Also here, the hydrocarbons were encountered in the Rijswijk Member. The Ammerlaan and Duijvestijn doublets both lie in the vicinity of the Pijnacker High and have the Rijswijk member as a secondary production target. They both produce dissolved gas in formation water and the Ammerlaan doublet, positioned closer to the Pijnacker High, has reported the production of small amounts of oil dispersed in formation water.

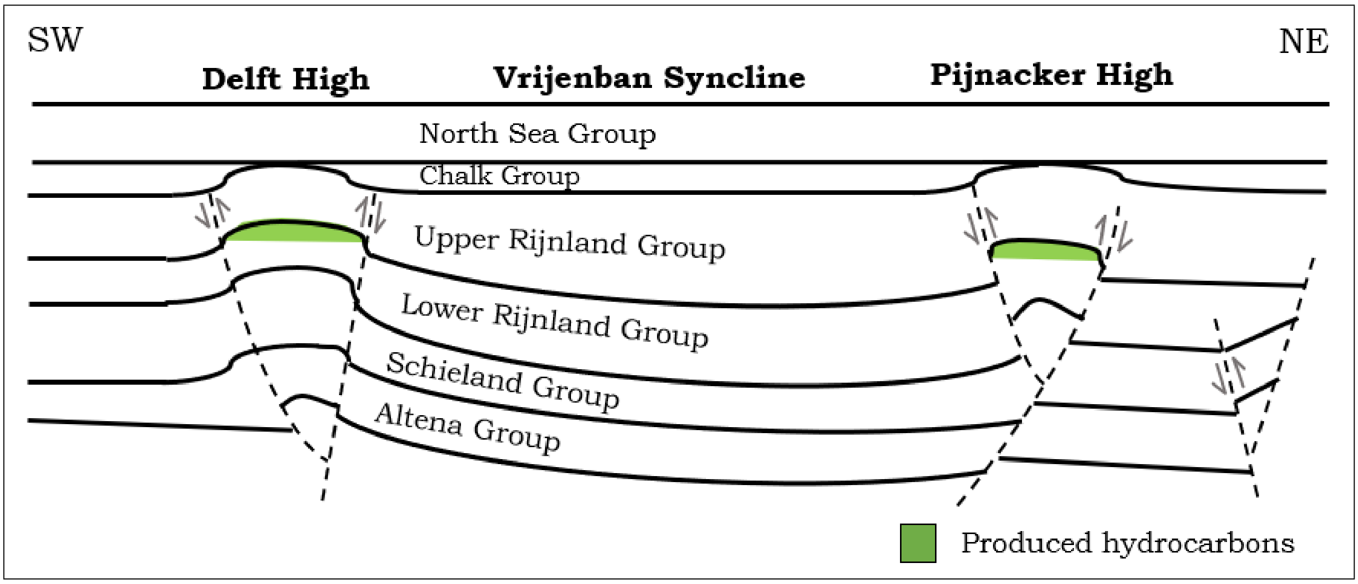

Figure 2.3.1: A simplified, schematic cross-section showing the relevant structural elements and the regional stratigraphy of the study area. Encountered hydrocarbons are indicated in green. The cross section has the same orientation as Figure 2.2.1.a.)

3

Data and Geothermal Physics

This chapter presents the used data and describes the geothermal physics and assumptions.

3.1. Data

The drilling and exploration for hydrocarbons in the WNB led to a vast amount of geological data that is now publicly available. This study utilized the data from seismic surveys, wireline logs, core studies, a cuttings study and the monthly production volumes of the Ammerlaan and Duijvestijn doublets. No new petrophysical data has been analysed for this study. Petrel was used for static reservoir modelling, Eclipse100 and DARTS for dynamic reservoir simulation and Python for the post-processing of data.

3.1.1. Seismic Survey

A reprocessed seismic survey, provided by PanTerra Geoconsultants B.V., has been used for seismic interpretation. This seismic cube was part of the merged and reprocessed L3NAM1990C (Monster, started acquisition in 1990), L3NAM1985P (Pijnacker, started acquisition in 1985) and L3NAM1989K (Leiden, started acquisition in 1988) (Weerd, 2016). Processing was done by Shell EPE-T-D and then merged and reprocessed by the NAM in 2013. The header is displayed in Figure 3.1.2 and summarizes its properties and processing methods. Polarity follows the non-SEG standard and the EBN colour convention (Appendix A.1). The cube covers an area much larger than the study area (Figure 3.1.1).

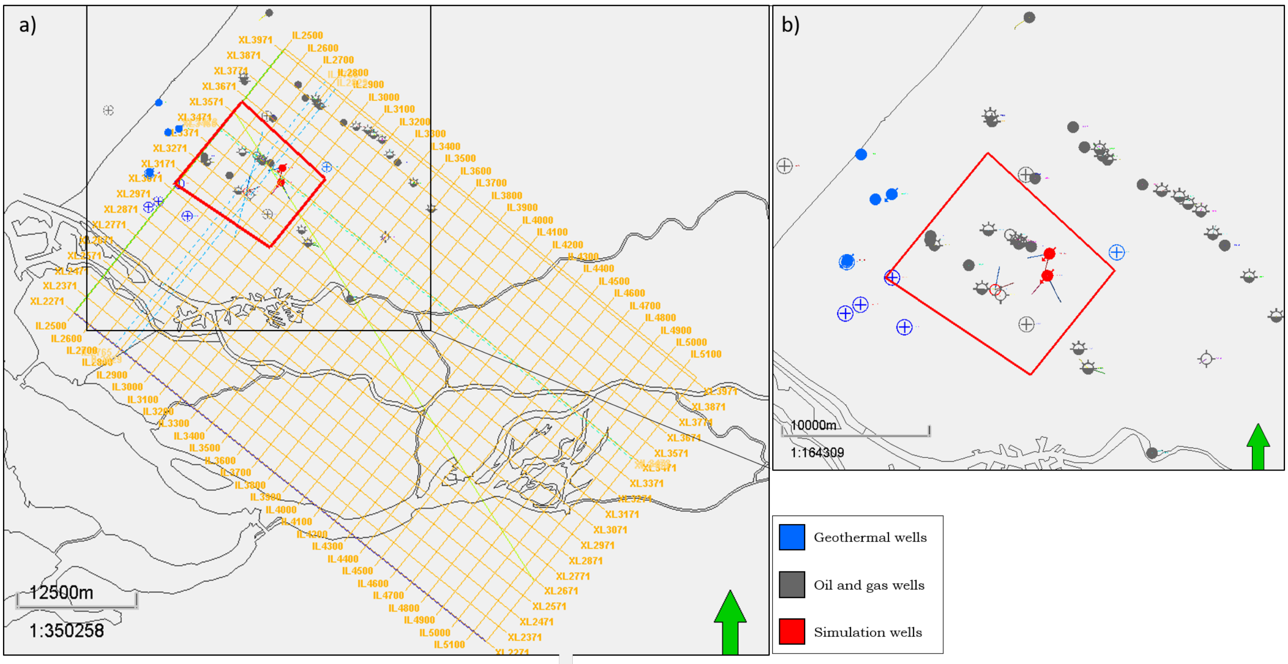

Figure 3.1.1: a) Top map view of the in- and cross-lines of the 3D seismic data set used for this study. b) Top map view of the 55 wells from which data is used in this study. The study area is indicated by the red square.

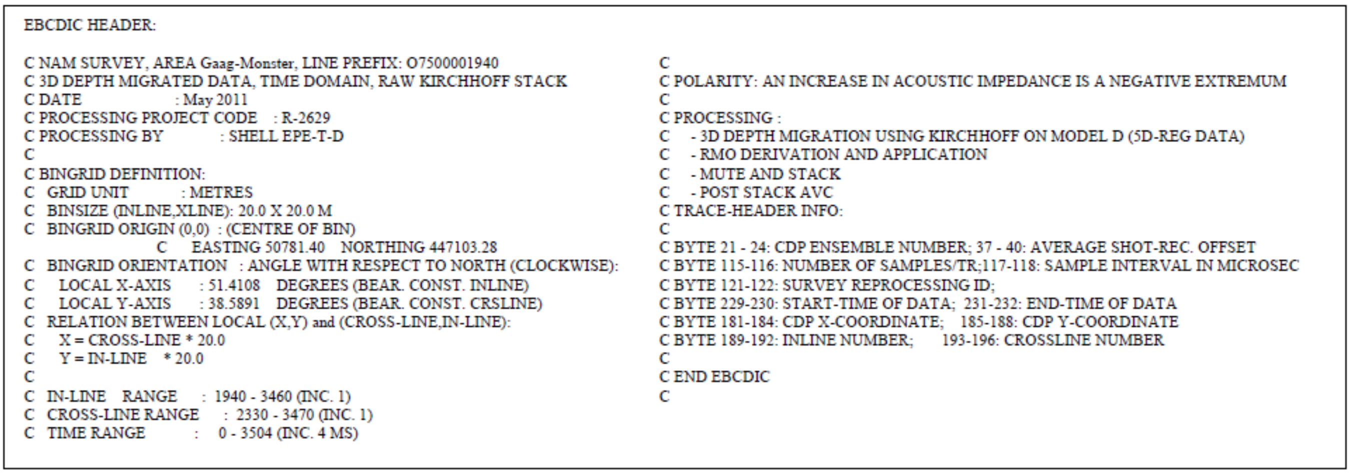

```
EBCDIC HEADER:

C NAM SURVEY, AREA Gaag-Monster, LINE PREFIX: O7500001940
C 3D DEPTH MIGRATED DATA, TIME DOMAIN, RAW KIRCHHOFF STACK
C DATE                    : May 2011
C PROCESSING PROJECT CODE   : R-2629
C PROCESSING BY            : SHELL EPE-T-D
C
C BINGRID DEFINITION:
C   GRID UNIT           : METRES
C   BINSIZE (INLINE,XLINE): 20.0 X 20.0 M
C   BINGRID ORIGIN (0,0)  : (CENTRE OF BIN)
                  C     EASTING 50781.40    NORTHING 447103.28
C   BINGRID ORIENTATION   : ANGLE WITH RESPECT TO NORTH (CLOCKWISE):
C     LOCAL X-AXIS      : 51.4108    DEGREES (BEAR. CONST. INLINE)
C     LOCAL Y-AXIS      : 38.5891    DEGREES (BEAR. CONST. CRSLINE)
C   RELATION BETWEEN LOCAL (X,Y) and (CROSS-LINE,IN-LINE):
C     X = CROSS-LINE * 20.0
C     Y = IN-LINE    * 20.0
C
C   IN-LINE    RANGE      :  1940 - 3460 (INC. 1)
C   CROSS-LINE RANGE      :  2330 - 3470 (INC. 1)
C   TIME RANGE          :    0 - 3504 (INC. 4 MS)
C
C POLARITY: AN INCREASE IN ACOUSTIC IMPEDANCE IS A NEGATIVE EXTREMUM
C
C PROCESSING :
C     - 3D DEPTH MIGRATION USING KIRCHHOFF ON MODEL D (5D-REG DATA)
C     - RMO DERIVATION AND APPLICATION
C     - MUTE AND STACK
C     - POST STACK AVC
C TRACE-HEADER INFO:
C
C BYTE 21 - 24: CDP ENSEMBLE NUMBER; 37 - 40: AVERAGE SHOT-REC. OFFSET
C BYTE 115-116: NUMBER OF SAMPLES/TR;117-118: SAMPLE INTERVAL IN MICROSEC
C BYTE 121-122: SURVEY REPROCESSING ID;
C BYTE 229-230: START-TIME OF DATA;  231-232: END-TIME OF DATA
C BYTE 181-184: CDP X-COORDINATE;    185-188: CDP Y-COORDINATE
C BYTE 189-192: INLINE NUMBER;       193-196: CROSSLINE NUMBER
C
C END EBCDIC
C
```

Figure 3.1.2: Header of seismic cube describing its properties and processing methods (Weerd, 2016).

3.1.2. Wireline Logs, Cores, Cuttings and Production Data

The wireline logs (GR, SP) of 55 wells, lying in the vicinity of the study area, are analyzed in this study (Figure 3.1.1.a). In 40 of these wells, the thickness of the Rodenrijs Claystone Member can be identified. In 37 wells this is possible for the DSSM. Wells that were not drilled deep enough to identify one of these entire intervals are only used for well-to-seismic matching of the Rodenrijs Claystone Member. Available cuttings from DEL-03 and MKP-11 were studied by Drost (2009). PNA-2, RWK-1 and MKP-11 were studied by Smits (2008). 159 cuttings from the geothermal wells VDB-GT-04, PNA-GT-02, HON-GT-01 and HON-GT-02 were analysed by Vondrak et al. (2018). The monthly injection and production volumes of the Ammerlaan and Duijvestijn injectors and producers were publicly available through the NLOG database (TNO, 2019).

3.1.3. Software Packages

- **Petrel**
  A student license from Schlumberger's Petrel was used to compile all subsurface data, perform seismic interpretation and build a 3D reservoir model.

- **Eclipse100**
  Eclipse100 is a multi-phase, multi-compositional dynamic reservoir simulator from Petrel. It is the industry standard for black-oil and dead-oil simulations but it also has a thermal module. This thermal module can simulate the propagation of a thermal front by convection and conduction of heat in a geothermal reservoir. It is important to note that Eclipse100 does not include the full thermal module, which is only available in Eclipse 300.

- **DARTS**
  The Delft Advanced Research Terra Simulator (DARTS) is a multi-purpose geothermal dynamic simulator developed within the faculty of Civil Engineering & Geosciences at Delft University of Technology. It is Python and C++ based and fit for multi-phase and multi-compositional modelling. It distinguishes itself from a conventional reservoir simulator by utilizing the Finite Volume Method combined with an Operator Based Linearization approach that makes the linearization process computationally efficient. The simulator is used with a Python-based interface.

3.2. Geothermal Physics

3.2.1. Conservation of Mass, Momentum and Energy

The principles of dynamic reservoir modelling are based on the conservation laws of physics. These conservation laws are generally categorized in the conservation of mass, momentum and energy. These equations, also given in Voskov (2017), are non-linear because of the inter-dependencies between parameters. For example, a quantity like viscosity is a function of pressure and temperature, creating non-linearity in the equation of the quantity. Heat transfer by convection is also dependent on viscosity, creating more non-linearity in the equation of the conservation of energy. The conservation of mass equation, for fluid flow in it's general form with n_j phases and n_c components, can be represented as follows:

$$\frac{\partial}{\partial t}\left[\phi\sum_{j=1}^{n_j} x_{cj}\rho_j s_j\right] - \nabla\left[\sum_{j=1}^{n_j} x_{cj}\rho_j u_j\right] + \sum_{j=1}^{n_j}\left[x_{cj}\rho_j\tilde{q}_j\right] = 0, \qquad c = 1, ..., n_c \tag{3.1}$$

ϕ - porosity
x_{cj} - the mole fraction of component c in phase j
ρ_j - phase molar density
s_j - phase saturation
u_j - superficial velocity in phase j
$\tilde{q}_j$ - source/sink term of phase j

The three terms describe respectively the accumulation of mass, mass flux and source/sink flux of mass. Since we are only dealing with water at 25-80 °C, and thus a one-phase and one-component system (n_p=n_c=1), the mass conservation equation boils down to:

$$\frac{\partial}{\partial t}(\phi\rho_w) + \nabla(\rho_w u_w) + \rho\tilde{Q}_m = 0 \tag{3.2}$$

Darcy's law is used as a simplified, generalized conservation of momentum equation for laminar fluid flow:

$$u_j = -\frac{K k_{rj}}{\mu_j}(\nabla p_j + \rho_j g \nabla D) \tag{3.3}$$

K - permeability tensor
k_{rj} - relative permeability of phase j
μ_j - phase viscosity
p_j - pressure in phase j
g - gravitational acceleration
D - depth

The first term describes the mobility properties of a fluid and the second term describes the potential. For a system that contains only compressible water, the conservation of momentum equation reduces to:

$$u_w = -\frac{K}{\mu_w}(\nabla p + \rho_w g \nabla D) \tag{3.4}$$

The hot reservoir rock is cooled down when cold water is injected. An energy balance equation is solved after the other material balances at each time step to determine the temperature in each grid block. In Eclipse100 and DARTS, the new pressures and temperatures were then used to calculate other parameters such as brine viscosities for the subsequent time step, for every grid cell (Schlumberger, 2014).

$$\frac{\partial}{\partial t}\left[\phi\sum_{j=1}^{n_j}\rho_j s_j U_j + (1-\phi)\rho_r U_r\right] + \nabla\left[\sum_{j=1}^{n_j} h_j\rho_j U_j\right] + \nabla[\kappa\nabla T] + Q_E = 0 \tag{3.5}$$

ϕ - porosity
ρ_j - phase molar density
s_j - phase saturations
U_j - phase internal energy
ρ_r - rock density
U_r - internal energy of the rock
h_j - phase enthalpy
κ - thermal conduction
∇T - temperature gradient
Q_E - source/sink term

The four terms describe respectively the internal accumulation of energy, heat transfer by convection, heat transfer by conduction and the source/sink of energy. For a system containing only compressible water, the conservation of energy equation reduces to:

$$\frac{\partial}{\partial t}[\phi \rho_w s_w U_w + (1-\phi)\rho_r U_r] + \nabla[h_w \rho_w U_w] + \nabla[\kappa \nabla T] + Q_E = 0 \tag{3.6}$$

3.2.2. Initial and Boundary Conditions

Initial pressure and temperature need to be specified for every grid cell. The initial condition of pressure and temperature-dependent parameters, such as brine viscosity, can then be computed for every grid cell. If a parameter is assumed to stay constant over time, for thermal conductivity in our case, it also needs to be given an initial condition for every grid cell.

In Eclipse100, all boundaries of the model domain are specified as no-flow boundaries. This so-called Neumann boundary condition imposes a mathematical constraint along the boundaries ($\frac{\partial p}{\partial n} = 0$). This constraint ensures that there is no flow transverse the outer boundary edges of the whole grid if no aquifer is specified. The conservation of energy relates to the pressure difference (driving force) where the default is a no-flow boundary (i.e no external pressure support). Therefore, also energy (temperature) is conserved within the boundaries of the model. If heat fluxes from outside the model are likely to be significant, the reservoir model must include blocks to act heat sinks or sources. In our simulations, only the production and injection wells function as sinks and sources for flow and heat. In DARTS, the 3D-grid is transposed to a 1D connection list where the two end-cells are the boundary condition. These cells are given a relatively large volume ($1*10^{10}$ m^3) compared to the grid cells in the connection list. DARTS thereby ensures a minimum heat loss towards the boundaries.

3.2.3. Additional Assumptions

In this study, several physical processes that can occur in a geothermal system have been neglected. Simplifications on the geological and numerical properties in the geothermal model were made. The assumptions that have not been already mentioned above can be summarized as follows:

- The pore space is filled with water. Capillary pressure effects and relative permeability is ignored.
- Brine density is constant over time so there is no convection by buoyancy.
- Brine salinity is constant over time. Salt precipitation is neglected.
- We neglect any skin factor that can be created by damaging the rock around the well-bore during drilling or by precipitation of minerals.
- Thermal cracking, that can occurs due to the temperature differences created near the injector, is neglected.
- We assume that the stratigraphic units are not fractured.
- The presence of hydrocarbons in the reservoir is neglected.
- Heat capacity of rock and brine are defined as one combined parameter and are in the lateral direction homogeneously distributed.
- Heat transfer is governed by conduction and/or convection. Heat transfer by radiation is neglected.

- When analysing the GR-logs, we neglect the presence of radioactive potassium feldspar minerals within the sandstones.
- The horizontal permeability in the X-direction is equal to the permeability in the Y-direction.
- The acoustic velocity is constant over each stratigraphic interval.
- There is no groundwater flow in the reservoir (e.g. active aquifers).
- Proposed well trajectories are equal for all simulations.
- Boundary conditions around the grid are defined as no-flow boundaries. An effect of this is that energy (temperature) is also conserved over the grid.
- During simulation, production is assumed to have a 100% up-time, running 24/7 throughout the defined simulation time.
- Production rates during the summer and winter are equal.
- The flow rate of the producer is equal to the flow rate of the corresponding injector at all times.

4

Simulator Benchmark

This chapter describes the methodology and results of the simulator benchmark. Eclipse100 and DARTS are benchmarked on a simplified box-model of the study area. The simulations are executed on the same desktop to have a fair comparison. The computational performance and modelling performance of the two simulators are compared and the results are discussed.

4.1. Methodology

For simplicity, we develop a simplified 3D box-model of the study area (Figure 4.1.1). The properties of the 3D box-model are displayed in Table 4.1.1. The simulations are performed on the same desktop with an equal simulation time and target time steps to have a fair comparison. The three doublets produce for 100 years with a target time step of 365 days. The number of newton iterations, linear iterations, CPU time and output are then compared to assess the performance of the simulators.

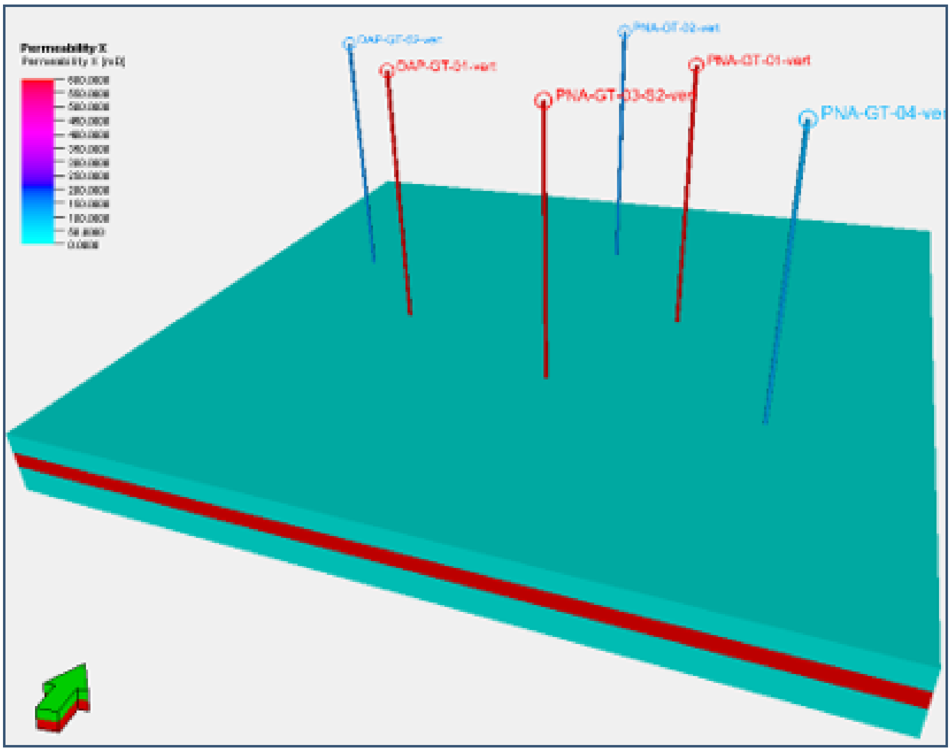

Figure 4.1.1: 3D box-model used for the simulator benchmark.

Table 4.1.1: Properties of the 3D homogeneous box-model used for simulator benchmark.

Parameter	Value	Unit
nx*ny*nz	118*114*20	-
dx*dy*dz	50*50*12	m
Location DUV producer-injector	67,40-97,37	X,Y
Location AMM producer-injector	81,52-64,28	X,Y
Location DAP producer-injector	38,63-21,45	X,Y
Uniform active filter	1	-
Uniform reservoir porosity	24	%
Uniform reservoir permeability	600	mD
Top reservoir depth	2157	m
Overburden thickness	160	m
Reservoir thickness	120	m
Underburden thickness	210	m
Uniform initial pressure	210	bar
Uniform initial temperature	77	°C
Water rate prod/inj	8400	m^3/day
Injection temperature	30	°C
Simulation time	100*365	days
Thermal conductivity rock	100	kJ/m/day/K
Heat capacity rock	2700	kJ/m^3/K

4.2. Computational Performance

The number of time steps, non-linear iterations and linear iterations in Eclipse100 and DARTS are displayed in Table 4.2.1. The CPU time of DARTS (228s) is much lower compared to Eclipse100 (845s). A possible explanation is that computations in Eclipse100 are performed on a 3D-grid while DARTS converts the 3D-grid to a 1D-array before a simulation is started. Eclipse100 uses an implicit finite difference scheme where the computations are done over a matrix. Computations over an array are cheaper than computations over a matrix. So even though DARTS needs more iterations to converge to a solution, the CPU time for the same simulation is less. Another possibility is that DARTS uses operator-based-linearization (OBL) for solving the conservation laws. This linearization method has proven to be computationally efficient compared to the conventional approach in reservoir simulation in which the Newton–Raphson method is applied. (Voskov, 2017). The number of points in the interpolation controls the accuracy of the approximation of the nonlinear physics. This is similar to controlling the grid size (up-scaling and refinement) for determining the accuracy of the approximation in space and time. For the simulator benchmark, 64 interpolation points were used.

Table 4.2.1: Time steps, (non-)linear iterations and CPU time of Eclipse100 and DARTS for a simulation of a simplified 3D box-model of the study area. The simulations were performed on the same desktop and CPU. The simulation time was 100 years with a target time step of 365 days.

Simulator	Time steps [-]	Non-linear iterations [-]	Linear iterations [-]	CPU time [s]
Eclipse100	104	104	588	845
DARTS	105	340	3718	228

4.3. Modelling Performance

Eclipse100 and DARTS incorporate temperature, pressure and density dependency of some parameters during simulations (Figure 4.3.1). Before a simulation takes place, the user sets the lower and upper limit value for pressure and temperature. DARTS and Eclipse100 then creates tables for every temperature and dependent parameter and use correlations to compute values for the intended parameter. The conservation equations for mass, momentum and energy are solved for each grid cell, in DARTS and Eclipse100. For every grid cell, the temperature- and pressure-dependent parameters are calculated by interpolating over the values in the tables. The number of inter-dependencies will increase the time it takes for a simulator to construct tables and perform a time-step. The inter-dependencies that are considered in Eclipse100 are limited to the available keywords. The advantage of DARTS is that it is flexible and inter-dependencies can be built in the model, using the correlations that the user finds most suitable. In Eclipse100 the inter-dependencies compressibility, formation water viscosity and formation water density are built in and cannot be altered by the user.

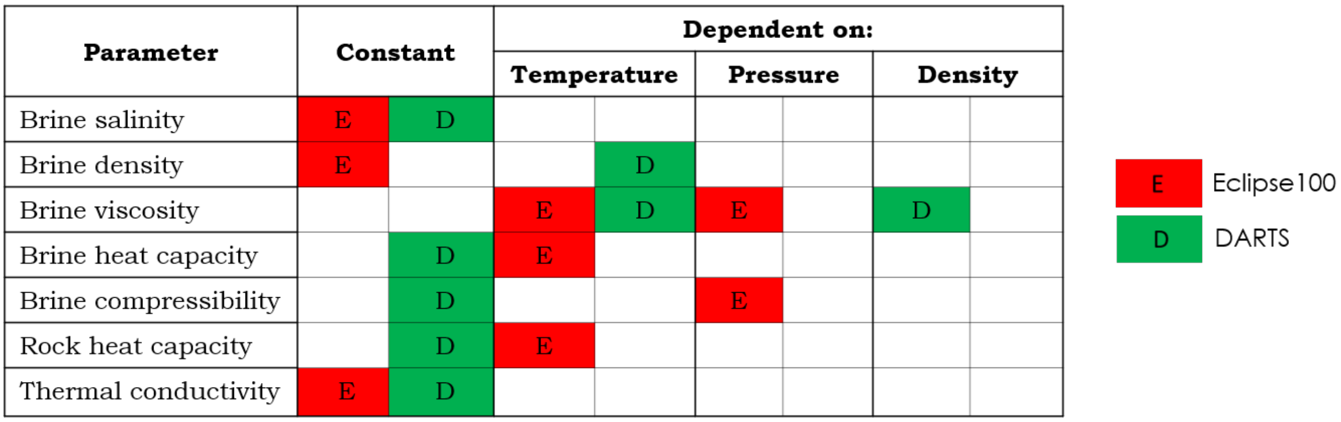

Parameter	**Constant**		**Dependent on:**					
			Temperature		**Pressure**		**Density**	
Brine salinity	🟥 E	🟩 D						
Brine density	🟥 E			🟩 D				
Brine viscosity			🟥 E	🟩 D	🟥 E		🟩 D	
Brine heat capacity		🟩 D	🟥 E					
Brine compressibility		🟩 D			🟥 E			
Rock heat capacity		🟩 D	🟥 E					
Thermal conductivity	🟥 E	🟩 D						

🟥 E Eclipse100
🟩 D DARTS

Figure 4.3.1: Overview of the incorporation of constant, pressure , temperature and density dependent parameters of rock and fluid in the reservoir simulators Eclipse100 (red) and DARTS (green). A parameter can be dependent on multiple parameters (e.g. in Eclipse100 viscosity is dependent on temperature and pressure).

The output of pressure and temperature are different for the two simulators. From a cross-section of the reservoir, it is observed that in Eclipse100 (Figure 4.3.2.a), the pressure distribution outside the influence area follows a vertical pressure gradient, caused by the gravity effect of the hydrostatic column. In DARTS (Figure 4.3.2.b), this effect has not been modelled, creating an initial uniform pressure distribution. Because of this, there is no pressure draw-down and pressure build-up effect at respectively the producer and the injector. In Eclipse100, these pressure effects around the well create a higher pressure gradient between the injector and producer, compared to DARTS. This enhances flow from the injector to the producer and is interpreted to be one reason that the cold waterfront has moved more towards the producer compared to the DARTS output (Figure 4.3.3).

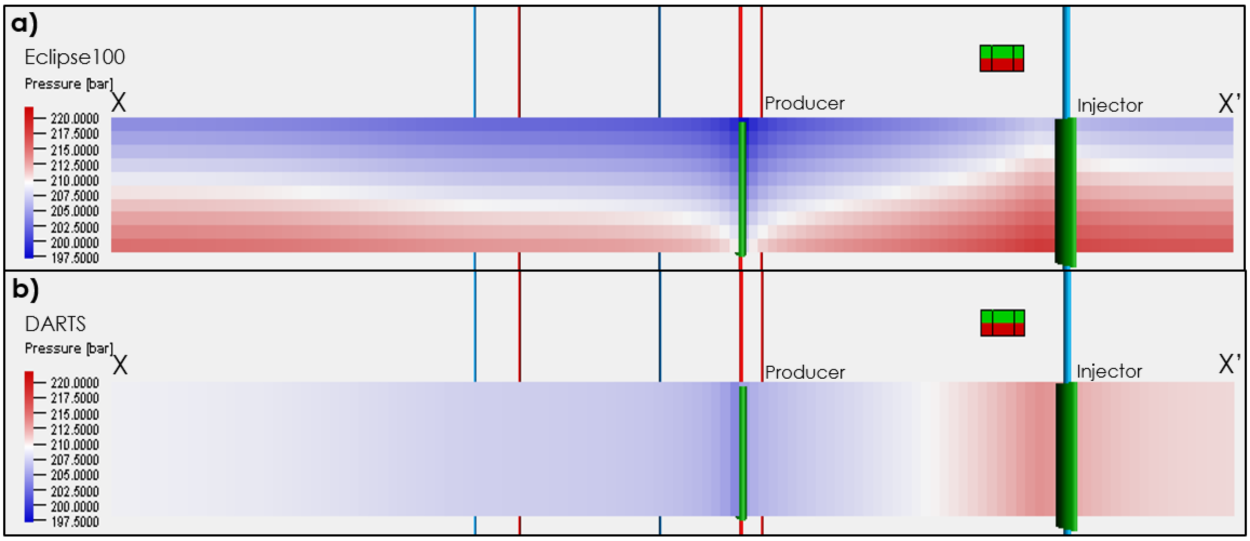

Figure 4.3.2: Benchmark test output of pressure is visualized in a cross-section side-view of the simplified 3D box-model of the study area for Eclipse100 (a) and DARTS (b). The cross-section is taken from X to X' which is displayed in Figure 4.3.4.

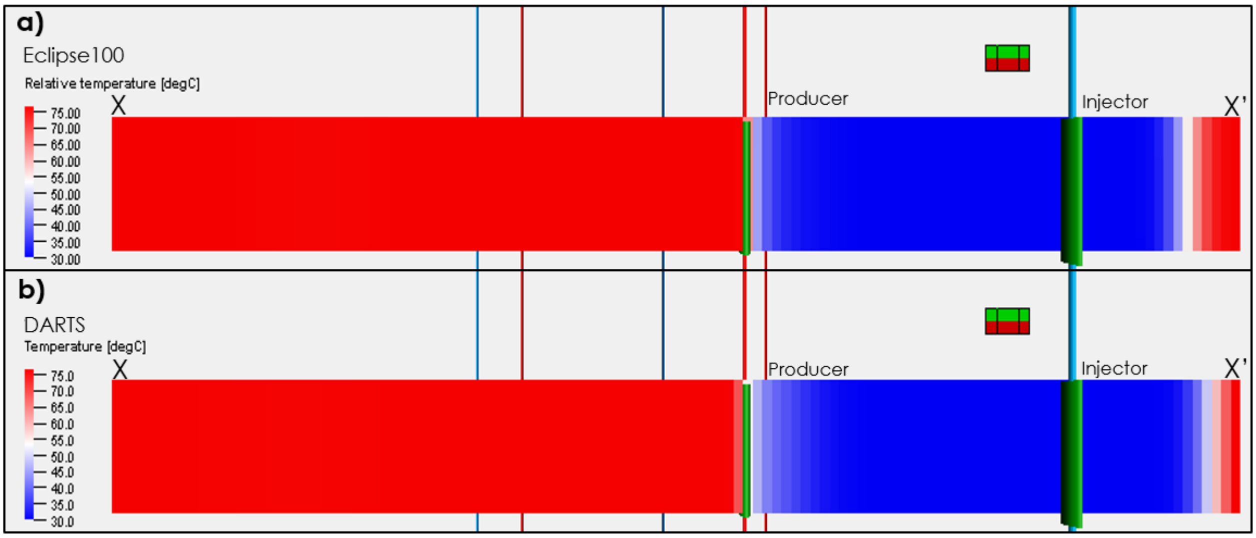

Figure 4.3.3: Benchmark test output of temperature is visualized in a cross-section side-view of the simplified 3D box-model of the study area for DARTS (a) and Eclipse100 (b). The cross-section is taken from X to X' which is displayed in Figure 4.3.4.

The way inter-dependencies of parameters are incorporated in the simulators can also cause deviations in the output of pressure and temperature. DARTS incorporates temperature-dependent density and density-dependent viscosity. However, since gravity effects are not included, these dependencies do not affect the output of pressure and temperature. Consequently, we can conclude that for this simulation in DARTS, the parameters displayed in Figure 4.3.1 are constant over time. Eclipse100 does incorporate temperature and pressure dependent viscosity. As cold water is injected, viscosity increases around the injector. The cold waterfront will move slower compared to a simulator that keeps viscosity constant over time. Temperature-dependent heat capacity will lead to a decrease in heat capacity, lowering the rate at which the rock is cooled down. This also results in a slower-moving cold waterfront. Since formation water compressibility is low (0.00003500/bar) and the pressure differences in the reservoir are roughly 23 bar, the effect that pressure differences have is a maximum compression in volume of 0.000805 of the original volume, and therefore not considered significant. The above-mentioned differences in modelling of the two simulators result in the deviations of the cold waterfront propagation, as displayed in Figure 4.3.4.

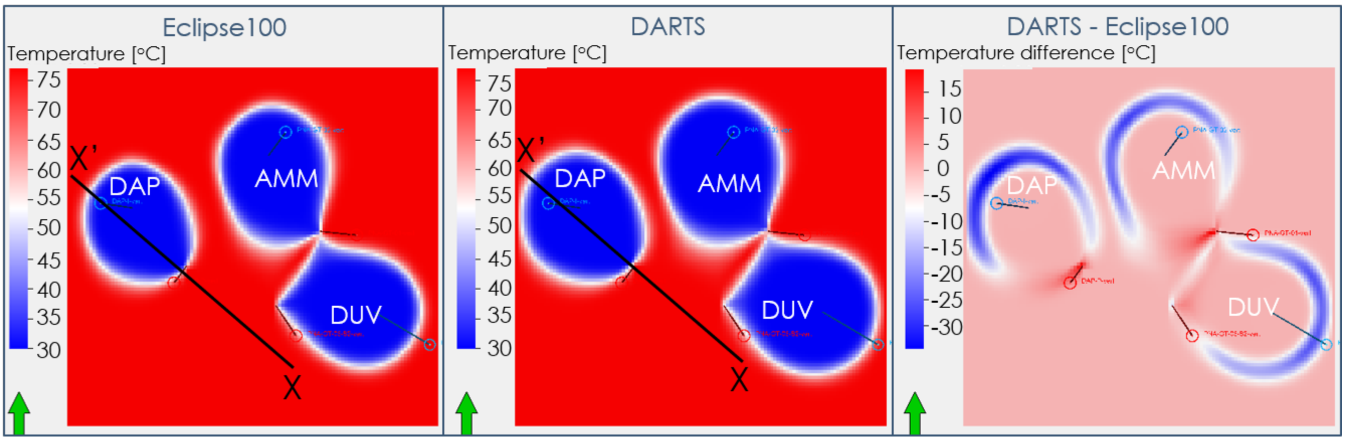

Figure 4.3.4: Top-view of the temperature output for Eclipse100 (a), DARTS (b) and the difference between them, subtracting Eclipse from DARTS (c). The cross sections for Figure 4.3.2 and Figure 4.3.3 are displayed for the absolute temperature figures (left and center).

4.4. Choice of Simulator

From this benchmark on-wards, all simulations were performed in Eclipse100. This decision is made for three reasons. The first reason is that Eclipse100 was available on a cloud server with a dual Intel(R) Xeon(R) CPU (2.60GHz, 2593 Mhz, 4 cores and 4 logical processors) that performs computations in 4-way parallel, dramatically decreasing the simulation time (Table 4.4.1). The second reason is that there was no Python GUI available on this cloud server. Hence it was not possible to run DARTS with a dual CPU. The third reason is that the high amount of parametric combinations for the discrete parameter analysis required a lot of iterative work. Since our static and dynamic reservoir model was created in Petrel, it was much more convenient to use the integrated Eclipse100 simulator instead of exporting and importing the grids to and from DARTS.

Table 4.4.1: Amount of time steps and simulation time of Eclipse100 running parallel on a dual-CPU compared to DARTS running on a single CPU. The target time step was 365 days.

Simulator	CPU [GHz]	Time steps [-]	Simulation time [s]
Eclipse100	2.6 & 2.6	104	59
DARTS	2.8	105	228

4.5. Discussion

Simulator benchmarks of different studies are difficult to compare since the performance of a simulator is dependent on the set up of the simulation and the CPU/GPU used for computations. Wang et al. (2019) has shown that DARTS achieves results that have good matches with the simulators AD-GPRS and TOUGH2 while simulation time was significantly reduced. The benchmark performed by Wang et al. (2019) used a model with fewer grid cells and wells compared to the benchmark of this study. Nonetheless, the simulation time in DARTS was 3.7 times lower than the simulation time in Eclipse100. It is not possible to pinpoint one reason for the higher computational performance since the physics of the model are not handled equally in the two reservoir simulators. Handling the physics differently causes deviations in the output of pressure and temperature. When incorporating a density-dependent hydrostatic pressure, a pressure gradient is created over a higher amount of cells compared to a situation with uniform pressure. It will then take more computations to converge to a solution for the conservation of momentum and mass. Also, not incorporating certain interdependencies of parameters, such as temperature-dependent heat capacity of rock and formation water, decreases the number of computations required for a time step. We can only fully contribute a reduction of simulation time to a more efficient linearization method (such as OBL) if the handling of the physics is equivalent to a simulation where linearization is performed conventionally (e.g. Newton-Raphson). Since the aim of this chapter is to benchmark the simulators, building in new physics in DARTS was considered to be beyond the scope. It is however possible and this chapter can be used to further develop DARTS and increase its modelling accuracy. The gravity effect on pressure is currently being implemented and tested in DARTS (Wang, pers. comm.).

5

Development of the Static Reservoir Model

This chapter describes the methodology for developing a static reservoir model. The results of seismic interpretation, well correlation, velocity modelling, isochoring, structural modelling and static property modelling are presented.

5.1. Methodology

The methodology for establishing a static reservoir model is visualized in Figure 5.1.1. Because reservoir modeling is an iterative process, the actual workflow is not as one-directional as displayed in this visualization. The first three steps in this process were executed by PanTerra (Weerd, 2016). They made a well-seismic-tie (step 1) by creating a synthetic seismogram. Such a seismogram is acquired by multiplying the sonic and density log. This log was then corrected with check-shot data that results in interval velocities and a time-to-depth relation. The synthetic seismogram was matched with the seismic reflection data, time-shifting the synthetic where necessary. Alternatively, a more pragmatic velocity modeling approach led to a velocity model that was applied to all the wells. The seismic interpretation (steps 2 and 3) of Weerd (2016) did not cover the whole study area. These steps are therefore repeated for our study area. The most expressive and relevant seismic horizons are picked and faults are interpreted. A large set of wells is analysed for regional well correlation. The seismic horizons are interpreted in time and then converted to depth with the established velocity model. Pillar gridding is used to establish a structural model. Petrophysical data from the wells that lied within and around the study area is processed, populated in the grid after facies modeling and then up-scaled, leading to a reservoir model that approximates the geological setting.

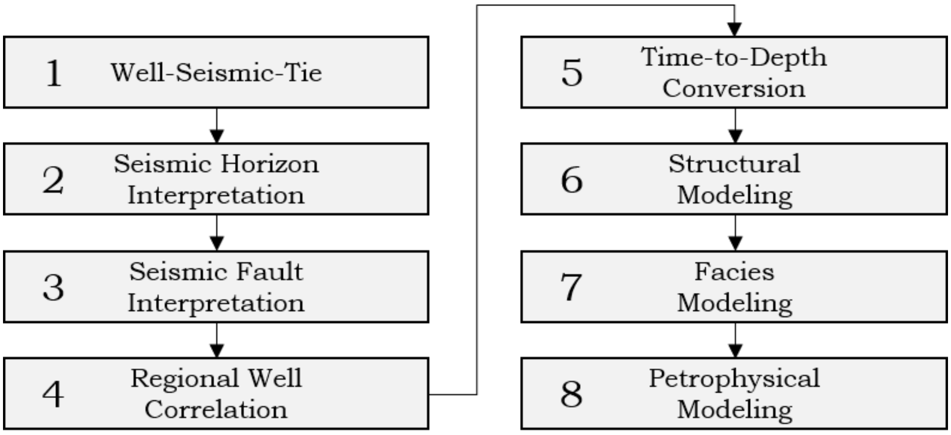

Figure 5.1.1: Proposed methodology for establishing a static reservoir model.

5.2. Seismic Horizon Interpretation

The seismic character of each horizon is defined to be able to identify the corresponding seismic reflectors (Table 5.2.1). The seismic data near the wells hold the least amount of uncertainty due to the encountered well tops during drilling. The first seismic picks are tracked on a composite line that cross through the wells because the cross- and inlines stand at a right angle on the fault strike. It is then easier to see the seismic expressions of the structures so it is chosen to first take steps along these lines. The stepping increment is set at 16 lines but is decreased as structural complexity increases. The seismic polarity convention and display can be found in Appendix A.1. The resulting horizons, after 3D-autotracking, can be found in Appendix A.2.

Table 5.2.1: Seismic horizon properties for the interpreted reflectors.

Transition	Kick	Stratigraphic transition
North Sea Grp. - Chalk Grp.	Hard	Sharp transition from grey sandstones and clays to dense limestones and marly limestones.
Chalk Grp. - Holland Grp.	Soft	From limestones to red-brown marls. This is mainly expressed as a decrease in GR and an increase in resistivity and sonic velocity.
Holland Grp. - Vlieland Fm.	Hard	Conformable contact with a transition from marls to very silty to sandy sediment with many intercalated siltstone and very fine sandstone beds.
Vlieland Fm. - Rodenrijs Claystone Mbr.	Hard	Unconformable transition from sandstones to silty to sandy lignitic claystones.
Rodenrijs Claystone Mbr. - Delft Sandstone Mbr.	Soft	Transition clay- and siltstones to fluvial sandstone deposits.
Delft Sandstone Mbr. - Pijnacker Unit	Hard	Transition from fluvial sandstone deposits to clay- and siltstones.

5.3. Seismic Fault Interpretation

The extensive faulting is easily spotted on seismic cross-sections of the study area. The major faults in the study area are tracked along the cross- and inlines. Minor faults are only interpreted within the relevant stratigraphic units (Rodenrijs, DSSM and Alblasserdam) and structural units (Pijnacker High, Delft High and Vrijenban Syncline). The reason for this is that it is assumed that the influence radii of the simulation wells would not affect the area outside these criteria. This assumption is validated with preliminary runs during dynamic reservoir simulation. A result of this validation can be found in Appendix F.1. A total number of 8 major faults and three minor faults are interpreted (Figure 5.4.1). The two most important faults in the study area are the fault that separates the Delft High from the Vrijenban Syncline (Fault 2) and the fault that separates the Pijnacker High from the Vrijenban Syncline (Fault 6). These are major faults that lie within the influence radii of the simulation wells. Studying and approximating the transmissibility of these faults is considered to be beyond the scope of this study. Instead, the fault transmissbility multiplier is varied from 1 (faults fully transmissible) to 0 (faults sealing) to see observe what effect is has on the output of the simulations.

5.4. Regional Well Correlation

Well correlation is performed for three reasons:

- Finding regional trends in the thicknesses of the Rodenrijs Claystone Member and Delft Sandstone Member.
- Gathering control data on the well top depths for time-to-depth conversion.
- Gathering control data on the member thicknesses for isochoring, necessary for the mapping of the DSSM horizon.

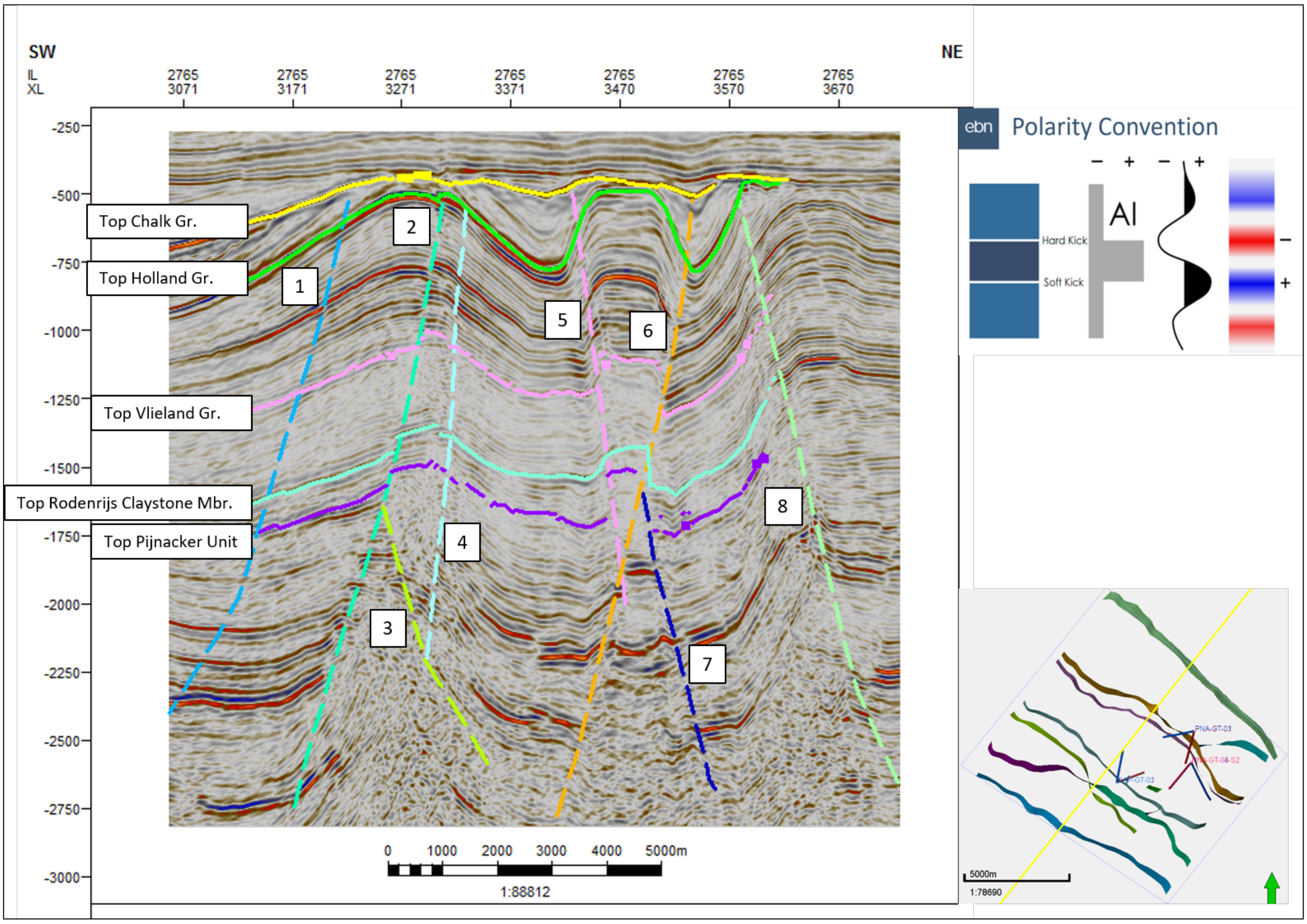

Figure 5.4.1: Interpretation window with the interpreted faults and horizons along inline 2765.

An extensive well correlation study was performed in previous work (Weerd, 2016). This study is reviewed and the more recently drilled geothermal wells are added to the study. Cross-sections are taken along (strike 1-3) and across (cross 1-5) the fault orientation (Figure 5.4.2). Only the wells that drilled through the DSSM accompanied with wireline log data are included in the correlation panels. The wells that do not fulfil these criteria are used as control data for time-to-depth conversion and as control data for isochoring (Section 5.6). A complete overview of all the thicknesses and correlation panels can be found in Appendix C. Cross panels 1-5 shows that the DSSM thickness decreases from the southwest towards the northeast (Figure 5.4.3), which contradicts the depositional model from Den Hartog Jager (1996) (Figure 2.2.1), where the opposite is proposed. Donselaar et al. (2015) proposes that the DSSM can be subdivided into three separate zones based on their GR-readings and the corresponding interpreted net-to-gross ratio. In most wells there is indeed a zone with a lower net-to-gross ratio but the lateral continuity of such zones in a migrating meandering channel belt system are often not very extensive. A migrating river would cut into the flood plain (that is expressive for the low net-to-gross zone encountered in the well), disrupting its continuity laterally. It is therefore chosen to not model these zones as continuous layers but instead respect the clay-content at these positions in the well when populating the grid with facies, porosity and permeability. In addition, it has been shown that in a meandering channel belt system, with a net-to-gross higher than 0.3, all channels are connected and able to flow (Larue and Hovadik, 2006). So modelling a continuous zone with a low permeability in the middle of our reservoir may not be realistic.

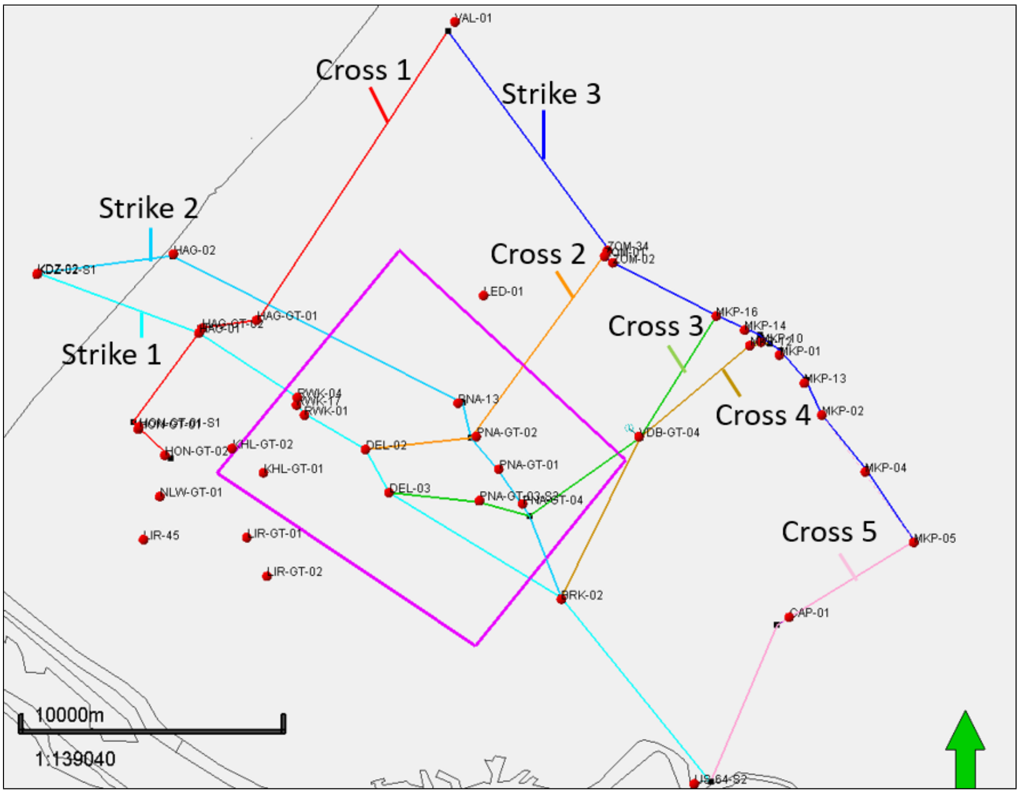

Figure 5.4.2: Well correlation cross-sections used for regional well correlation. Study area is indicated in purple.

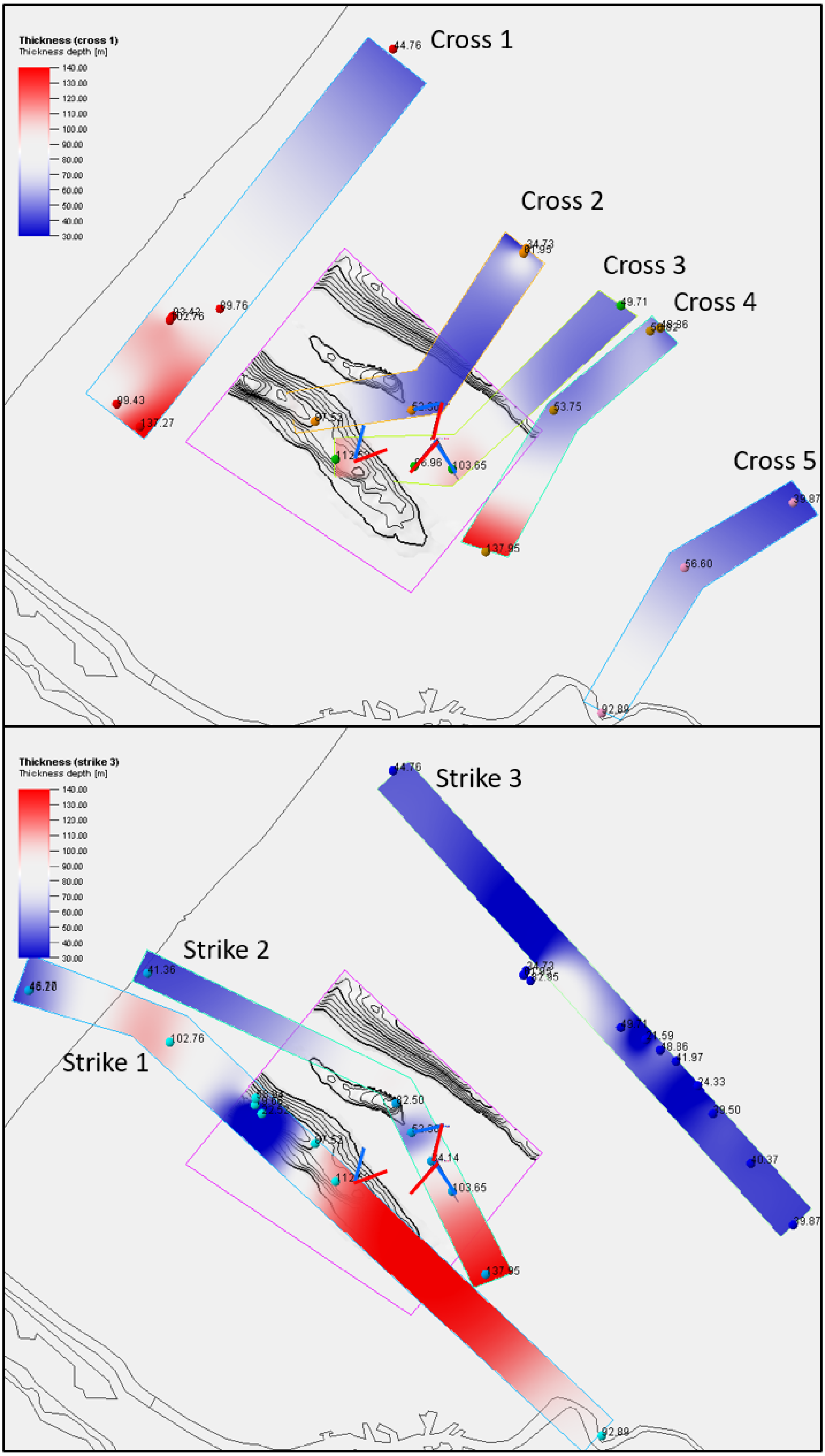

Figure 5.4.3: Regional thickness trends of the DSSM for the correlation panels displayed in Figure 5.4.2

.

5.5. Time-to-Depth Conversion

A well-to-seismic tie can be used to relate features and well data to the peaks and troughs on the seismic line that passes through the well location. The old oil and gas wells, drilled in the highs around the study area, provide sufficient velocity data (density logs, sonic logs and check-shot data) to establish such a velocity model. However, there was a lack of data acquisition done for the geothermal wells, drilled in the flanks of the crests, towards the lows in and around the study area. This results in a biased sampling of the velocity field. Nevertheless, Weerd (2016) performed a well-to-seismic tie for PNA-13, that was drilled through the Pijnacker High. A synthetic was established with a zero-phase wavelet, extracted from full stack at PNA-13 (~15 Hz). Figure 5.5.1 shows that the match between synthetics and seismic results in a reasonable match.

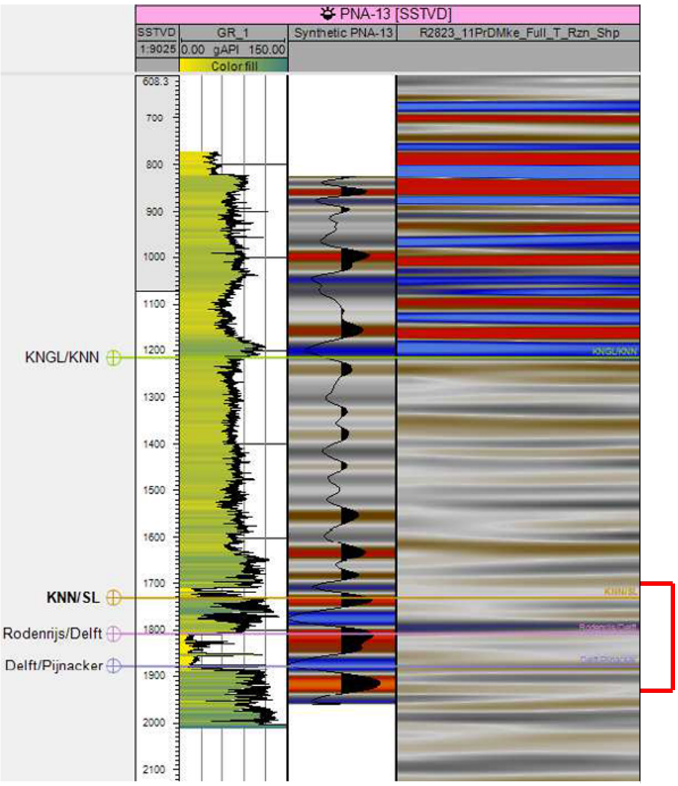

Figure 5.5.1: Well-to-seismic tie for PNA-13 with the inconclusive zone indicated in red. Polarity as displayed in Appendix A.1.

Note that this result is considered inconclusive around the reservoir zone (Figure 5.5.1). Besides, it would mean that the domain conversion of a synclinal area would be based on a time-depth relation retrieved from data of one well in a nearby anticline. Weerd (2016) made the decision to expand the velocity data pool by examining more velocity data from wells within the WNB. Velocity data from a subset of wells from the VELMOD-2 velocity study (Dalfsen et al., 2007) is used to establish a more representative data set. This study used the velocity model created by Weerd (2016) to convert the horizons and faults to depth. Figure 5.5.2 displays the method for the assignment of a z_{mid} value to a deviated borehole. The velocity relations are derived by simple least-squares regression from the V_{int}-Z_{mid} data points (Figure 5.5.3). The whole stratigraphy was exposed to compaction during the burial phase so that the velocity increases with depth (Dalfsen et al., 2007). The velocity model can therefore be described by the linear pseudo velocity equation:

$$v = v_0 + k * Z \tag{5.1}$$

where v is the layer-velocity, v_0 and k are the regression coefficients and Z is depth. The final layer-cake velocity model derived through this methodology is shown in Table 5.5.1.

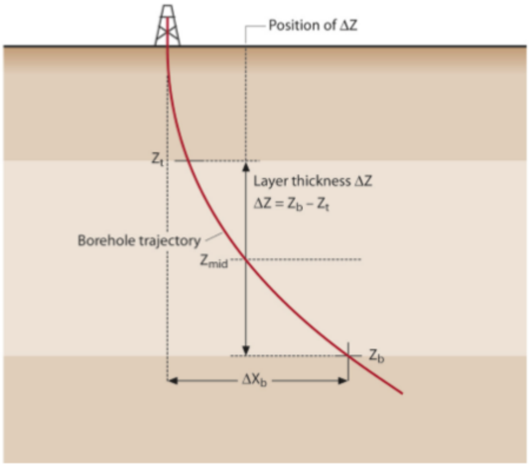

Figure 5.5.2: Assignment of layer cake data (Z_{mid} and ΔZ) to a deviated borehole (Dalfsen et al., 2007).

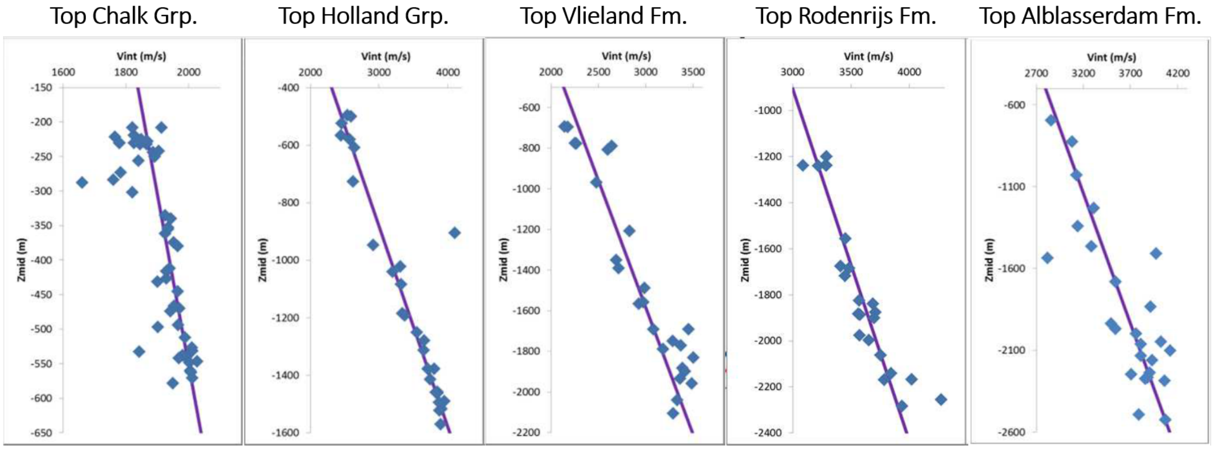

Figure 5.5.3: Z_{mid} and ΔZ data points from wells within the WNB. Regression lines define the v_0+k_z relationship.

Table 5.5.1: Layer-cake velocity model used for time-to-depth conversion.

Surface	**V_0 [m/s]**	**K [-]**
Top Chalk Grp.	1777.6	-0.4015
Top Holland Grp.	1737.1	-1.4319
Top Vlieland Fm.	1731.4	-0.8009
Top Rodenrijs Claystone Mbr.	2406.7	-0.6543
Top Pijnacker Unit	2481.8	-0.6293

Quality control gives an indication of the accuracy of the proposed layer-cake velocity model. Surfaces are created in the time domain and converted to depth with the proposed velocity model. A residual value is calculated by subtracting the converted surface depth in the well from the corresponding well top depth in the same well. A complete overview of the surfaces in depth, the residual values and the residual value maps can be found in Appendix B. A common rule-of-thumb is that a residual value should not be greater than 2% of the depth of the surface encountered in the well. All residuals fulfill this requirement except for the Rodenrijs Claystone Mbr in well PNA-02, PNA-08, PNA-09, RWK-01, RWK-06 and RWK-18-S1. For PNA-08 this is caused because it encounters several faults. RWK-01, PNA-02 and PNA-09 are also drilled in the highs and in the vicinity of faults, where the seismic quality was low. The SP logs show well top depths deeper than interpreted on seismic. It could be that due to faulting the seismic reflector is deeper than interpreted. There are no other logs available to check if the interpreted well top depth is correct. The wells with high residuals are very old wells (1954-1957) and the other newer wells (1977-

1994), drilled in the same anticlines, do follow the seismic reflector. We choose to not use these deviant older well tops for well top correction during the surface creation process.

5.6. Isochoring for the Top Delft Sandstone Member Horizon

The DSSM reflector is not laterally continuous and therefore difficult to track on seismics. This is caused by the fact that the DSSM consists of fluvial deposits that were bound to lateral migration of fluvial systems while the overlying and underlying deposits were also sand-bearing, but to a lesser extent. Therefore, there is no sharp transition in acoustic impedance and no clear marker visible on seismic. Other factors are the limitation of seismic resolution and the presence of faults, both affecting the seismic quality.

Therefore, it is decided to extrapolate the top reservoir (DSSM) surface from the Rodenrijs Claystone Mbr. and Pijnacker Unit surfaces by respectively subtracting and adding the interpolated true-vertical-thickness (TVT) isochore maps (Figure 5.6.1). Because there is enough control data around the study area, the isochore interpolation algorithm is used. If there would not have been enough control data, the isochore interpolation method would cause divergence of the TVT values around the edge of the map.

In 46 wells the TVT of the Rodenrijs Claystone Mbr is encountered and in 43 wells the TVT of the DSSM. The average TVT of the Rodenrijs Claystone Mbr. and the DSSM is respectively 93 and 55 meter. The spread of the TVT values of the Rodenrijs Claystone Mbr. is higher than the TVT values of the DSSM (Figure 5.6.2.a).

In Figure 5.6.2.b, it is shown that DSSM TVT decreases from the southwest towards the northeast, which is also shown in the regional well correlation (Section 5.4). There are two bulls-eyes in the west of the study area where low and high TVT's were encountered. The low cases are encountered in old oil wells drilled through the Delft High and the high cases are encountered in geothermal wells drilled through the lows, next to the Delft High.

The resulting final top DSSM surface depths range from 1600-2000m in the highs and from 2000-2300m in the lows (Figure 5.6.3).

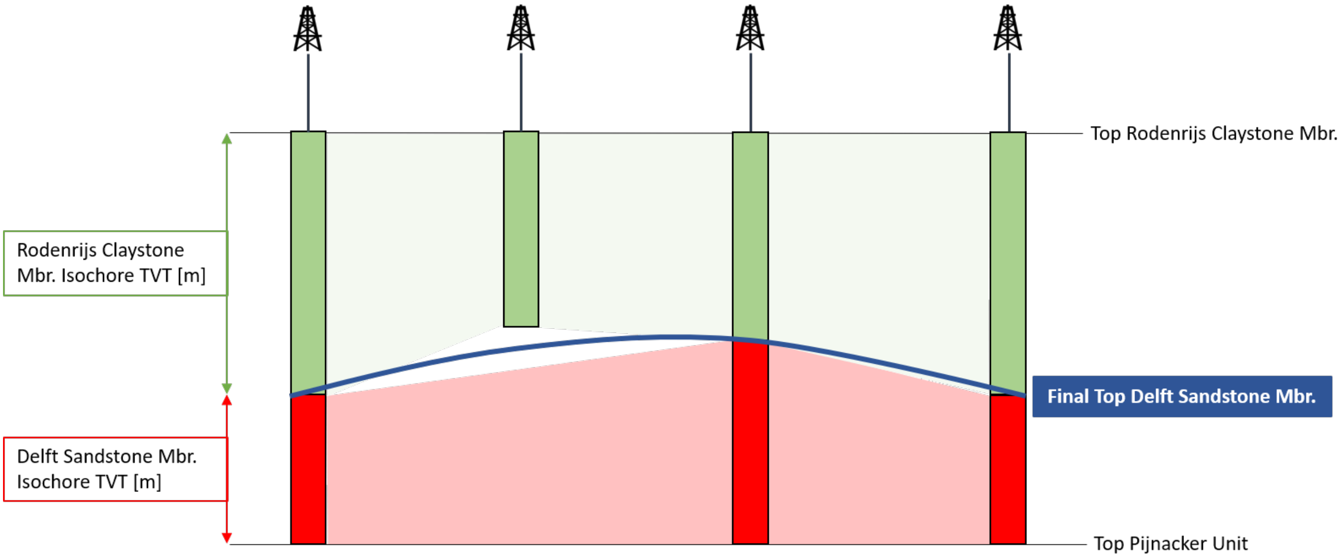

Figure 5.6.1: Illustration on the methodology to establish the final Delft Sandstone Mbr. surface by averaging the horizons that resulted from adding and subtracting the isochore maps from the Pijnacker Unit and the Rodenrijs Claystone Mbr. depth surfaces.

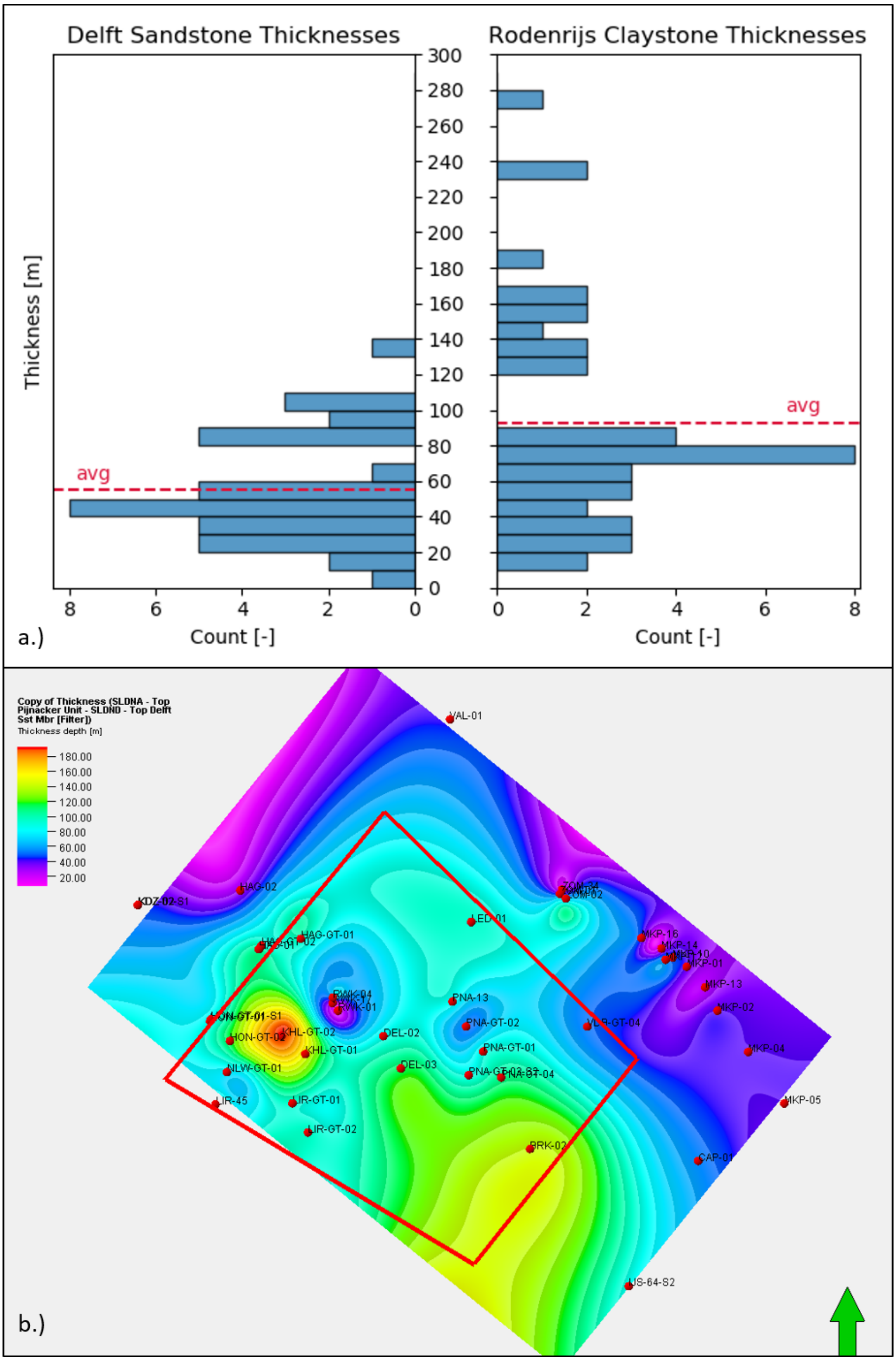

Figure 5.6.2: a.) DSSM (43 counts) and Rodenrijs Claystone Mbr. (46 counts) isochore thicknesses and average isochore thicknesses (red line). b.) DSSM isochore map with the study area indicated in red.

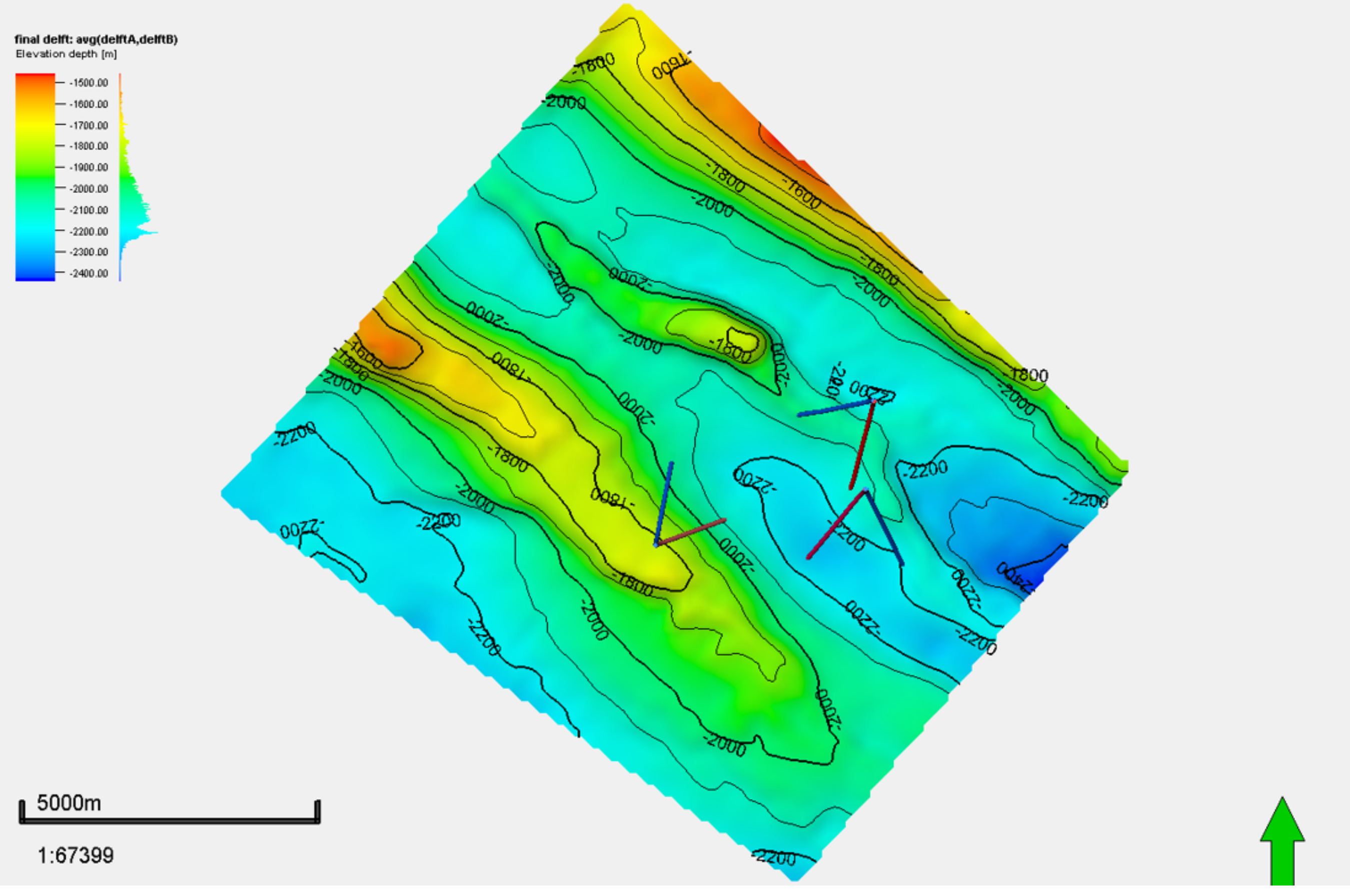

Figure 5.6.3: Final Top Delft Sandstone Member surface.

5.7. Structural Modeling

Having all the necessary surfaces and faults in depth, it is possible to build a structural reservoir model. The simplest model, used for the simulator benchmark in Chapter 4, is a box model with a homogeneous reservoir zone and a confined overburden without porosity or permeability. A more complex structural facies model is constructed that includes faults and heterogeneities on porosity, permeability, cell thicknesses and thermal conductivity. A 3D-grid is created through pillar gridding, using the top of the Rodenrijs Claystone Member as the top of the overburden, the top of the DSSM as the top of the reservoir, the top of the Pijnacker Unit as the top of the underburden and the top of the Papekop Unit as the bottom of the underburden. The cell increment in the lateral direction is set at 50m by 50m and the gridding direction is set along the orientation of the major faults (NW-SE). After importing the faults into the 3D-grid, structural modelling is required to ensure that the cell geometry would not give convergence problems during dynamic simulations. All faults are given a pillar increment of 500m, small enough to capture the changes in inclination over the length of the faults . They are then truncated, smoothed and merged where required. The final faults and grid skeletons are displayed in Figure 5.7.1. The average grid cell width in the x and y direction is 50m. The average height of the grid cells in the reservoir zone was 6.5m. Vertical layering determined vertical cell heights. The overburden, reservoir and underburden are divided in respectively 3, 20 and 3 layers resulting in an average cell height of respectively 27m, 7m, and 34m.

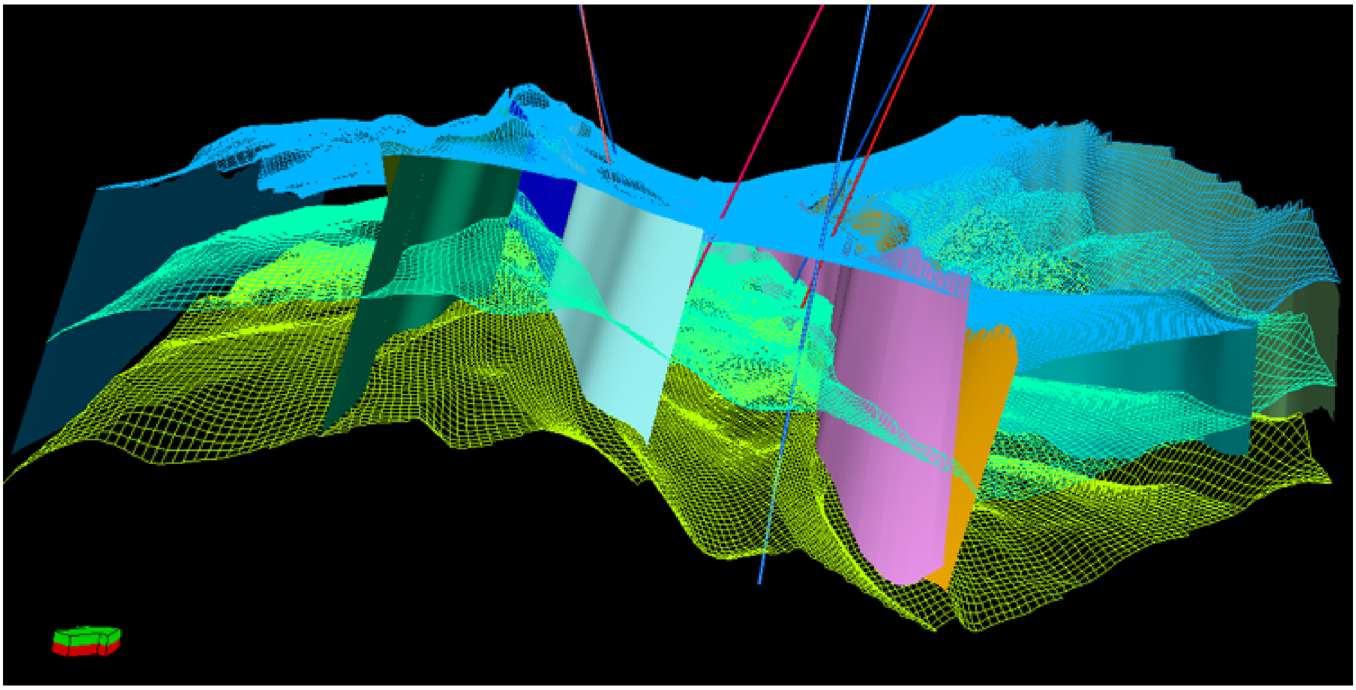

Figure 5.7.1: Structural reservoir model with grid skeletons and fault planes. The vertical scale is exaggerated by a factor of 2 compared to the horizontal scale.

5.8. Static Property Modeling

Property modeling is performed to populate the structural reservoir model with static reservoir properties. These properties are assumed to stay constant over time. The results of reviewing literature and petrophysical analysis are used to establish three discrete realizations of lithology and porosity models. For every realization, three different permeability models are defined.

5.8.1. Lithology and Porosity Model

A discrete lithology log is created based on GR-logs of the wells in the study area. Four lithology classifications are defined (Table 5.8.1). Note that the GR-log readings are not normalized over the different wells.

Table 5.8.1: Lithology log based on GR-reading in the wells.

Lithology	**GR Range**
Coarse Sand	GR<30
Fine Sand	30<GR<60
Shaly Sand	60<GR<100
Shale	GR>100

The object-based modeling algorithm is used to model fluvial channels. The lithology logs are proportionally up-scaled to populate the facies in the 3D grid while respecting the lithology determined at the wells. Proportions of the different facies are derived by trial-and-error so that the distribution of the lithologies of our facies model matched the distribution of the lithologies as they are interpreted for the wireline logs. Shale and shaly sand are populated in the floodplains. Fine sand is populated in the overbank deposits and coarse sand in the channel deposits. The fluvial channels are given the following geometrical properties:

- Channel thickness varies from 1.5 to 4.5 m with an average of 3 m (Loerakker, 2009).
- Channel width varies from 12 to 195 m with an average of 92 m Davies et al. (1992); Gilding (2010).
- Channel sinuosity values are set to Petrel default: Wave length of 1500 m, amplitude of 800 m and a drift of 0.2.

- Three geological realizations are created with varying channel orientation of 285°, 315° and 345° (Vondrak et al., 2018).

Porosity values are available from porosity logs of PNA-15, MKP-10, MKP-11, MKP-12, MKP-13 and MKP-14. These were a product of neutron-density logs and sonic logs and supported by core data. However, no spread check of the differences was performed and values have been taken from all well sections over the entire well and of all wells (Gilding, 2010). Therefore, the data is not considered as a proper analogue for the DSSM in the study area. Instead, porosity normal distributions are defined for every lithology and populated to every corresponding lithology classification. It is assumed that shale forms a no-flow boundary during a simulation. Because it can still play a significant role through thermal conduction, it is given a very small ($1 \cdot 10^{-13}$) non-zero porosity value to prevent the cells from being inactive during simulations. A top-view of the porosity distribution with a channel orientation of 315° is displayed in Figure 5.8.1 with the corresponding histogram of the porosity values in the Delft Sandstone Member.

Table 5.8.2: Lithology log based on GR with the corresponding porosity model distributions.

Lithology	Porosity Range [%]	Mean [%]	Std [-]
Coarse Sand	0.21 - 0.30	0.25	0.02
Fine Sand	0.16 - 0.25	0.22	0.02
Shaly Sand	0.04 - 0.21	0.17	0.03
Shale	$1 \cdot 10^{-13}$	-	-

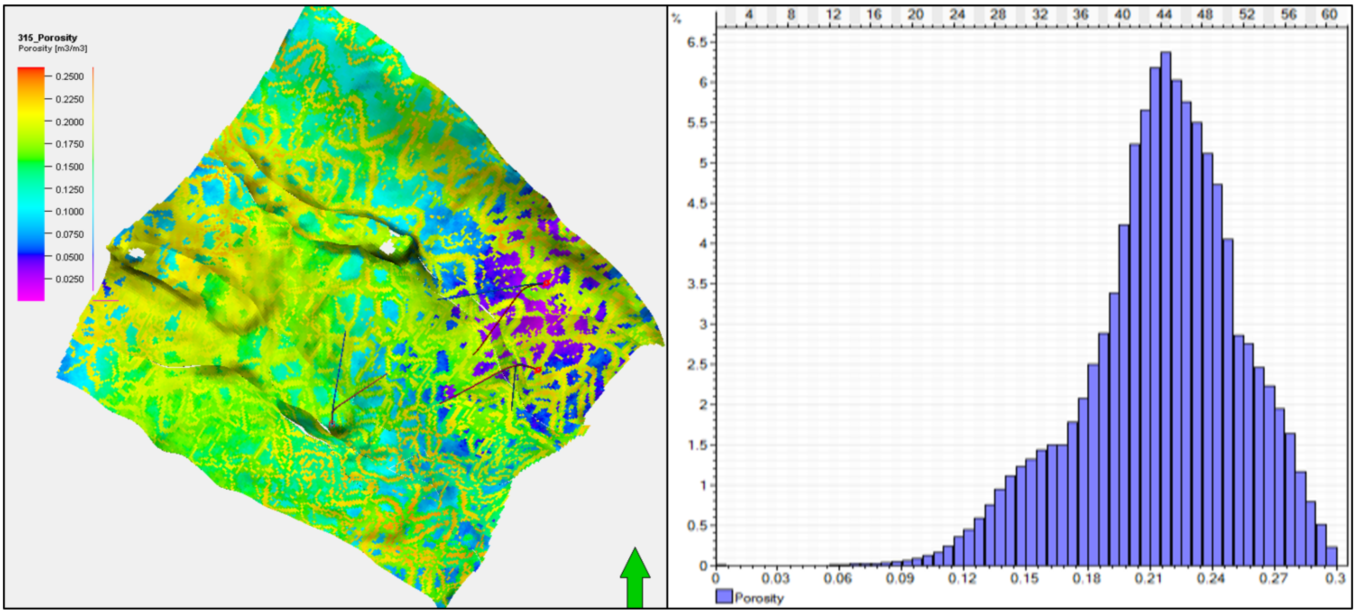

Figure 5.8.1: Left. Top view of the porosity distribution for the Delft Sandstone Member (DSSM) in the middle layer. Right: Histogram of the porosity values of the DSSM.

5.8.2. Permeability Model

Previous studies have performed core-plug studies to determine porosity-permeability relations (Drost, 2009; Loerakker, 2009). Other studies (Aramburo, 2017; Gilding, 2010; Groot, 2014; Loerakker, 2009; Smits, 2008; Willems, 2012) have used a graph with core-plug porosity and permeability data points from MKP-11, PNA-02 and RWK-01 (Figure 5.8.2.a) to establish a porosity-permeability relation. In these studies, the source of the data was not published and could not be obtained for this study. Also, the values of RWK-01 did not match the data points that are found in the core plug database of EBN. It was also not possible to obtain core-plug measurement data from PNA-02. Therefore, the graph is not assumed to be a very accurate source for establishing a porosity-permeability relation for the study area. Instead, the core-plug measurements of MKP-11, PRN-01-S1, RWK-01, Q13-01, Q13-02, Q13-08 and Q13-09 are used to establish porosity-permeability relations. The average porosity values and spread of the values of MKP-11 are much higher than the other wells. This well also encounters the DSSM at a much lower depth than the other wells (Table 5.8.3). Hence it is possible that the DSSM was exposed to less compaction than the DSSM encountered in the study area. It can therefore be doubted if the DSSM at MKP-11 is a proper analogue for the study area.

Table 5.8.3: Overview of the wells where core-plug measurements of the Delft Sandstone Mbr. were taken with the respective depths, porosity range, average porosity and standard deviation in the spread of values.

Well	TVD Top DSSM [m]	Number of samples	Porosity Range [%]	Mean porosity [%]	Std [-]
PRN-01-S1	2044	3	2-3.7	2.7	0.9
Q13-01	1960	1	NA	23.0	NA
Q13-02	1830	59	14.6-18.6	16.4	0.8
Q13-08	1843	59	2.9-28.4	13.6	4.1
Q13-09	1880	11	1.2-19.5	12.9	8.4
RWK-01	1644	2	19.8-20.2	20.0	0.3
MKP-11	761	87	7.2-42.2	26.9	8.1

However, Smits (2008) gave a justification for using MKP-11 as an analogue for the study area: The Posidonia Shale, which was the source of the oil encountered in the Moerkapelle Field, belongs to the Altena Group, found at around 2km depth at the MKP-11 location and around 3km depth at the study area location. Before inversion, this group must have been in the oil window at around 3000-4000 m. Therefore, the depth of the DSSM must also have been between 1000-2000m lower, between 1700-2700 m. The period after inversion is much shorter than the period of oil generation and migration and it is therefore likely that the DSSM has been at a similar depth at both locations for such a long time that porosity values resemble each other.

The porosity-permeability data from the deeper wells is used to establish a low-permeability scenario and the data from the deeper wells is used to establish a high-permeability scenario. The average of the two results in a medium-permeability scenario (Figure 5.8.2.b). The actual well test of the Ammerlaan production well (PNA-GT-01) resulted in an average permeability*thickness of 40 D*m. A reservoir thickness of 266m results in an average permeability of 150 mD. In our reservoir model, the medium permeability scenario (base case) has an average horizontal reservoir permeability of 258 mD and a summed permeability at PNA-GT-01 of 148 mD. We can therefore conclude that the base case permeability is similar to the measured permeability at PNA-GT-01. The final permeability relations are displayed in Table 5.8.4. Figure 5.8.3 shows the medium permeability scenario property in cross-sections between the bottom-hole location of the injector and producer for every doublet.

There is no data available for the relation between horizontal permeability (k_h) and the vertical permeability (k_v). It is therefore chosen to vary the relation in the discrete parameter analysis and assess the impact it has on the performance of the doublets (Section 7.1). In a stacked meandering river belt system, vertical permeability is in general much lower than the horizontal permeability. This is caused by the stacking of low-permeable flood plain sediment and permeable channel fill sediment. Because of this, a base case value of 100 is chosen for the k_h/k_v-ratio.

Table 5.8.4: Porosity-permeability relations for a low, medium and high permeability scenario.

Scenario	Porosity-permeability ($\phi - k$) relation
High	$k = 10^{-6.1+3.08*ln(\phi)}$
Medium	$k = 10^{-6.785+3.1*ln(\phi)}$
Low	$k = 10^{-7.47+3.13*ln(\phi)}$

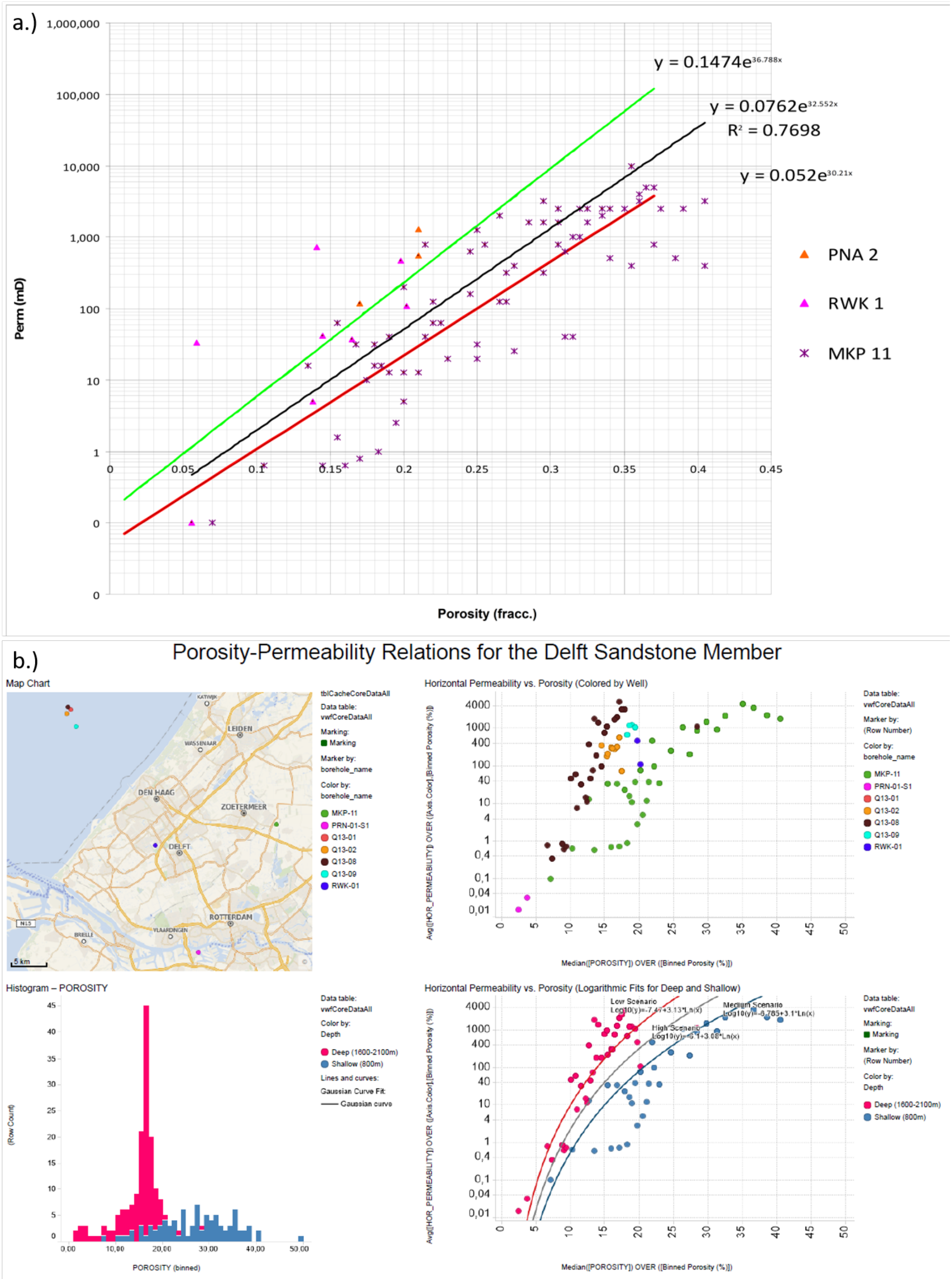

Figure 5.8.2: a.) Porosity-permeability relations for the DSSM used by Aramburo (2017); Gilding (2010); Groot (2014); Loerakker (2009); Smits (2008); Willems (2012). b.) Final porosity-permeability relations for the DSSM used in this study with top left: core plug locations, top right: porosity-permeability data points categorized per well, bottom left: porosity distribution categorized for the deep and shallow wells, bottom right: porosity-permeability data points categorized by deep and shallow wells and the porosity-permeability relations for low, medium and high permeability scenarios.

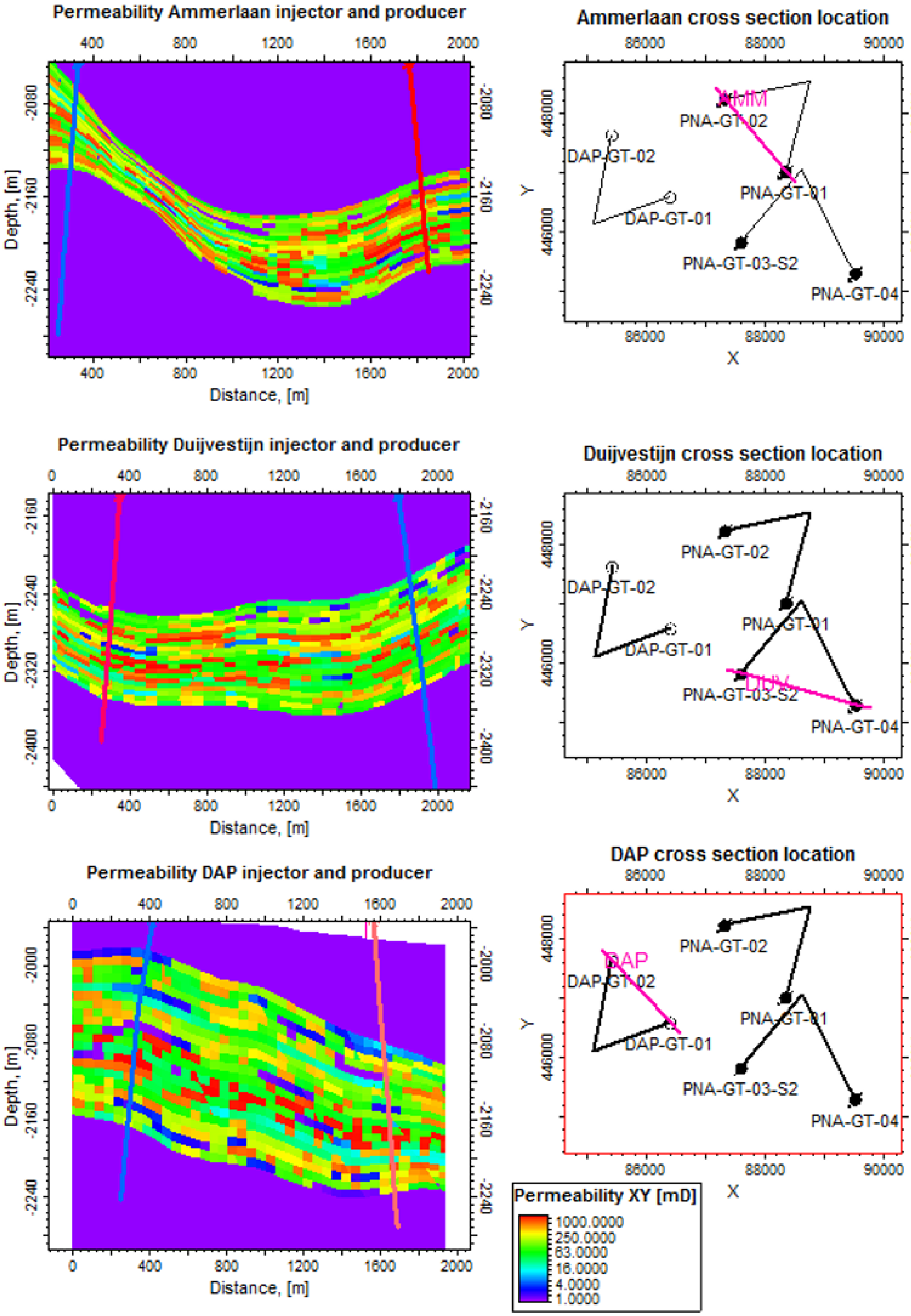

Figure 5.8.3: Cross-sections taken through the bottom-hole location of the injector and producer for every doublet to showcase permeability heterogeneity and the variation in reservoir depths and thicknesses. Top to bottom: Ammerlaan, Duijvestijn and DAP.

6

Development of the Dynamic Reservoir Model

This chapter describes how this static reservoir model is populated with dynamic properties. Dynamic properties vary over space and time. Data from the study area, analogue fields and empirical correlations are used to determine these properties. The initial and operational conditions under which a simulation takes place is defined. This chapter is concluded with a summary of the base case parameters for the dynamic simulations.

6.1. Methodology

During geothermal production, pressure and temperature will vary as cold water is injected and hot water is produced. The initial state of these properties have to be defined. Moreover, the rock and fluid properties contain pressure and temperature-dependent parameters like viscosity and heat capacity that have to be taken into account. The available production data is limited to monthly production volumes for the Ammerlaan and Duijvestijn doublet. The operating pressure and flow rate conditions have to be approximated since there was no real-time pressure data available. This is done by calculating the maximum allowable bottom-hole pressure at the injection well. This value is defined by SodM and has a linear relationship with the depth of the injector. The pressure drop along the production well is calculated for the assumed flow rates and ESP depths.

6.2. Rock and Fluid Properties

During production, changes occur in pressure, temperature and salinity. Salinity is assumed to stay constant over time. A summary of the base case values of the rock and fluid properties is displayed in Table 6.2.1. This section further elaborates on the estimation of the rock and fluid parameters for this study case.

Table 6.2.1: Base case values for the rock and fluid properties of the reservoir model.

Parameter	Value	Unit
Heat capacity of rock	1198	kJ/kg*K
Heat capacity of formation water	3.71	kJ/kg*K
Formation water salinity	106406	ppm
Formation water density	1076.7	kg/m^3
Thermal conductivity of saturated sandstone	3.5	W/m/K
Thermal conductivity of saturated shale	2.25	W/m/K
Formation water viscosity	0.41	cP
Formation water compressibility	$3.5*10^{-5}$	/bar

6.2.1. Heat Capacity of the Rock

The heat capacity is the amount of heat energy transferred to the rock to the resulting increase in its temperature by one unit degrees (Bridgwater and Boocock, 2013). During reservoir simulation in Eclipse100, the rock's heat capacity is modified as a function of temperature for the subsequent time step. This is also done for the formation water heat capacity (Section 6.2.2). The volumetric heat capacity of rock is set at 1998 kJ/m^3/K for our average initial reservoir temperature of 74.6°C (Lake and Society of Petroleum Engineers, 1986).

6.2.2. Formation Water Heat Capacity

The heat capacity of the formation water depends on temperature and salinity. In this study, all other influencing factors are neglected. An increase in salinity leads to a decrease in heat capacity while an increase in temperature leads to an increase in heat capacity. According to (Grunberg, 1970), the heat capacity of water at isobaric conditions as a function of temperature and salinity can be described by the following empirical correlation:

$$\begin{aligned} c_p = {} & (+5.328 - 9.760 \cdot 10^{-2} * S + 4.040 \cdot 10^{-4} * S^2) \\ & +(-6.913 \cdot 10^{-3} + 7.351 \cdot 10^{-4} * S - 3.150 \cdot 10^{-6} * S^2)T \\ & +(+9.600 \cdot 10^{-6} - 1.927 \cdot 10^{-6} * S + 8.230 \cdot 10^{-9} * S^2)T^2 \\ & +(2.5 \cdot 10^{-9} + 1.666 \cdot 10^{-9} * S - 7.125 \cdot 10^{-12} * S^2)T^3 \end{aligned} \tag{6.1}$$

Where:

- c_p = water heat capacity [kJ/(kg*K)]
- S = salt content (salinity) of the water [g/kg]
- T = temperature [K]

We neglect the effect that pressure can have on heat capacity of the water. Formation water at 74.6 °C with a salinity of 106.406 g/kg, returns a heat capacity of 3.71 kJ/kg*K.

6.2.3. Salinity of Formation Water

An average salinity of 106406 ppm was measured in the VDB doublet, producing from the Delft Sandstone Member and located approximately 5 km from the study area (Weerd, 2016; Willems, 2012). This is taken as the salinity of the fluid model as salinity data from wells within the study area was not available.

6.2.4. Density of Formation Water

The density of the formation water is dependent on pressure, temperature and salinity. With the empirical correlation of Spivey and McCain Jr (2003), an initial formation water density of 1076.7 kg/m^3 is determined. The density is assumed to be constant over time as Eclipse100 simulations do not incorporate the dependency on temperature, pressure and salinity over time. The assumption implies that free-convection (buoyancy) is not incorporated in the simulation. A sensitivity analysis of density on the propagation of the cold waterfront can be found in Appendix F.2.

6.2.5. Thermal Conductivity of Rock and Formation Water

The thermal conductivity is defined by the quantity of heat that flows through a unit area in a unit time under a unit temperature gradient (Hamdhan and Clarke, 2010). It is well known that thermal conductivity is affected by various factors; temperature, pressure, mineralogical composition, porosity, fractional content of quartz, porous rock microstructure, stratification, distribution, orientation, size and shape of the components, and nature of the formation fluid (Abdulagatova et al., 2009; Hamdhan and Clarke, 2010). An increase in pressure or the density of a soil results in an increase in its thermal conductivity. Quartz is a highly conductive mineral and the most important mineral indicator for the estimation of thermal conductivity in sedimentary rocks. Saturated, quartz-bearing, sandstone found in the reservoir rock is generally more conductive than the saturated shale non-reservoir rock (Robertson, 1988). The graphs from laboratory experiments, that were conducted at 300 K and 50 bar, show a thermal conductivity that ranges from 1.5-7 W/m/K for sandstone with quartz content ranging from 0% to 100% (Appendix E). Within the temperature range (25-125°C) of low-enthalpy geothermal systems, temperature has a negative correlation with thermal conductivity. At higher temperatures (500-800°C), the correlation becomes positive (Robertson, 1988). The measured thermal conductivity values decrease slightly at reservoir conditions compared to the laboratory conditions (300 K, 50 bar) since it also has a strong positive correlation with pressure. The previously mentioned dynamic parameters influence the value of thermal conductivity during production. However, as Eclipse100 does not incorporate the dependency on these factors, thermal conductivity is kept as a constant. The combined thermal conductivity of rock and formation water can be described by the following equation:

$$k_{th} = \varphi_{avg} * k_{th,water} + (1 - \varphi_{avg}) * k_{th,rock} \tag{6.2}$$

With:

- k_{th} = combined thermal conductivity [W/m/K]
- φ_{avg} = average porosity [-]
- $k_{th,water}$ = thermal conductivity of formation water at reservoir conditions [W/m/K]
- $k_{th,rock}$ = thermal conductivity of rock [W/m/K]

The average porosity of the reservoir zone in our model is 18.0%. Typical values for thermal conductivity were taken from literature (Table 6.2.2) and set as a base case (Table 6.2.3). To study the impact of thermal conductivity on the thermal recharge of the reservoir, an uncertainty range is established for saturated sandstone (2-5 W/m/K) and saturated shale (1.5-3 W/m/K).

Table 6.2.2: Thermal conductivity values found in literature for saturated sandstone and saturated shale (1: Robertson (1988), 2: Ondrak et al. (1998), 3: Muntendam-Bos (2008), 4: Poulsen et al. (2015), 5: Daniilidis et al. (2016) , 6: Shetty (2018), 7: Wang et al. (2019)).

Literature	$k_{th,sandstone}$	$k_{th,shale}$	Formation
1	2.0-5.0	1.5-3	Laboratory experiments with variable quartz content (Appendix E)
2	1.9	NA	Late Cretaceous
3	2.89	1.74	Rotliegend Fm.
4	4.66	2	Bunter Fm.
5	2.9	2.65	Rotliegend Fm.
6	2.65	2	Delft Sandstone Mbr.
7	3	2.2	Delft Sandstone Mbr.

Table 6.2.3: Base case values for the combined thermal conductivity of rock and formation water.

Zone	Combined thermal conductivity [W/m/K]
Reservoir - sandstone	3.5
Non-reservoir - shale	2.25

6.2.6. Formation Water Viscosity

During reservoir simulation in Eclipse100, the water viscosity is modified as a function of temperature for the subsequent time step. Meehan (1980b) proposed an empirical water viscosity correlation that accounts for the effects of varying pressure, temperature and salinity (Ahmed, 2018):

$$\mu_{wT} = (109.574 - 8.40564 * S + 0.313314 * S^2 + 8.72213 \cdot 10^{-3} * S^3) * (T - 460)^{-D} \tag{6.3}$$

With:

$$D = 1.12166 - 0.0263951 * S + 6.79461 \cdot 10^{-4} * S^2 + 5.47119 \cdot 10^{-5} * S^3 - 1.55586 \cdot 10^{-6} * S^4 \tag{6.4}$$

And then the pressure effect can be estimated from:

$$\mu_w = \mu_{wT}(0.9994 + 4.0295 \cdot 10^{-5} * P + 3.1062 \cdot 10^{-9} * P^2) \tag{6.5}$$

Where:

- μ_w = formation water viscosity at the prevailing pressure and temperature [cP]
- μ_{wD} = formation water viscosity at atmospheric pressure and reservoir temperature T [cP]
- T = reservoir temperature [°R]
- S = weight percentage of salt in formation water [%]
- P = pressure [psi]

So that for example water at the average reservoir pressure 227 bar, an average reservoir temperature 74.9 °C and a salinity of 0.10406 weight percentage has a viscosity of 0.41 cP.

6.2.7. Formation Water Compressibility

Fluid compressibility is the fractional change in volume per unit increase in pressure and depends on temperature and salinity. Fluids, and especially water, are often regarded as incompressible. At the initial reservoir conditions, water has an approximate compressibility of 0.00003500/bar (Meehan, 1980a). This parameter and its dependency on temperature and pressure is automatically incorporated during simulations in Eclipse100.

6.3. Initial Conditions

In this section, we describe how we have defined the initial conditions for pressure and temperature.

6.3.1. Initial Reservoir Pressure

The initial reservoir pressure is defined by the density of the formation water, the gravitational constant, depth of top reservoir and the atmospheric pressure, which equals 1 bar. The reference value for the BHP for each well equals the initial reservoir pressure calculated at each specific well location. The approximation of the initial reservoir pressure can thus be formalized by the equation:

$$P_{init} = \rho_w * g * z + P_{atm} \tag{6.6}$$

Where:

- P_{init} = pressure [Pa]
- ρ_w = density formation water at initial reservoir conditions = 1076.7 kg/m^3 (See Section 6.2.4)
- g = gravitational constant = 9.81 m/s^2
- z = depth [m]
- P_{atm} = atmospheric pressure = $1{\cdot}10^5$ Pa

This resulted in an average reservoir pressure of 221 bar. The lateral distribution of the reservoir pressure at top of the DSSM is displayed in Figure 6.3.1. The initial BHP reference depths and BHP values for the simulation wells are displayed in Table 6.3.1.

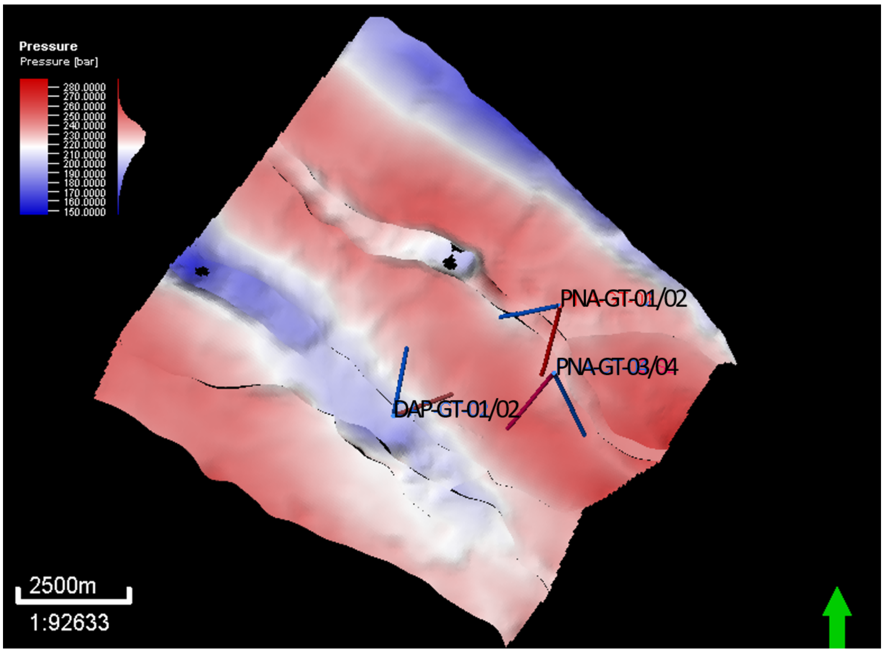

Figure 6.3.1: 2D top-view of the reservoir pressure at top reservoir depth.

Table 6.3.1: Initial reservoir pressures of the simulation wells at bottom-hole reservoir depth.

Well	BH reference depth [m]	Initial BHP [bar]
PNA-GT-01	2222	236
PNA-GT-02	2070	220
PNA-GT-03-S2	2355	250
PNA-GT-04	2308	245
DAP-GT-01	2229	236
DAP-GT-02	2170	230

6.3.2. Initial Reservoir Temperature

The initial temperature is governed by the geothermal gradient. The local geothermal gradient in the WNB can show anomalies but can be approximated by an average of 0.031 °C/m (Bonté et al., 2012). The production temperature of the nearby Van den Bosch doublet (VDB-GT-01 and VDB-GT-02) also shows that the local geothermal gradient is a good approximation (Weerd, 2016). The governing equation to determine the initial reservoir temperature can be formalized as:

$$T_{init} = T_{surface} + Z * \nabla T_{geo} \tag{6.7}$$

Where:

- T_{init} = initial temperature [°C]
- $T_{surface}$ = average annual surface temperature = 10 °C
- Z = depth [m]
- ∇T_{geo} = average geothermal gradient [°C/m.]

The measured production temperature at surface of PNA-GT-01 and PNA-GT-03 was respectively 76 °C and 80 °C (Weerd, 2016). Since there were no down-hole temperature logs available, it is assumed that the temperature is cooled down by 1.5 °C as it travels to the surface. This resulted in the average initial production temperature found in Table 6.3.2. These values show small discrepancies compared to the measured production temperatures. These discrepancies (0.1-0.2 °C) are considered acceptable and therefore the geothermal gradient is used to estimate the initial temperature at reservoir depth for DAP-GT-01. The resulting initial temperature at top reservoir depth for DAP-GT-01 is established at 76.8 °C.

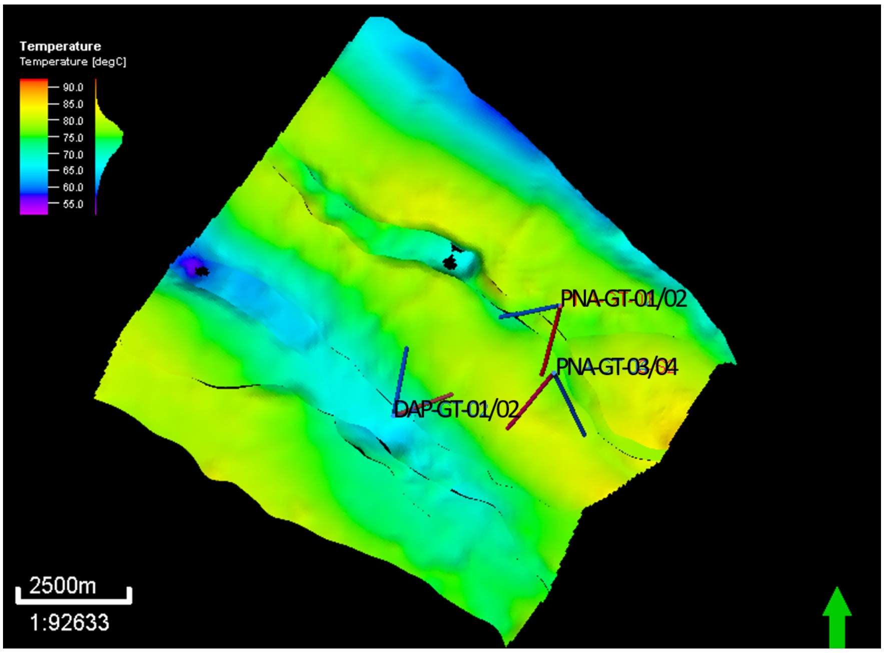

Figure 6.3.2: 2D top-view of the reservoir temperature at top reservoir depth.

Table 6.3.2: Initial temperature of the production wells (calculated with the proposed geothermal gradient), the temperature measured at the surface and the temperature after correcting with a cooling-down effect of 1.5°C.

Well	$T_{\text{calculated,geogradient}}$ [°C]	$T_{\text{measured,surface}}$ [°C]	$T_{\text{measured,+1.5°C}}$ [°C]
PNA-GT-01	77.6	76	77.5
PNA-GT-03-S2	81.7	80	81.5
DAP-GT-01	76.8	NA	NA

6.4. Operating Conditions

In this section, the production history of Ammerlaan and Duijvestijn is reported and the method for approximating the operating flow rate and pressure conditions is described.

6.4.1. Production History

Monthly volume production data of the Ammerlaan and Duijvestijn doublets (Figure 6.4.1) are available through NLOG. These doublets produce from the DSSM and the Rijswijk Member. Therefore, the production volume cannot be seen as a reliable matching target for a reservoir model that only incorporates the primary DSSM target. For this study, the monthly historic production rates are converted to daily rates and it is assumed that these are daily rates that could be achieved at a minimum. Hence it is chosen to set the base case rates equivalent to the upper limit of the monthly production data.

The operators Ammerlaan and DAP have plans to increase the thermal power by increasing the flow rates to respectively 350 m^3/h and 380 m^3/h. It is interesting to investigate the effects of this increase on productivity and lifetime of the doublets. The operators will also want to know if these rates can be maintained while keeping the draw-down of the producers at a physically realizable level and also not exceeding the legally prescribed maximum injection pressure.

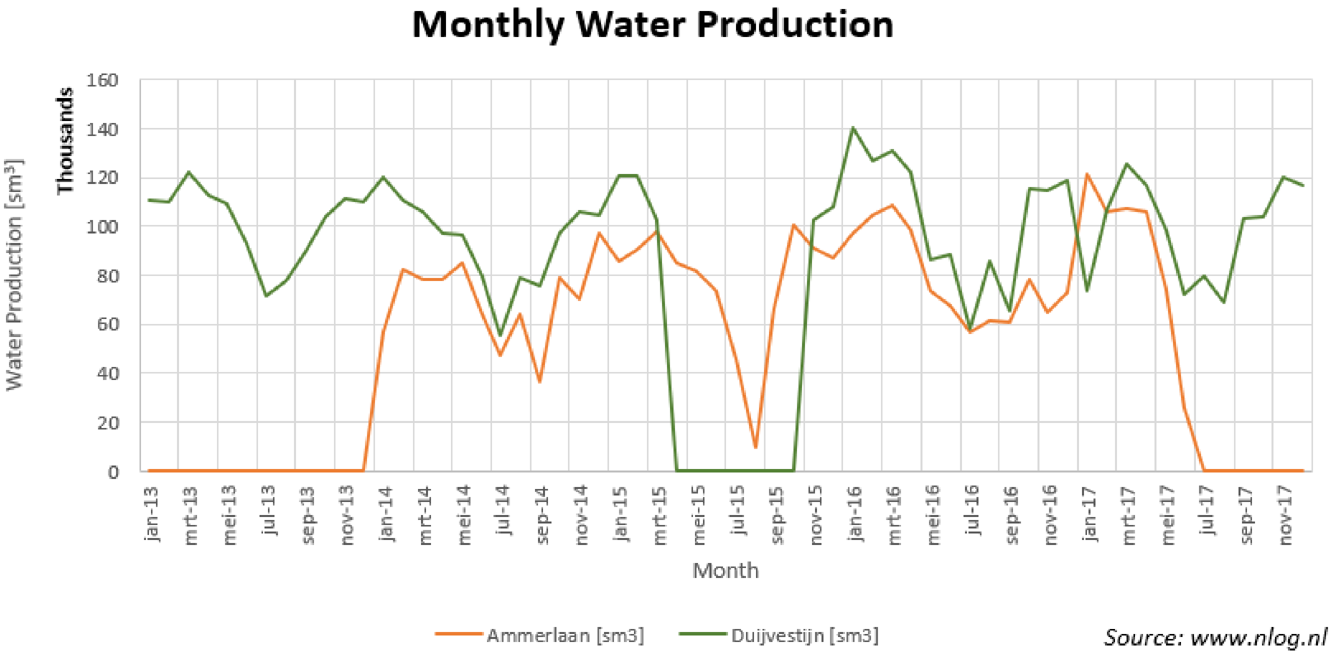

Source: www.nlog.nl

Figure 6.4.1: Monthly water production data of the Ammerlaan and Duijvestijn doublets (TNO, 2019).

6.4.2. Production Rates and Pressures

During simulations, the producers are controlled on flow rates while surface conditions are not taken into account. Therefore, one should always check if during simulation the BHP at the producer is not accompanied by a pressure drop along the borehole that causes a negative pressure at the surface. Because there are no BHP measurements available from the PNA-GT wells, BHP values are approximated by calculating the pressure drop over each borehole. This is done by assuming vertical wells for simplicity. The pressure drop is governed by the gravitational head, friction losses and acceleration losses (Jansen, 2016). This is also the order of the impact on the pressure drop. Acceleration losses are not significant because the fluid consists of one water phase and barely expands (See Section 6.2.7), and thus does not accelerate when it travels to the surface. The equation (Jansen, 2016) can be formalized as follows:

$$\frac{dP}{ds} = -\rho g - \frac{\rho}{2d} f v|v| - \rho v \frac{dv}{ds} \tag{6.8}$$

Where:

- dP = pressure drop [Pa]
- ds = pipe length [m]
- ρ = formation water at reservoir conditions = 1076.7 $\mathrm{kg/m^3}$
- g = gravitational acceleration = 9.81 $\mathrm{m/s^2}$
- d = well diameter [m]
- f = friction factor [-]
- v = production rate [m/ s]

The friction factor (f) can be approximated by the following equation (Zigrang and Sylvester, 1982):

$$f = \Big(-2 * log_{10}[\frac{2\epsilon}{3.7} - \frac{5.02}{N_{Re}} log_{10}(\frac{2\epsilon}{3.7} + \frac{13}{N_{Re}}]\Big)^{-2} \tag{6.9}$$

Where the pipe roughness (ϵ) can be defined as follows:

$$\epsilon = \frac{e}{d} = \frac{0.0006}{d} \tag{6.10}$$

- ϵ = pipe roughness [-]
- e = pipe roughness parameter [-]
- d = pipe internal diameter [m]

$$N_{Re} = \frac{\rho v D_{in}}{\mu} \tag{6.11}$$

And the Reynolds number (N_{Re}) is a dimensionless number that describes the flow regime:

- N_{Re} = Reynolds Number [-]
- v = flow rate [m/s]
- D_{in} = tubing diameter [m]
- μ = formation water viscosity at reservoir conditions [Pa*s]

The pressure drop is calculated over the length of the wellbore where the pressure drop is created. For producers, this is from the bottom of the electric submersible pump (ESP) to the top of the perforations. For injectors, the pressure drop is created from surface level to the top of the perforations. There is no data available for the ESP operating pressures so a default value of 50 bar is taken for all production wells. ESP depths and tubing diameter at the perforations are taken from the well reports (TNO, 2019). The results of the analysis can be found in Table 6.4.1. Note that increasing the flow rate from the base case to the high rate does not have a significant impact on the flowing bottom-hole pressure (FBHP) because the increase in friction is negligible compared to the pressure drop created by the hydrostatic column. Also, note that a simulated FBHP lower than the calculated FBHP is physically realizable by increasing the power of the ESP or placing it at greater depth so that it increases the pressure drop over the pipe length.

Table 6.4.1: BHP approximation for the production wells.

Parameter	PNA-GT-01	PNA-GT-03	DAP-GT-01
Diameter at perforation [inch]	6	6 1/8	8 5/8
ESP depth [m]	348	500	620
Wellbore length between ESP and TD [m]	1787	1768	1482
Base case flow rate [m^3/h]	155	180	150
High case flow rate [m^3/h]	350	350	350
Calculated FBHP [bar]	215	213	213

6.4.3. Injection Pressures

In the field, the injection flow rate is increased until a target tubing head pressure (THP) has been reached. During simulations, wells are controlled on bottom hole pressure (BHP) and flow rates. No lift tables are therefore required and well-bore diameter at the perforation is not incorporated in the calculation of flow. Since produced water is re-injected by the injector, it is assumed that the flow rate of the producer is equal to the flow rate of the injector. To ensure this, a production balancing rule is imposed on the doublets. When one produces at higher flow rates, one needs to inject at higher flow rates and therefore apply more pressure. The injection of cold water at high pressures in a reservoir can cause fracturing and/or thermal cracking. To mitigate these risk, a maximum BHP for the injector has been imposed by SodM (SoDM, 2013). It can be determined by the following equation:

$$P_{BHP,max} = Z_{inj} * 0.135 \tag{6.12}$$

Where:

- $P_{\mathrm{BHP,max}}$ = maximum BHP [bar]
- Z_{inj} = true vertical bottom-hole reservoir depth of the injector [m]

The different depths of the injectors of Ammerlaan, Duijvestijn and DAP lead to different values for the maximum allowed pressure build-up (Table 6.4.2 and Figure 6.4.2). The allowable BHP at the injector is a function of depth (Eq. 6.12) and has a higher slope coefficient than the hydrostatic pressure. The slope coefficient approximates the fracture gradient of the rock. There is no pressure data available for the injectors. Therefore it is not possible to check if the pressure output is in accordance with the actual pressures in the field. Instead, the maximum prescribed BHP's are used to see under which operational parameters, given the geological parameters, it is not possible to maintain the target flow rates.

Table 6.4.2: Maximum allowed pressure build-up for the injectors of Ammerlaan (PNA-GT-02) and Duijvestijn (PNA-GT-04) and DAP (DAP-GT-02).

Injector	BH reference depth [m]	Calculated BHP [bar]	Max legal BHP [bar]	Max pressure build-up [bar]
PNA-GT-02	2070	215	279	64
PNA-GT-04	2308	240	312	72
DAP-GT-02	2170	226	293	67

6.4.4. Operational Constraints

The development strategy describes the constraints, defined by rules in Eclipse100, under which the field is producing and injecting (Figure 6.4.3). To mimic reality, four rules are impose on the wells:

1. The Duijvestijn and Ammerlaan doublets have been producing since respectively 2013 and 2014. The DAP doublet is expected to start production in 2021. Doublets start production at the first day (January 1) of these years.
2. Producers are controlled on a target water rate.
3. Injectors are controlled on a target flow rate and limited on BHP, defined by the maximum allowable injection pressure (SoDM, 2013). The BH reference depth is defined by the true vertical depth at which the bottom of the perforation is positioned.

4. The production balancing rule ensures that the volume of water that is produced is also injected. This is especially important when we are dealing with a scenario where we are limited by the allowable injection pressure. If we would then not impose this rule, the production rate would exceed the injection rate. This is not realistic since there is no storage room available for the produced water above the surface.

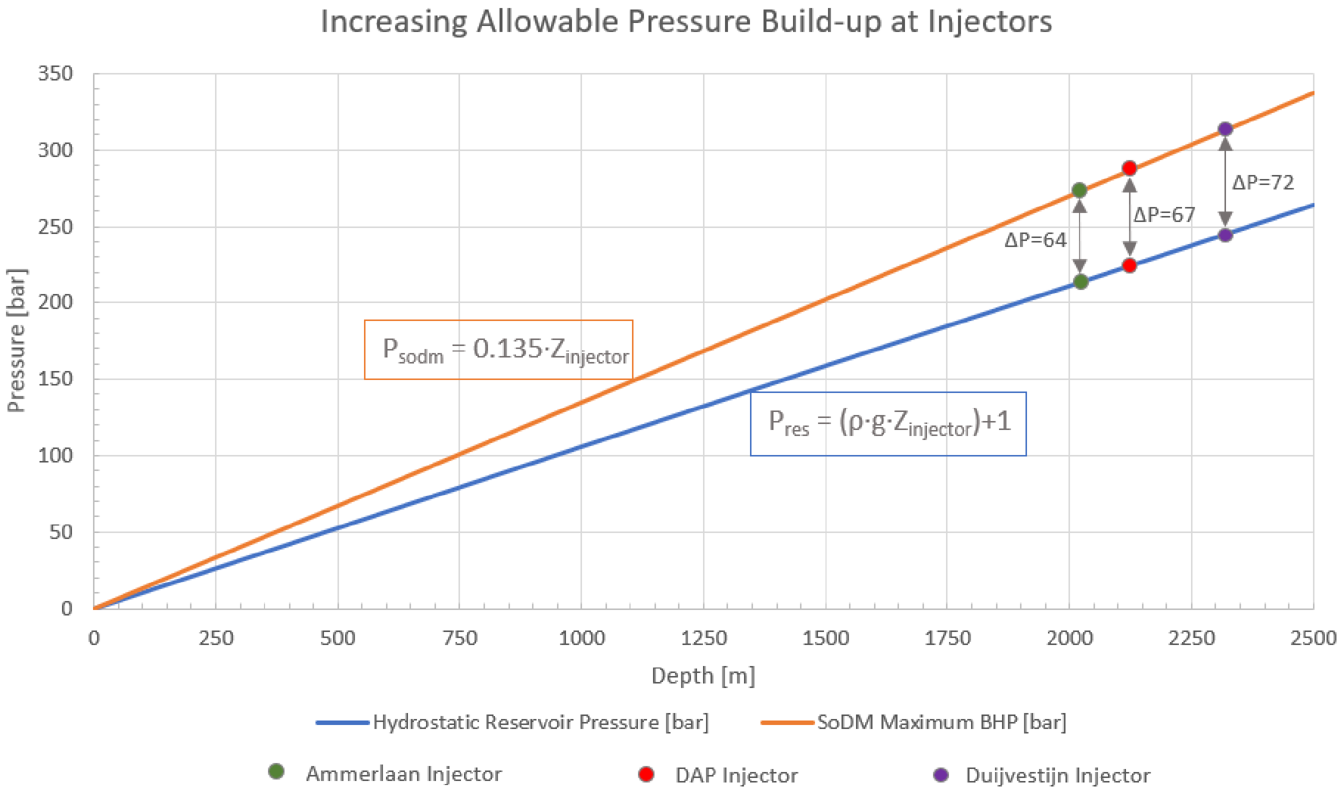

Figure 6.4.2: The hydrostatic pressure (P_{res}: Eq.6.6) as function of injector depth (Zinj) and the function for the allowable BHP at which an injection well is allowed to inject water in the onshore subsurface of the Netherlands (P_{SodM}: Eq.6.12). Since the slope coefficient of the hydrostatic pressure is smaller, the allowable pressure build-up (ΔP) increases with depth.

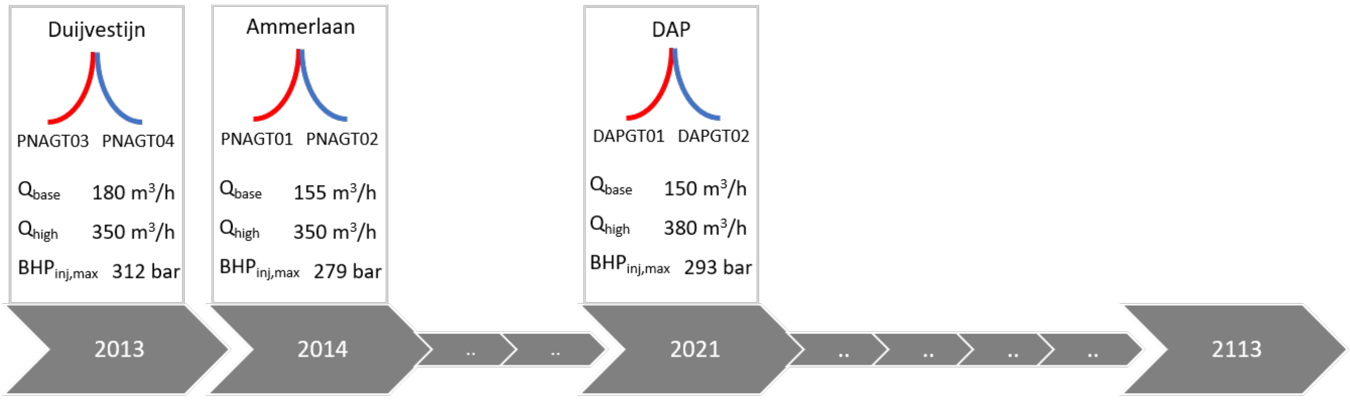

Figure 6.4.3: Development strategy for the Duijvestijn, Ammerlaan and DAP doublets. Base case target flow rate (Q_{base}) and high case target flow rate (Q_{high}) are prescribed for the producers. A maximum allowable BHP ($BHP_{inj,max}$) are prescribed for the injectors.

6.5. Base Case Summary

This section gives a summary of the parameters used for the base case model (Table 6.5.1) and a summary of all the relevant parameters for the simulated wells (Table 6.5.2). The static reservoir model is displayed in Figure 6.5.1.

Table 6.5.1: Properties of the 3D structural reservoir model used for dynamic reservoir simulation to study interference effects and thermal recharge.

Parameter	Value	Unit
Reservoir dimensions (averaged)	7.6*5.6*0.2	km*km*km
nx*ny*nz	230*206*30	-
average dx*dy*dz	50*52*7	m*m*m
Well spacing Ammerlaan doublet	1590	m
Well spacing Duijvestijn doublet	1950	m
Well spacing DAP doublet	1420	m
Average reservoir thickness	105	m
Average initial reservoir pressure	221	bar
Average initial reservoir temperature	74.6	°C
Injection temperature	35	°C
Thermal conductivity sandstone	3.5	W/m/K
Thermal conductivity shale	2.25	W/m/K
Fault transmissibility multiplier	1	-
Average facies channel orientation	315	°
k_h/k_v-ratio	100	-
Average permeability	260	mD

Table 6.5.2: Parameters for the simulation wells. True vertical depth (TVD) of the reservoir zones depth of the electric submersible pump (ESP), reservoir pressures and temperatures, flow rates, perforation lengths, tubing diameters and skin factors.

Property	PNA-GT-01	PNA-GT-02	PNA-GT-03-S2	PNA-GT-04	DAP-GT-01	DAP-GT-02
TVD_{top} [m]	2138	2018	2268	2204	2102	2032
TVD_{middle} [m]	2180	2044	2311	2256	2166	2101
TVD_{BHP} [m]	2222	2070	2355	2308	2229	2170
$TVT_{reservoir}$ [m]	84	52	87	104	127	138
ESP Depth [m]	348	-	500	-	620	-
$T_{init,avg}$ [°C]	77.6	-	81.6	-	77.1	-
BHP [bar]	236	220	250	245	236	230
BHP_{max} [bar]	279	-	312	-	293	-
$Q_{base,high}$ [m^3/h]	155,350	155,350	180,350	180,350	150,380	150,380
$Q_{base,high}$ [m^3/day]	3720,8400	3720,8400	4320,8400	4320,8400	3600,9120	3600,9120
$L_{perf,MD}$ [m]	180	79	115	431	182	177
D_{tubing}[inch]	6	6	6 1/8	6 1/8	8 5/8	9 5/8
Skin factor [-]	0	0	0	0	0	0

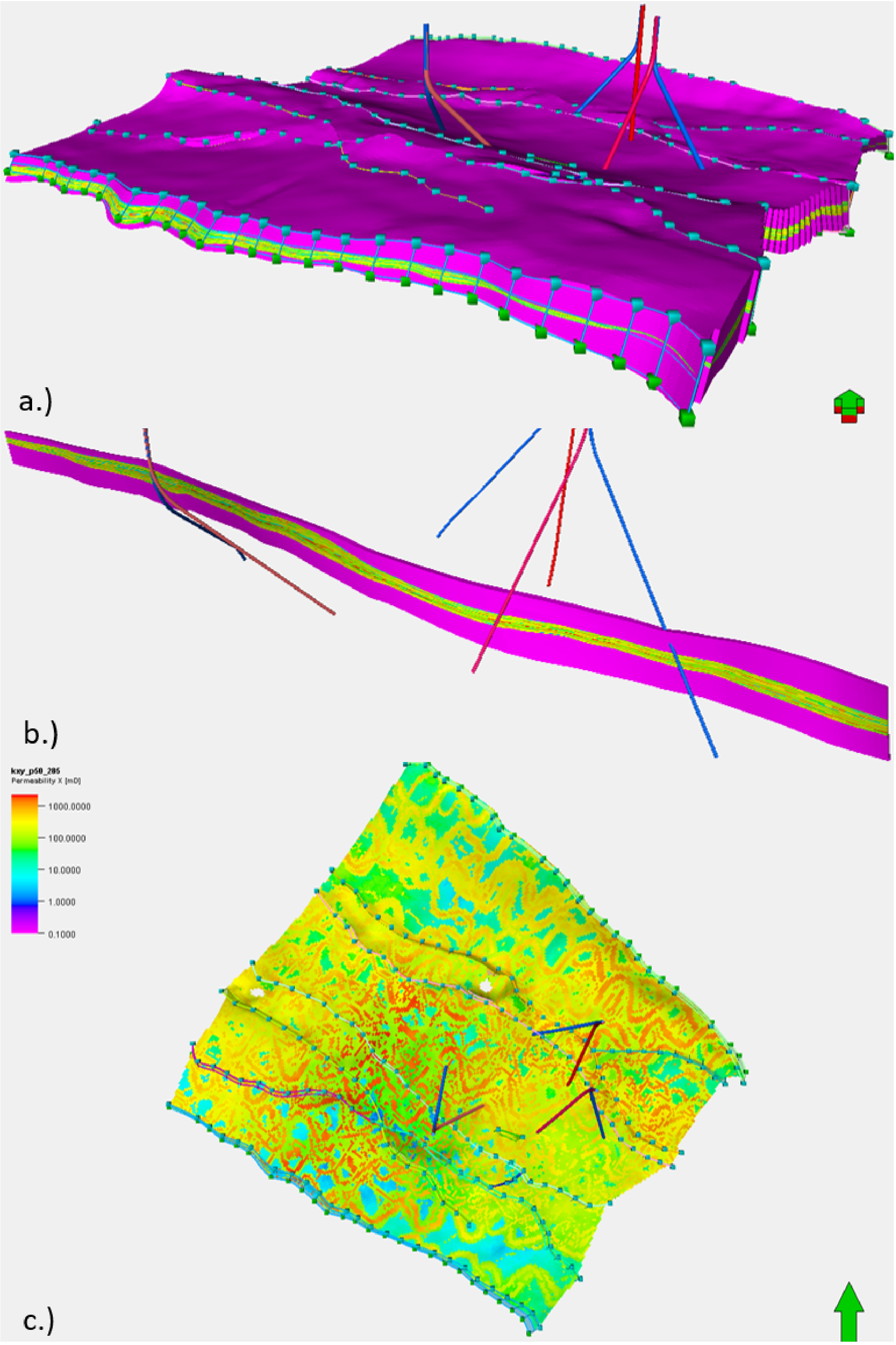

Figure 6.5.1: a.) Side view of the base case model displaying the permeability distribution including the faults, over- and underburden. b.) Side view of a cross-section of the middle of the base case model displaying the permeability of the reservoir and non-reservoir zone. c.) Top view of the base case model displaying the faults and the 15th layer of the reservoir rock with the permeability and facies channel distribution.

7

Doublet Performance

The dynamic reservoir model is used to perform simulations and determine the performance of the three doublets. To capture the uncertainty in the geological and operational parameters, a discrete parameter analysis is proposed. Four geological and four operational parameters are varied. For each parameter, 2 or 3 discrete values are evaluated and all possible combinations of these values result in a full factorial design of 864 scenarios. Three performance indicators are analysed for these scenarios: lifetime, thermal power and interference. Two types of interferences are observed: on pressure and on temperature. Both types can affect a doublet positively or negatively. For all scenarios, interference is observed on temperature. Interference on pressure also occurs for all scenarios but only has an effect on injection and production rate for the scenarios that are limited by the maximum allowable injection pressure imposed by SoDM. These scenarios are referred to as 'pressure constraint simulations' and the the cause and the effects of these constraint simulations is investigated. The impact that pressure and temperature interference has on the total energy production of the doublets separately and on the total production of energy of the doublets together is quantified.

7.1. Methodology

The dynamic simulations are performed under the operational constraints described in Section 6.4.4. The geological and operational parameters that are incorporated in our static and dynamic reservoir model bear a significant amount of uncertainty. These uncertainties are generally represented by a set geological realizations, referred to as an ensemble of models (Matthews et al., 2008). Different methodologies have been proposed for setting up such an ensemble to capture the uncertainties. In this study, eight parameters are considered that could bear uncertainty while also having an impact on the behaviour of the thermal processes and fluid dynamics. A basic methodology to assess the uncertainty is the subsequent variation of each parameter separately. This method is suitable to quantify the sensitivity of one parameter on the output but fails to capture the complete uncertainty that the combination of parameters can have on the output of the model. A Monte Carlo method is more extensive and samples from a distribution so that it gives probabilistic results that not only show what could happen but also how likely each outcome is. A method that captures the combined uncertainty of multiple parameters in a deterministic way is a discrete parameter analysis. This method simulates all possible combinations of discrete parameters where the selection of the discrete values have been based on data, literature or just a hypothetical assumption.

To capture the full uncertainty in the dynamic reservoir model, a discrete parameter analysis is performed. A full Monte Carlo simulation would give a better understanding of the occurrence of the events but it is considered too time-consuming for the number of parametric combinations. The chosen methodology is similar to that proposed by Daniilidis et al. (2016) and is visualized in Figure 7.1.1. The uncertainties are categorized in geological and operational uncertainties. Varying the parameters enables us to study the effect they have on the proposed performance indicators defined by lifetime, thermal power, pressure interference and temperature interference. Pressure interference is quantified for the pressure constraint scenarios and temperature interference is quantified for the rate constraint scenarios. To assess whether the total interference effect has positive or negative effect, the total average energy production is compared between the doublets, running together and running stand-alone.

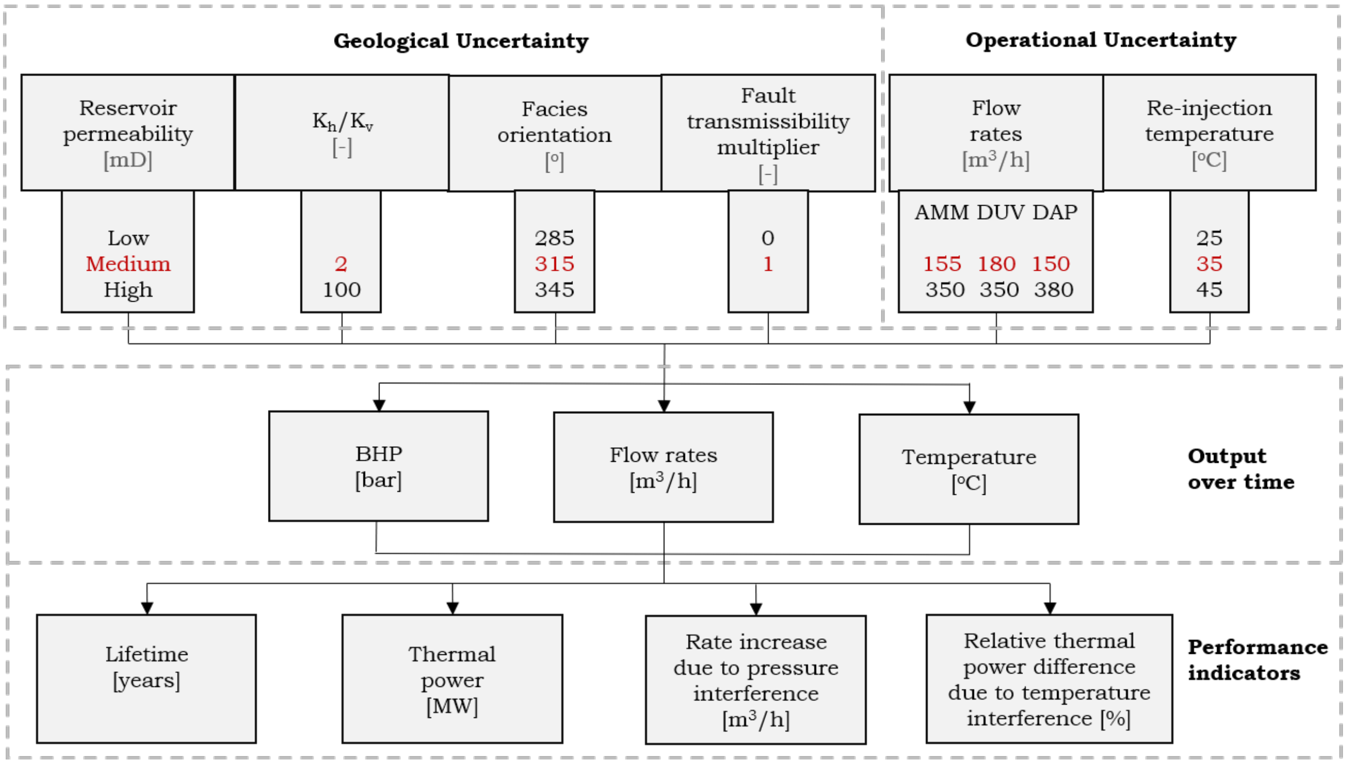

Figure 7.1.1: Proposed methodology for the discrete parameter analysis. AMM and DUV indicate the Ammerlaan doublet and the Duijvestijn doublet. The total amount of parametric combinations between the uncertain parameters is 864. The output of the analysis for the six simulated wells is bottom-hole pressure (BHP), flow rate and temperature. The performance indicators are defined by lifetime, thermal power, pressure interference and temperature interference.

Lifetime

The lifetime of a doublet is defined to be the amount of time necessary for the reservoir temperature to reach to 90% of its initial value. Note that this percentage is specific for each situation and highly dependent on the heating purposes and the economical parameters forming the business case.

Thermal power

Thermal power over time, issued to the heat exchanger, is given by:

$$P_{th}(t) = Q_w(t) * \rho_w * c_P(t) * \Delta T(t) \tag{7.1}$$

Where:

- t = time of production [year]
- $P_{thermal}$ = thermal power [kW]
- Q_w = flow rate [m^3/s]
- ρ_w = density water [kg/m^3]
- c_P = heat capacity water [kJ/(kg*K)]
- ΔT = temperature decrease at the heat exchanger; difference production and injection temperature [K]

Total Energy Production

Total energy production is obtained by multiplying the thermal power with the simulation time, a coefficient of performance (COP) and the operational up-time. We assume an up-time of 80% and an average of 8760 hours in a year. The COP is the ratio of energy output to the energy required by the injection and production pump. At higher flow rates, the injection and production pump require relatively more energy compared to the energy output, decreasing the COP (Doddema, 2012). For simplicity, we assume a (negative) linear relationship between flow rate and COP. We assume that a flow rate of 150 m^3/h and 350 m^3/h result in a COP of respectively 30 and 20. For example, a doublet that operates at 150 m^3/h and a constant thermal power output of 5 MW over 1 year, results in a COP of 30 and a total yearly energy production of 122 TJ.

Pressure interference
Interference on pressure only includes simulation scenarios that are constraint on the BHP of the injector. It is studied by running these scenarios with the doublets together and as stand-alone. The pressure interference is then quantified by the absolute increase or decrease in production rate of doublet 1, due to the start of the production by doublet 2 or 3.

Temperature interference
Temperature interference only includes simulation scenarios that are controlled by flow rate, because the output of these scenarios represent the impact of the varied geological parameters. Temperature interference is defined as the relative increase or decrease that the production of doublet 2 and 3 have on the production temperature of doublet 1. To quantify this impact, the simulations are performed as stand-alone and with neighbouring doublets turned on. Because the produced heat is dependent on the varying flow rates and the re-injection temperature, thermal power is used as a quantity for a fair comparison between the different doublets. The temperature interference over time in thermal power is expressed as follows:

$$IF(t) = \frac{P_{th,all}(t) - P_{th,alone}(t)}{P_{th,alone}(t)} * 100\% \tag{7.2}$$

Where:

- t = time of production [year]
- IF = interference effect [%]
- $P_{th,all}$ = thermal power of doublet with neighbouring doublets turned on
- $P_{th,alone}$ = thermal power doublet with neighbouring doublets turned off

So if a doublets thermal power is 5 MW as stand-alone and 4.5 MW with neighbouring doublets turned on, the interference effect is -10%.

7.2. Pressure Interference

For 240 of the 864 parametric combinations, the three doublets could not reach their target rates due to the limit on the BHP of the injectors. Under all low permeability scenarios, Ammerlaan and Duijvestijn could not reach their base case target rate, nor their high case target rate. The DAP doublet was able to reach the base case target rates under the low permeability scenario but failed to reach the high case target rate because of the limited allowable BHP at the injector (Figure 7.2.1). The maximum achievable rates vary between the different doublets and slightly vary between the base case and high case scenarios (Table 7.2.1). Only the DAP doublet achieves its base case flow rate of 150 m^3/h. Also, the DAP doublet achieves double the rate of Ammerlaan (200 m^3/h compared to 96 m^3/h). The discussion Section 7.6.1 describes an attempt to investigate the cause of these variations.

As stated before, the Duijvestijn, Ammerlaan and DAP doublets start producing in respectively 2013, 2014 and 2021. An interesting phenomenon occurs during the simulation of the production of the three doublets. **The reservoir pressure is decreased at the injector when a neighbouring production well starts producing (Figure 7.2.2). This allows the injector to inject at a higher flow rate.** This pressure interference is demonstrated for a high case rate scenario (Table 7.2.2).

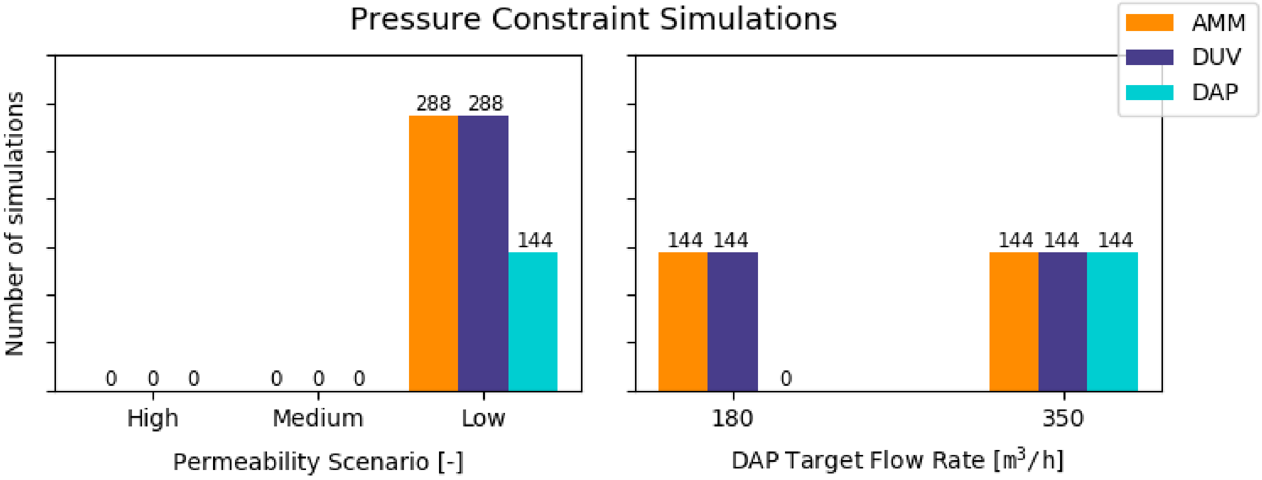

Figure 7.2.1: Histogram showing the parameter values that define the number of pressure constraint simulations for Ammerlaan (AMM), Duijvestijn (DUV) and DAP. The x-axis shows the permeability scenario (left) and the DAP rate (right), with their corresponding values.

Table 7.2.1: The target rates (Q_{target}) and achieved rates ($Q_{achieved}$) are displayed under the low permeability scenario for the three doublets

Doublet flow rate scenario	**Q_{target} [m³/h]**	**$Q_{achieved}$ [m³/h]**
AMM base case	155	99
AMM high case	350	99
DUV base case	180	140
DUV high case	350	142
DAP base case	150	150
DAP high case	380	204

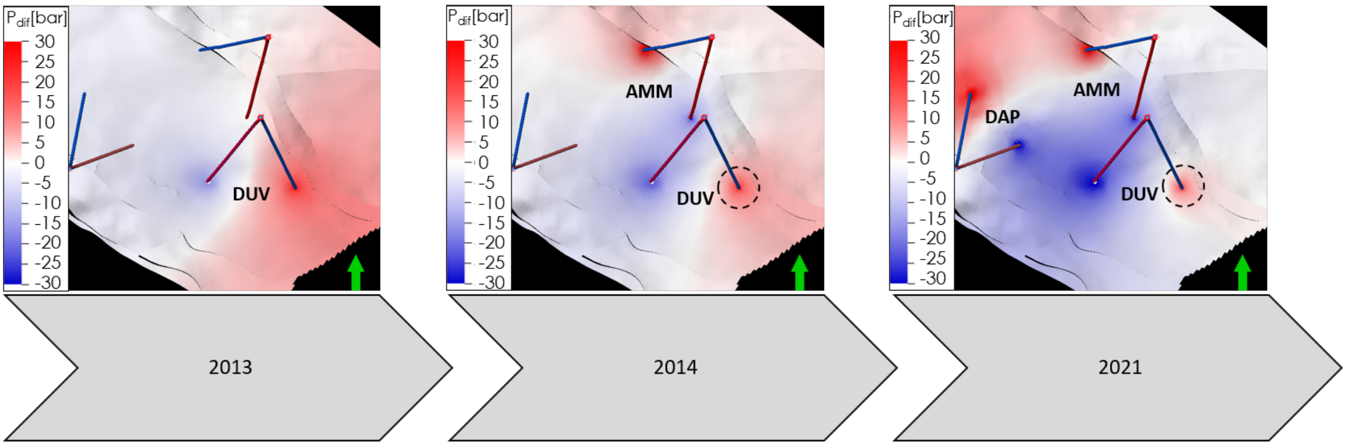

Figure 7.2.2: The pressure difference for the years 2013 (Duijvestijn), 2014 (Ammerlaan) and 2021 (DAP) compared to the initial reservoir pressure. Red indicates a pressure increase and blue a pressure decrease. Black dashed circle indicates the pressure drop around the Duijvestijn injector. This allows it to inject at a higher rate after 2014 and 2021 compared to 2013.

Table 7.2.2: Values of the discrete analysis parameters for the scenario that simulated the pressure and rate output shown in Figure 7.2.3. Simulation time is from 2013 to 2030. A fault transmissbility (TM) of 0 indicates sealing faults and 1 fully transmissibile faults.

Permeability	**Fault TM**	**K_h/K_v**	**$T_{reinject}$**	**Facies Orientation**	**DUV Rate**	**AMM Rate**	**DAP Rate**
Low	1	100	35 °C	315°	$350\ \mathrm{m^3/h}$	$350\ \mathrm{m^3/h}$	$380\ \mathrm{m^3/h}$

When constraint on injection pressure, the pressure drop at the injector allows it to inject at a higher rate. For Duijvestijn, this pressure drop occurs twice: in 2014 when Ammerlaan starts production and in 2021 when DAP starts production (Figure 7.2.3). A pressure drop at the Duijvestijn producer of 9.1 bar is observed after 2014 and a drop of 11.6 bar after 2021. Note however that it is the pressure drop at the injector that results in the flow rate increase. Since the scenarios are at all times pressure constraint on the injector, the injector BHP stays constant on the value of the maximum allowable BHP.

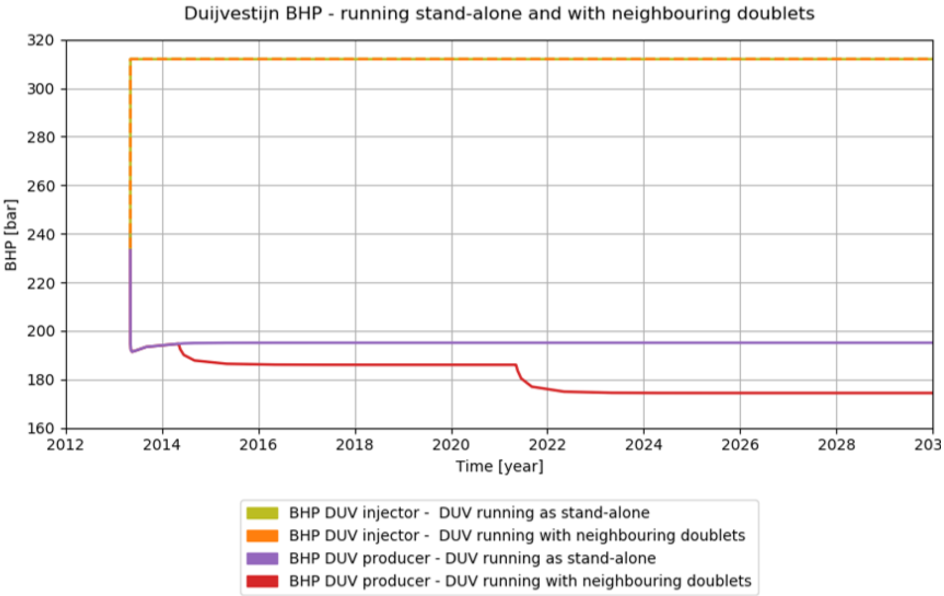

Figure 7.2.3: Duijvestijn BHP of injector and producer plotted over time for running Duijvestijn as stand-alone and with neighbouring doublets. Injector BHP stays constant for both configurations and coincides with the maximum allowable BHP. Producer BHP stays constant when running as stand-alone. When running with neighbouring doublets, a pressure drop at the Duijvestijn producer is observed in 2014 (Ammerlaan start-up) and 2021 (DAP start-up). Scenario parameters are displayed in Table 7.2.2.

Figure 7.2.4 displays the corresponding flow rates for the two configurations (stand-alone and running all). Production and injection are equal at all times because of the production balancing rule. A Duijvestijn flow rate increase of 10.8 m^3/h is observed after 2014 and an increase of 10.5 m^3/h after 2021. For Ammerlaan, there is a decrease of pressure at the injector when DAP starts, resulting in an increase in the injection rate and production rate of Ammerlaan. This pressure drop is not observable for DAP since it starts production in 2021, when the other doublets are already producing.

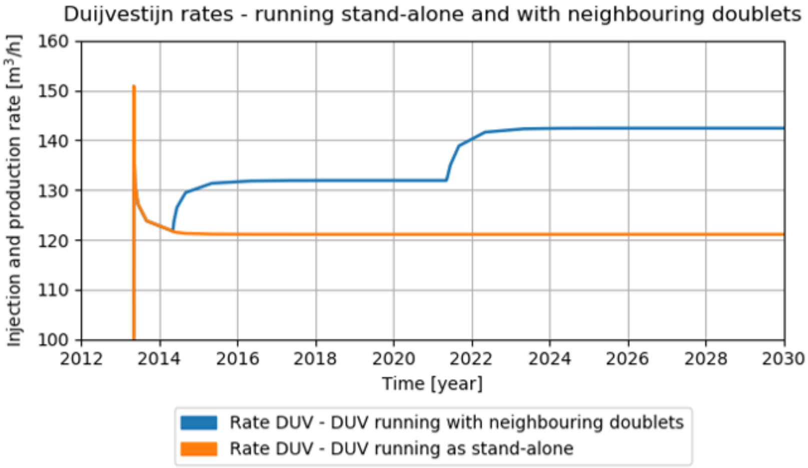

Figure 7.2.4: Duijvestijn flow rate plotted over time for running Duijvestijn as stand-alone and with neighbouring doublets. Blue: Production rate plotted over time for the Duijvestijn producer when running with neighbouring doublets. Jump in production rate when Ammerlaan starts (2014) and when DAP starts (2021). Orange: Production rate of DUV plotted over time for running DUV as stand-alone. Scenario parameters displayed in Table 7.2.2.

Figure 7.2.5 displays how varying the values of geological parameters (fault transmissibility, (K_h/K_v)-ratio and facies orientation) has an impact on the pressure interference at the Duijvestijn producer due to the start-up of the Ammerlaan producer. Some of the parameters that are included in the discrete parameter analysis are not included in this figure. Duijvestijn and Ammerlaan rates are target rates are not being reached for these low permeability scenarios and therefore the achieved rates do not vary for the different scenarios. Because the achieved rates and other parameters are equal, varying the target rate does not have an impact on the pressure interference. Re-injection temperature also does not affect pressure and therefore does not affect the pressure interference. No separate plots are created for these parameters because they do not affect the pressure interference and thus do not affect the rate increase.

The increase in production rate of Duijvestijn, due to the start-up of Ammerlaan, ranges from 9.0 to 19.8 m^3/h. Closed faults result in higher (13-18 m^3/h) production increases compared to open faults (9-14 m^3/h) because of the proximity of the doublets to the faults separating the Pijnacker High and Delft High from the Vrijenban Syncline (indicated in green). The pressure can not dissipate towards the southwest and northeast (Figure 7.2.6), causing a higher pressure drop within the syncline and at the Duijvestijn injector. A lower (K_h/K_v)-ratio results in a higher vertical permeability, a higher pressure gradient and a higher increase in production rate. A facies orientation of 315° results in a slightly higher rate increase than 345°. An orientation of 285° gives an even lower average rate increase. These orientations seem to have a preferential path for flow from the Ammerlaan injector (PNAGT01) to the Duijvestijn injector (PNAGT04). From Figure 7.2.7 it can be seen that a fluvial channel orientation of 345° has a better alignment with the shortest flow path from well-to-well than 315° and 285°.

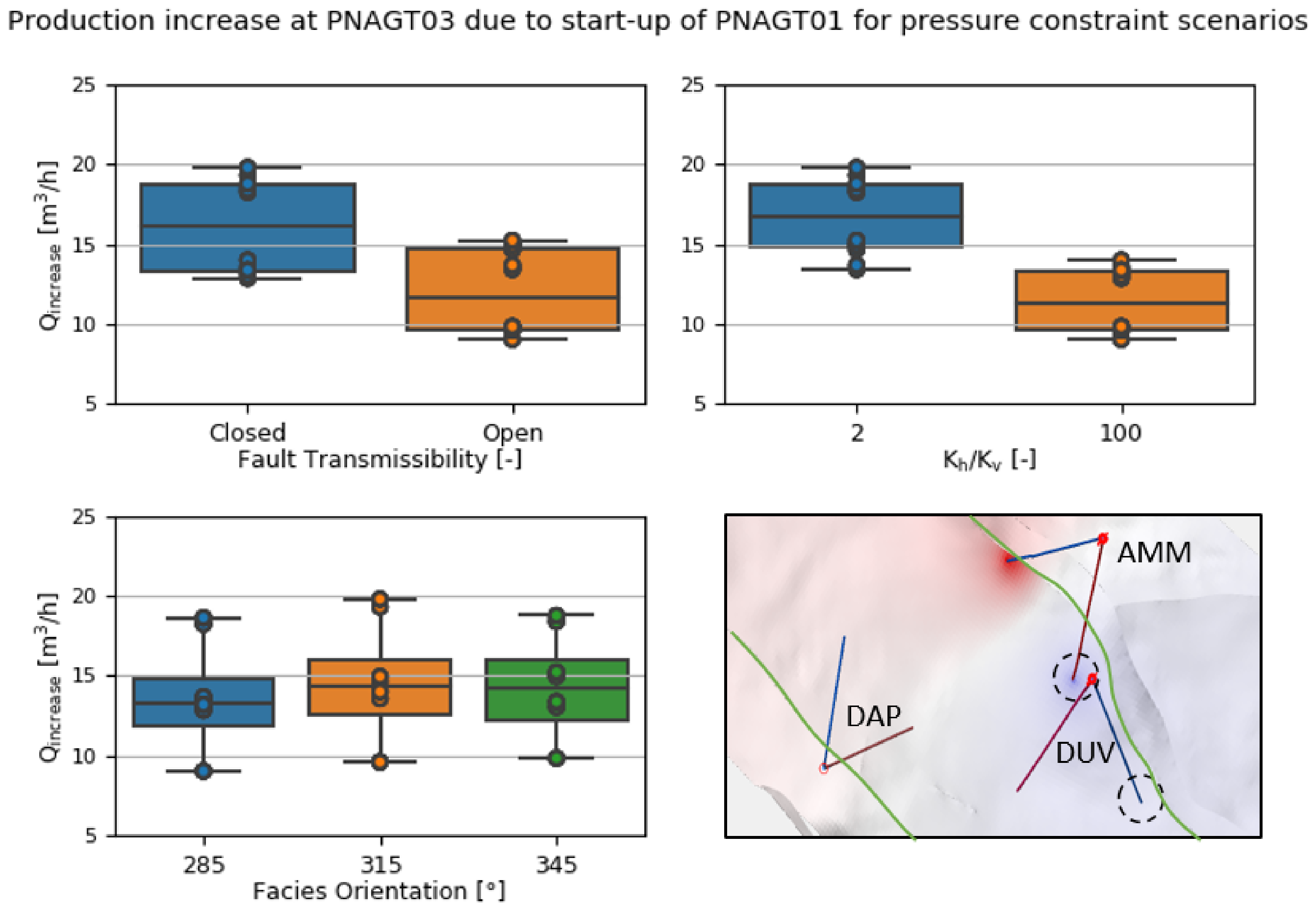

Figure 7.2.5: Box-and-whisker plots display the variation in production rate increase at the Duijvestijn producer, due to the start-up of the neighbouring Ammerlaan doublet, for the geological parameters fault transmissibility, (K_h/K_v)-ratio and facies orientation. The map view displays the pressure drop (blue) and the pressure increase (red) that is created by respectively the Ammerlaan producer and Ammerlaan injector.

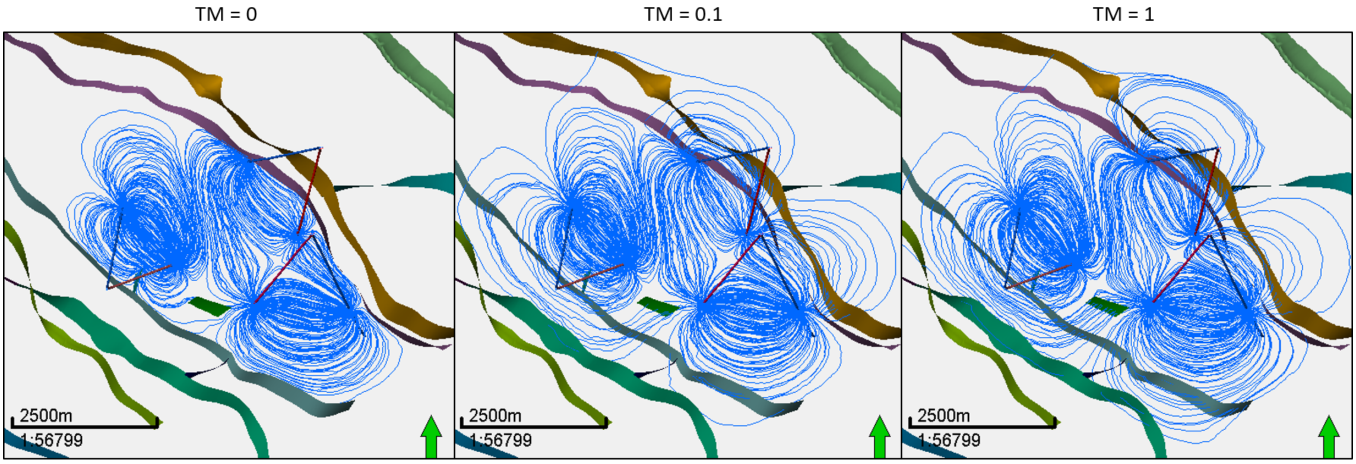

Figure 7.2.6: The streamlines represent flow from injectors to producers for three scenarios. Left: Transmissibility multiplier is 0 so that faults are sealing. Center: Tranmissibility multiplier is 0.1 so that faults are partially sealing. Right: Tranmissibility multiplier is 1 so that faults are completely transmissible.

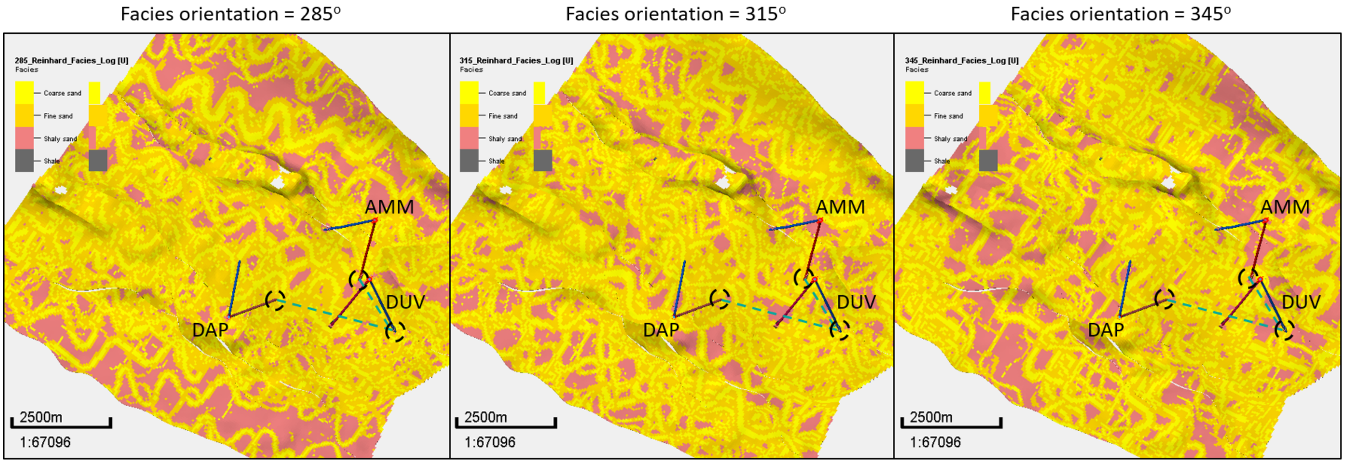

Figure 7.2.7: The facies are shown for a facies orientation of, from left to right, 285°, 315° and 345°. The doublets Ammerlaan (AMM), Duijvestijn (DUV) and DAP are indicated. Also indicated is that shortest flow path from the AMM producer to the DUV injector and from the DAP producer to the DUV injector.

Figure 7.2.8 displays box-and-whisker plots for the rate increase as a cause of pressure interference for varying geological parameters. In this figure, the values of geological parameters have an impact on the pressure interference at the Duijvestijn producer due to the start-up of the DAP producer. This is illustrated with the top-view of the pressure distribution after starting production of the DAP doublet. The rate increase data points are plotted on the box-and-whisker plots. Note that for the DAP doublet only the high target rate (380 m^3/h) scenarios are pressure constraint. The production rate increase due to pressure interference ranges from 6.8 to 24.1 m^3/h. For the same reason described above, the closed faults resulsure in higher (13-18 m^3/h) production increases compared to open faults (9-14 m^3/h). A facies orientation of 315° results in a higher rate increase compared to 285° and 345°. From Figure 7.2.7, it can be seen that an orientation of 345° has the worst alignment with the direction from the DAP producer to the Duijvestijn injector. However, 285° seems to create a more preferable flow path than 315°. This can be caused by the observation that the difference in angle is small (30°) and there are only two realizations. There is a chance that the wells penetrate an interval that has a high connectivity through the sand bodies from the producer to the injector. Creating more geological realizations with different facies orientations can confirm which facies orientation results in the largest pressure interference effect.

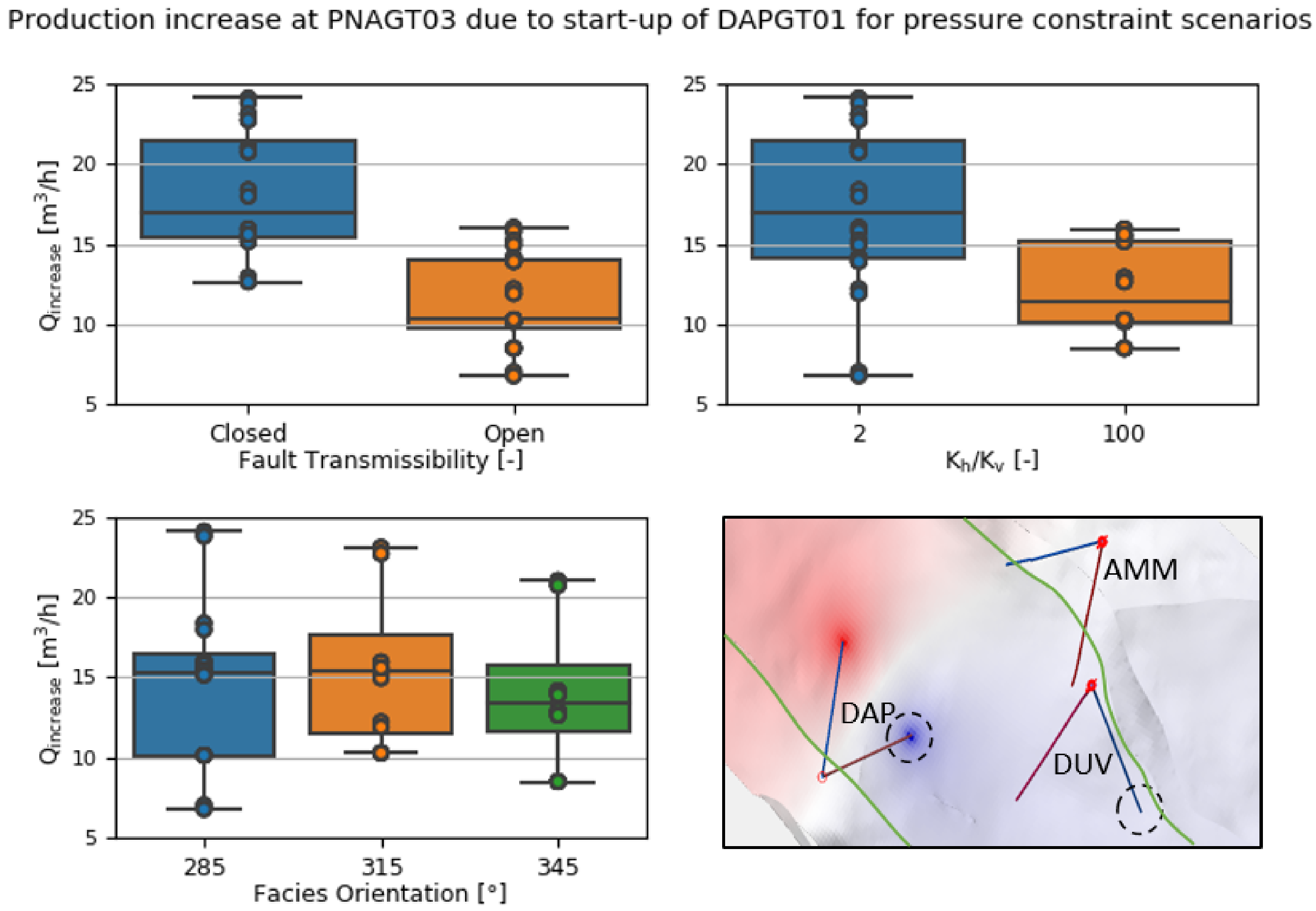

Figure 7.2.8: The variation in production rate increase at the Duijvestijn producer, due to the start-up of the neighbouring DAP doublet, for the geological parameters fault transmissibility, (K_h/K_v)-ratio and facies orientation. The map view displays the pressure drop (blue) and the pressure increase (red) that is created by respectively the DAP producer and DAP injector.

7.3. Temperature Interference

In this section, the temperature interference that occurs during the simultaneous production of the three doublets is quantified. This section only describes the rate constraint simulations, since only this output represents the geological parameters that were varied. The temperature interference is quantified by the thermal power difference over time of a doublet for a stand-alone configuration and a configuration where the neighbouring doublets are also running. The relative differences between these two configurations are presented, the absolute thermal output values can be found in Appendix F.3. Only the base case re-injection temperature (35°C) scenarios are presented in this section. A negative interference on temperature is observed by the Duijvestijn injector to the Ammerlaan producer. The relative difference in thermal power ranges from 2.5% to 15% when Duijvestijn produces at base case rates and from 7% to 33% when Duijvestijn produces at high rates. The interference effect is also very much dependent on the transmissibility of the nearby fault. When the fault is fully transmissible, cold water from the Duijvestijn injector can escape towards the northeast. The smaller variance for the different scenarios for rate and fault transmissibility is created by differences in medium and high scenario permeability, (K_h/K_v)-ratios and facies orientations.

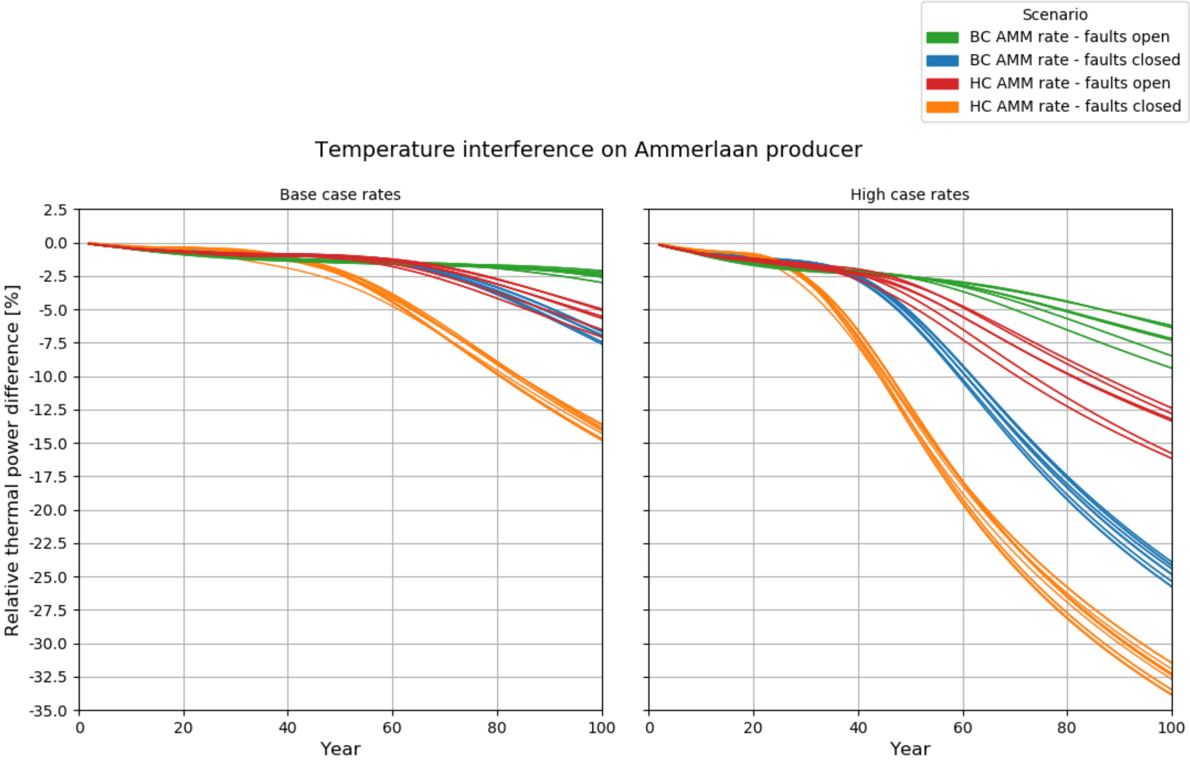

Figure 7.3.1: Temperature interference is plotted by the relative thermal power difference, because of temperature interference, over time for the Ammerlaan (AMM) doublet. It is the thermal power output of AMM running with neighbouring doublets minus the thermal power output of AMM running as stand-alone. In the graph on the left, neighbouring doublets are running with base case rates and on the right graph with high case rates.

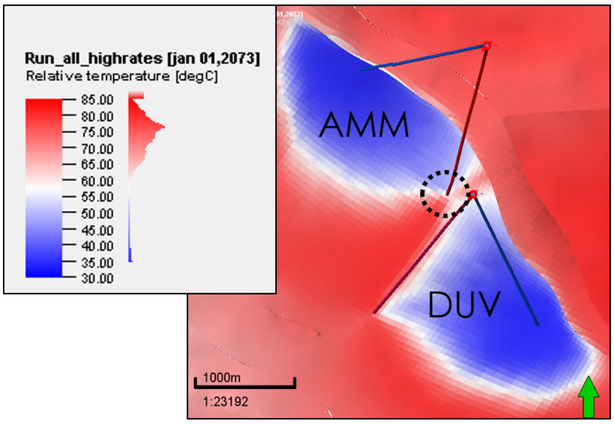

Figure 7.3.2: Top view of the temperature in the middle layer of the reservoir zone after 60 years of production. The temperature interference from the Duijvestijn injector to the Ammerlaan producer is visible.

The DAP doublet is also negatively interfered on temperature (Figure 7.3.3). The interference is caused because the DAP producer lies in the vicinity of the Ammerlaan (AMM) injector. The relative difference in thermal power ranges from 0.3% to 7.5% when AMM produces at base case rates and from 2% to 16% when AMM produces at high rates. Fault transmissibility has a smaller influence (1-6%) because the faults lie further away from the interfering wells. The interference is less compared to the interference found at the Ammerlaan producer. This can be explained by the observation that the distance between the Duijvestijn injector and the Ammerlaan producer (1600 m) is larger compared to the distance between the Ammerlaan injector and the DAP producer (2085 m). Also, the flow path of the former (345°) coincides more with the facies orientation (285°-345°) compared to the flow path of the latter (220°) (See Figure 7.2.7).

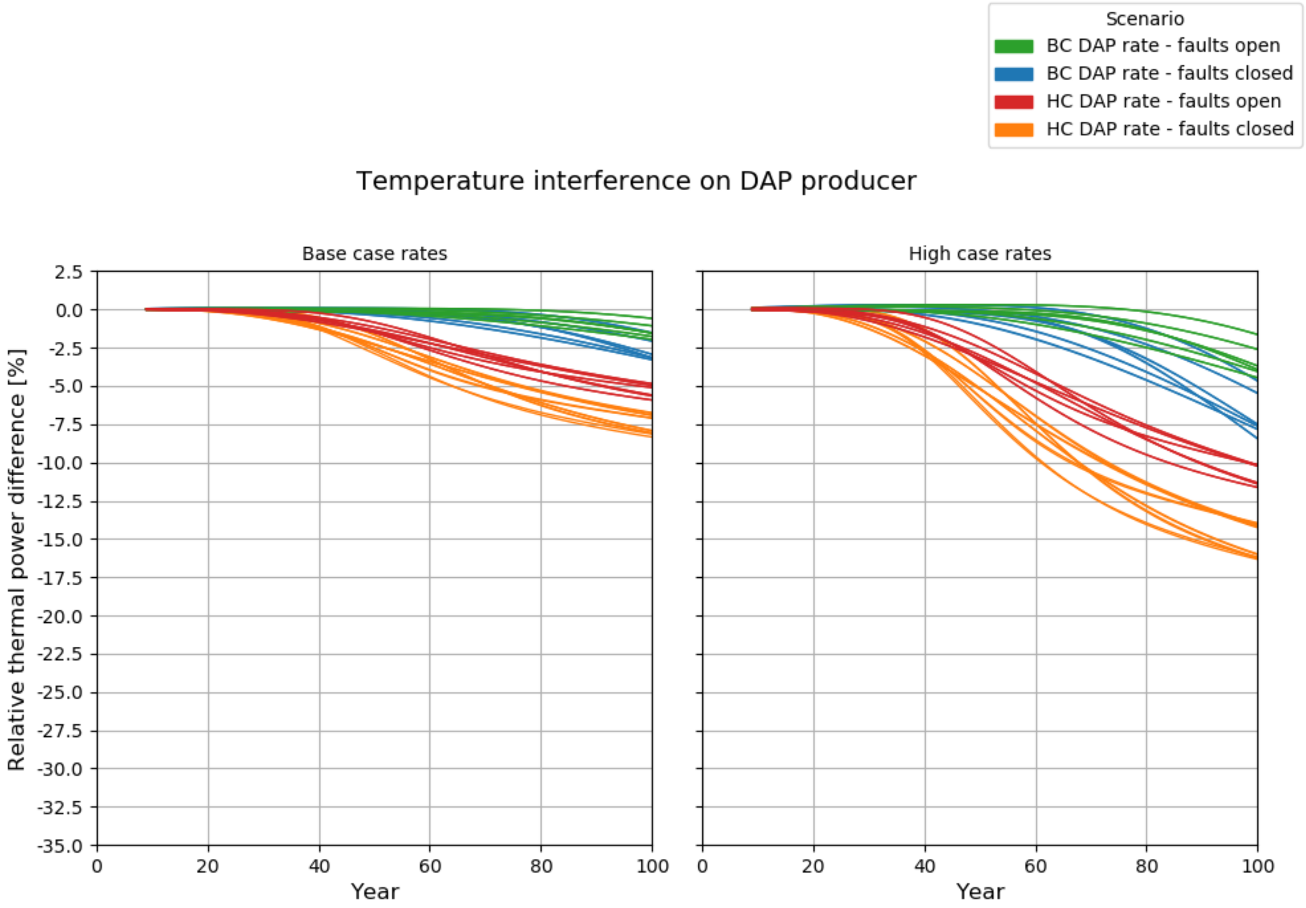

Figure 7.3.3: The relative thermal power difference is plotted over time for the DAP doublet. It is the thermal power output of DAP running with neighbouring doublets minus the thermal power output of DAP running as stand-alone. In the graph on the left, neighbouring doublets are running with base case rates and on the right graph with high case rates.

For the Duijvestijn (DUV), doublet a positive interference effect is found on temperature (Figure 7.3.4). The Ammerlaan producer creates a draw-down so that less of the cold waterfront reaches the DUV producer (Figure 7.3.5). The relative difference in thermal power ranges from 1% to 7% when AMM produces at base case rates and from 2% to 15% when AMM produces at high rates. Fault transmissibility is, in this case, the most important factor because of the nearby lying fault. With fully transmissible faults, the positive interference effect is very small (0-4%). The smaller variance for the different scenarios for rate and fault transmissibility is created by differences in medium and high scenario permeability, (K_h/K_v)-ratios and facies orientations.

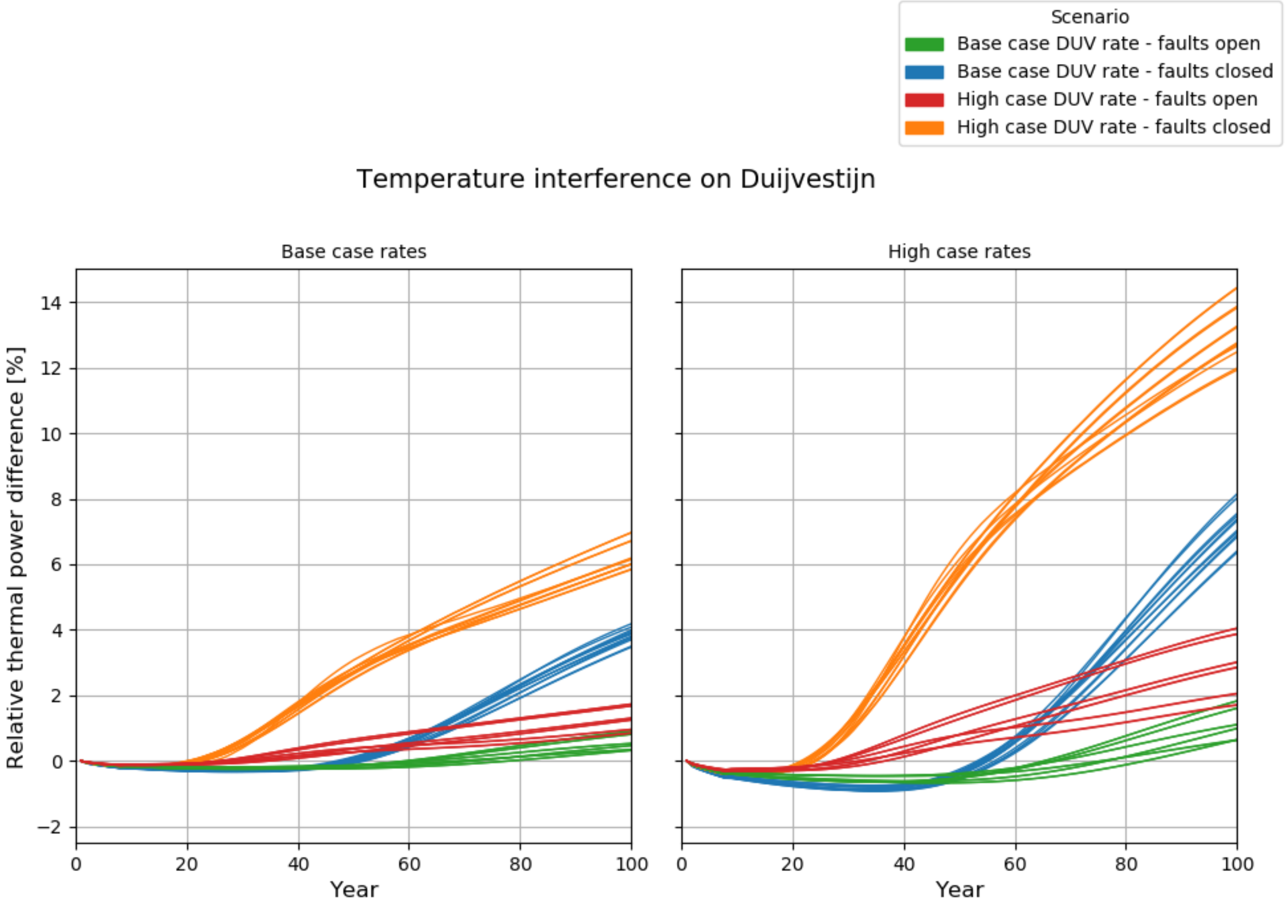

Figure 7.3.4: The relative thermal power difference is plotted over time for the Duijvestijn (DUV) doublet. It is the thermal power output of DUV running with neighbouring doublets minus the thermal power output of DUV running as stand-alone. In the graph on the left, neighbouring doublets (Ammerlaan and DAP) are running with base case rates and on the right graph with high case rates.

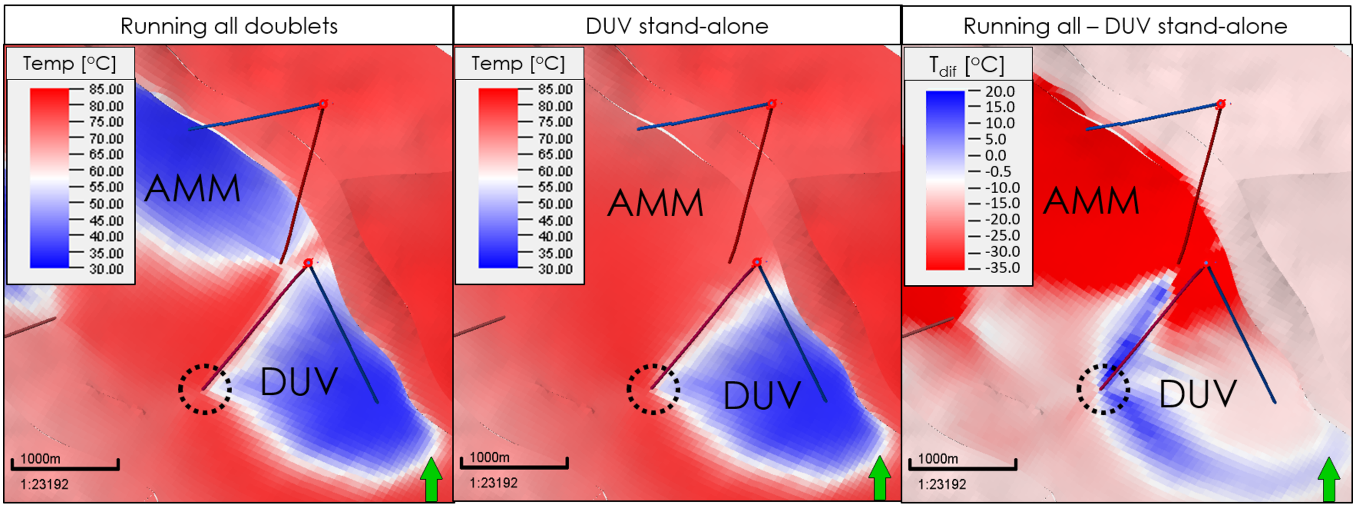

Figure 7.3.5: Left: Temperature after 60 years after production with all doublets running. Temperature interference visible from Duijvestijn injector to Ammerlaan producer. Center: Temperature after 60 years after production with Duijvestijn running in stand-alone configuration. Right: The temperature difference where the left figure (running all) is subtracted from the center figure (running stand-alone).

7.4. Doublet Lifetime

For this study, the lifetime of a doublet is defined by the time that it takes for the production temperature to reach 90% of its initial temperature. Figure 7.4.1 displays the production temperature over time for the different doublets. Under all considered scenarios, the lifetime of all doubles is at least 33 years. At base case rates, the lifetime of Duijvestijn and DAP has not been reached after 100 years of production. At high case rates the lifetime of the Duijvestijn and DAP doublet range from respectively 46-76 years and 45-90 years. For Ammerlaan, the spread in lifetime is wide at high case rates. This can be related to the higher impact of temperature interference displayed in Figure 7.3.1. A short increase in temperature is visible for the Ammerlaan producer for scenarios with sealing faults. This can be explained by the location of the producer, closer to a fault. When this fault is sealed, flow is trapped and therefore hotter water from deeper in the reservoir can reach the producer during the first 10 years of production. The DAP doublet starts production in 2021, 9 years after Duijvestijn starts production. The initial production temperature for DAP is 0.1-0.4 °C lower when Ammerlaan and Duijvestijn produce at high rates. This shows that in these scenarios, the DAP doublet is subject to temperature interference at the start of production.

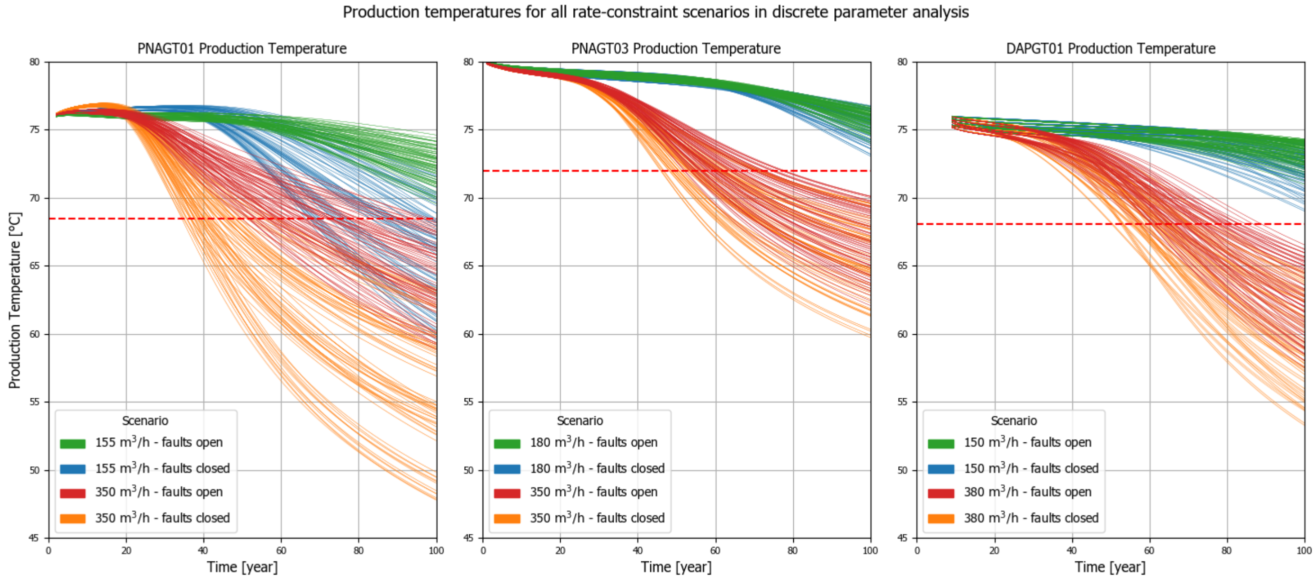

Figure 7.4.1: Production temperature over time for the Ammerlaan (left), Duijvestijn (center) and DAP (right) doublet for base case rates, high case rates combined with transmissible and sealing faults. The temperature that defines the end of life for the doublets is indicated with a horizontal dashed line.

7.5. Total Energy Production

This section presents what impact pressure and temperature interference has on the total energy production over the entire simulation time (100 years). This total is averaged for the simulated scenarios. The pressure constraint scenarios (See Figure 7.2.1) are separated from the rate constraint scenarios. This is done because for rate constraint scenarios, the production rates are the same for a doublet when running with neighbours and running them in stand-alone configuration. These scenarios are therefore only affected by interference on temperature (positively and negatively). For pressure constraint scenarios, the production and injection rates vary over the entire simulation time when comparing the same scenarios for running the doublets together and running them as stand-alone. The variation in production and injection rate is caused by the pressure interference (See Section 7.2). An increase in production rate over time results in an increase in total energy produced. It can however also cause the cold waterfront to reach the producer in a shorter time, decreasing the total energy produced. The total energy production when running all doublets together is compared to the total energy production when running them as stand-alone to determine if the net effect on the total energy produced is positive or negative.

7.5.1. Rate Constraint Scenarios

The rate constraint scenarios are the scenarios where the target rates are reached without exceeding the maximum allowable injection BHP (imposed by SodM). These scenarios are all the low permeability scenarios with base case DAP rates and all the medium and high permeability scenarios. This study has shown that the Ammerlaan and DAP producers are negatively impacted by temperature interference while the Duijvestijn producer is positively impacted (Section 7.3). When the neighbouring doublets are running at base case rates, the average relative difference in total energy produced for the Duijvestijn, Ammerlaan and DAP doublet is respectively +3.2%, -2.0% and -2.5% (Table 7.5.1). This confirms the statement above. The combined relative difference in total energy produced at base case rates is -1.3%. When the neighbouring doublets are running at high case rates, the average relative difference in total energy produced for the Duijvestijn, Ammerlaan and DAP doublet is respectively +4.3%, -5.6% and -2.9%. The combined relative difference in total energy produced at high case rates is -4.3%. That the difference for high case neighbouring rates is higher than for low case neighbouring rates is simply because at a higher production rate the cold waterfront of the neighbouring injector reaches the producer in a shorter time. If the base and high case neighbouring rates are considered, the doublets combined produce 0.5 PJ less energy over 100 years when they are running together compared to when they are running as stand-alone. This amounts to a relative difference of -2.8% on the total energy production of the three doublets combined.

Table 7.5.1: The total energy production averaged over the different rate constraint scenarios for the doublets running together and as stand-alone. The base case rates and high case rates of the neighbouring doublets are separated. The absolute and relative differences are displayed for the doublets Duijvestijn (DUV), Ammerlaan (AMM), DAP separately and for the the three doublets combined.

Configuration	**DUV**	**AMM**	**DAP**	**Combined**
Stand-alone production [PJ]	28.2	24.8	23.9	76.9
Running-all production (base case neighbouring rates) [PJ]	29.1	24.3	23.3	76.7
Absolute difference [PJ]	+0.9	-0.5	-0.6	-0.2
Relative difference	+3.2%	-2.0%	-2.5%	-1.3%
Running-all production (high case neighbouring rates) [PJ]	29.4	23.4	23.2	76.0
Absolute difference [PJ]	+1.2	-1.4	-0.7	-0.9
Relative difference	+4.3%	-5.6%	-2.9%	-4.3%
Running-all production (all neighbouring rates) [PJ]	29.3	23.9	23.3	76.4
Absolute difference [PJ]	+1.1	-1.0	-0.6	-0.5
Relative difference	+3.7%	-3.8%	-2.7%	-2.8%

7.5.2. Pressure Constraint Scenarios

This study shows that, under pressure constraint scenarios, the doublets are positively impacted on the injection and production rate when a neighbouring producer starts production (Section 7.2). Pressure constraint scenarios are all the low permeability scenarios except for the low permeablity scenarios where DAP produces at high case rates (Figure 7.2.1). With the varied geological parameters (facies orientation, k_h/k_v, fault transmissibility) this amounts to 120 (48+48+24) scenarios in stand-alone configuration. Base case and high case neighbouring target rate scenarios are not separated because the achievable rates are similar, simply because the injector cannot inject at higher rates (due to the maximum allowable BHP on the injector). The average relative difference in total energy produced for the Duijvestijn, Ammerlaan and DAP doublet is respectively +22.1%, +3.2% and +1.4% (Table 7.5.2). The total energy production when running the doublets together is 4.0 PJ higher compared to when they are running as stand-alone. This amounts to a relative increase of 7.9% in total energy production. For these scenarios, all doublets are benefiting through pressure interference, resulting in an increase in production rate and total energy production. That the Duijvestijn doublet has a much higher difference in energy production because of pressure interference also follows from the higher difference in average production rate because of pressure interference (Table 7.5.3).

Table 7.5.2: The total energy production averaged over the different pressure constraint scenarios for the doublets running together and as stand-alone. The absolute and relative differences are displayed for the doublets Duijvestijn (DUV), Ammerlaan (AMM), DAP separately and for the the three doublets combined.

Configuration	**DUV**	**AMM**	**DAP**	**Combined**
Stand-alone production [PJ]	14.7	10.8	24.8	50.1
Running-all production [PJ]	18.0	11.2	25.0	54.1
Absolute difference [PJ]	+3.3	+0.3	+0.4	+4.0
Relative difference	+22.1%	+3.2%	+1.4%	+7.9%

Table 7.5.3: The injection and production rate of the doublets, averaged over the different pressure constraint scenarios and displayed for the doublets running together and as stand-alone. The absolute and relative differences are displayed for the doublets Duijvestijn (DUV), Ammerlaan (AMM), DAP separately and for the the three doublets combined.

Configuration	**DUV**	**AMM**	**DAP**	**Combined**
Stand-alone production rates [m^3/h]	131	110	259	500
Running-all production rates [m^3/h]	157	115	261	533
Absolute difference [m^3/h]	+26	+5	+2	+33
Relative difference	+19.8%	+4.5%	+0.8%	+6.6%

7.6. Discussion

This section discusses an approach that aims to validate the differences in flow rate output between the different doublets while pressure constraint on the injection BHP. The observed interference on pressure and temperature are reflected upon and compared to other studies.

7.6.1. Flow Rate Differences for Pressure Constraint Simulations

This study shows that the constraint on the BHP of the injectors leads to pressure constraint simulations for low permeability scenarios (Section 7.2). The doublets achieve different flow rates under these scenarios. The maximum achievable flow rate could vary per doublet for different reasons:

1. Connectivity between injector and producer
2. Permeability around the injector
3. Pressure interference between doublets
4. Proximity to a sealing fault
5. Length of the injection perforation interval that has contact with the reservoir
6. Well spacing injector and producer
7. Geometry of the reservoir
8. Depth of the injector and producer

An approach is discussed that aims to identify what factors contribute to the differences in flow rates. Ideally, all factors are omitted to see how every factor influences the achievable flow rate. However, reservoir geometry is a result of seismic interpretation and well trajectories for our study case are finalized or have already been drilled. It is therefore not possible to omit factors 5-8. Differences in connectivity (1) and permeability (2), are created by the heterogeneity in the meandering channel belt system. To omit these differences, the reservoir is populated with a homogeneous porosity (12%) and permeability (80 mD). To omit any pressure interference effects between the doublets (3), the simulations are running in a stand-alone configuration. To omit any pressure build-up effects due to the proximity of a fault (4), the faults are set to be fully transmissible.

Table 7.6.1 shows the rates that are achieved for base case target rates and high case target rates under a homogeneous low permeability scenario. Having eliminated factors 1-4, the resulting rates are now subject to differences in factors 5-8. A larger length of the injection perforation interval (5) will result in a larger pressure gradient between injector and producer and a higher flow rate. A larger well spacing has the opposite effect and leads to a lower pressure gradient and therefore a lower flow rate. This can explain why DAP has the highest flow rates since it has the largest length of the injector perforation and the smallest well spacing. Reservoir geometry (7) also seems to play a significant role because of the variation in reservoir thickness and the inclination of the horizons (Figure 7.6.1). The reservoir thickness between the Ammerlaan injector and producer decreases and the pressure towards the producer increases due to the increase in depth. The pressure at the injector tends to build up quicker compared to the DAP doublet where the reservoir thickness and inclination stays fairly constant between injector and producer. It can partially explain why the achieved rates of Ammerlaan are lower compared to DAP. The Duijvestijn doublet has smaller reservoir thicknesses than DAP but they stay fairly constant between the injector and producer, compared to the Ammerlaan doublet. This study has shown that the differences in the depth of the injectors (8) lead to different allowable pressure build-up (Section 6.4.3). The lowest allowable pressure build-up for Ammerlaan also contributes to the doublet reaching the lowest achieved flow rate. The difference in depth between the doublets producer and injector creates an initial pressure difference. The Ammerlaan injector requires more injection pressure to drive flow towards the producer because the pressure difference is the largest compared to the other doublets. This is another reason why the Ammerlaan doublet flow rates are lower compared to Duijvestijn and DAP.

Table 7.6.1: The target and achieved rates (Q) are displayed for a homogeneous (80 mD) scenario with the varying injector perforation lengths (L_{perf}) of the injectors, well spacing and initial pressure difference (ΔP_{init}) for every doublet.

Case	Q_{target} [m^3/h]	$Q_{reached}$ [m^3/h]	L_{perf} [m]	Well spacing [m]	ΔP_{init} [bar]
AMM base case	155	57	79	1590	14
AMM high case	350	57			
DUV base case	180	142	143	1950	6
DUV high case	350	142			
DAP base case	150	150	165	1420	7
DAP high case	380	172			

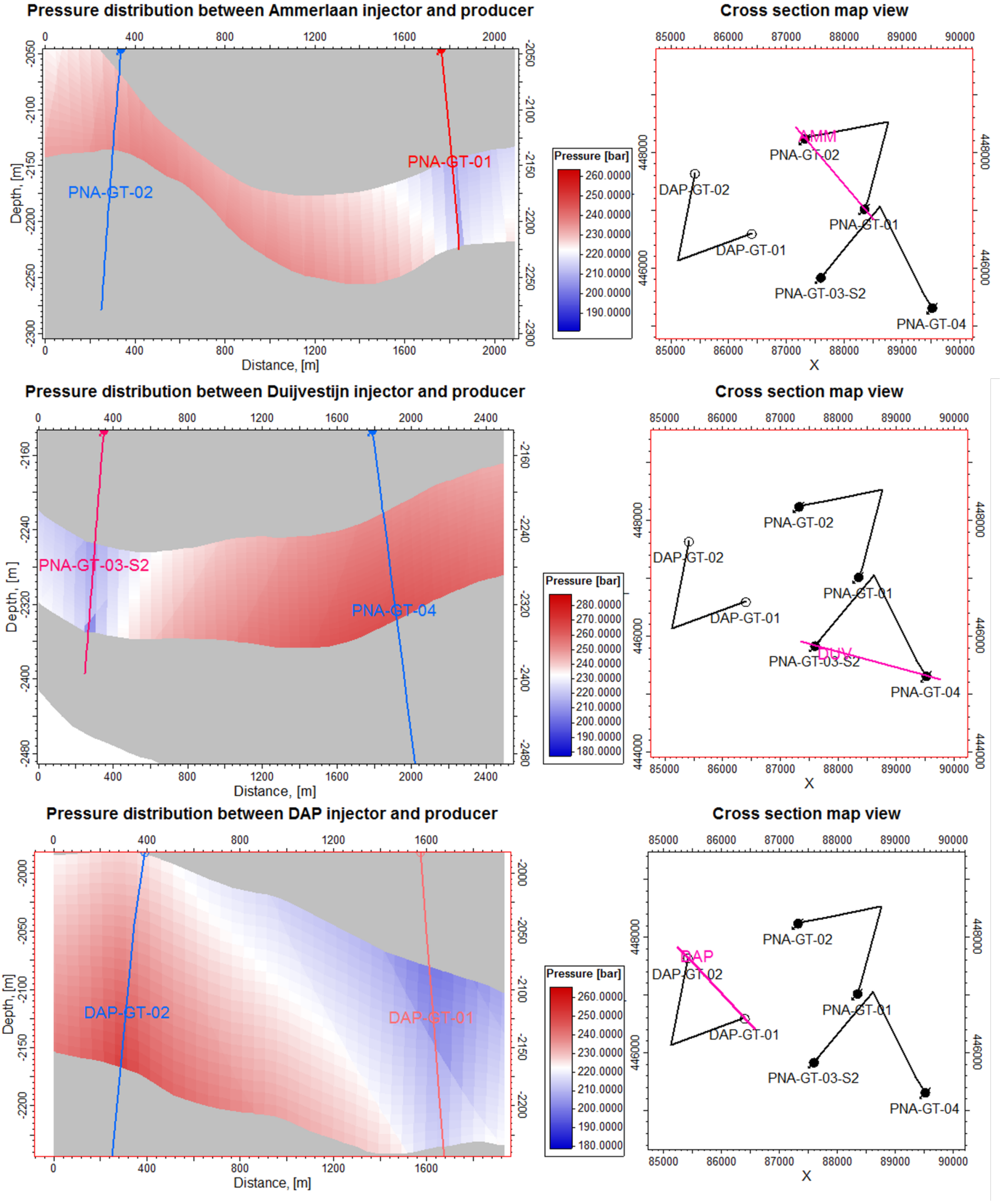

Figure 7.6.1: Left: Pressure distribution during production along the cross-sections of the injector and producer for Ammerlaan (top), Duijvestijn (center) and DAP (bottom). Right: Map view of the well trajectories of the doublets. The corresponding cross-section on the left of every map view is indicated in pink. Note that the scale of the vertical axis is highly exaggerated compared to the scale of the horizontal axis.

7.6.2. Pressure and Temperature Interference

The initial hypothesis, as stated in the introduction, was that there is a possibility that interference can have a negative effect on the production temperature of a neighbouring doublet. Willems et al. (2017a) showed this negative effect on temperature for 2D-homogeneous box models. This study confirms this negative effect uses 3D-heterogeneous models and shows that this kind of interference can indeed impact a doublet negatively, but also positively. Negative temperature interference occurs when the injector of a neighbour drives cold water towards the producer, reducing the thermal power over time. Positive temperature interference occurs when the producer of a neighbour creates a draw-down and drives the cold water of the injector to the neighbours producer. This reduces the time that the cold waterfront reaches our producer, increasing our thermal power over time.

For all simulated scenarios, the minimal time that temperature interference becomes significant is 20 years. Hence it can be doubted how relevant these interference effects are when a Stimulering Duurzame Energieproductie (SDE+) subsidy expires after 15 years. However, as the geographical density of geothermal projects increases, doublets can be placed closer together and these temperature interference effects can start to play a more important role.

But besides interference on temperature, this study also observed interference on pressure between the doublets. Pressure interference is noticeable when the pressure wave reaches the neighbouring well. This takes a couple of hours after production has started and follows an asymptotic increase or decrease. SodM prescribes a maximum allowable injection BHP (Section 6.4.3). We call an injector pressure constraint when it cannot inject more because it will otherwise exceed this pressure limit. When this is the case, an injector can be positively affected when a neighbouring production well starts producing. The draw-down of the neighbouring production well reduces the reservoir pressure at the injection well, allowing it to inject at a higher flow rate. It is vice-versa also possible that a doublet has to decrease its production rate when a neighbouring doublet is shut-in, causing an increase in reservoir pressure at the operating injection well, forcing it to decrease its injection rate. Willems et al. (2017a) observed changes in pressure distribution due to interference but only related that to the consequences it has for temperature interference (since the changing pressure distribution is the driving force for the flow of the re-injected cold water). The effect on the injection rate has been overlooked while it is very relevant because the production rate of all operating doublets in The Netherlands are constraint by the maximum allowable injection pressure.

The observation that the neighbouring wells are communicating on pressure is subject to all the uncertainties and limitations of our model. It can be argued however that the observation is a valid approximation of reality when one looks at the well spacing between the six simulated wells (Figure 7.6.2). The Duijvestijn injector and producer have to be communicating on pressure, otherwise it would have measured an increasing pressure build-up at the injector during injection. The well spacing between the Duijvestijn wells is 1.71km while the well spacing between the Ammerlaan producer and the Duijvestijn injector is 1.62km. Because the latter are communicating on pressure it is highly likely that the former are as well. The same holds for the DAP producer and the Ammerlaan injector (1.4km between DAP wells and 1.98km between DAP producer and Ammerlaan injector). Well interference tests can determine the degree to which the doublets are actually communicating on pressure and will also establish the necessity for the individual operators to communicate their operational planning with their neighbour.

The starting point of studying interference on temperature in this area is work that has been executed at Delft University of Technology (Ammiwala, 2018). A similar box-model, as proposed for the simulator benchmark, was created to study temperature interference effects. In this work, no seismic interpretation was performed, making the determination of the top reservoir depth of the DAP wells difficult. The geographical locations of the perforations were different compared to ours. In the previous study, the first interference effect is observed between the Ammerlaan injector and the DAP producer. In our box model and as well as in our structural model, the first interference effects were observed between the Duijvestijn injector and the Ammerlaan producer (Figure 7.6.3). The difference between the box-models can be fully contributed to the differences in the location of the perforation because properties are homogeneous and reservoir geometry is equal. It shows that prior to the planning of well trajectories, an extensive reservoir modelling study can prevent negative interference effects and can create positive interference effects.

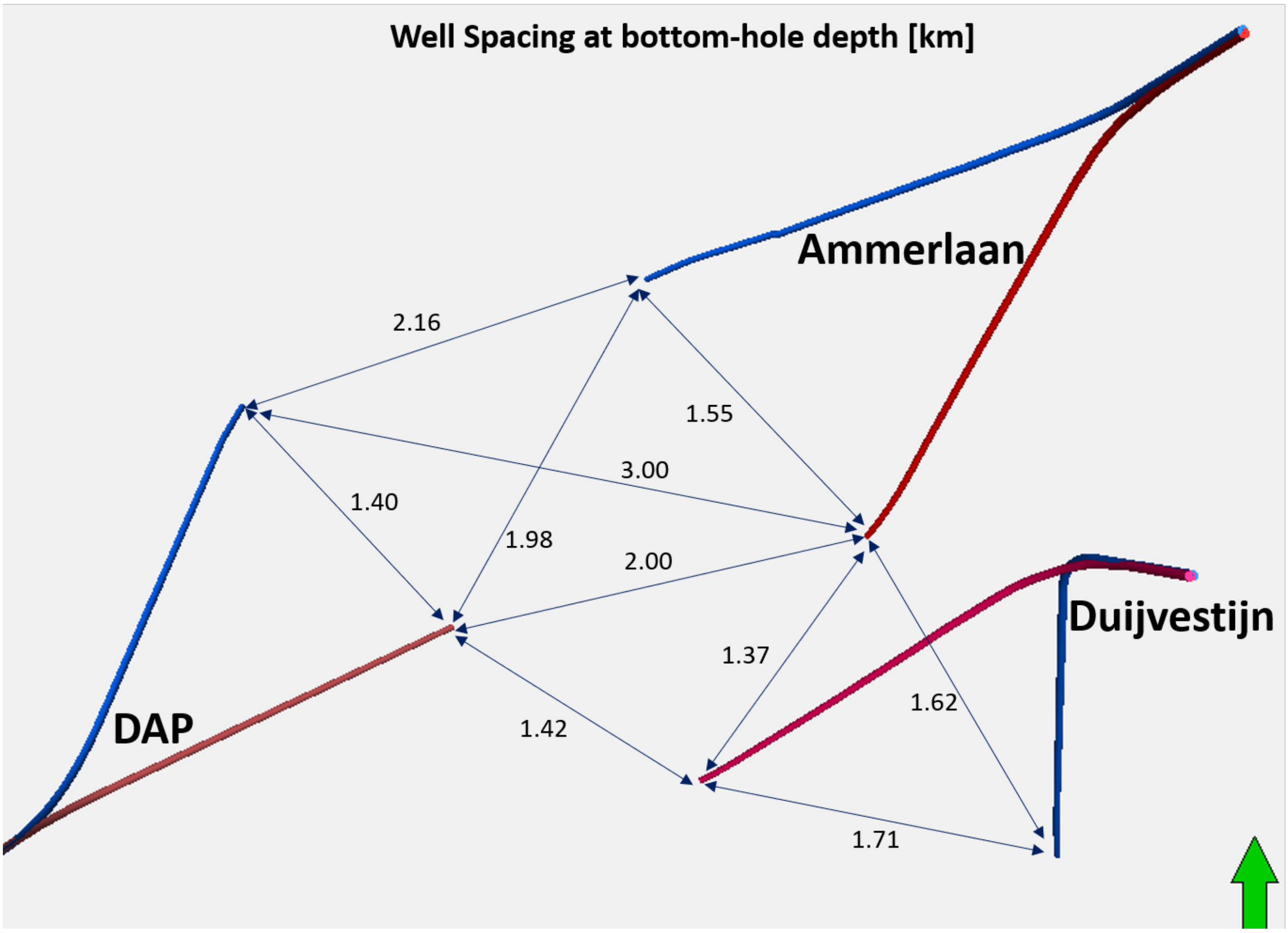

Figure 7.6.2: Top-view of the simulation wells with the corresponding well spacing (in km) between the producers (red) and injectors (blue).

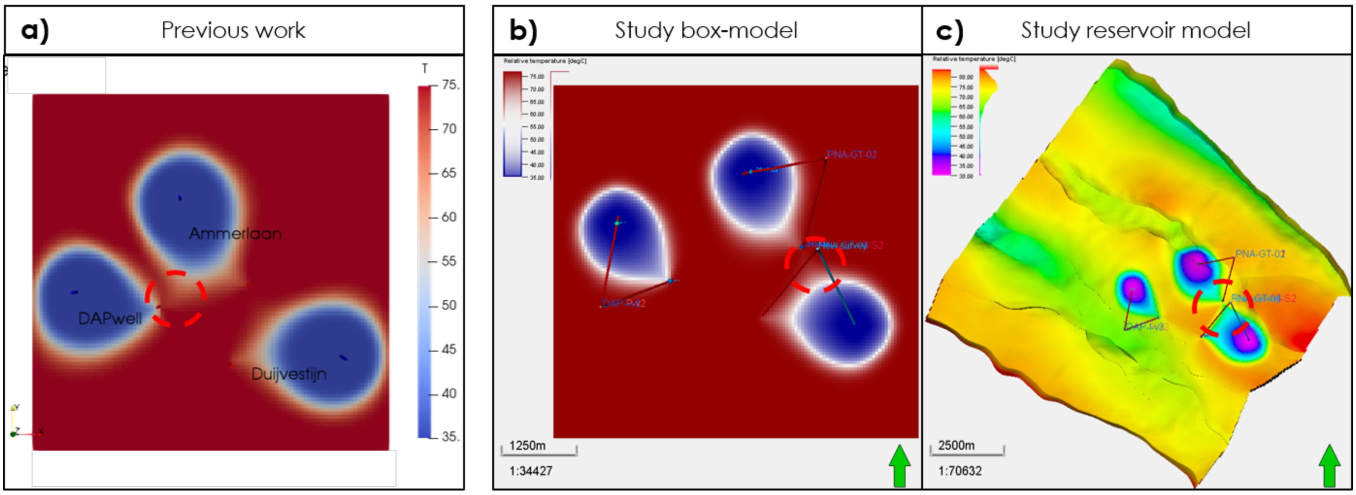

Figure 7.6.3: First temperature interference interference occurs between Ammerlaan injector and the DAP producer in previous work (a) and between the Duijvestijn injector and the Ammerlaan producer in study box-model (b) and the study reservoir model (c). First interference location is circled in red.

8

Implications for Policy Measures

This chapter aims to investigate the implications that the findings of this research have on the policy measures for geothermal operations in dense production areas. First, the methodology for doing this is laid out. The most relevant stakeholders for geothermal projects in The Netherlands are described. The geothermal license application and approval process is reviewed and tested for the study case. A comparison is made with the way interference is coordinated in the oil and gas industry. Policy measures for handling pressure interference are presented. The policy measure that limits the injection pressure is discussed. This chapter is finalized by presenting the conclusions on the possible changes in policy measures for geothermal projects.

8.1. Methodology

The first step in researching the implications on the policy measures that the findings of this research might have is describing the stakeholder landscape. This allows us to determine who the stakeholders are, how they interact and what coordination mechanisms are in place. The determination of the license area is described in more detail since it is crucial for amplifying or mitigating interference effects. The application and approval process for a geothermal license is reviewed to be able to determine if it serves the purpose of optimal heat recovery. Several interviews have been conducted to give insights in the current policy measures and obtain different views on how they can be improved (Table 8.1.1).

Table 8.1.1: The interviewees with their respective organization and function. TUD = Delft University of Technology.

Full Name	Organization	Function
Harmen Mijnlieff	TNO-AGE	Senior Geologist
Jan-Dirk Jansen	Civil Engineering & Geosciences, TUD	Dean
Rien Herber	University of Groningen	Professor
Barbara Cox	Hydreco Geomec (affiliated with DAGO)	Subsurface Manager
Berend Scheffers	EBN B.V.	Director Strategy & Technology

8.2. Involved Stakeholders

This section briefly describes the important stakeholders in the Dutch geothermal industry. The different tasks such as authorization, advisory, supervision and facilitation are divided among the different stakeholders. The detailed description of these roles can also be accessed through EBN (2019) (in Dutch).

8.2.1. EZK

EZK (Ministery of Economic Affairs and Climate / Ministerie van Economische Zaken en Klimaat) represents the Dutch State for all operations related to the ownership of resources. Parties must request an exploration, production or storage license from EZK. EZK can refuse the license or change or withdraw a license that has already been issued. EZK can only refuse a license based on grounds laid down in the Mining Act (the Mijnbouwwet). EZK is also the competent authority for environmental licenses that mainly concern mining (e.g., installations for geothermal heat, gas or salt extraction). The supervision of SodM falls under the responsibility of the minister. The minister is advised on these manners by the

Mining Council, SodM, EBN B.V. and TNO. EZK is also the sole shareholder of the private company EBN B.V. and thereby determines the activities in which the private company can participate and invest.

8.2.2. The Mining Council

The role of the Mining Council is to advise EZK on issues such as granting exploration and production licenses. The Mining Council is independent and assesses whether granting is justified. To do this, they view the application and recommendations from TNO, SodM and the relevant province council, municipality and water board. Rules regarding the functioning of the Mining Council are laid down in the Mining Act.

8.2.3. SodM

SodM (State Supervision of Mines / Staatstoezicht op de Mijnen) is a government inspection service for mining activities. The service falls under the responsibility of EZK and is led by the Inspector-general of Mines. SodM ensures compliance with legal rules concerning the exploration, extraction, storage and transport of resources. Reasons for this integrated supervision are the specific nature of mineral extraction. The prevention of undesirable situations in the areas of safety (accidents), health (sickness absence), environment (contaminants) and soil movements (seismicity). Such a situation usually requires comparable interventions, and treatment together is therefore effective and efficient. SodM has a role as an advisor and as a supervisor. At the request of EZK, SodM assesses the technical capacity of the applicant(s) of the exploration license: is the applicant able to safely carry out the desired activities? SodM also advises EZK on the granting of an environmental license. The holder of an exploration license must submit a work plan to SodM. This includes, among other things, drilling plans and documents about safety and health care. SodM supervises compliance with all laws and regulations with regard to mining works or mining activities. To this end, SodM makes use of the supervisory powers from, among others, the Mining Act, Working Conditions Act and the General Administrative Law Act. SodM can also take enforcement measures, such as applying administrative enforcement, imposing a penalty or fine or prescribing a measure. Many SodM inspectors are also empowered to draw up official reports in case of a criminal offense.

8.2.4. Geothermal Operator

The geothermal operator is the person (natural or legal person) who is designated by the license holder to perform the actual work or to give instructions for this. Several parties can participate in a license and are then together referred to as 'the license holder'. The appointment of the party that executes the work is not final after the license is approved. Another party may be appointed after the license holder has obtained written permission from EZK. In the Netherlands two types of operators are active. The first are active in the greenhouse industry for growing fruits and vegetables. The primary reason to extract heat from the subsurface is for supplying the greenhouses of heat. This type of operator is active locally, in the vicinity of its greenhouses. The second type of operator can be defined as an energy supplier and is active on a national scale. It looks at opportunities where there is geothermal potential and heat demand. It is important to distinguish the two types of operators since they can have different viewpoints when it comes to policy measures for geothermal projects.

8.2.5. DAGO

DAGO (Dutch Association Geothermal Operators) is the branch association for geothermal operators in the Netherlands. These operators are legal or natural persons who are the license executor of at least one extraction license in which mining activities take place or will take place in the future. DAGO represents the collective interests of these geothermal operators in the Netherlands and contributes to the safety and effectiveness of geothermal energy generation. Within DAGO, operators bundle and share their experiences and knowledge of geothermal energy in an open and equivalent manner. Through this bundling and communication of experiences, DAGO improves and accelerates the possibilities in standardization policy, efficiency and the accessibility of the knowledge gained. As of 2019, DAGO counts 21 affiliated members and 7 prospective members.

8.2.6. EBN B.V.

EBN (Energie Beheer Nederland B.V.) is a state enterprise that participates on behalf of the State in the exploration, production and sale of gas and oil in the Netherlands. The tasks of EBN are laid down in the Mining Act. Based on the Mining Act, EBN invests together with companies in both the exploration and extraction of oil and gas in the Netherlands. In addition, EBN is a 40% shareholder in GasTerra and, upon request, provides the minister with the information necessary to assess the feasibility of the proposed energy policy. At the request of the Ministry of Economic Affairs, EBN has had a role since 2017 in bringing together, sharing and providing access to knowledge about the subsurface for geothermal energy. As of 2019, the Mining Act obligates every geothermal operator to offer EBN to take a minority stake in their geothermal project. EBN plays a role as a knowledge partner in both oil and gas, and in geothermal energy, and uses its knowledge of the subsurface to maximize the use of energy potential from the subsurface and to make energy management more sustainable.

8.2.7. TNO-AGE

TNO (Toegepast Natuurwetenschappelijk Onderzoek) is a research institute with the objective to apply scientific knowledge in practice. It is a non-profit organization and has been designated by the State to share knowledge about the Dutch subsurface. The AGE (Advisory Group for Economic Affairs) department of TNO advises the Mining Council and EZK in its decisions on permitting, operations and other activities related to the subsurface.

8.2.8. Province Councils, Municipality Councils and Water Boards

Province councils, municipality councils and water boards are governmental institutions that will look after the environmental impact and spatial planning of the area that is assigned to them. For geothermal operations, they are mostly concerned with visual and noise disturbance through operations and safeguarding drink-water aquifers.

8.3. Geothermal License Approval Process

Geothermal projects are accompanied by major investments. A common practice, also seen in the oil and gas industry, is that several parties apply for a license together for a certain field or area. This way they share costs and risks. The geothermal operator carries out the actual work, so that the other license holders are not required to be registered as a mining company. Several entities can participate in a license. All entities together are considered as one ”license holder”. An applicant has to go through a licensing approval process to receive a license area where a doublet can be drilled and geothermal heat can be extracted. Such a process should aim to only allocate licenses to safe and economically feasible projects to ensure optimal utilization of the heat in the subsurface. There are three main licenses an applicant has to obtain before it can start operation:

1. Exploration license (opsporingsvergunning)
2. Environmental license (omgevingsvergunning)
3. Extraction license (winningsvergunning)

Exploration License

The exploration license is the first license that needs to be applied for at EZK. The different steps and interaction between the involved stakeholders are displayed in Figure 8.3.1. With this application, the initiator requests exclusivity to be allowed to investigate an area on the presence of geothermal energy. The application for an exploration license must be accompanied by the submission of (Ministry of Economic Affairs, 2014; NLOG, 2014; SodM, 2017):

- Geological survey: a quick scan based on existing knowledge and information from the geological potential to extract geothermal energy.
- Investigation plan: how will the investigation and future extraction be executed?
- Safety and health: a description of policy, organization, planning, implementation, procedures, available resources, monitoring, evaluation, internal company screening and improvement to improve the safety and health of employees and the environment.

- Technical and financial requirements: the applicant must demonstrate that he is both technically and is financially able to complete the project.

EZK will ask the appointed institutions for advice and test the application on criteria related to (Figure 8.3.1):

- 2a - the financial viability of the applicants is investigated. It is still under consideration under what criteria and by whom this will be investigated.
- 2b - TNO-AGE advises on the geological substantiation of the application. In addition, TNO-AGE advises whether the work program fits in with the requested license duration and the size of the requested area.
- 2c - It is mandatory that the local authorities are involved and consulted on issues that they find relevant for the well-being of the environment and the surroundings.
- 2d - SodM advises EZK concerning the technical capacities of the applicant to carry out the intended activities, the efficiency and sense of responsibility of the applicant, the substantiation of expected operational risks and any risks for the environment.

The advice of the institutions is compiled, reviewed by EZK and send to the Mining Council to supply EZK with the final advise on the approval of the license (3). EZK can then make a final decision on the approval of the geothermal license. After approval, the exploration license is valid for 3 to 5 years (4).

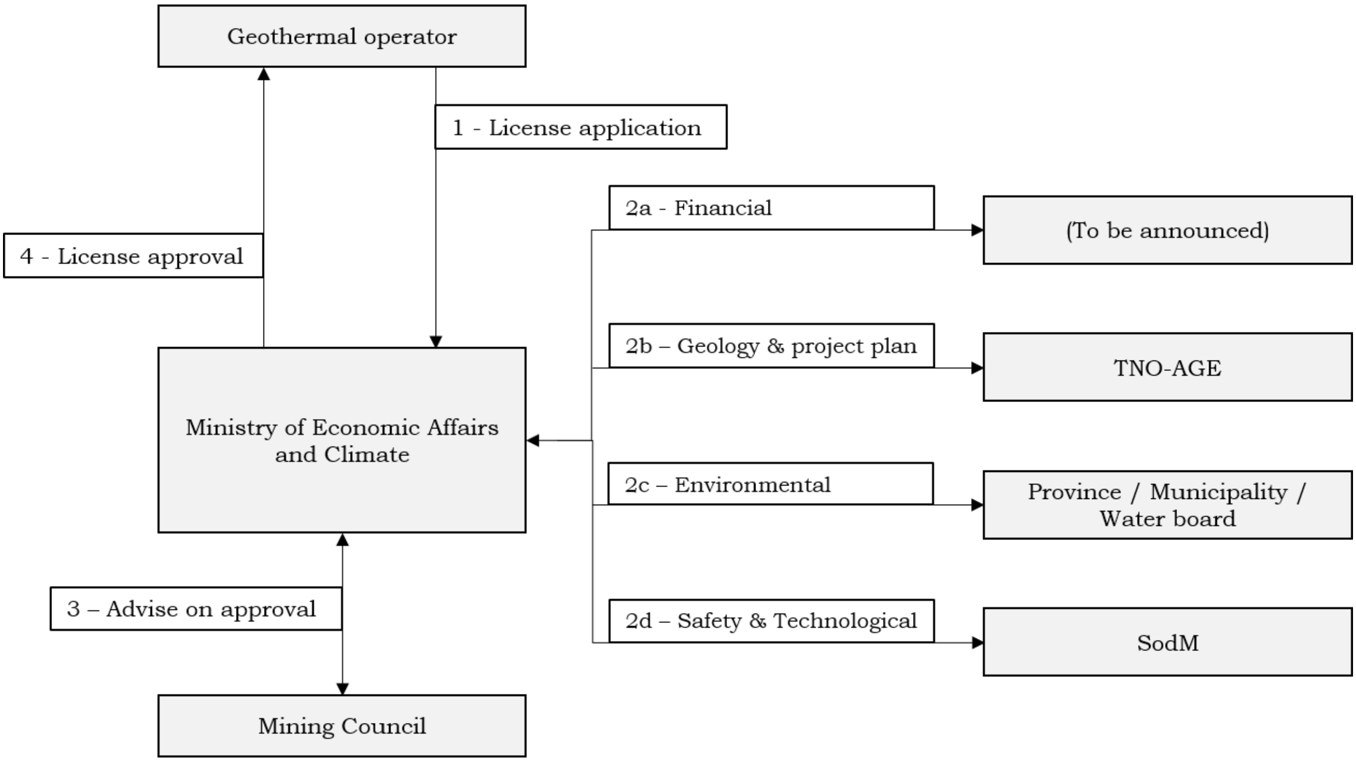

Figure 8.3.1: Stakeholder interaction of the application of the operator for an exploration license (1), to the phase where several institutions test the application on different criteria (2), the advisory by the Mining Council (3) and the final approval of the exploration license (4).

Environmental License

In this period, the license holder needs to apply for the environmental license. The following steps have to be conducted (Ministry of Economic Affairs, 2014; NLOG, 2014; SodM, 2017):

- Further geological research to determine the optimum location of the production and injection well(s), the drilling design and the expected risks, especially with regard to the production of (residual) hydrocarbons and possible induced seismicity. How the optimal well location is to be found is not prescribed by the Mining Act but TNO-AGE expects the applicant to at least have performed seismic interpretation adequately and analysed the available subsurface data in the area.

- Feasibility study to gain insight if the project is economically viable.
- Drilling design with different drilling options and their effect on feasibility and risks.
- Application for an environmental license to get permission for the actual construction of the drilling site and the drilling of the doublet.
- Tender and contracting of a drilling company based on the drilling design and program.
- Project preparation with clear division of tasks, responsibilities and authority.
- Preparation of drilling project, in which the initiator must demonstrate to SodM that the drilling will take place safely and according to the legal rules.

Extraction License
After an environmental license has been approved, an extraction license is required. The same stakeholder interaction, as displayed in Figure 8.3.1, holds for this procedure. A long-term plan must be submitted stating how the applicant intends to exploit the geothermal source. It should include the expected amount of heat produced, expected operational costs, energy consumption and risk management. The exact boundaries of the license area have to be determined. This is currently done by applying the 'French Method'. This method has been formulated by TNO-AGE after consultation with EZK (Mijnlieff and van Wees, 2009; TNO-AGE, 2014):

1. Two circles are drawn around the injector and producer at reservoir depth. These locations have been determined through seismic interpretation during the application of environmental license. The two circles coincide in between the two wells (Figure 8.3.2). The two circles are thus only dependent on well spacing and do not incorporate any properties of the subsurface.
2. A rectangle is drawn around the two circles, determining the license boundary.
3. The production duration of the doublet is defined by the time that it takes for the rock, located at the boundaries of the license, is cooled down by 1°C. The applicant is expected to investigate this through reservoir modelling, which is then reviewed by TNO-AGE. EZK can also request TNO-AGE for further investigation if it is thought to be necessary. There is no prescribed modelling or simulation approach. The other criterion for determining the production duration of the doublet is that the induced pressure difference at the boundaries of the license should not more than 1 bar.

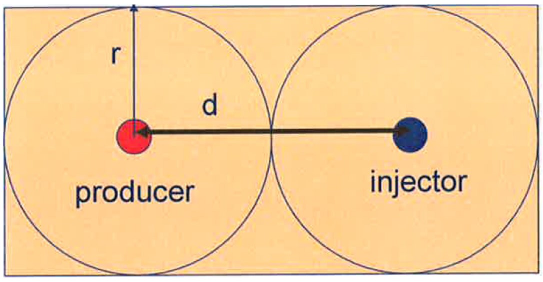

Figure 8.3.2: French Method for determining license boundaries. Two equally sized circles are drawn around the injector and producer. The well spacing is the diameter (d) of a circle and the two circles coincide at the radius (r) distance from each well (Mijnlieff and van Wees, 2009; TNO-AGE, 2014).

8.4. Study Case License Boundaries

The base case scenario is simulated for base case rates and high case rates (Table 8.4.1) to test the criteria prescribed by TNO-AGE on the license boundaries of our study case area. Duijvestijn and Ammerlaan have been assigned an exploration license duration of 35 years by EZK (extraction license has not been reported) (Staatscourant van het Koninkrijk der Nederlanden, 2017a,b). At base case rates, the Ammerlaan and Duijvestijn doublets seem to fulfill this criterion. The injection wells cool down the boundary of the license area by 1 °C after respectively 61 and 38 years (Figure 8.4.1). At high case rates, they both surpass this criterion after 15 years. According to the output of this simulation, the doublets should be given a shorter production time on their extraction license if they increase flow rates to the high case levels. The DAP license duration has not been approved as of yet but both base case rate and high case rates fulfill the criterion for at least 44 years.

None of the doublets fulfill the criterion of inducing a maximum pressure difference of 1 bar at the boundaries of the license area, after reaching a steady-state pressure regime. The induced pressure difference was measured at a location along the boundary of the license area where the difference exceeds the prescribed limit. The Ammerlaan, DAP and Duijvestijn doublets induces a pressure difference at those locations of respectively 2, 2.2 and 5.6 bar (Figure 8.4.1). The time that it takes for the pressure wave to arrive at the boundary has been observed to be less then a month.

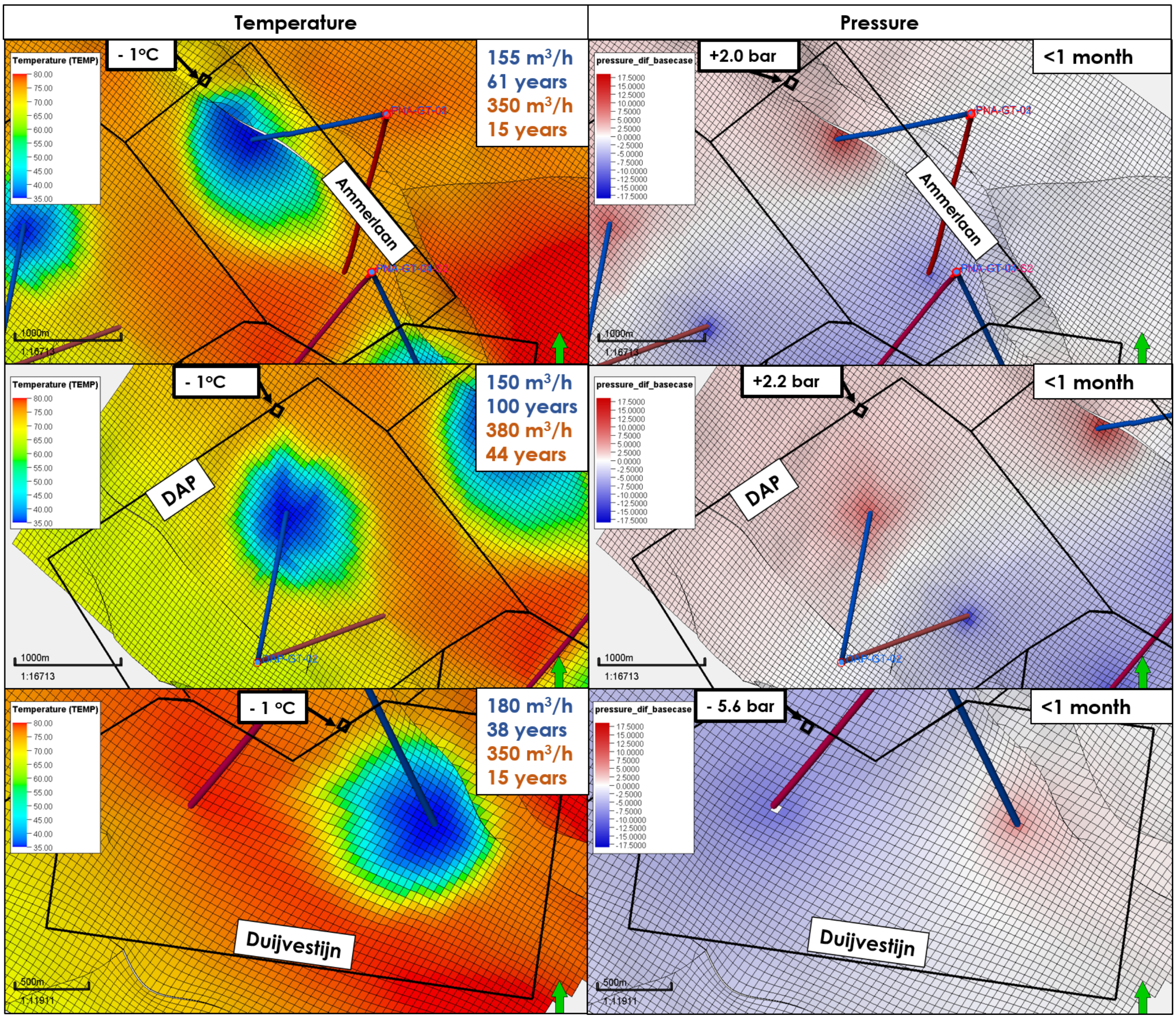

Figure 8.4.1: Temperature (left) and pressure (right) differences at the boundary of the Ammerlaan (top), DAP (center) and Duijvestijn (bottom) license area. Displayed on the top right is the achieved flow rate and time it takes for the temperature to drop with 1°C or a pressure difference with more than 1 bar.

Table 8.4.1: Values of the discrete analysis parameters for the base case, used to determine the lifetime according to the 'French Method'. Simulation time is from 2013 to 2113.

Permeability	**Faults**	**K_h/K_v**	**T_{inj}**	**Facies Orientation**	**AMM Rate base case high case**	**DAP Rate base case high case**	**DUV Rate base case high case**
Low	Open	100	35 °C	315°	155 m^3/h 350 m^3/h	150 m^3/h 380 m^3/h	180 m^3/h 350 m^3/h

8.5. Interference in the Oil and Gas Industry

It is often suggested that the developing geothermal industry should learn from the more matured oil and gas industry. The State Supervision of Mines also highlights this in the report on the state of the geothermal sector (Ministry of Economic Affairs, 2014; NLOG, 2014; SodM, 2017). There are indeed enough similarities between the two. There are however also specific differences that make it difficult to transfer knowledge of the oil and gas industry and apply it directly to the geothermal industry without adjustments. It is beyond the scope of this research to discuss all the similarities and differences of the two sectors. This section will be focused on how the oil and gas industry arranges production in a reservoir by multiple operators and how this can be applied in the geothermal industry.

8.5.1. Rule of Capture vs. Unitization

Interference in both industries work similarly; two or more operators are seeking to extract the targeted resource from the same reservoir unit. In the premature phase of the oil and gas industry, there was no coordination in the case of interference; it meant that operators acted on a 'rule of capture' mechanism. This phrase describes a way of production where individual operators placed as many production wells along the boundaries of their license area to maximize their production. Throughout the years, it became clear that this approach led to a very inefficient way of production and sub-optimal recovery of resources. This made the industry move to unitization agreements. Before production, neighbouring operators would agree on a development strategy that would benefit all parties in accordance with their part of the license area. This optimized the recovery efficiency and thereby economic profits. For hydrocarbon production, the targeted resource is the limited volume of hydrocarbons. This makes it possible to have periodic checks on the produced hydrocarbons, possibly redistributing profits if one operator has produced more or less than earlier agreed on. These kind of agreements are self-enforcing provisions and can be categorized as peer-to-peer coordination. The process of unitization creates transaction costs for all parties. These higher costs lead to lower profits and thus lower tax revenues from which society can benefit. It is why EBN, who has a 40% stake in almost all of the fields and looks after the interests of the State, has as a coordinating role in these agreements to ensure that transaction costs are minimized.

8.5.2. Unitization for Geothermal Projects

The first difference with geothermal production, compared to hydrocarbon production, is that the targeted resource is not a limited quantity but a specific property (heat) of an abundant resource (water) in the deep part of the subsurface. Because the resource is abundant, the quantity of the produced resource is not what the operators are competing on and thus not what has to be agreed on. The agreement has to be made on the speed at which the cold waterfront of an injector is cooling down the neighbouring license area(s). It is not possible to have periodic checks on the distance that the cold waterfront has traveled because one can only measure the temperature down-hole at the wells. An operator will only know if he made a fair agreement when the neighbours cold waterfront has reached his producer. By then, the only correction that can be made is a temporary shut-in of the neighbouring well. But since the temperature decrease at a production well could also be caused by its own injector, an inevitable dispute will arise.

Extensive reservoir modelling, as executed in this research, is required to determine the order in which the injectors will cause thermal breakthrough (at the agreed production rates). It is shown in this study that this order varies when the location of the perforation is interpreted differently (Section 7.6.2). If all parties agree on the production rates and the order of thermal breakthrough, future disputes can be avoided. An organization with knowledge of the subsurface and reservoir modelling can coordinate the negotiation of the agreement to perform quality control on the modelling efforts and to minimize transaction costs. After a unitization agreement is made, coordination or supervision is necessary to make sure the agreement is honored. This would require real-time data (pressure, temperature, flow rates) from the doublets to be shared with the coordinating party. The designated organization to do this is TNO-AGE since they are already provided with this data and have advanced modelling and simulation software in-house. This would require extra investments from the government and would give TNO-AGE more of an operational role compared to its current advisory role. After building a structural reservoir model, reservoir management techniques can be applied to optimize production under the constraints of the unitization agreement.

8.5.3. Play-based Approach

The second difference is the heterogeneity of the stakeholders in the geothermal industry. Oil and gas companies in the Netherlands have been active in more then one location. As described in Section 8.2.4, in the geothermal sector two types of operators can be identified. The first operates on a local level and restricts itself to geothermal production in the area where it can supply heat for its primary business activity (e.g. growing crops). For the second type, heat production is (one of) the primary business activities which allows it to be active on a more regional scale. They look into the up-scaling of projects where multiple doublets are drilled and connected to a district heating network. The heterogeneity of these stakeholders can lead to misalignment when they are operating in the vicinity of each other. For example, (greenhouse) industry and a heating district network. The first type profits from a flexible way of licensing where the well placement and operational constraints are not restricted so that the heat extraction is maximized locally. The second type benefits from a more integrated approach of licensing where the heat utilization of a larger area is optimized. This tendering process has proven to be successful in the subsidy reliant offshore wind sector.

An example of the latter is the play-based approach, another phrase that has its origin in the oil and gas industry. The play, a group of concessions in the same region that are controlled by the same set of geological circumstances, is developed as a whole so that well placement and production is optimized for the whole area. It can thereby have a benefit for society over a single doublet approach. Current policy measures are however rather flexible and minimize the restriction of operators in the area they are applying for, in the well placement and in alignment with neighbouring doublets. The current policy is based on a first-come-first-serve rule and therefore does not stimulate a play-based approach. This study focuses on a study case area in the West Netherlands Basin where the development of geothermal energy has been ongoing for several years. A lot of plays have a producing doublet or have an approved exploration license. It is therefore too late to apply a play-based approach in this region for the first lifetime cycle of doublets. Future development of other regions in The Netherlands can benefit from a change in policy where the play is identified and analysed prior to the drilling of doublets from individual operators. A coordinating party, with knowledge of the subsurface and reservoir modelling, can then identify the geothermal plays. These plays can be tendered and winning bid(s) can start production, preferably after a unitization agreement has been made.

8.6. Coordination for Pressure Interference

In Section 7.2 it is shown that the draw-down of a producer results in a decrease in reservoir pressure at the neighbouring injector. Vice versa, the shut-in of that producer results in the reservoir pressure at that injector to increase back to its initial state. The former creates opportunities for optimizing heat production where the latter can cause an injector to exceed the maximum allowable injection pressure. In this section, policy measures are proposed to deal with pressure interference.

8.6.1. Optimizing Well Placement for Pressure Interference

This study shows that pressure interference can lead to a significant increase in total heat recovery. This implies that there is not a trade-off between minimizing interference and achieving the highest possible efficiency, as stated in TNO-AGE (2014). Instead, negative interference should be mitigated and positive interference should be amplified. In other words, interference effects should be optimized. It is shown that the impact of pressure interference varies with well spacing, permeability, fault transmissibility, reservoir thickness, flow rates and being pressure constraint on the injection pressure or not. It is therefore not straightforward to predict interference effects without adequate reservoir modelling and simulation. Current policy measures for the approval of well placement does not prescribe that the evaluation of pressure interference should be incorporated to find the optimal well location for producer and injector. Extensive reservoir modelling, prior to going through the application process, would be necessary to do this but not all operators have the adequate software packages readily available. It would require the operator to hire a third-party to execute this work. When a play-based approach is applied, as described in Section 8.5.3, this work could also be executed by the coordinating party.

8.6.2. Mitigation of Pressure Exceedance

The shut-in of a producer can result in a neighbouring injector to exceed the maximum allowable injection pressure. This pressure increase is asymptotic and the largest pressure increase occurs when the pressure wave arrives. A fast increase above the maximum allowable injection pressure can induce fracturing of the reservoir around the well. In The Netherlands, injectors either have an auto-stop or an alarm on the injection pump. An auto-stop automatically stops injection and production if the injection pressure meter exceeds the maximum allowable injection pressure. The other option sends an alarm to the phone of the operator so that he can act accordingly. For geothermal projects in The Netherlands, there is not always an operator present on-site. An alarm system is connected to the operators phone, at which he is available 24/7. The largest increase in reservoir pressure occurs when the pressure wave, created by the neighbouring production well, reaches the injector. After the pressure wave has arrived, the pressure increases asymptotically. Fractures can be created in the 15-30 minutes that the injector is injecting above the maximum allowed pressure. This fracturing can be prevented by two possible mitigation measures:

- Make auto-stops on a geothermal injection well mandatory by law. These auto-stops should have some time margin at which they act because geothermal wells tend to clog up when they are shut-in on a frequent basis.
- Make it mandatory by law to share operational planning, shutting in production wells in specific, with neighbouring operators. This would require supervision by SodM.

8.7. Policy Measures for the Limit on Injection Pressure

SodM prescribes a maximum allowable injection pressure that increases with depth at a constant slope coefficient (See Section 6.4.3). SodM does not differentiate this slope coefficient for varying geological settings. This prescribed maximum injection pressure is however the constraining factor for geothermal projects to achieve higher flow rates, higher heat production and a quicker return on investment. Using a slope coefficient that is too conservative leads to sub-optimal heat production. SodM allows for customization provided that an additional geological substantiation is provided with the license application which demonstrates that this is possible in a responsible manner, without negatively affecting the top sealing layer or nearby lying faults (SoDM, 2013). There are no guidelines or prescriptions on what kind of substantiation is required to obtain a customized slope coefficient. For example, the results of a leak-off test can be used to obtain the fracture gradient. This interpretation can be reviewed by TNO-AGE and then used as the slope coefficient for the maximum injection pressure after applying a safety correction factor.

8.8. Conclusions

This chapter has analysed the current policy measures under which the described stakeholders interact. Several propositions for changes in policy measures are presented. From these, the following conclusions can be drawn:

- The current coordination between stakeholders in the geothermal industry is centralized by EZK. The Mining Act prescribes the steps which an applicant has to follow in order to obtain an exploration, environmental and extraction license. Policy measures for determining pressure and temperature interference are poorly defined. There are no specific prescriptions of what a reservoir modelling and simulation study should incorporate.
- The current policy measure for determining the boundaries of an extraction license only incorporates well distance and neglects any properties of, and heterogeneity in, the subsurface. The base case scenario shows that the method leads to for the Ammerlaan and Duijvestijn doublet an extraction license period of respectively 61 and 38 years, sufficient for the license period of 35 which they have been assigned. At high case flow rates, the boundary of the licenses have cooled down by 1 °C after 15 years. Future plans to raise flow rates should therefore be reviewed for the current extraction license period of 35 years. The Mining Act does not prescribe how these situations are handled. The second criterion prescribes that production should not induce a pressure difference of more than 1 bar at the boundaries of an extraction license. The base case scenario shows that none of the doublets honor this criterion. It is highly probable that this is not a realistic criterion. In addition, this study shows that it can be beneficial to have boundary exceeding pressure differences. The pressure criterion should therefore be reviewed by TNO-AGE.

- A trade-off between flexibility and integration is identified for the geothermal licensing policy. The current policy leans toward flexibility and gives no incentive for unitization agreements and a play-based approach. These approaches can enable operators to optimize production and can therefore be beneficial for society. Such a shift can however restrict a geothermal operator that is only interested in operating a single doublet in a specific location.
- Extensive reservoir modelling can be prescribed to incorporate pressure interference effects to optimize well placement. A third party can be hired to execute the modelling work. Alternatively, the work can be allocated to the coordinating party when the reservoir is unitized and the reservoir management is outsourced to this coordinating party. It would require extra investments from the government and would give TNO-AGE more of an operational role compared to its current advisory role.
- There are currently no policy measures in place to mitigate pressure exceedance of an injector when a neighbouring production well is shut-in. This chapter proposes two possible policy measures; Making auto-stops (with a time margin) in injection wells mandatory or supervising the operators on the communication of operational planning with the neighbouring doublets.
- The slope coefficient that determines the maximum allowable injection pressure should be customized for different geological settings. The current policy does not prescribe what the adequate substantiation to customize this slope coefficient should entail. Leak-off tests can be interpreted to determine the fracture gradient of the reservoir rock. The optimization of the slope coefficient could lead to more economical production.

9

Thermal Recharge Analysis

The dynamic reservoir model is used to analyse the thermal recharge of the reservoir after production has stopped. A a low, medium and high thermal conductivity scenario is presented. Then four scenarios are presented in which the overburden and underburden thickness of the model is increased. In the last scenario, the cell height increment of the overburden and underburden is increased towards the upper and lower boundary of the reservoir model.

9.1. Methodology

Thermal recharge is the degree to which the temperature of the reservoir is recharged by heat transfer after production has stopped. Heat transfer is governed by conduction, convection and radiation. In this study, the possibility of heat transfer by radiation is neglected. During production heat transfer is then governed by convection and conduction. It was assumed that after production there is no groundwater flow driven through the reservoir. By assuming this, the convection term in the conservation of energy equation (Eq.3.6) diminishes and the heat transfer is only governed by conduction. The degree to which conduction takes place is dependent on the spatial temperature gradient and the thermal conductivity of rock and fluids. The uncertainty in the thermal conductivity of the saturated sandstone, shales and fluid is studied to determine the impact it has on the rate of thermal recharge. Because there is only the thermal conductivity parameter (λ) that needs to be varied, uncertainty analysis is much less time consuming compared to the discrete parameter analysis. The thermal recharge rate and energy production are studied for the field considering a low, medium and high thermal conductivity scenario (Table 9.1.1). The only heterogeneity of thermal conductivity is introduced in the reservoir and non-reservoir zones. Any other anisotropy or heterogeneity of the thermal conductivity of the rock is neglected. The reasoning behind the specific values can be found in Section 6.2.5. A scenario where overburden and underburden are neglected is added as a reference.

Table 9.1.1: Thermal conductivity values for rock and fluid for the low, medium and high scenario.

λ-scenario	**$\lambda_{\text{reservoir}}$ [W/m/K]**	**$\lambda_{\text{non-reservoir}}$ [W/m/K]**
Low	2.0	1.1
Medium	3.5	1.9
High	5.0	2.8

For all simulations, doublets are following the same development strategy as the discrete parameter analysis (Section 7.1). Wells are then shut-in and the reservoir is thermally recharged for 1000 years (Figure 9.1.1). The thermal recharge time is defined by the time it takes for the average reservoir temperature and the temperature at the producer to reach 99% of its initial temperature (Daniilidis et al., 2016). The average reservoir temperature is calculated by averaging the temperature property of every grid cell that has been accounted to the reservoir zone. The initial average reservoir temperature was 74.6 °C, the recharged temperature thus 73.1 °C.

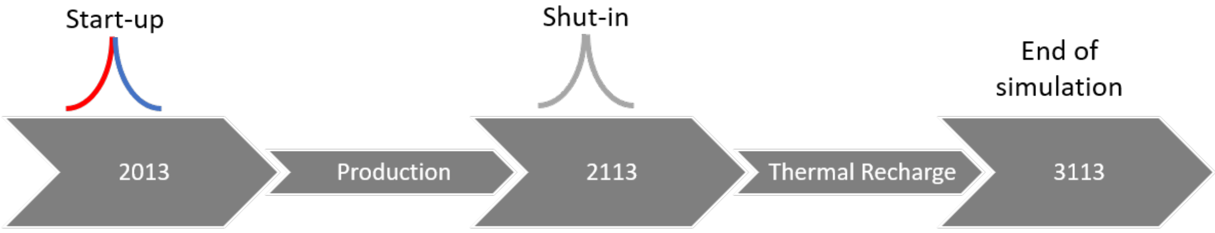

Figure 9.1.1: Development strategy for the thermal recharge analysis. The development strategy up to 100 years is the same to that proposed for the discrete parameter analysis (Figure 6.4.3). Wells are then shut-in and thermal recharge takes place for 1000 years.

Overburden and underburden thicknesses are then varied to determine the impact it has on its capacity to recharge the reservoir (Figure 9.1.2). The first scenario neglects any overburden (OB) and underburden (UB). Scenario I represents the base case thicknesses established from seismic interpretation. Thicknesses are then increased with 1000m (Scenario II) and afterwards with another 225m for the overburden and 2000m for the underburden (Scenario III). The increase in overburden thickness for Scenario III is limited by the surface level (Figure 9.1.2). The final models are displayed in Figure 9.1.2 and the final average thicknesses, the number of cells and layers are displayed in Table 9.1.2. For all simulations, a medium thermal conductivity scenario is assumed (Table 9.1.1). By increasing the overburden and underburden thicknesses, any heterogeneous properties of rock above and below the overburden and underburden is neglected. What is also neglected is that the shallow part of the overburden is unsaturated, the varying temperature gradient up to the surface and the thermal flux of the Earth's interior to the surface. Note that the geothermal gradient assumes an annual average surface temperature of 10 °C.

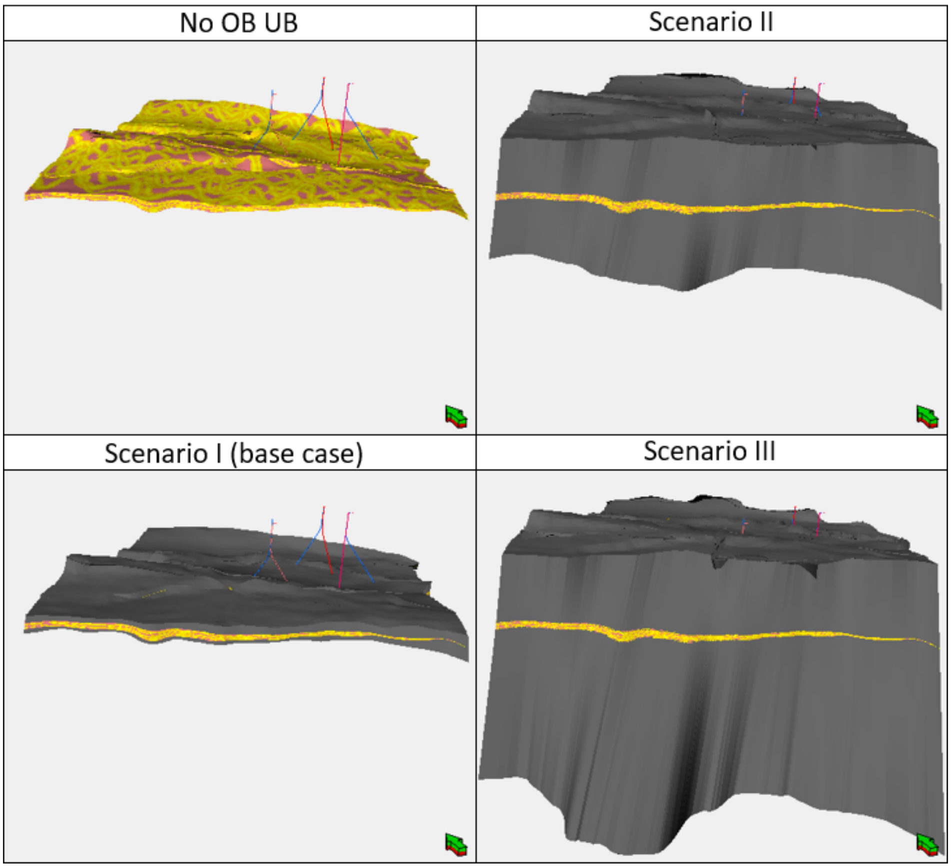

Figure 9.1.2: Only OB UB: only considering the reservoir zone and no overburden or underburden. Scenario I: Base case model with overburden and underburden interpreted from seismic. Scenario II: Increased overburden and underburden by 1000m compared to Scenario I (base case). Scenario III: Increased overburden and underburden by 1275m and 3000m compared to the Scenario I (base case).

Table 9.1.2: Number of cells and layers and the overburden (OB) and underburden (UB) thicknesses of scenario I, II, III and IV.

Grid property	Scenario I	Scenario II	Scenario III	Scenario IV
Average OB thickness [m]	0	130	1130	1355
Aveage UB thickness [m]	0	225	1225	4225
Number of cells [-]	334.800	499.120	1.002.214	1.673.090
Number of layers [OB-reservoir-UB]	0-20-0	3-20-3	16-20-26	20-20-80

The layering method for the overburden and underburden is then changed from equal cell height for every layer to decreasing cell height for overburden and underburden towards the interface of the non-reservoir and reservoir zone (Figure 9.1.3). This aimed to capture the high-temperature gradient at the interface of the reservoir and non-reservoir zones. This is done for thickness Scenario II (Figure 9.1.2) to ensure that the thickness of over- and underburden is not limiting the capacity of thermal recharge. A low, medium, high and extreme thermal conductivity scenario are evaluated (Table 9.1.3).

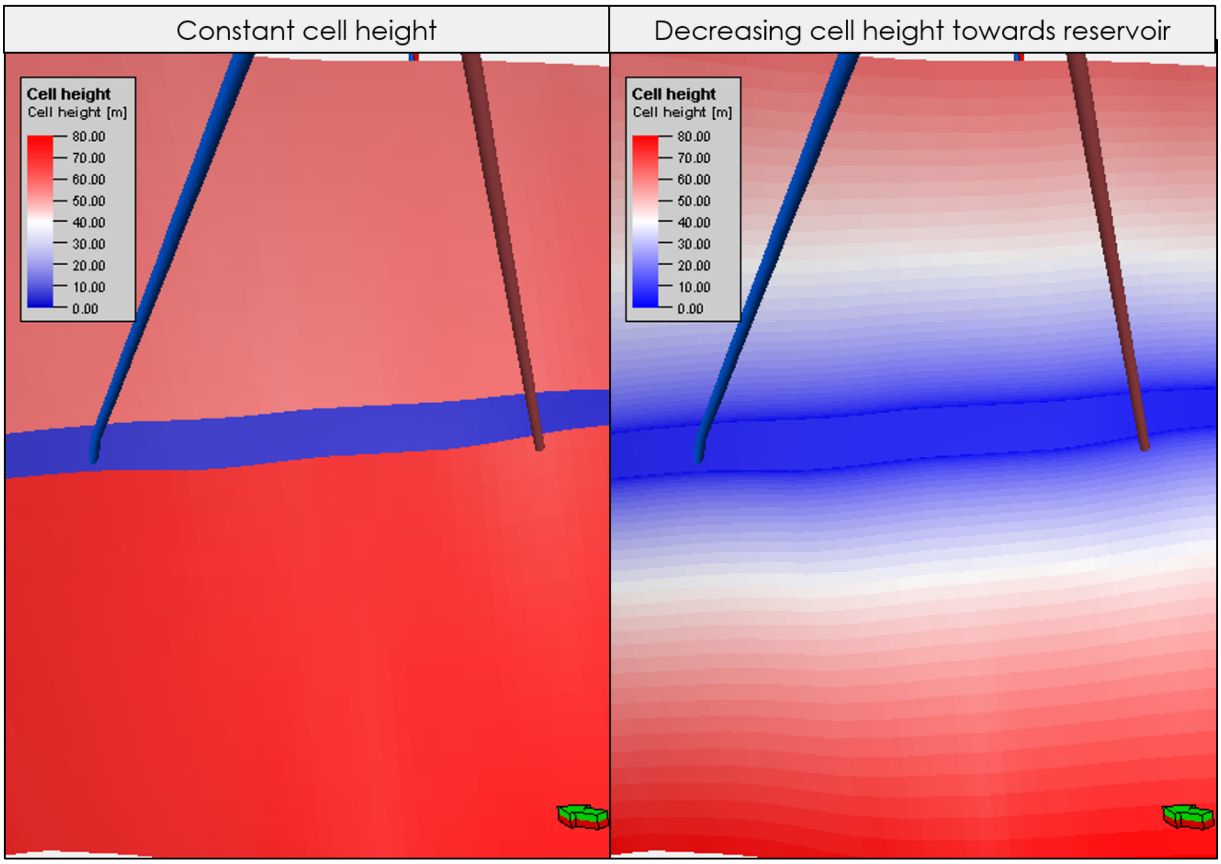

Figure 9.1.3: Left: Constant (left) and decreasing (right) cell height of overburden and underburden. Thickness Scenario II is used (Figure 9.1.2).

Table 9.1.3: Thermal conductivity values for rock and fluid for the low, medium, high and extreme scenario.

λ-scenario	$\lambda_{\text{reservoir}}$ [W/m/K]	$\lambda_{\text{non-reservoir}}$ [W/m/K]
Low	2.0	1.1
Medium	3.5	1.9
High	5.0	2.8
Extreme	23.1	12.7

9.2. Thermal Conductivity Scenarios

The conductivity scenarios for the reservoir model with the base case overburden and underburden thicknesses (Scenario I) are evaluated. The average reservoir temperature after 100 years of production is 68.0, 68.5 and 68.8 °C for respectively a low, medium and high thermal conductivity scenario (Figure 9.2.1). The reservoir is recharged by respectively 96.1%, 96.4% and 96.5% of the initial average reservoir temperature after 1000 years of thermal recharge. Without overburden and underburden, reservoir temperature drops to 66.9 °C and does not recharge afterwards. For the other scenarios, an asymptotic increase in average reservoir temperature is observed. During thermal recharge, the thermal conductivity of the rock and fluids stays constant and the temperature gradient decreases. As the temperature gradient decreases, the rate of thermal recharge decreases, resulting in an asymptotic increase in temperature.

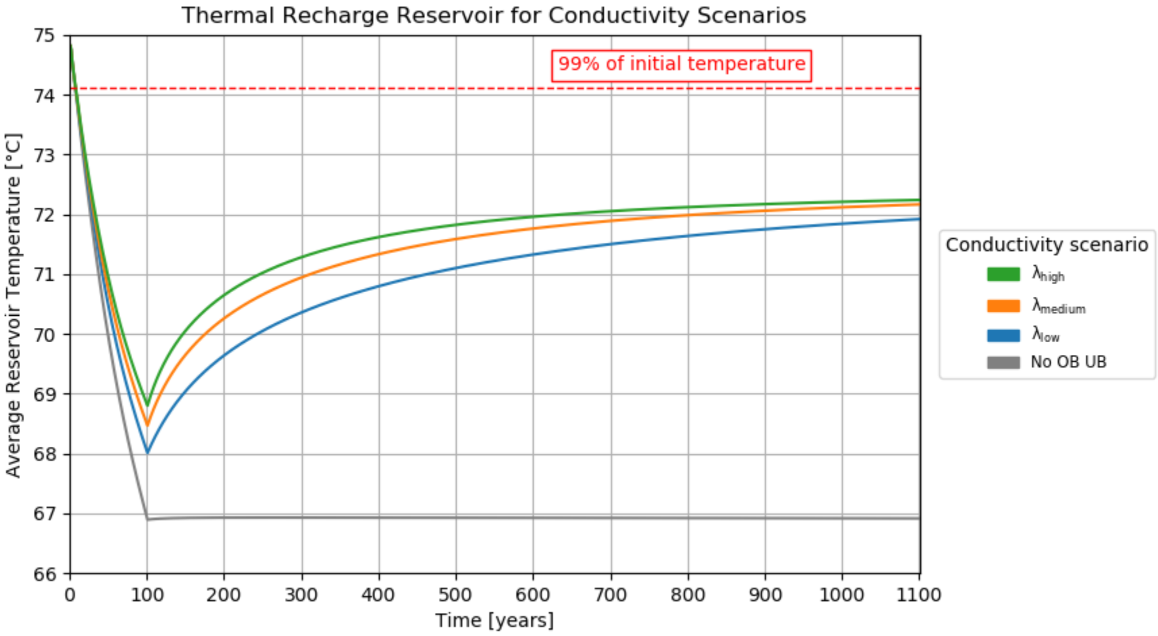

Figure 9.2.1: Average reservoir temperature over time for the low, medium and high case thermal conductivity scenarios. The first 100 years all doublets are running simultaneously and are then shut-in for 1000 years of thermal recharge. Base case overburden and underburden thicknesses were used.

Figure 9.2.2 displays the top view of the reservoir with on the left the cold waterfront after 100 years of production and on the right, the difference in temperature after 700 years of recharge compared to the temperature distribution after 100 years of production. Only a small negative temperature differences between the re-heated front of the injection well is observed. It can be concluded that in this case, the lateral thermal recharge is small compared to the vertical reheating. This is also confirmed by the lack of thermal recharge when overburden and underburden are neglected (Figure 9.2.1). It can be explained by the difference in the size of the contact area of the rock through which conduction can take place. This area is relatively small along the sides (~0.4 km^2) of the reservoir compared to the area on top and bottom of the reservoir (~4.5 km^2). In other words, the ratio of thickness to lateral surface area is small in the study case (0.09). A higher reservoir thickness increases the lateral contact area and thereby increase the contribution of thermal recharge in the lateral direction.

For all thermal conductivity scenarios, the target recharged temperature of 99% of the initial temperature is not reached. Figure 9.2.3 displays in cross-sections of the reservoir, the reservoir with the overburden and underburden, between the DAP injector and producer. It shows the reservoir temperature after production and the difference in temperature, compared to temperature after production, with time steps of 100 years. The overburden and underburden is cooled down after 300 years, limiting its capacity to recharge the reservoir.

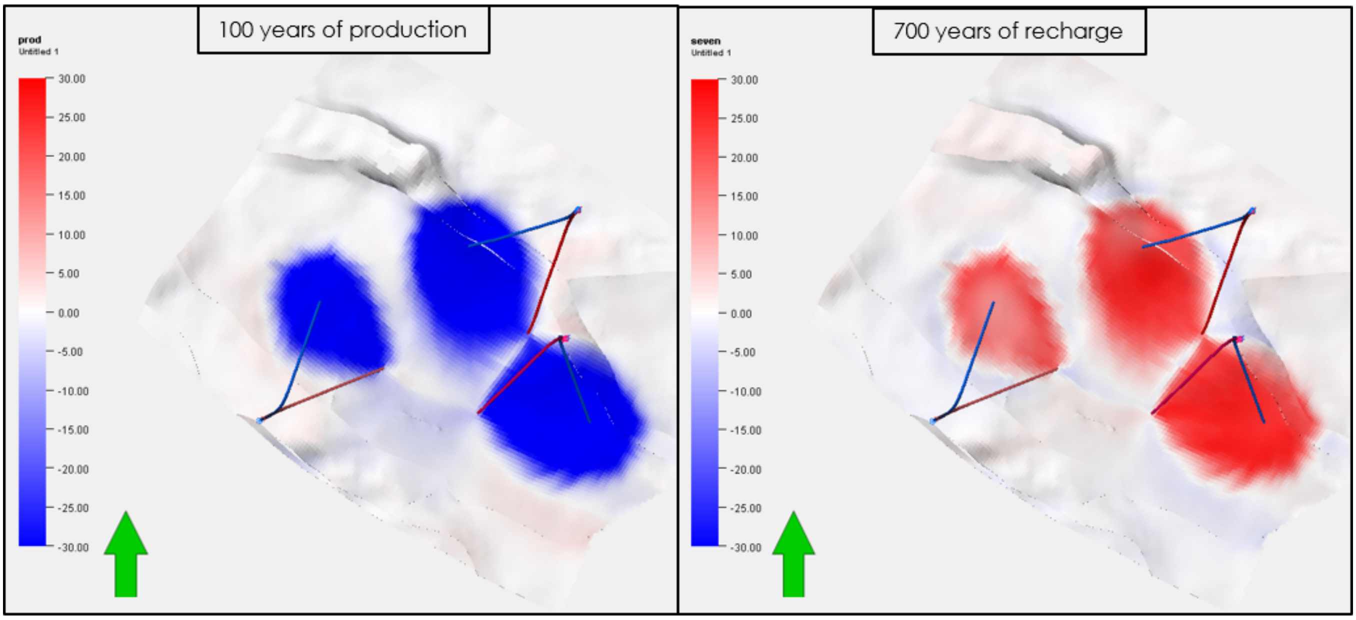

Figure 9.2.2: Left: Top-view of the middle reservoir layer with the difference in temperature from the moment after 100 years of production compared to the start of production. Right: Top-view of the middle reservoir layer temperature distribution after 700 years of thermal recharge, compared to the distribution after 100 years of production. A high temperature means that the rock has been heated compared to the moment after 100 years of production.

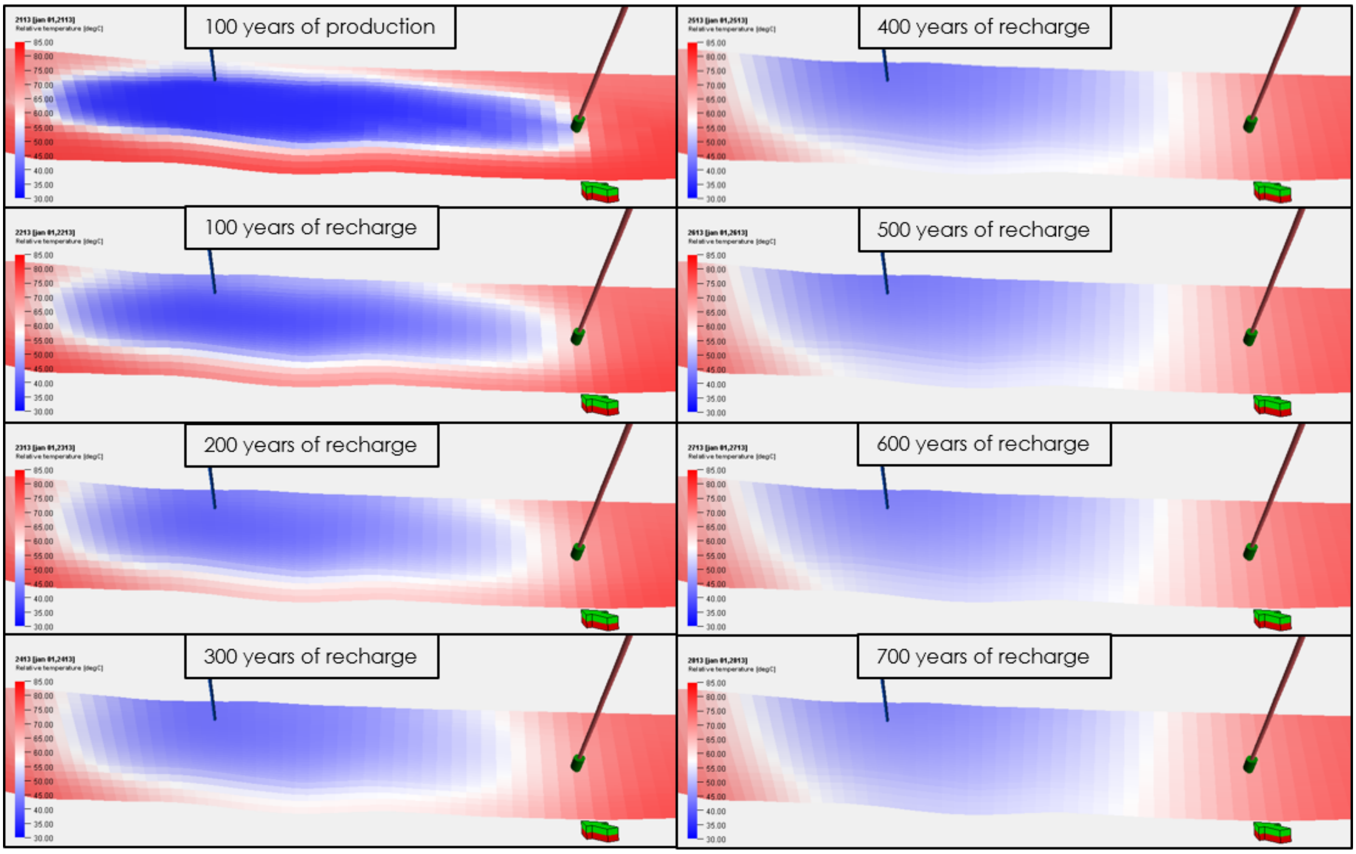

Figure 9.2.3: Side-view of the DAP doublet temperature distribution of the overburden, reservoir and underburden after 100 years of production and after 100, 200, 300, 400, 500, 600 and 700 years of thermal recharge.

Figure 9.2.4 displays the difference in temperature between the moment after 100 years of production and after 700 years of thermal recharge. There is a positive difference, meaning that it has been heated up over the 700 years of thermal recharge. The underburden has a lower value than the overburden. This can be explained by the geothermal gradient that results in a higher initial temperature in the underburden compared to the overburden. Hence the thermal rate of recharge and the absolute temperature loss is higher in the underburden.

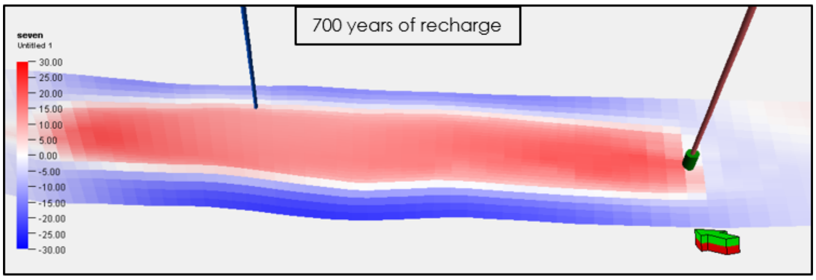

Figure 9.2.4: Side-view of the DAP doublet temperature distribution of the overburden, reservoir and underburden. The temperature displayed is the difference between the moment after 700 years of thermal recharge compared to the moment after 100 years of production. A high temperature means that the rock has been heated compared to the moment after 100 years of production and vice versa.

During thermal recharge, a sharp increase in temperature at the production wells is observed (Figure 9.2.5). We can explain this sharp increase with the spatial insights displayed in Figure 9.2.6. The pressure draw-down created by the producer results in a pressure gradient that drives flow towards the production well. When production wells are shut-in, there is a hot water zone adjacent to every production well. The high-temperature gradient allows the hot water zone to quickly recharge the rock around the production wellbore in the reservoir interval. The temperature increase in these areas is steeper compared to the average reservoir temperature. Also here it is observed that the 99% recharged temperature is not achieved (Ammerlaan 94.8%, Duijvestijn 92.4% and DAP 91.0%).

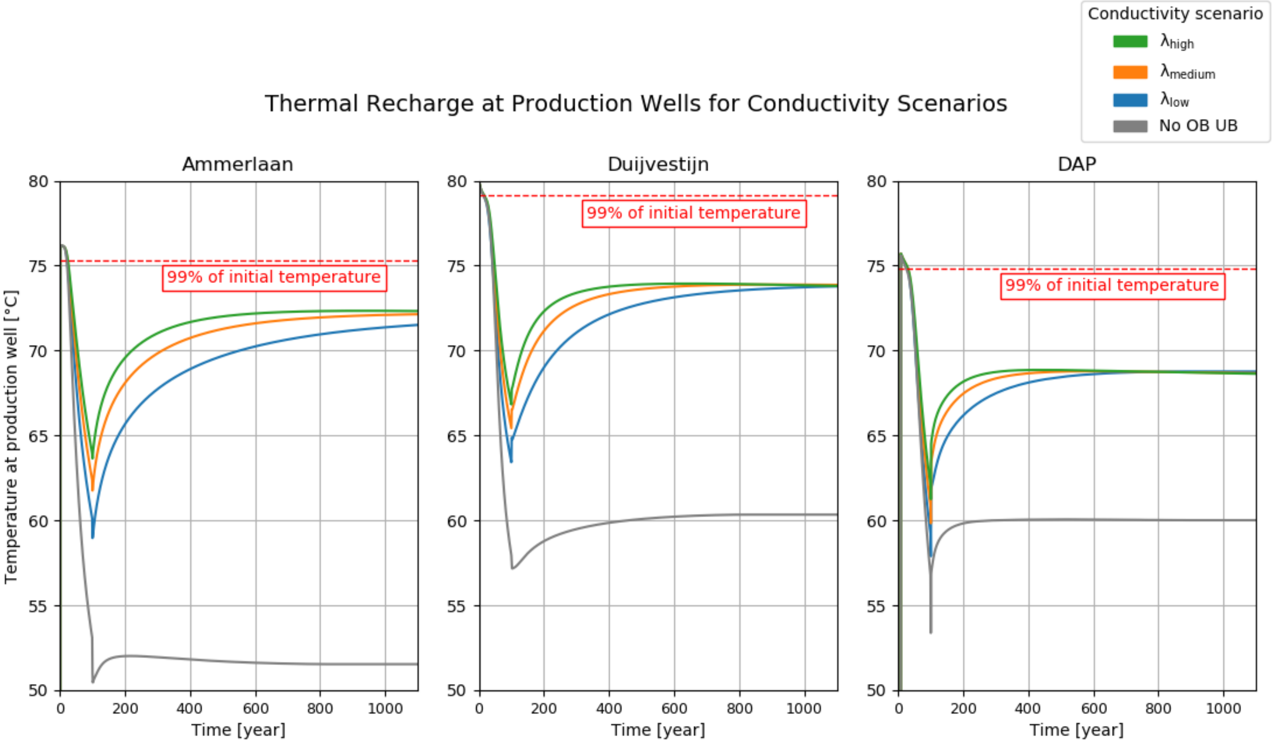

Figure 9.2.5: Temperature at the production wells over time for the low, medium and high case thermal conductivity scenarios. The first 100 years, all doublets are running simultaneously and are then shut-in for 1000 years of thermal recharge.

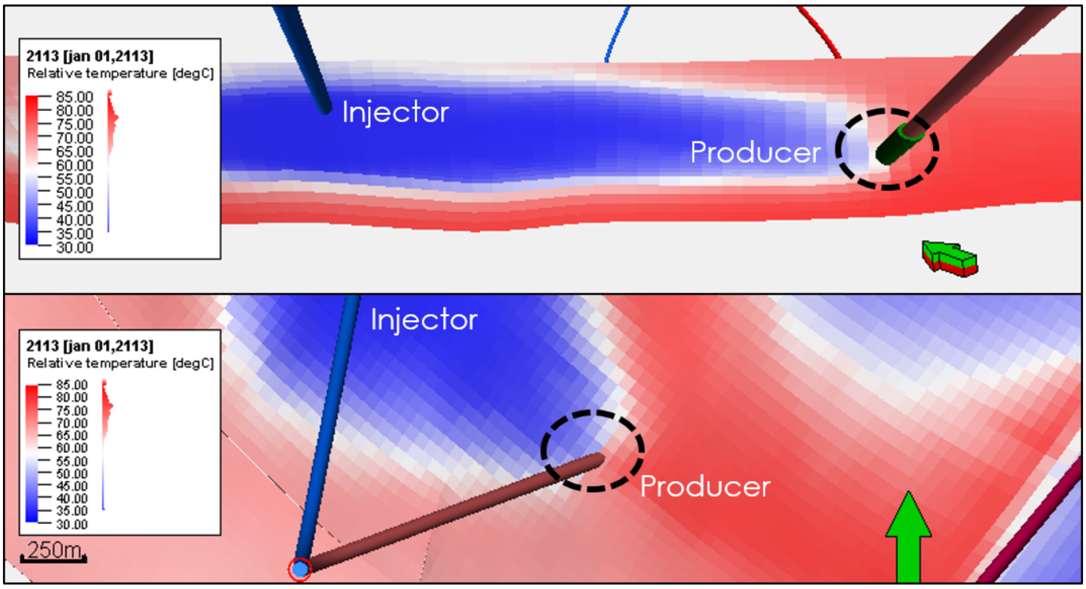

Figure 9.2.6: Side-view (top figure) and top-view (bottom figure) of the temperature in overburden, reservoir and underburden between the DAP producer and injector after 100 years of production. The dashed circle indicates the cold water breakthrough at the production well with a hot-water zone adjacent to the bottom-hole location.

9.3. Increased Overburden and Underburden Thicknesses Scenarios

The overburden and underburden thicknesses are increased to see if the cooling down of the overburden and underburden is limiting the capacity to reach the thermal recharged temperature of 99% of the initial temperature. Increasing the thicknesses of the overburden and underburden leads to a 0.9°C increase in maximum achievable recharged temperature (Figure 9.3.1 and Table 9.3.1). Scenario III does not improve the capacity to recharge the reservoir compared to Scenario II. Also, the base case thicknesses, used to study interference effects, are sufficient during production because the temperature profile is equal to the scenarios with increased thicknesses.

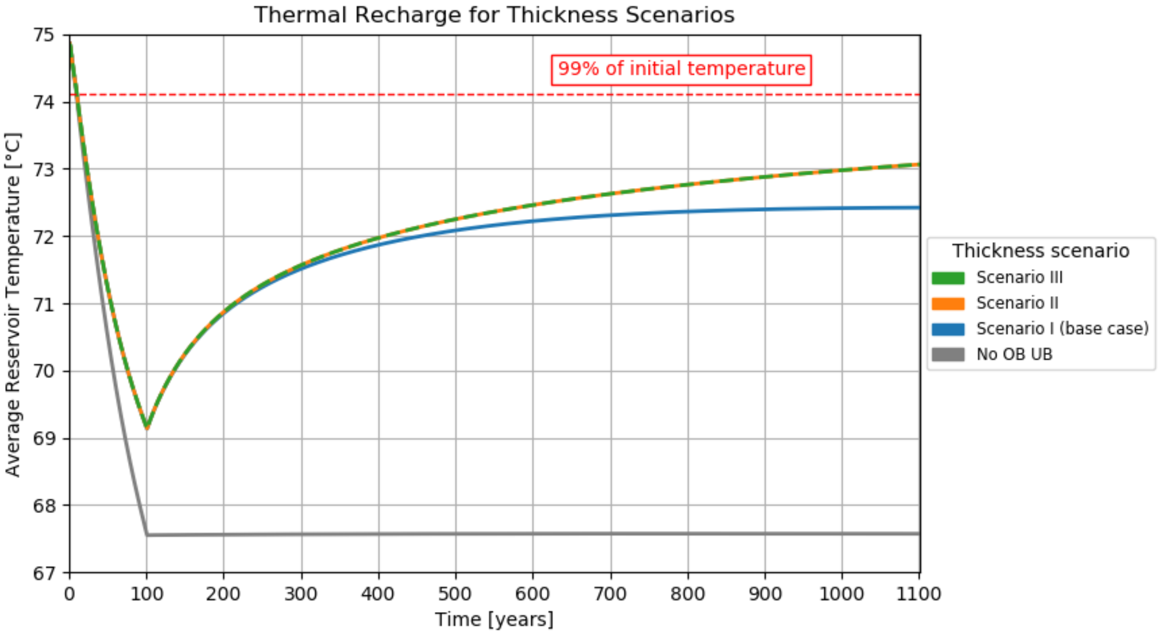

Figure 9.3.1: Average reservoir temperature over time for scenario I, II and III. The first 100 years all doublets are running according to the development strategy and are then shut-in for 1000 years of thermal recharge.

Table 9.3.1: Recharged temperature in absolute degrees and the relative thermal recharge as a percentage of the initial temperature for Scenario I, II, III and IV. Simulations were performed with a medium thermal conductivity scenario.

Thickness scenario	**Thermal recharged temperature [°C]**	**Relative thermal recharge [%]**
I (base case)	72.4	96.7
II	73.1	97.6
III	73.1	97.6

9.4. Decreasing Overburden and Underburden Cell Height Scenarios

The cell height towards the interface of the non-reservoir and reservoir zone is decrased to see if it will increase the models capacity to reach the thermal recharged temperature of 99% of the initial temperature. This analysis is performed for thickness Scenario II that reached 97.6% of its initial temperature with a constant cell height and a medium thermal conductivity scenario (Table 9.3.1). For the same thermal conductivity scenario, decreasing the cell height does not affect the capacity to recharge the reservoir (Table 9.4.1). Decreasing the cell height of the overburden and underburden only leads to a slight increase (0.4%) in maximum achievable recharged temperature for the high thermal conductivity scenario compared to the scenarios with constant cell height (Figure 9.4.1). Increasing the thermal conductivity to an unrealistically extreme value does not further increase the capacity to thermally recharge the reservoir.

Table 9.4.1: Recharged temperature in absolute degrees and the relative thermal recharge as a percentage of the initial temperature after 1000 years of recharge. Overburden and underburden are modelled with decreasing cell height towards to top and bottom of the model boundaries for the low, medium, high and extreme thermal conductivity scenario.

λ-scenario	**Thermal recharged temperature [°C]**	**Relative thermal recharge [%]**
Low	72.4	96.7
Medium	72.6	97.0
High	72.9	97.4
Extreme	72.9	97.4

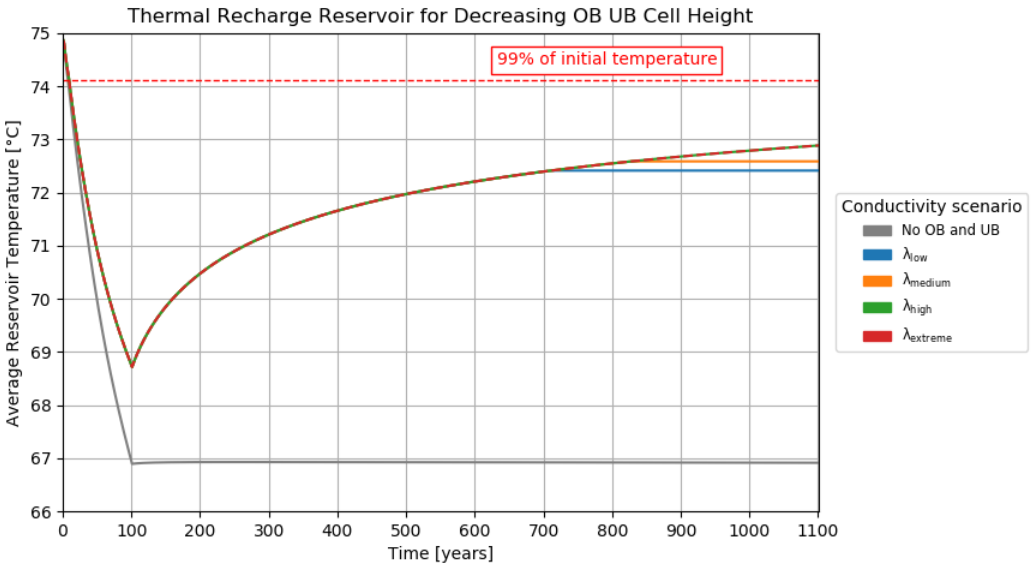

Figure 9.4.1: Average reservoir temperature over time for a low, medium, high and extreme thermal conductivity scenario. Cell height increases towards the bottom and top of the reservoir model. The first 100 years all doublets are running simultaneously and are then shut-in for 1000 years of thermal recharge.

9.5. Discussion

In this section, the thermal recharge analysis is compared to other studies and reflected upon. The objective of this thermal recharge analysis was to determine the capacity of the reservoir to thermally recharge. This will determine to what degree the application of geothermal energy can be seen as renewable.

This study applied different modelling approaches for the overburden and underburden that aimed to reach the defined recharged temperature of 99% of the initial reservoir temperature. Note that this assumed target temperature can vary for every doublet since it is dependent on the heating application and development strategy. The maximum achievable recharged temperature was 97.6% of the initial reservoir temperature over 1000 years of recharging. Another study performed simulations on a reservoir model that incorporated salt intrusions which underlies the geothermal prospect (Daniilidis et al., 2016). Under different scenarios, the reservoir recharged to 99% of its initial temperature after 114-172 years. The lowest reservoir temperature at the start of recharge was 88% of the initial temperature while in this study it was 92% of the initial temperature. We can conclude that the rate of recharge observed by (Daniilidis et al., 2016) was much larger compared to the rate of recharge observed in this study. The difference cannot be related to the presence of the conductive underlying salt layer because it was given a thermal conductivity of 3.1-5.5 W/m/K which is smaller than the extreme case conductivity scenario (12.7 W/m/K).

The lack of thermal flux at the top and bottom of the reservoir can explain the models inability to thermally recharge to 99% of the initial reservoir temperature. The assumed geothermal gradient creates a vertically linear distribution and horizontally uniform distribution for the initial temperature. Through geothermal production, energy from the model at reservoir zone depth is extracted which is not recovered afterwards. Because we do not add the lost energy again, a new temperature equilibrium is established. Most of the thermal recharge takes place from the underburden to the reservoir zone. This causes the vertical temperature profile to move slightly downward, resulting in a slightly lower average temperature at the depth of the reservoir zone (Figure 9.5.1). Throughout the simulation, conduction takes place from the bottom of the model towards the top of the model. This cause the bottom half of the model to cool down while the top half of the model is heated up. The reservoir zone lies in the bottom half of the model and is thus cooled down through 1100 years of conduction (100 years of production and 1000 years of recharging). In reality, heat is supplied from the mantle and lost to the atmosphere. To mimic this, a thermal influx should be added to the bottom boundary and a thermal outflow on the top boundary. This can prevent a shift in the vertical temperature gradient as observed in this study and increase the rate of recharge of the reservoir.

We have also shown that sufficient overburden and underburden thicknesses should be incorporated when performing geothermal reservoir simulation, also if only the production period is analyzed. Smaller cell heights can be used to capture the high-temperature gradient at the interface of the non-reservoir and reservoir. To minimize the number of cells and simulation time, one can decrease the cell height towards the interface of reservoir and non-reservoir. This did not have a significant effect on the maximum achievable recharged temperature.

There is currently no consensus on how long it takes for a sedimentary reservoir at 2km depth to be reheated after it has been cooled down by geothermal production. It is known that the Earth's mantle supplies the subsurface of heat and that divergence of the tectonic plates is the cause of the thinning of the Earth's crust, creating a high geothermal gradient in the shallow subsurface (e.g. Iceland, Italy and Japan). Low and high conductive stratigraphic units can cause non-linear geothermal gradients. In the long term, there is still doubt what the exact role of conduction and convection is in recharging the reservoir with heat. To what extent is there free groundwater flow at 2km depth that re-supplies the reservoir with heat through convection? Is heat supplied through convection from the deeper subsurface through high-permeable fault zones by buoyancy effects? Are there non- to very low conductive layers underlying the reservoir that limit the ability of the Earth's mantle to re-supply the reservoir with heat? These are questions that are still left unanswered, also by this study.

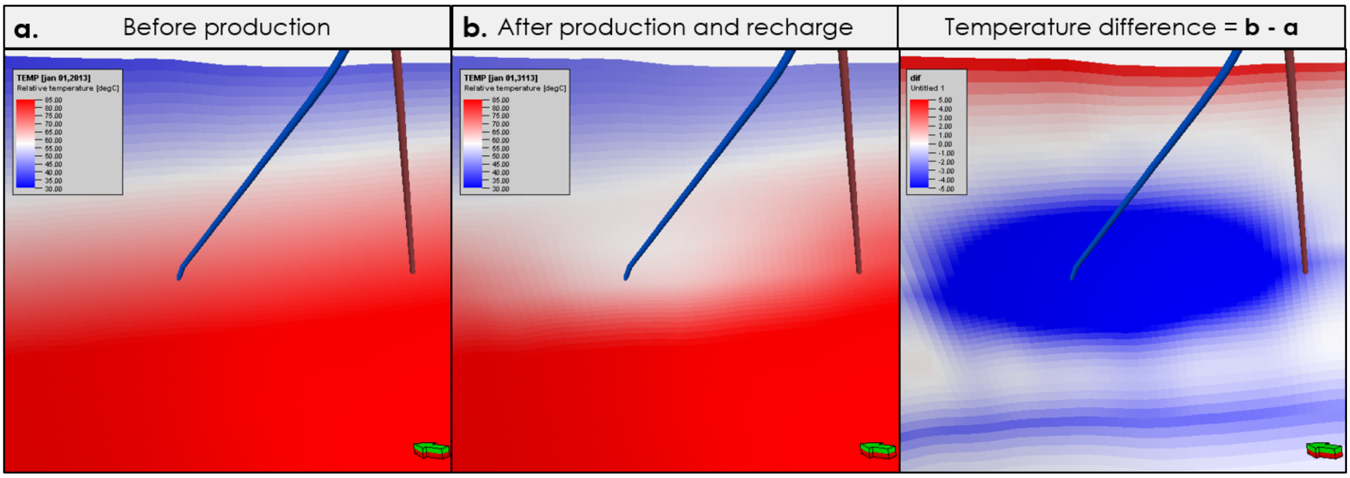

Figure 9.5.1: Side-view of the temperature distribution between the DAP injecor and producer before production (a) and after production and thermal recharge (b). On the right we see the difference if we subtract a) from b). Blue indicates a colder area after 1000 years of recharging and 100 years of production compared to the situation before production. The area between the injector and producer has not heated up completely. The underburden has cooled dan and the area at the surface has heated up.

10

Limitations in Reservoir Modelling

This chapter is devoted to discussing the limitations of reservoir modelling related to this study.

10.1. Reservoir Boundaries

The under-sampling of the subsurface and the different scales across the measurements are causes of uncertainty in the parameters of our dynamic reservoir model (de Hoop, 2017). In this study, the largest source of uncertainty is the boundary of our reservoir. It is not possible to pick the top reservoir horizon due to the weak seismic reflection. Instead, the top reservoir horizon is determined through isochoring at the existing wells and interpolating between these wells and between the top Rodenrijs Claystone Member (top overburden) and Top Pijnacker Unit (top underburden). The existing well tops provide control data at a very limited amount of locations. In between these points, we assume that the top reservoir horizon follows the horizons of the top overburden and top underburden. The determination of those horizons was also limited by the vertical seismic resolution of our seismic cube. This resolution counts for the top overburden and top underburden and can vary between 20-30m at the depth of our reservoir (Kallweit and Wood, 1982). This has a high impact considering that the average reservoir thickness in our model is 110m. We converted the time picked horizons to depth surfaces with a layer-cake velocity model. This velocity model assumes that within one formation layer, the velocity is constant over the whole interval. In reality, sedimentary processes such as local compaction can cause velocity discrepancies within an interval in the horizontal and vertical direction. The effects of this simplification also causes uncertainty in the accuracy of the seismic interpretation of horizons and faults. All of these uncertainties propagate through to the determination of the top reservoir horizon. We also assume that the Top Pijnacker Unit is a no-flow boundary while GR-logs still read some sandstone intervals (e.g. PNAGT02, PNAGT03 and PNAGT04). This shows that our underburden can still possess decent flow properties. In summary, the thickness distribution of our reservoir is highly uncertain and therefore the possible flow rates of the production and injection wells are also highly uncertain. The area around the DAP wells have not been drilled and bear higher uncertainty compared to the area around the Ammerlaan and Duijvestijn wells. Integrating the data that will be retrieved from future drilling and logging of the DAP wells increases the accuracy of the reservoir thickness distribution.

10.2. Reservoir Properties

The scale and availability of porosity and permeability measurements was another important limitation in this study. We have assumed porosity distributions for the different lithologies. The porosity-permeability relations retrieved from analogues had a wide spread and lied far away from the study area and sometimes at a much shallower depth. As a consequence, we were forced to establish a low, medium and high permeability scenario to evaluate a range of possibilities. The medium permeability scenario did correspond to the permeabilities found during the Ammerlaan well test. The scale of permeability measurements is performed over tenths of meters and is upscaled to a volume of around 2.5 km^3. This operation neglects almost all heterogeneity that the actual subsurface has which is then approximated by studying the geological history and assuming a depositional model. We can therefore say it is far-fetched to say that this does approximate reality but that it is rather a scenario development strategy wherein the scenarios have been selected based on the available knowledge and data.

11

Conclusions

The objectives of this research were to benchmark two reservoir simulators, quantify the positive and negative interference effects that occur during simultaneous production of the doublets, investigate the implications on policy measures and analyse the rate of thermal recharge of the reservoir after production. The four research questions are presented, followed by the corresponding conclusions.

- **How does the computational and modelling performance of Eclipse100 compare to that of DARTS for the case of a simplified 3D box-model of the reservoir?**

It is shown that for the same simulation case, DARTS spends 3.7 times less CPU time for a 3D box-model simulation while performing more linear and non-linear iterations, compared to Eclipse100. Possible explanations are that DARTS incorporates fewer interdependencies between parameters and uses an operator-based linearization method that can be computationally more efficient. Gravity effects need to be included to simulate the increasing pressure of the hydrostatic column with depth. If it is not, the pressure draw-down effect at the producer and the pressure build-up effect at the injector are not modelled. This results in a horizontal pressure gradient between the producer and injector. Pressure differences are smaller between injector and producer compared to the diagonal pressure gradient that results from including gravity effects. Since the pressure gradient is the driving force for flow, it can be concluded that not incorporating density effects leads to an underestimation of the time in which the cold waterfront reaches the producer.

- **How large is the interference on pressure and temperature over time between the Ammerlaan, Duijvestijn and DAP doublets and how will this affect their own and combined heat production?**

For Ammerlaan and Duijvestijn, the base and high case scenario target flow rates were not reached in the low permeability scenarios. The DAP doublet was only able to reach the base case target production rates. Under these scenarios, and for this specific case study, the injector is pressure constraint on the maximum allowable BHP of the injector. A pressure interference effect is then noticeable at the neighbouring injection well. The reservoir pressure is decreased at the injector when a neighbouring production well starts producing. This allows the injector to inject at a higher flow rate. For this case study, the increase in flow rate can reach up to 24 m^3/h. From the geological parameters that are varied, fault transmissibility and K_h/K_v-ratio have the largest influence on this interference effect. Facies orientation also plays a minor role but can play a greater role in systems with a lower N/G. The Duijvestijn, Ammerlaan and DAP doublets production rate increases with respectively 22%, 3% and 1%, averaged over the ensemble of scenarios. This results in an increase in total energy production of 8% of the three doublets combined. The average increases in flow rates over the entire simulation time of the Duijvestijn, Ammerlaan and DAP doublets are respectively 26, 5 and 2 m^3/h because of pressure interference. For this study case and under all pressure constraint scenarios, the doublets benefit from pressure interference through a higher energy production.

Interference on temperature causes a decrease in production temperature and thus on thermal power. The thermal power of Ammerlaan and DAP is decreased through temperature interference. The interference intensifies over time as the cold water-front of the neighbouring doublet reaches the production well.

The Ammerlaan and DAP doublets total energy production over 100 years of production decreases with respectively 3.8% and 2.7% over 100 years compared to a situation where the doublets would operate in stand-alone configuration. Ammerlaan is negatively interfered by the Duijvestijn injector while the DAP producer is negatively interfered by the Ammerlaan injector. This causes a thermal power increase that reaches up to 33% after 100 years compared to a situation where it would operate as a stand-alone doublet. For Duijvestijn we observe a positive interference effect on temperature. The neighbouring Ammerlaan producer causes a pressure draw-down that drives part of the cold waterfront of the Duijvestijn producer towards its own producer. This causes a thermal power increase that reaches up to 15% after 100 years compared to a situation where it would operate as a stand-alone doublet.

- **What are the implications that interference has on the policy measures for geothermal projects operating in dense production areas?**

Policy measures for determining pressure and temperature interference are poorly defined. The current policy measure for determining the boundaries of an extraction license only incorporates well distance and neglects any properties of, and heterogeneity in, the subsurface. Such a policy is not very prudent and can lead to disputes between neighbouring doublets. According to the simulations in this study, the projected plans of Ammerlaan to increase its flow rates to 350 m^3/h would only allow it to produce for 15 years, instead of awarded 35 years by EZK. A trade-off is identified between flexibility and integration for the geothermal licensing policy.The current policy leans toward flexibility and gives no incentive for a play-based approach and unitization agreements. There are currently no policy measures in place to mitigate pressure exceedance of an injector when a neighbouring production well is shut-in. There should be a policy measure that makes communication of operational planning or the installation of auto-stops in the injection well pump mandatory. Current policy does not prescribe what the adequate substantiation is to customize the slope coefficient for the maximum allowable injection pressure. Leak-off tests during completion can be used to determine the fracture gradient. The optimization of the slope coefficient could lead to more economical production.

- **How large is the effect of thermal conductivity of the fluid and rock on the thermal recharge rate of the Delft Sandstone Member reservoir zone?**

This study has shown that, with an average reservoir thickness of 110m, the contribution of thermal recharge from hot rock laterally is much smaller than the contribution from top and bottom. The underburden has a larger contribution than the overburden. This is caused by an higher temperature gradient between the reservoir and the underburden compared to the reservoir and the overburden. The reservoir has been recharged by respectively 96.1%, 96.4% and 96.5% of the initial average reservoir for the low, medium and high thermal conductivity scenarios after 1000 years of thermal recharge. Different modeling approaches of the overburden and underburden did not achieve the target recharge temperature of 99% of the initial reservoir temperature. It is concluded that to mimic reality, a thermal influx should be added to the bottom boundary and a thermal outflow on the top boundary of the reservoir model.

12

Recommendations

In this chapter, we supply future studies with recommendations to decrease the uncertainties, improve the accuracy of the model and gain a better understanding of the relevant physical processes.

- In this study, we assume constant production rates throughout each year. It can be interesting to investigate what happens if you stop production in summer when you don't need heat. With how much time would it extend the lifetime of the doublet?
- The underburden of our reservoir model is assumed to be a no-flow boundary. By assuming this, there is no thermal recharge possible through convection from the underlying stratigraphic unit. There are real-world geothermal concessions, such as the Dogger aquifer in the Paris Basin, that are recharged by convection. Performing thermal recharge analysis on such an aquifer and comparing it to the results from this study can give insights into the renewable character of geothermal energy in different geological settings.
- Applying a thermal influx at the bottom boundary of the model can mimic the heat supply of the Earth's mantle through conduction. The effect of an active aquifer, re-supplying the reservoir with heat through convection, can be investigated. As shown in this study, overburden and underburden thicknesses must be sufficiently thick during a simulation. Small increments in overburden and underburden cell heights close to the reservoir are required to capture the relatively high-temperature gradient that exists between the cold waterfront and the overburden and underburden of the reservoir.
- This study has shown that when large faults are in the vicinity of the doublets, varying the fault transmissibility has a large effect on the lifetime and the interference effects between the doublets. When faults are closed, the area of influence is confined and the pressure draw-dawn is distributed over a smaller area. Determining the transmissibility of the faults will decrease the uncertainty in the lifetime of the doublets and the effects of interference on pressure and temperature.
- The methodology presented in this study can be used to quantify interference effects and capture the uncertainty before planning a well trajectory. The well trajectory can thereby be optimized by minimizing the possibility of negative interference effects and maximizing the positive interference effects.
- The DAP doublet is promised to be one of the most technologically advanced doublets in the geothermal industry. Multiple logging tools, down-hole temperature measurements, down-hole pressure measurements and the proposed coring study will supply the involved partners with a vast amount of data that can be used to fine-tune the static reservoir model as well as the dynamic reservoir simulations. We also recommend performing well interference tests with the neighbouring doublets (Ammerlaan and Duijvestijn) to confirm or rule out the possibility of pressure interference effects. If these doublets are willing to share their production data, history matching can be performed with the newly drilled DAP wells. This improves the ability to characterise the reservoir and optimize heat production.

A

Seismic Interpretation

A.1. Polarity Convention

The seismic data was shot in non-SEG and displayed in non-SEG with the EBN color convention (Figure A.1.1). This implies the following:

- Increase in acoustic impedance results in a hard kick, a negative amplitude and a trough (red) reflector.
- Decrease in acoustic impedance results in a soft kick, a positive amplitude and a peak (blue) reflector.

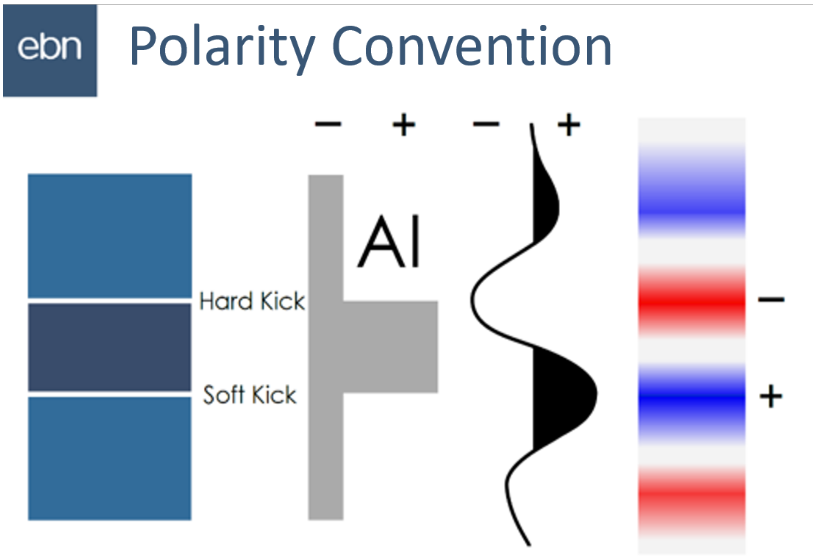

Figure A.1.1: Polarity convention and display used in this study.

A.2. Seismic horizons

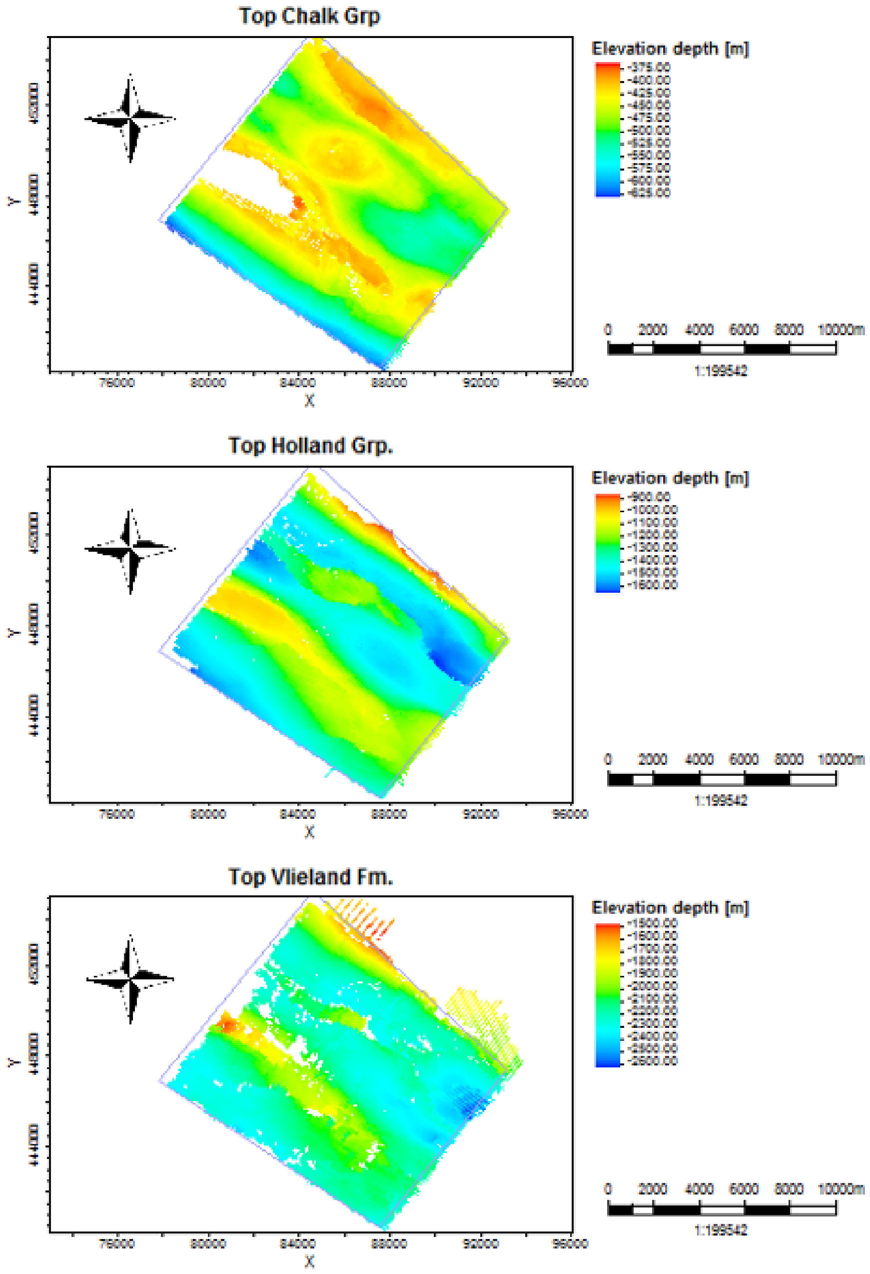

Figure A.2.1: Top Chalk Group, Top Holland Group and Top Vlieland Formation time horizons.

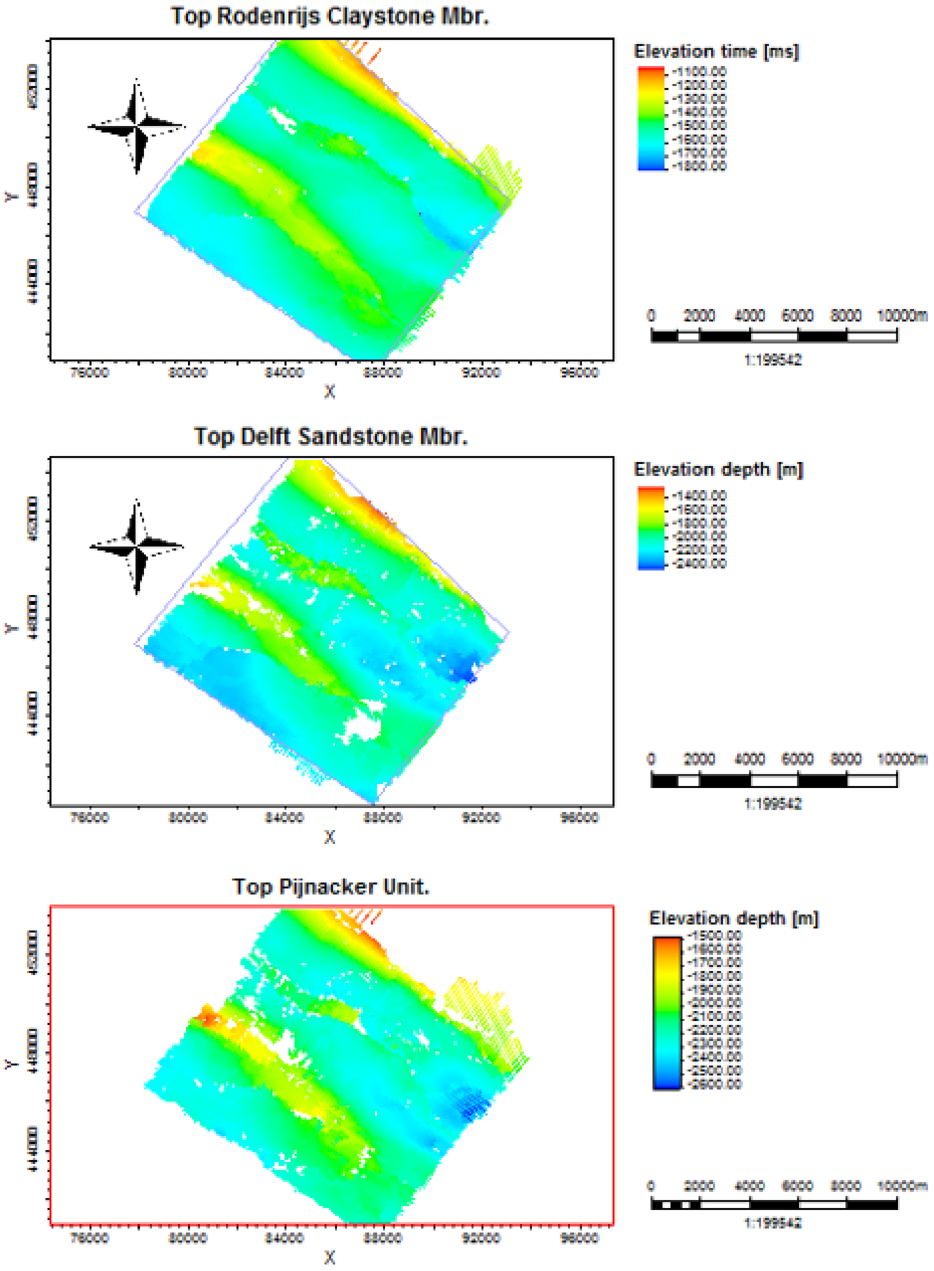

Figure A.2.2: Top Rodenrijs Claystone Member, Top DSSM and Top Alblasserdam Member time horizons.

B

Velocity Model Residuals

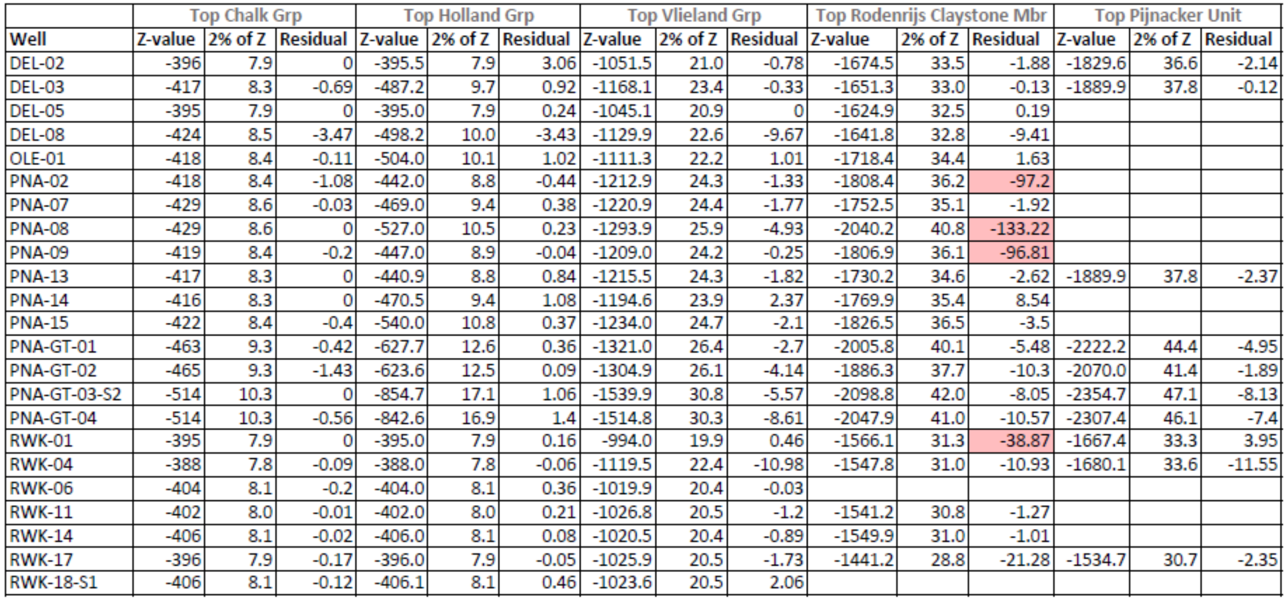

	Top Chalk Grp			Top Holland Grp			Top Vlieland Grp			Top Rodenrijs Claystone Mbr			Top Pijnacker Unit		
Well	Z-value	2% of Z	Residual	Z-value	2% of Z	Residual	Z-value	2% of Z	Residual	Z-value	2% of Z	Residual	Z-value	2% of Z	Residual
DEL-02	-396	7.9	0	-395.5	7.9	3.06	-1051.5	21.0	-0.78	-1674.5	33.5	-1.88	-1829.6	36.6	-2.14
DEL-03	-417	8.3	-0.69	-487.2	9.7	0.92	-1168.1	23.4	-0.33	-1651.3	33.0	-0.13	-1889.9	37.8	-0.12
DEL-05	-395	7.9	0	-395.0	7.9	0.24	-1045.1	20.9	0	-1624.9	32.5	0.19			
DEL-08	-424	8.5	-3.47	-498.2	10.0	-3.43	-1129.9	22.6	-9.67	-1641.8	32.8	-9.41			
OLE-01	-418	8.4	-0.11	-504.0	10.1	1.02	-1111.3	22.2	1.01	-1718.4	34.4	1.63			
PNA-02	-418	8.4	-1.08	-442.0	8.8	-0.44	-1212.9	24.3	-1.33	-1808.4	36.2	-97.2			
PNA-07	-429	8.6	-0.03	-469.0	9.4	0.38	-1220.9	24.4	-1.77	-1752.5	35.1	-1.92			
PNA-08	-429	8.6	0	-527.0	10.5	0.23	-1293.9	25.9	-4.93	-2040.2	40.8	-133.22			
PNA-09	-419	8.4	-0.2	-447.0	8.9	-0.04	-1209.0	24.2	-0.25	-1806.9	36.1	-96.81			
PNA-13	-417	8.3	0	-440.9	8.8	0.84	-1215.5	24.3	-1.82	-1730.2	34.6	-2.62	-1889.9	37.8	-2.37
PNA-14	-416	8.3	0	-470.5	9.4	1.08	-1194.6	23.9	2.37	-1769.9	35.4	8.54			
PNA-15	-422	8.4	-0.4	-540.0	10.8	0.37	-1234.0	24.7	-2.1	-1826.5	36.5	-3.5			
PNA-GT-01	-463	9.3	-0.42	-627.7	12.6	0.36	-1321.0	26.4	-2.7	-2005.8	40.1	-5.48	-2222.2	44.4	-4.95
PNA-GT-02	-465	9.3	-1.43	-623.6	12.5	0.09	-1304.9	26.1	-4.14	-1886.3	37.7	-10.3	-2070.0	41.4	-1.89
PNA-GT-03-S2	-514	10.3	0	-854.7	17.1	1.06	-1539.9	30.8	-5.57	-2098.8	42.0	-8.05	-2354.7	47.1	-8.13
PNA-GT-04	-514	10.3	-0.56	-842.6	16.9	1.4	-1514.8	30.3	-8.61	-2047.9	41.0	-10.57	-2307.4	46.1	-7.4
RWK-01	-395	7.9	0	-395.0	7.9	0.16	-994.0	19.9	0.46	-1566.1	31.3	-38.87	-1667.4	33.3	3.95
RWK-04	-388	7.8	-0.09	-388.0	7.8	-0.06	-1119.5	22.4	-10.98	-1547.8	31.0	-10.93	-1680.1	33.6	-11.55
RWK-06	-404	8.1	-0.2	-404.0	8.1	0.36	-1019.9	20.4	-0.03						
RWK-11	-402	8.0	-0.01	-402.0	8.0	0.21	-1026.8	20.5	-1.2	-1541.2	30.8	-1.27			
RWK-14	-406	8.1	-0.02	-406.0	8.1	0.08	-1020.5	20.4	-0.89	-1549.9	31.0	-1.01			
RWK-17	-396	7.9	-0.17	-396.0	7.9	-0.05	-1025.9	20.5	-1.73	-1441.2	28.8	-21.28	-1534.7	30.7	-2.35
RWK-18-S1	-406	8.1	-0.12	-406.1	8.1	0.46	-1023.6	20.5	2.06						

Figure B.0.1: Overview of velocity model residuals. The deviating residualvalues (>2% of depth) are highlighted in red.

C

Well Correlation Panels

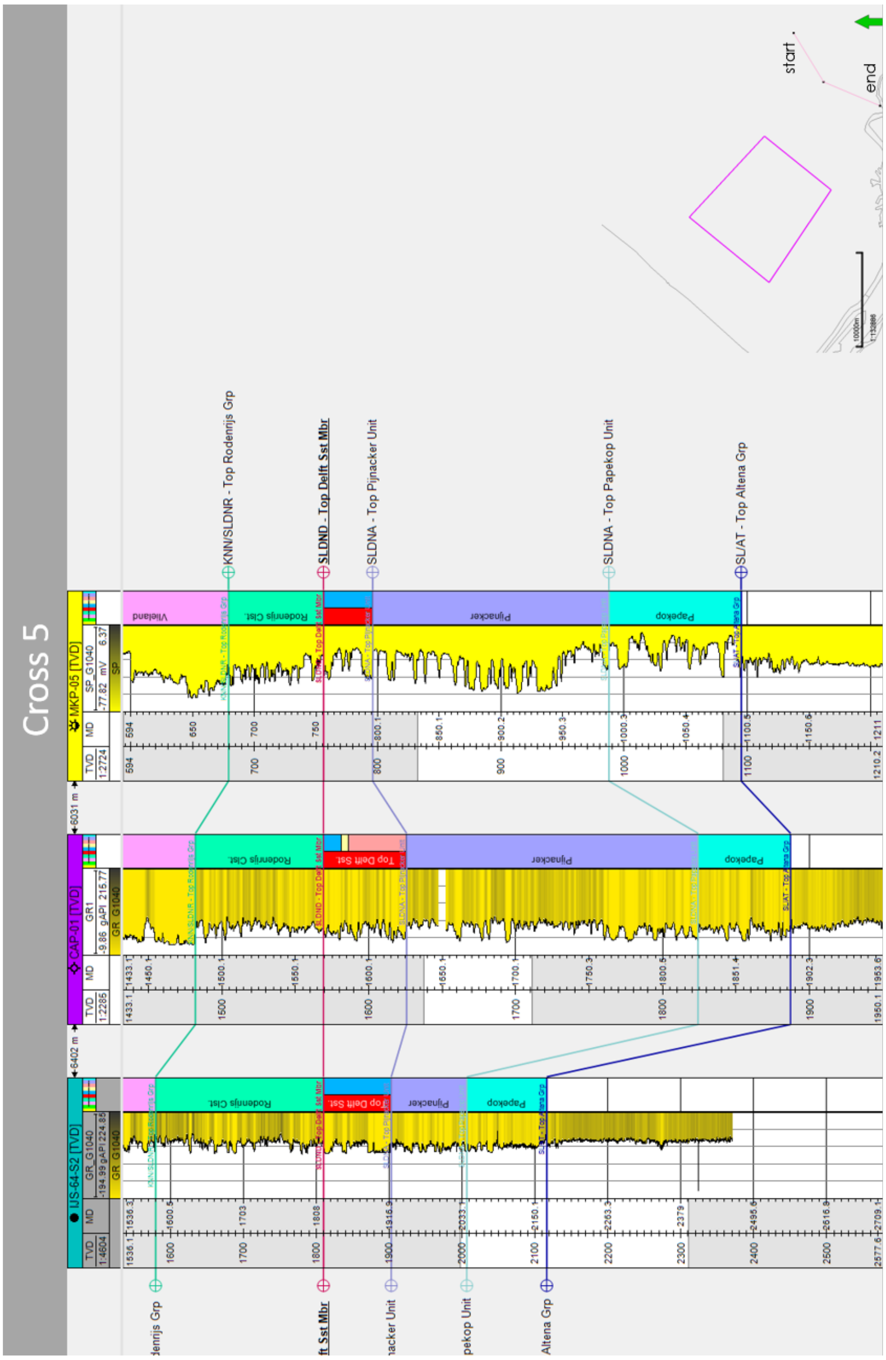

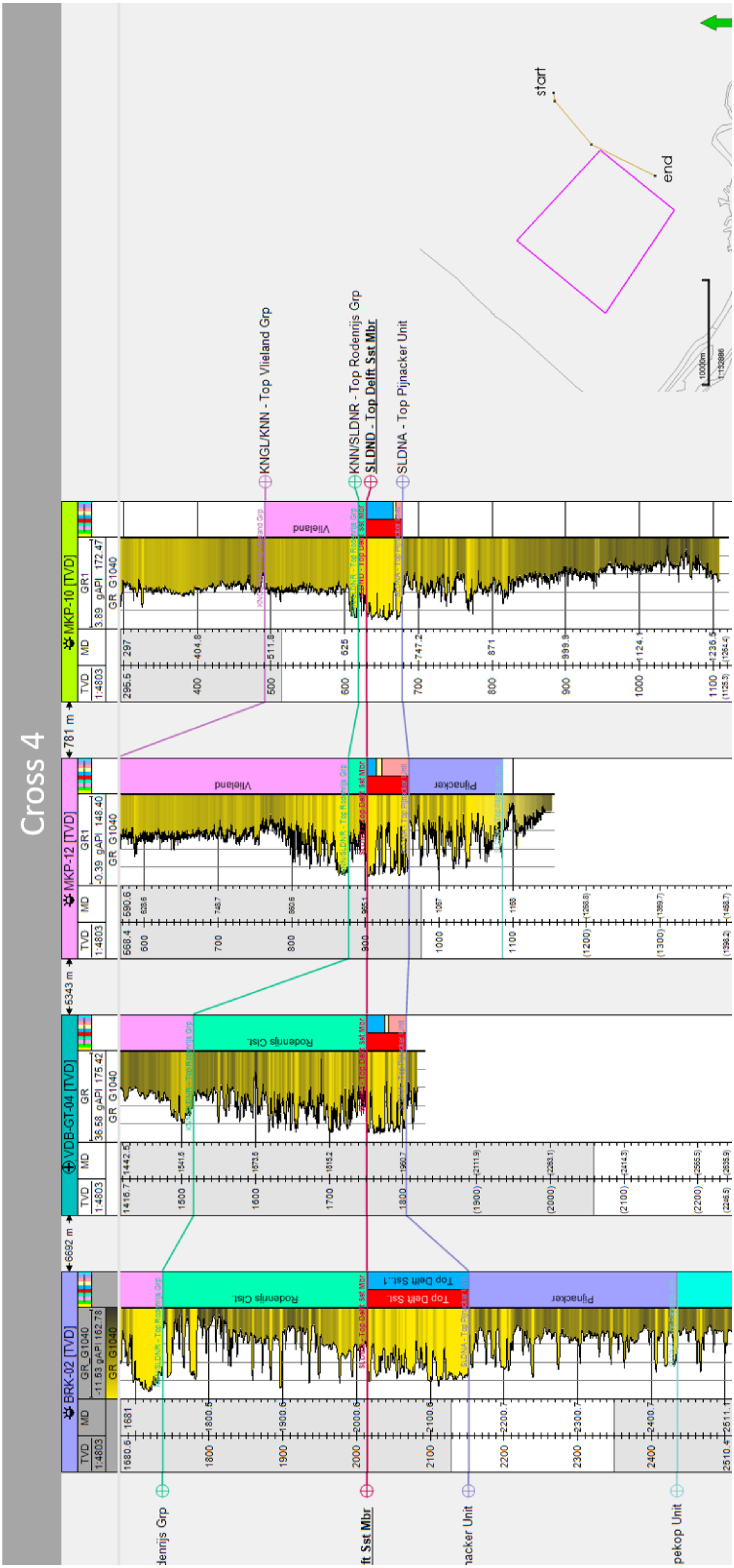
Cross 4
BRK-02 [TVD]
VDB-GT-04 [TVD]
MKP-12 [TVD]
MKP-10 [TVD]
6692 m
5343 m
781 m
TVD
1:4803
MD
GR_G1040
GR1
KNGL/KNN - Top Vlieland Grp
KNN/SLDNR - Top Rodenrijs Grp
SLDND - Top Delft Sst Mbr
SLDNA - Top Pijnacker Unit
Vlieland
Rodenrijs Clst.
Top Delft Sst.
Top Delft Sst.1
Pijnacker
start
end
10000m
1:132886

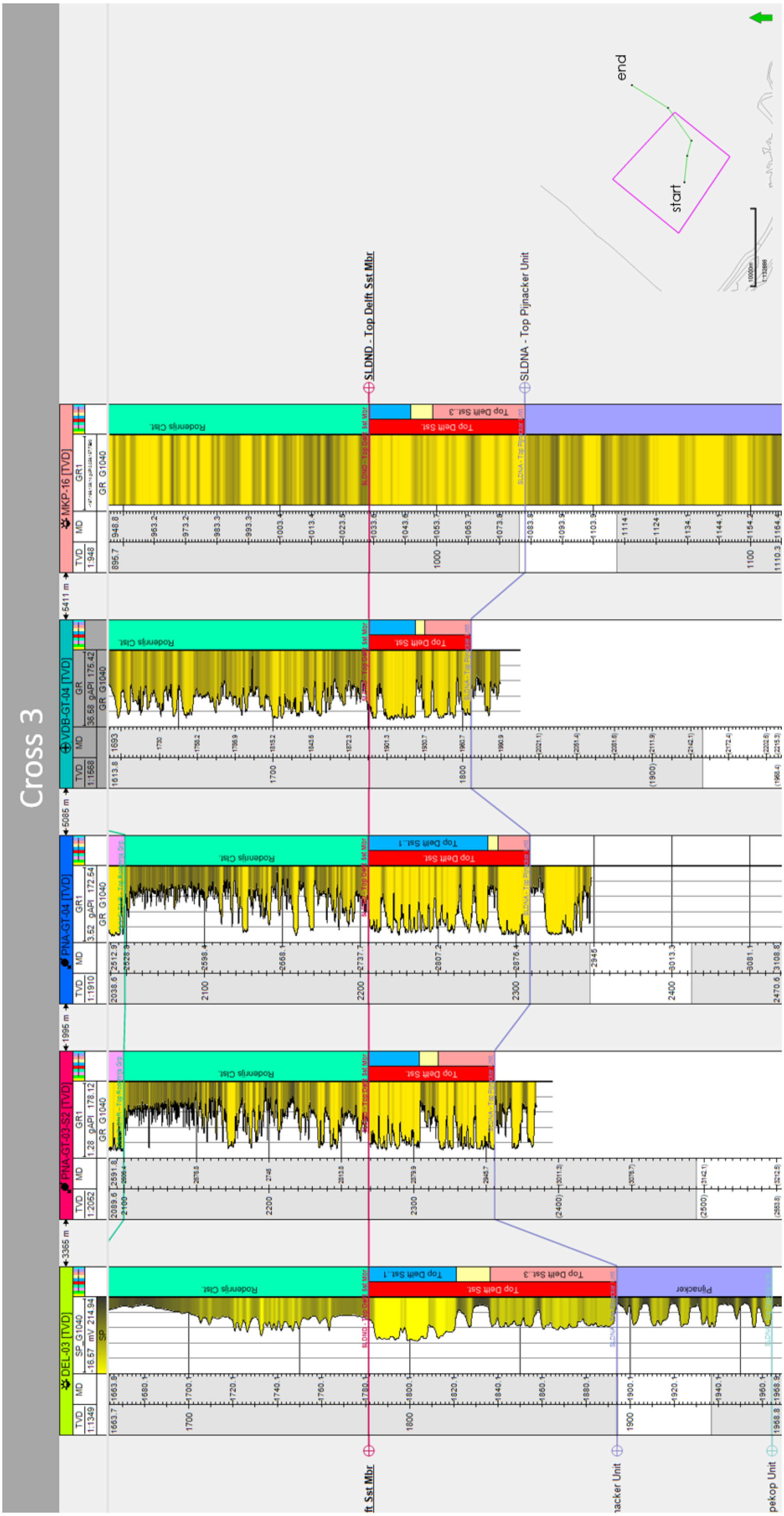

Cross 3

DEL-03 [TVD]
PNA-GT-03-S2 [TVD]
PNA-GT-04 [TVD]
VDB-GT-04 [TVD]
MKP-16 [TVD]
3365 m
1995 m
5085 m
5411 m
TVD
MD
GR1
GR G1040
SP_G1040
SP
Rodenrijs Clst.
Top Delft Sst.
Top Delft Sst.1
Top Delft Sst.3
Pijnacker
SLDND - Top Delft Sst Mbr
SLDNA - Top Pijnacker Unit
ft Sst Mbr
acker Unit
pekop Unit
start
end
10000m

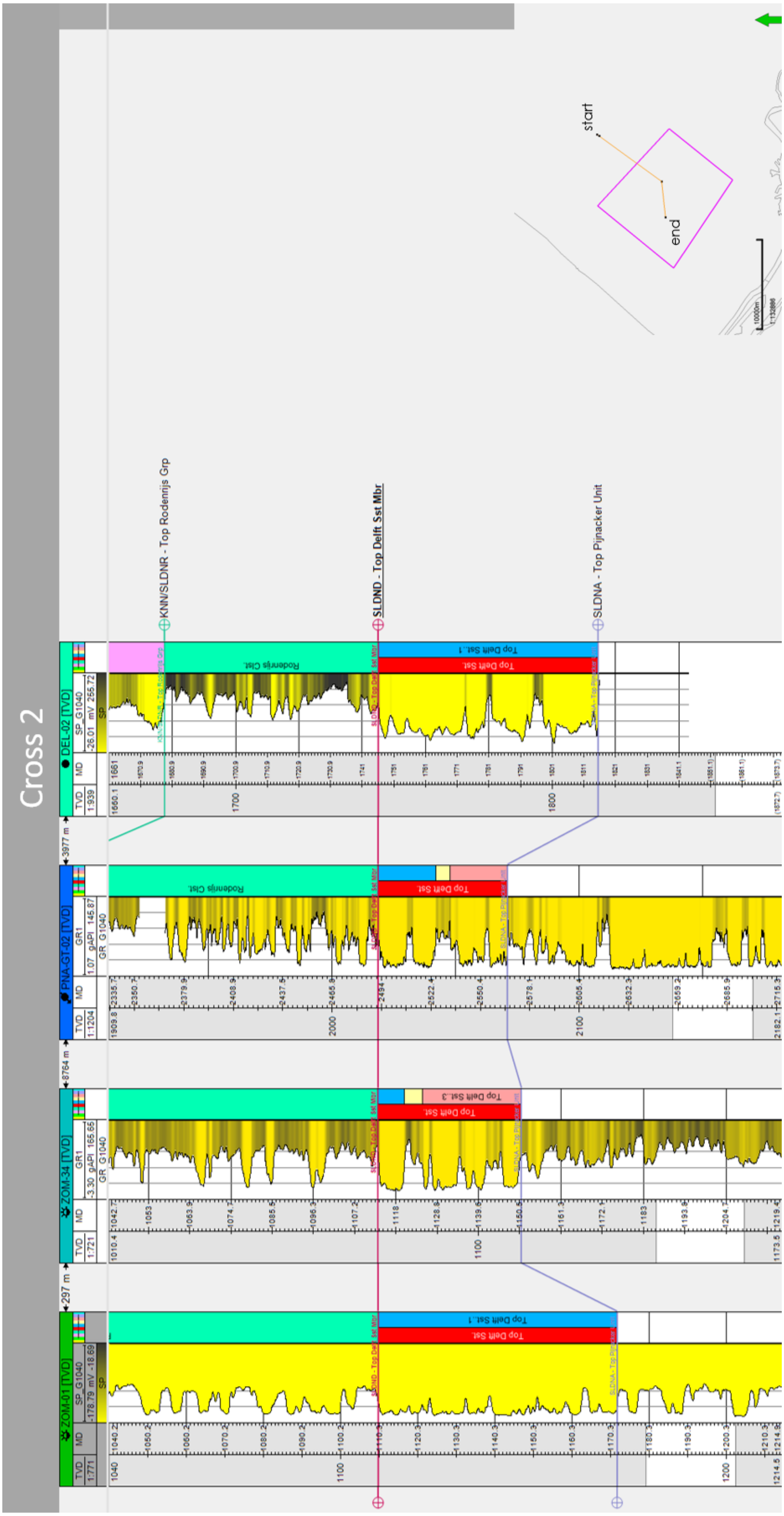
Cross 2
ZOM-01 [TVD]
TVD 1:771
MD
SP_G1040
-178.79 mV -18.69
SP
297 m
ZOM-34 [TVD]
TVD 1:721
MD
GR1
-3.30 gAPI 165.65
GR_G1040
8764 m
PNA-GT-02 [TVD]
TVD 1:1204
MD
GR1
1.07 gAPI 145.87
GR_G1040
3977 m
DEL-02 [TVD]
TVD 1:939
MD
SP_G1040
-26.01 mV 256.72
SP
KNN/SLDNR - Top Rodenrijs Grp
SLDND - Top Delft Sst Mbr
SLDNA - Top Pijnacker Unit
Rodenrijs Clst.
Top Delft Sst.
Top Delft Sst..1
Top Delft Sst..3
start
end
10000m
1:132886

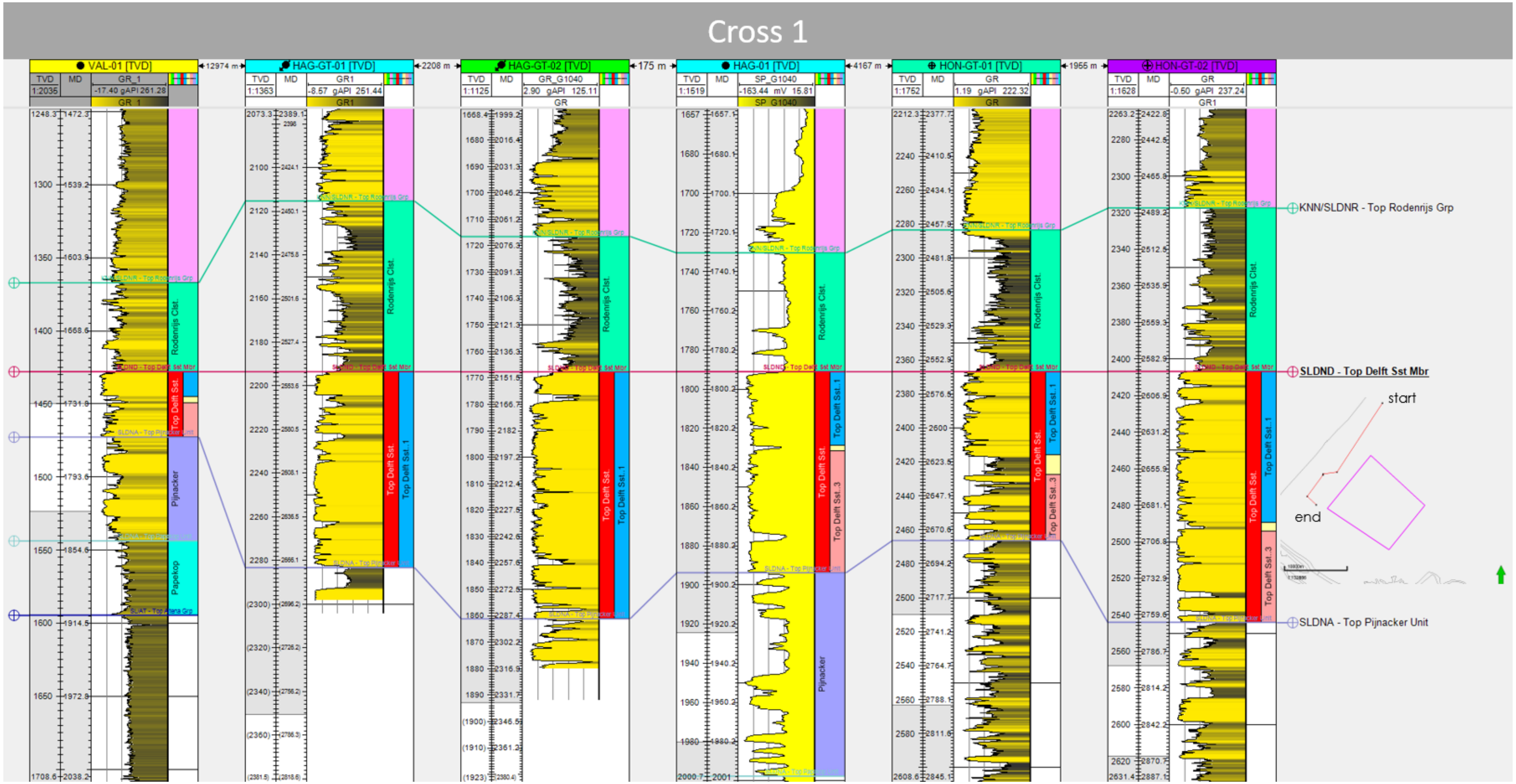
Cross 1
VAL-01 [TVD]
12974 m
HAG-GT-01 [TVD]
2208 m
HAG-GT-02 [TVD]
175 m
HAG-01 [TVD]
4167 m
HON-GT-01 [TVD]
1955 m
HON-GT-02 [TVD]
TVD
MD
GR_1
GR1
GR_G1040
SP_G1040
GR
Rodenrijs Clst.
Top Delft Sst.
Top Delft Sst._1
Top Delft Sst._3
Pijnacker
Papekop
KNN/SLDNR - Top Rodenrijs Grp
SLDND - Top Delft Sst Mbr
SLDNA - Top Pijnacker Unit
SLAT - Top Alena Grp
start
end

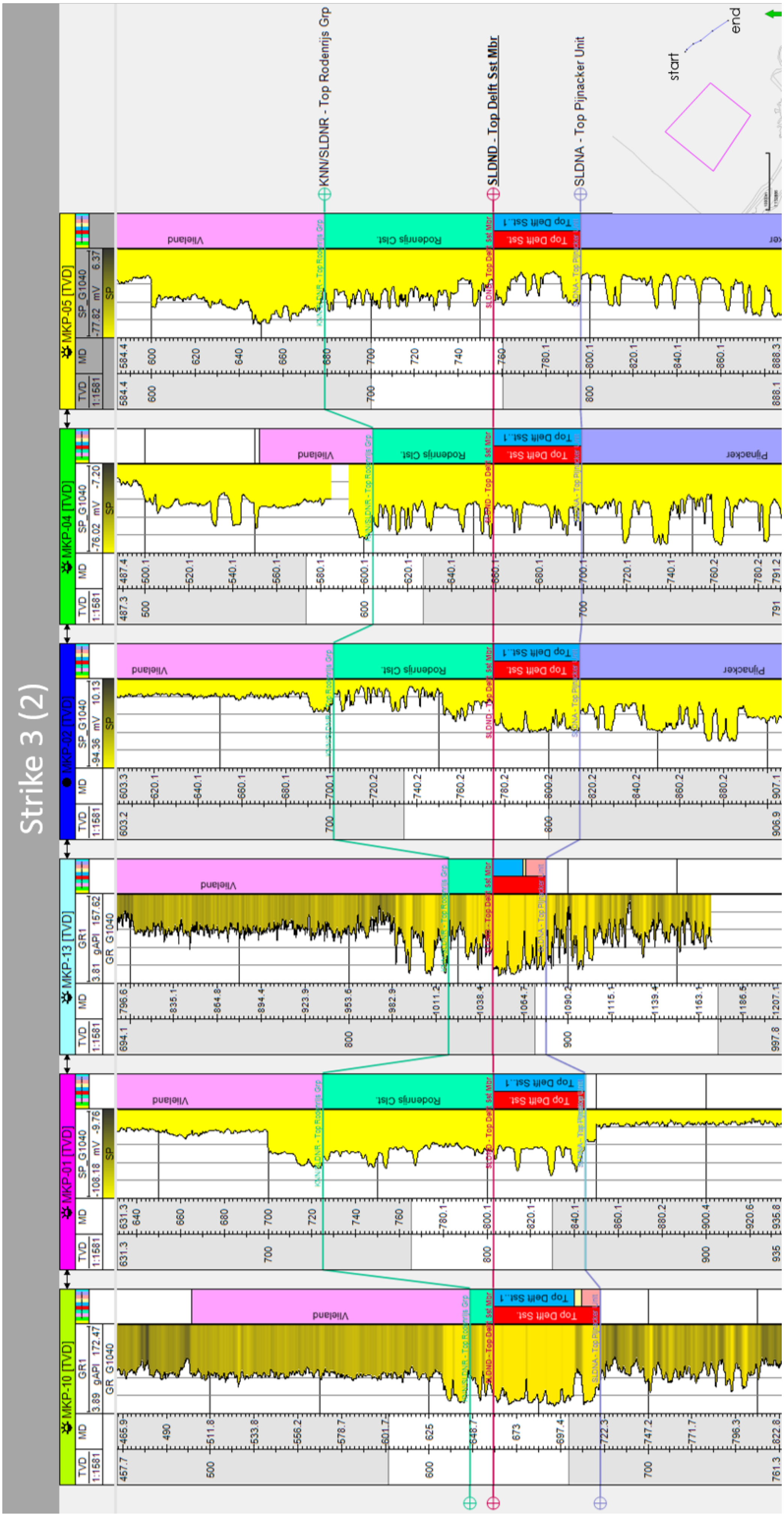
Strike 3 (2)
MKP-10 [TVD]
GR1 gAPI 3.89 172.47
GR_G1040
MKP-01 [TVD]
SP_G1040 mV -108.18 -9.76
SP
MKP-13 [TVD]
GR1 gAPI 3.81 157.62
GR_G1040
MKP-03 [TVD]
SP_G1040 mV -94.36 10.13
SP
MKP-04 [TVD]
SP_G1040 mV -76.02 -7.20
SP
MKP-05 [TVD]
SP_G1040 mV -77.82 6.37
SP
TVD 1:1581
MD
Vlieland
Rodenrijs Clst.
Top Delft Sst.
Top Delft Sst.1
Pijnacker
KNN/SLDNR - Top Rodenrijs Grp
SLDND - Top Delft Sst Mbr
SLDNA - Top Pijnacker Unit
start
end

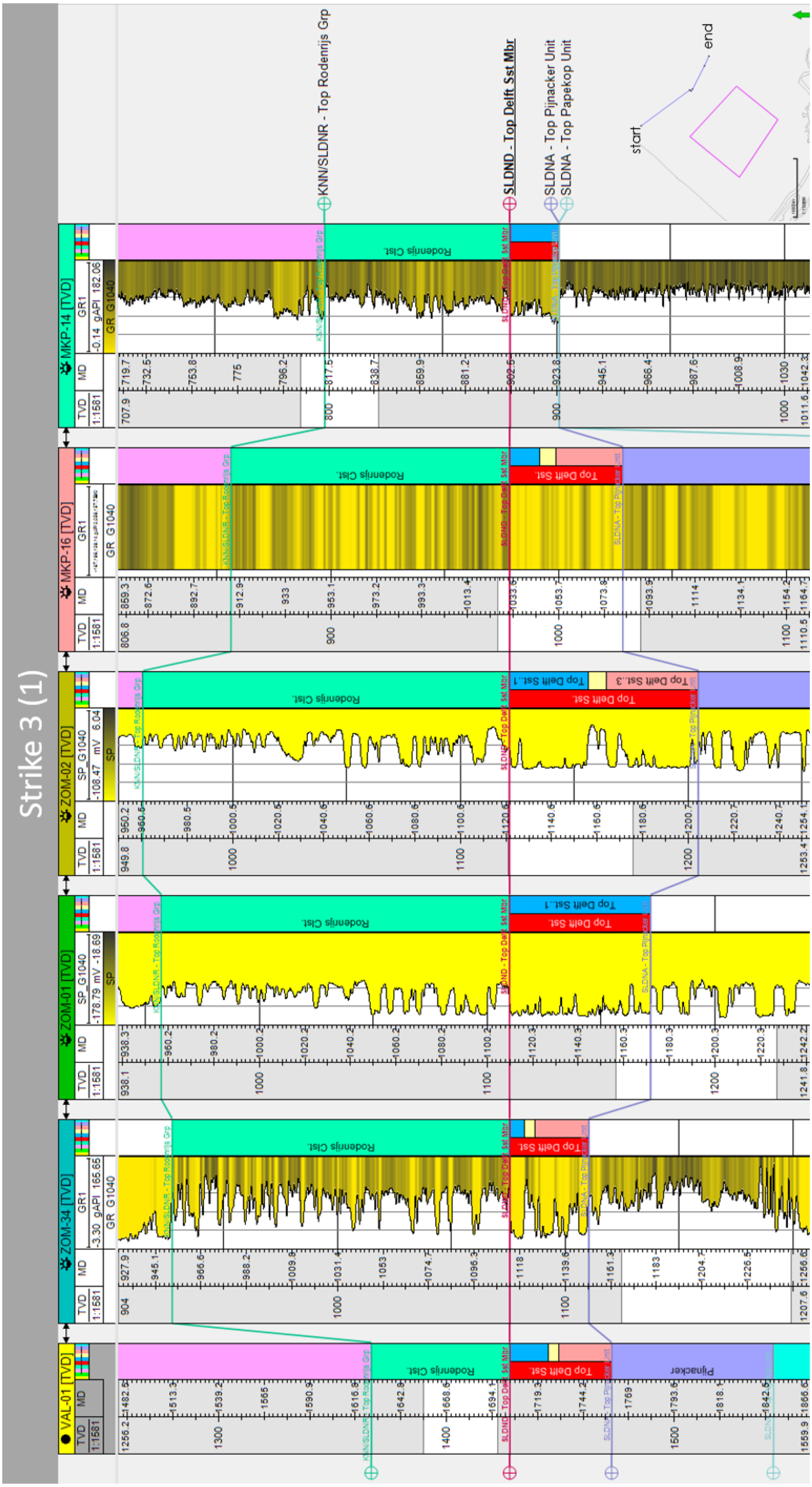
Strike 3 (1)
VAL-01 [TVD]
ZOM-34 [TVD]
ZOM-01 [TVD]
ZOM-02 [TVD]
MKP-16 [TVD]
MKP-14 [TVD]
TVD 1:1581
MD
GR1
GR G1040
SP_G1040
SP
Rodenrijs Clst.
Top Delft Sst.
Top Delft Sst..1
Top Delft Sst..3
Pijnacker
KNN/SLDNR - Top Rodenrijs Grp
SLDND - Top Delft Sst Mbr
SLDNA - Top Pijnacker Unit
SLDNA - Top Papekop Unit
start
end

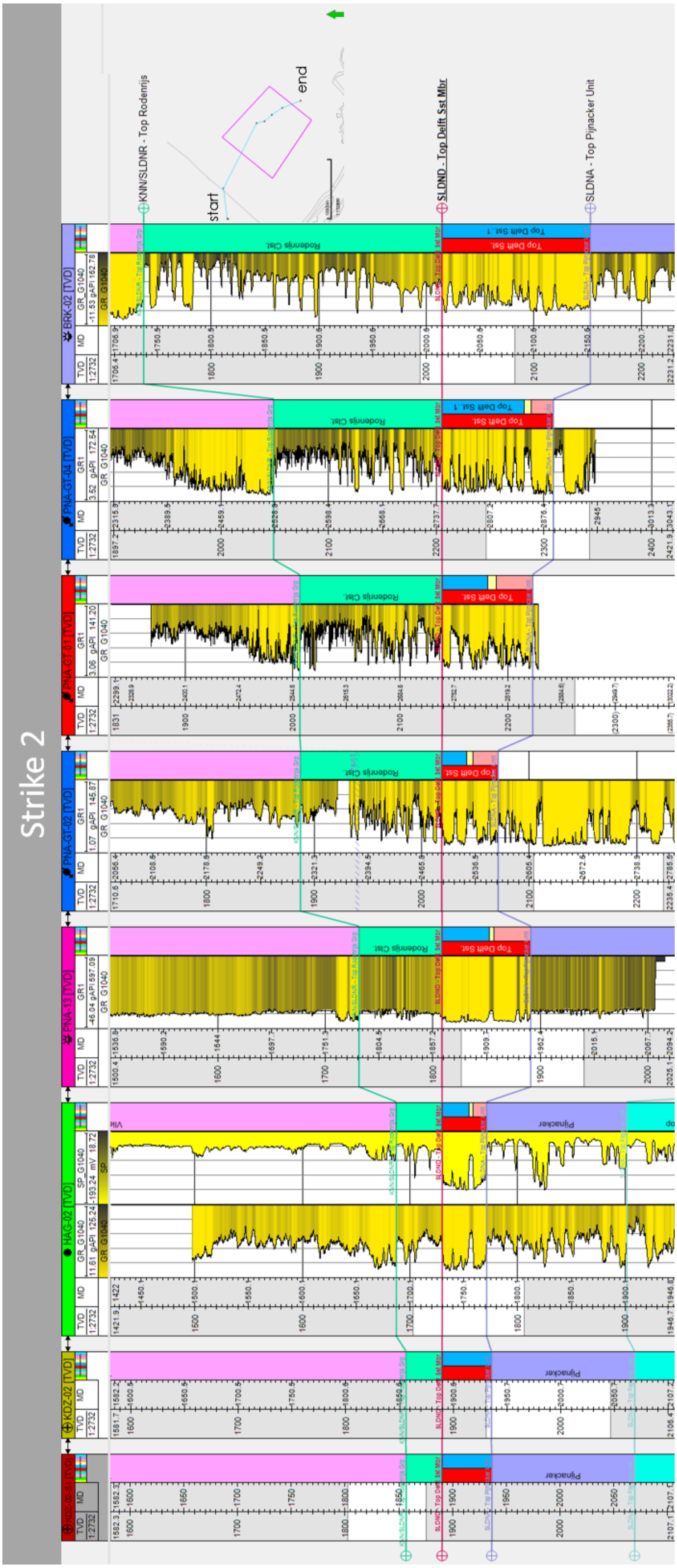
Strike 2
start
end
KNN/SLDNR - Top Rodenrijs
SLDND - Top Delft Sst Mbr
SLDNA - Top Pijnacker Unit
BRK-02 [TVD]
PNA-GT-04 [TVD]
PNA-GT-01 [TVD]
PNA-GT-02 [TVD]
PNA-13 [TVD]
HAG-02 [TVD]
KDZ-02 [TVD]
KDZ-02-S1 [TVD]
TVD
MD
1:2732
GR_G1040
GR1
SP_G1040
gAPI
mV
Rodenrijs Clst.
Top Delft Sst.
Top Delft Sst..1
Pijnacker

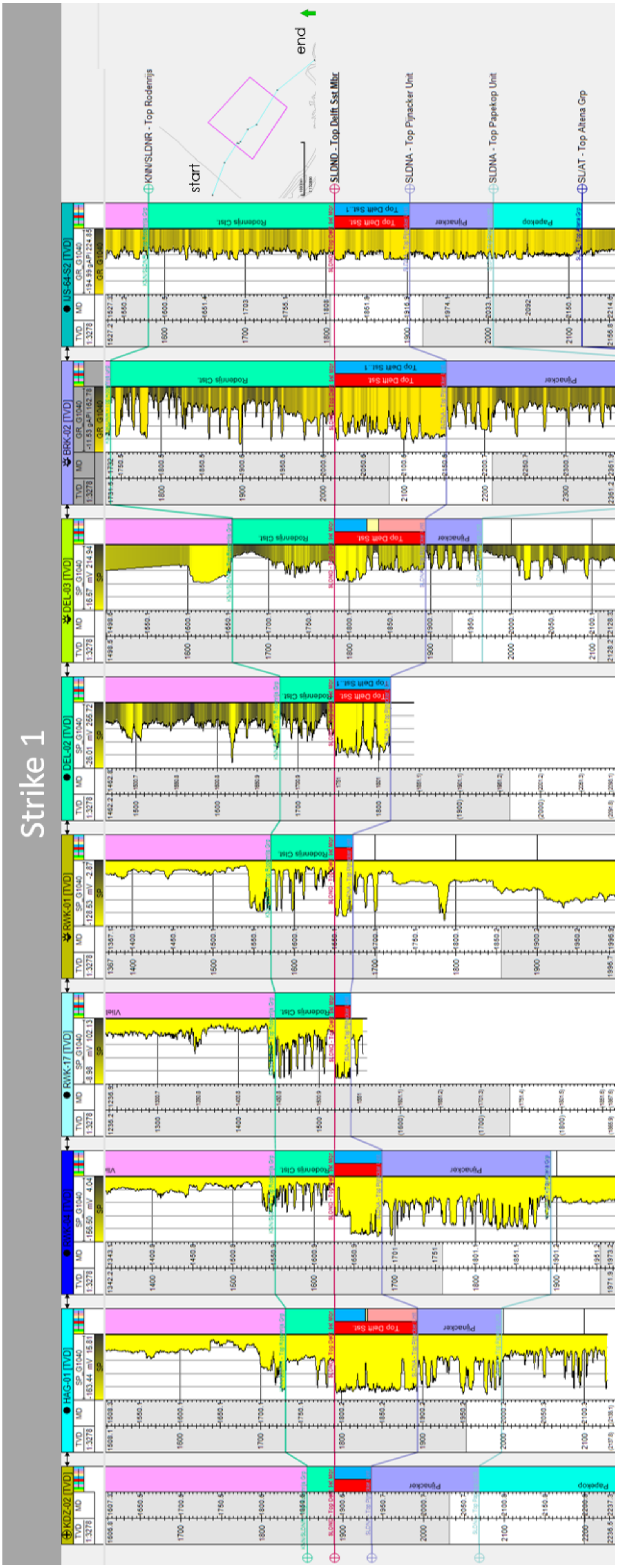
Strike 1
start
end
KNN/SLDNR - Top Rodenrijs
SLDND - Top Delft Sst Mbr
SLDNA - Top Pijnacker Unit
SLDNA - Top Papekop Unit
SL/AT - Top Altena Grp
US-64-S2 [TVD]
BRK-02 [TVD]
DEL-03 [TVD]
DEL-02 [TVD]
RWK-01 [TVD]
RWK-17 [TVD]
HAG-01 [TVD]
KDZ-02 [TVD]
TVD
MD
1:3278
GR_G1040
SP_G1040
Rodenrijs Clst.
Top Delft Sst.
Top Delft Sst._1
Pijnacker
Papekop
Vlieland

D

Well Designs

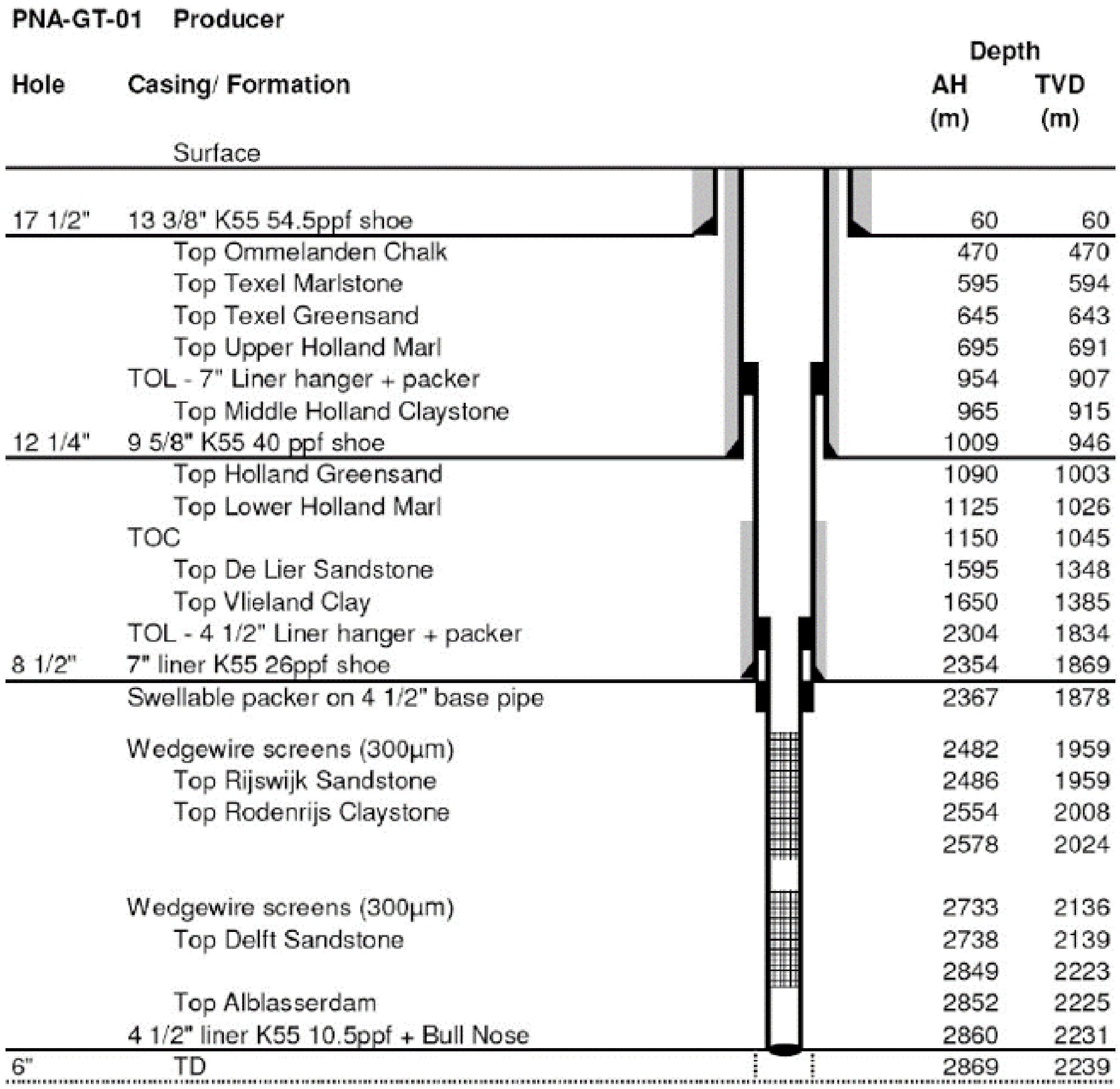

PNA-GT-01 Producer

Hole	Casing/ Formation	Depth AH (m)	 TVD (m)
	Surface		
17 1/2"	13 3/8" K55 54.5ppf shoe	60	60
	Top Ommelanden Chalk	470	470
	Top Texel Marlstone	595	594
	Top Texel Greensand	645	643
	Top Upper Holland Marl	695	691
	TOL - 7" Liner hanger + packer	954	907
	Top Middle Holland Claystone	965	915
12 1/4"	9 5/8" K55 40 ppf shoe	1009	946
	Top Holland Greensand	1090	1003
	Top Lower Holland Marl	1125	1026
	TOC	1150	1045
	Top De Lier Sandstone	1595	1348
	Top Vlieland Clay	1650	1385
	TOL - 4 1/2" Liner hanger + packer	2304	1834
8 1/2"	7" liner K55 26ppf shoe	2354	1869
	Swellable packer on 4 1/2" base pipe	2367	1878
	Wedgewire screens (300µm)	2482	1959
	Top Rijswijk Sandstone	2486	1959
	Top Rodenrijs Claystone	2554	2008
		2578	2024
	Wedgewire screens (300µm)	2733	2136
	Top Delft Sandstone	2738	2139
		2849	2223
	Top Alblasserdam	2852	2225
	4 1/2" liner K55 10.5ppf + Bull Nose	2860	2231
6"	TD	2869	2239

Figure D.0.1: Well design of PNA-GT-01.

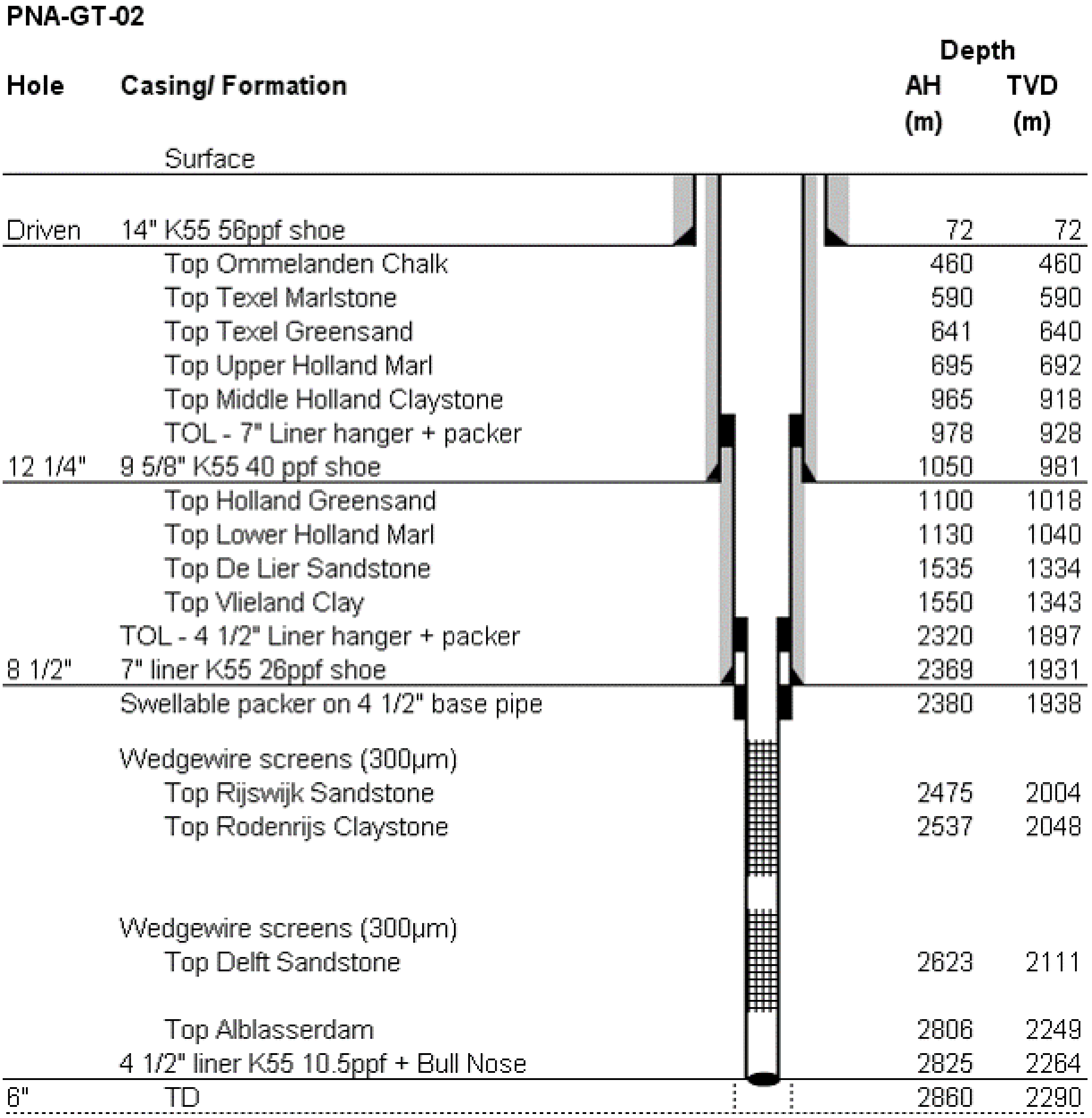

PNA-GT-02

Hole	Casing/ Formation	Depth	
		AH (m)	TVD (m)
	Surface		
Driven	14" K55 56ppf shoe	72	72
	Top Ommelanden Chalk	460	460
	Top Texel Marlstone	590	590
	Top Texel Greensand	641	640
	Top Upper Holland Marl	695	692
	Top Middle Holland Claystone	965	918
	TOL - 7" Liner hanger + packer	978	928
12 1/4"	9 5/8" K55 40 ppf shoe	1050	981
	Top Holland Greensand	1100	1018
	Top Lower Holland Marl	1130	1040
	Top De Lier Sandstone	1535	1334
	Top Vlieland Clay	1550	1343
	TOL - 4 1/2" Liner hanger + packer	2320	1897
8 1/2"	7" liner K55 26ppf shoe	2369	1931
	Swellable packer on 4 1/2" base pipe	2380	1938
	Wedgewire screens (300µm)		
	Top Rijswijk Sandstone	2475	2004
	Top Rodenrijs Claystone	2537	2048
	Wedgewire screens (300µm)		
	Top Delft Sandstone	2623	2111
	Top Alblasserdam	2806	2249
	4 1/2" liner K55 10.5ppf + Bull Nose	2825	2264
6"	TD	2860	2290

Figure D.0.2: Well design of PNA-GT-02.

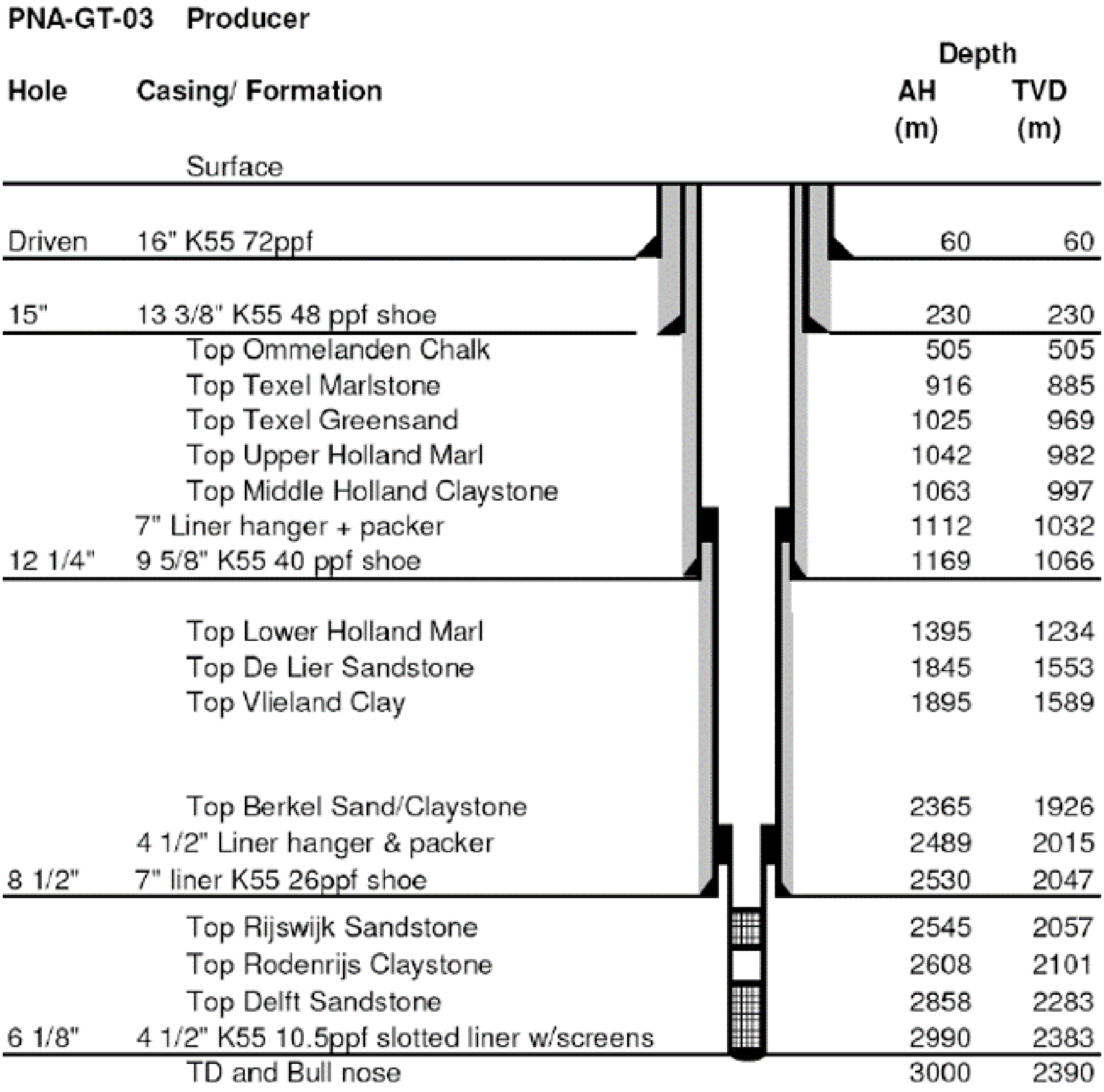

PNA-GT-03 Producer

Hole	Casing/ Formation	Depth AH (m)	Depth TVD (m)
	Surface		
Driven	16" K55 72ppf	60	60
15"	13 3/8" K55 48 ppf shoe	230	230
	Top Ommelanden Chalk	505	505
	Top Texel Marlstone	916	885
	Top Texel Greensand	1025	969
	Top Upper Holland Marl	1042	982
	Top Middle Holland Claystone	1063	997
	7" Liner hanger + packer	1112	1032
12 1/4"	9 5/8" K55 40 ppf shoe	1169	1066
	Top Lower Holland Marl	1395	1234
	Top De Lier Sandstone	1845	1553
	Top Vlieland Clay	1895	1589
	Top Berkel Sand/Claystone	2365	1926
	4 1/2" Liner hanger & packer	2489	2015
8 1/2"	7" liner K55 26ppf shoe	2530	2047
	Top Rijswijk Sandstone	2545	2057
	Top Rodenrijs Claystone	2608	2101
	Top Delft Sandstone	2858	2283
6 1/8"	4 1/2" K55 10.5ppf slotted liner w/screens	2990	2383
	TD and Bull nose	3000	2390

Figure D.0.3: Well design of PNA-GT-03.

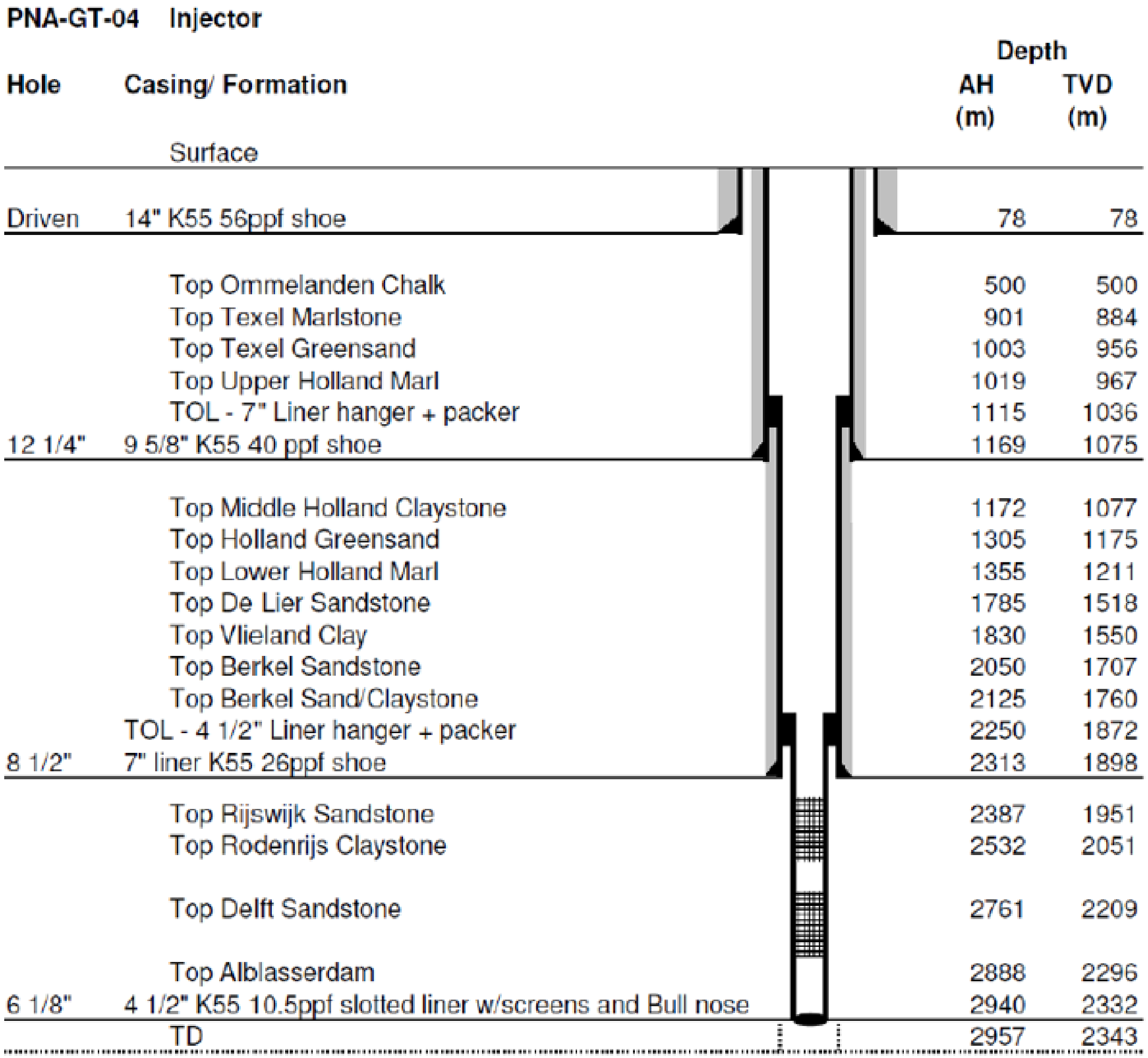

PNA-GT-04 Injector

Hole	**Casing/ Formation**	**Depth** AH (m)	TVD (m)
	Surface		
Driven	14" K55 56ppf shoe	78	78
	Top Ommelanden Chalk	500	500
	Top Texel Marlstone	901	884
	Top Texel Greensand	1003	956
	Top Upper Holland Marl	1019	967
	TOL - 7" Liner hanger + packer	1115	1036
12 1/4"	9 5/8" K55 40 ppf shoe	1169	1075
	Top Middle Holland Claystone	1172	1077
	Top Holland Greensand	1305	1175
	Top Lower Holland Marl	1355	1211
	Top De Lier Sandstone	1785	1518
	Top Vlieland Clay	1830	1550
	Top Berkel Sandstone	2050	1707
	Top Berkel Sand/Claystone	2125	1760
	TOL - 4 1/2" Liner hanger + packer	2250	1872
8 1/2"	7" liner K55 26ppf shoe	2313	1898
	Top Rijswijk Sandstone	2387	1951
	Top Rodenrijs Claystone	2532	2051
	Top Delft Sandstone	2761	2209
	Top Alblasserdam	2888	2296
6 1/8"	4 1/2" K55 10.5ppf slotted liner w/screens and Bull nose	2940	2332
	TD	2957	2343

Figure D.0.4: Well design of PNA-GT-04.

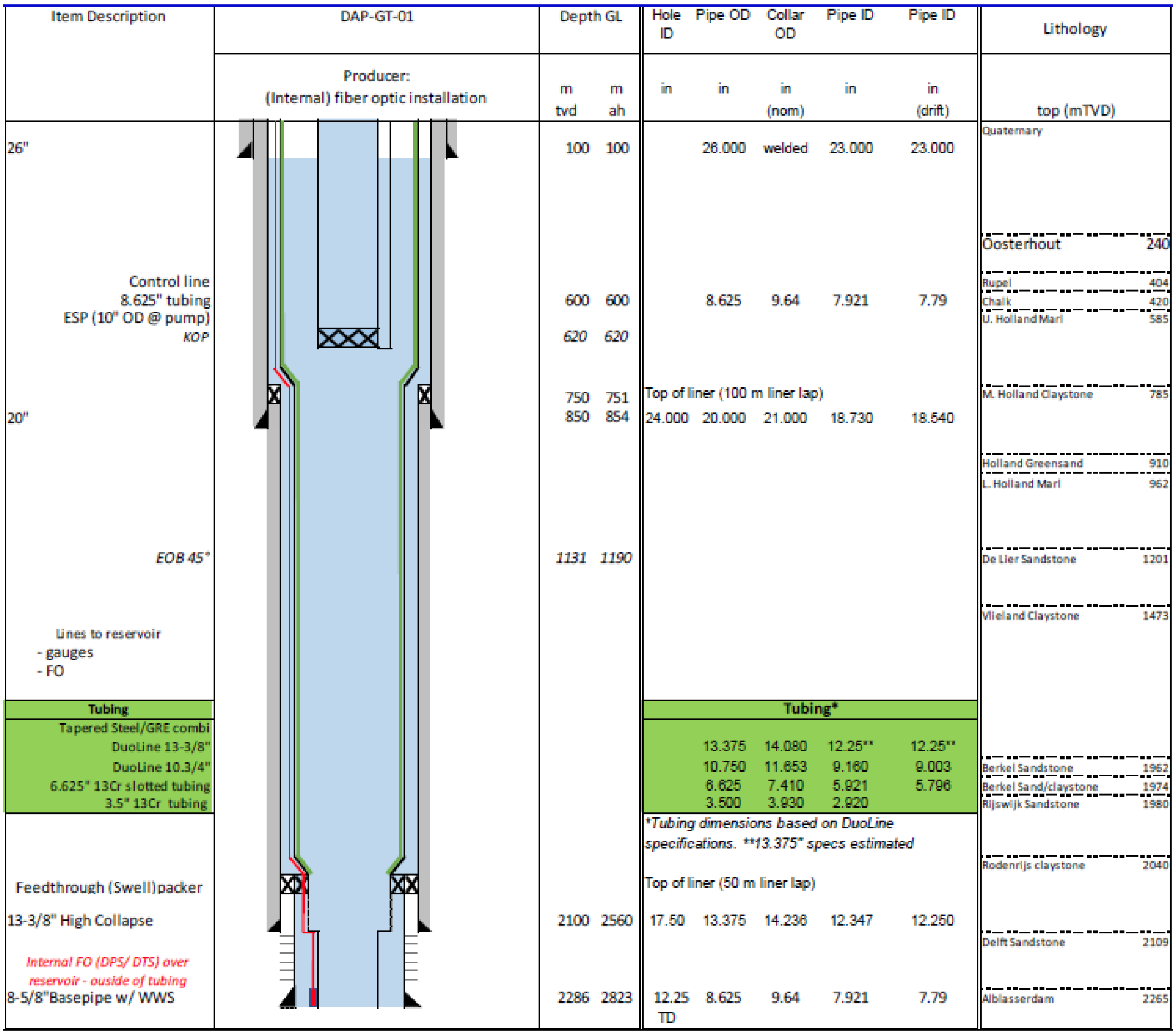

Item Description	Depth GL m tvd	 m ah	Hole ID in	Pipe OD in	Collar OD in (nom)	Pipe ID in	Pipe ID in (drift)
26"	100	100		26.000	welded	23.000	23.000
Control line 8.625" tubing ESP (10" OD @ pump)	600	600		8.625	9.64	7.921	7.79
KOP	*620*	*620*					
	750	751	Top of liner (100 m liner lap)				
20"	850	854	24.000	20.000	21.000	18.730	18.540
EOB 45°	*1131*	*1190*					
Lines to reservoir - gauges - FO							
Tubing			**Tubing***				
Tapered Steel/GRE combi							
DuoLine 13-3/8"				13.375	14.080	12.25**	12.25**
DuoLine 10.3/4"				10.750	11.653	9.160	9.003
6.625" 13Cr slotted tubing				6.625	7.410	5.921	5.796
3.5" 13Cr tubing				3.500	3.930	2.920	
			**Tubing dimensions based on DuoLine specifications. **13.375" specs estimated*				
Feedthrough (Swell)packer			Top of liner (50 m liner lap)				
13-3/8" High Collapse	2100	2560	17.50	13.375	14.236	12.347	12.250
Internal FO (DPS/ DTS) over reservoir - ouside of tubing							
8-5/8"Basepipe w/ WWS	2286	2823	12.25 TD	8.625	9.64	7.921	7.79

Lithology	top (mTVD)
Quaternary	
Oosterhout	240
Rupel	404
Chalk	420
U. Holland Marl	585
M. Holland Claystone	785
Holland Greensand	910
L. Holland Marl	962
De Lier Sandstone	1201
Vlieland Claystone	1473
Berkel Sandstone	1962
Berkel Sand/claystone	1974
Rijswijk Sandstone	1980
Rodenrijs claystone	2040
Delft Sandstone	2109
Alblasserdam	2265

Figure D.0.5: Well design of DAP-GT-01.

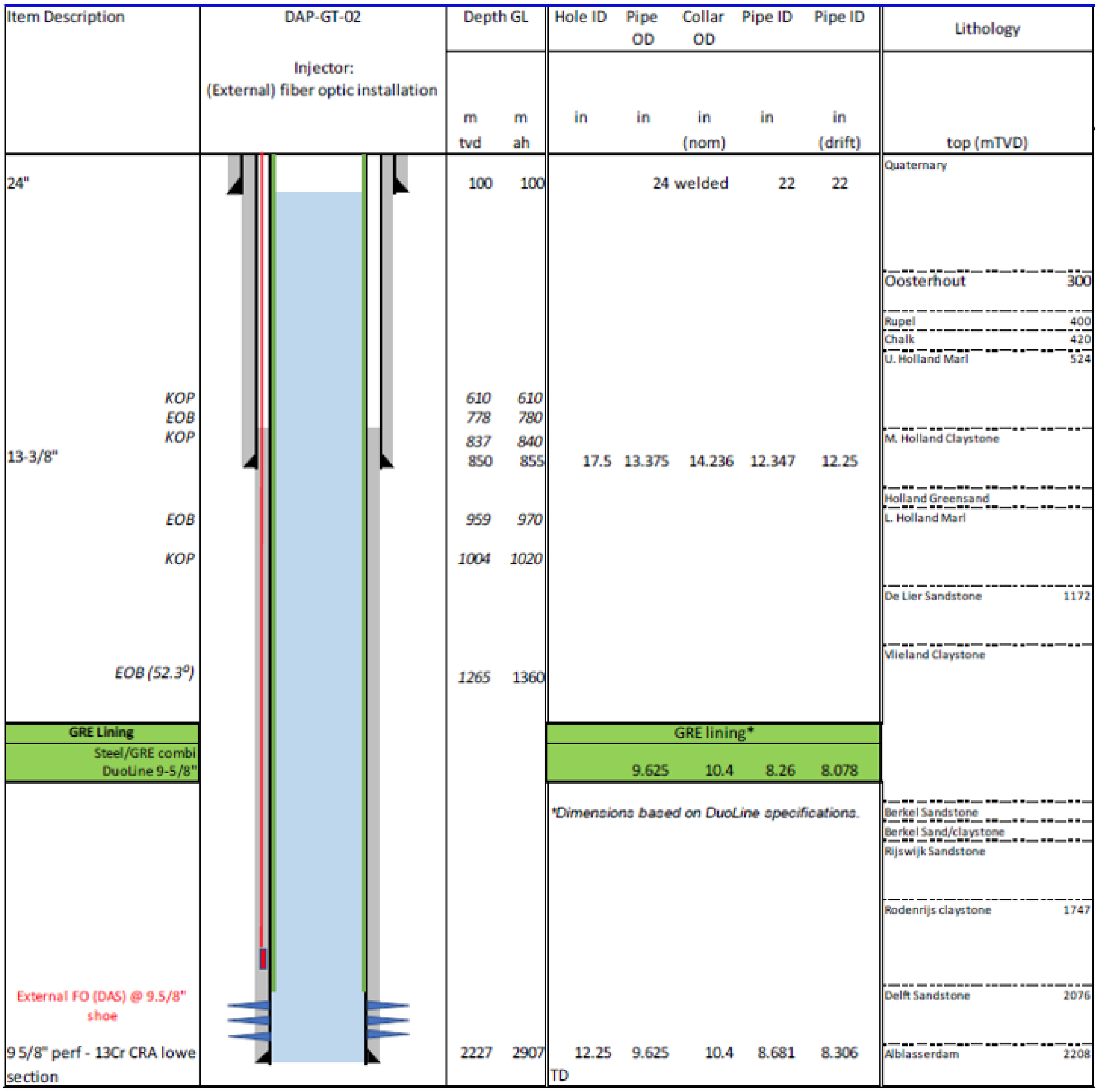

Figure D.0.6: Well design of DAP-GT-02.

E

Thermal Conductivity Values

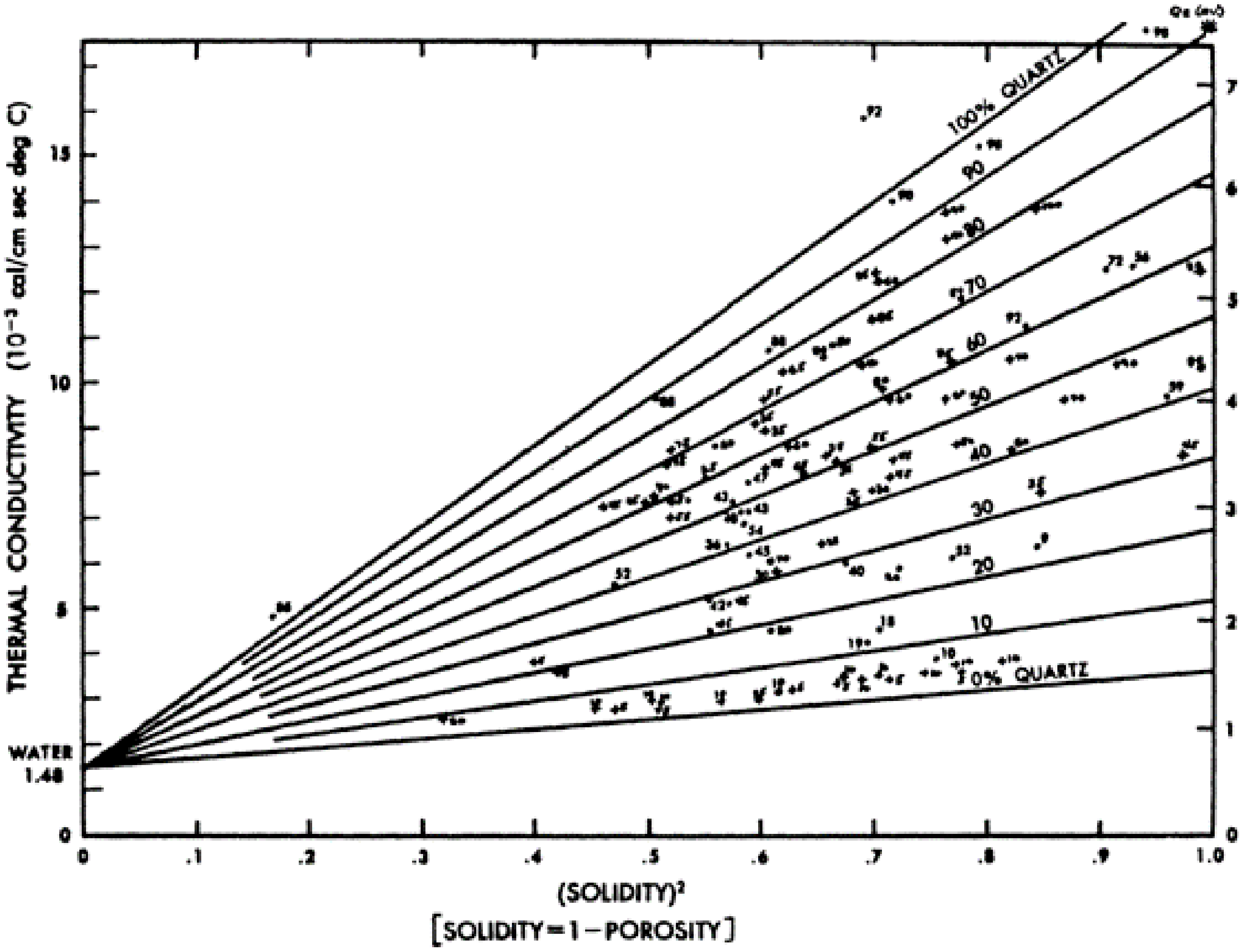

Figure E.0.1: Thermal conductivity of sandstone with water in the pores, shwoing variation with solidity and quartz content, at 300 K, 5 MPa (Robertson, 1988).

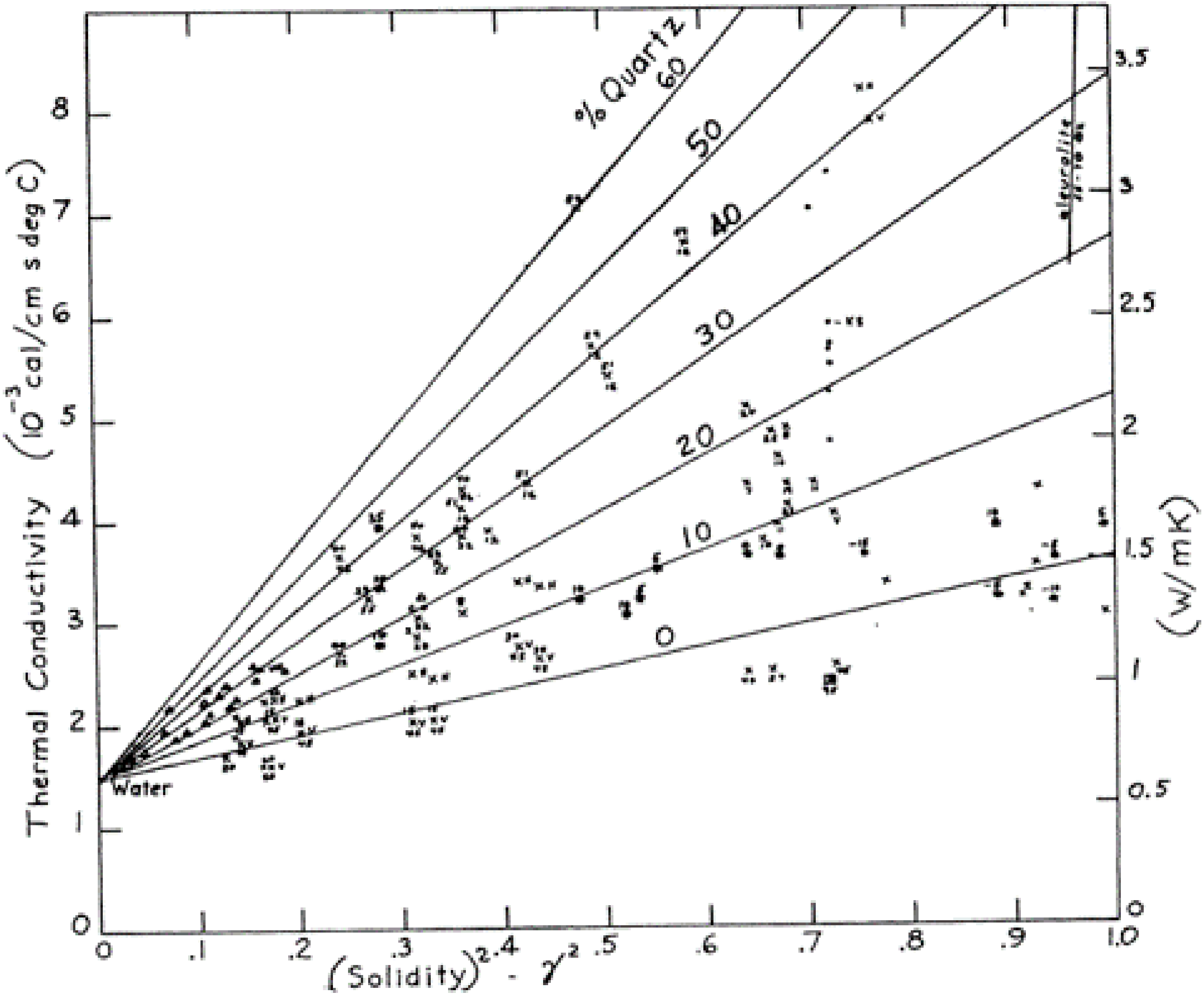

Figure E.0.2: Thermal conductivity of shale with water in the pores, shwoing variation with solidity and quartz content, at 300 K, 5 MPa (Robertson, 1988).

F

Dynamic Reservoir Simulation

F.1. Sensitivity Analysis: Reservoir Boundary Establishment

The amount of cells were in the reservoir model were minimized to decrease the simulation time. The reservoir model was cut off by applying a cell active filter on the x and y-axis of the reservoir model. The numerical discrepancy between the large and the cut-off model reservoir model was evaluated (Figure F.1.1). The maximum discrepancies for pressure and temperature were respectively 1.52 bar and 0.6 °C. The amount of cells were reduces from 1.099.791 to 365.202 cells.

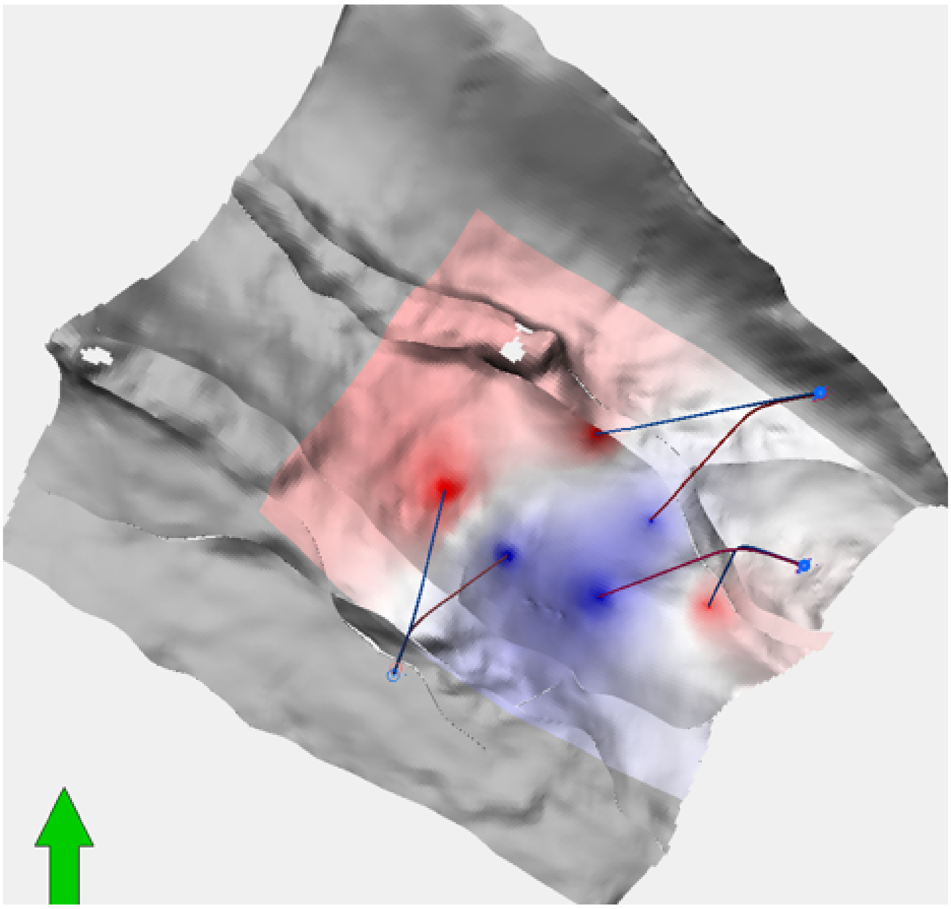

Figure F.1.1: Top view of the reservoir displaying the inactive cells (734.589) in grey and the active cells (365.202) wherein the pressure distribution is shown during production.

F.2. Sensitivity Analysis: Formation Water Density and Salinity

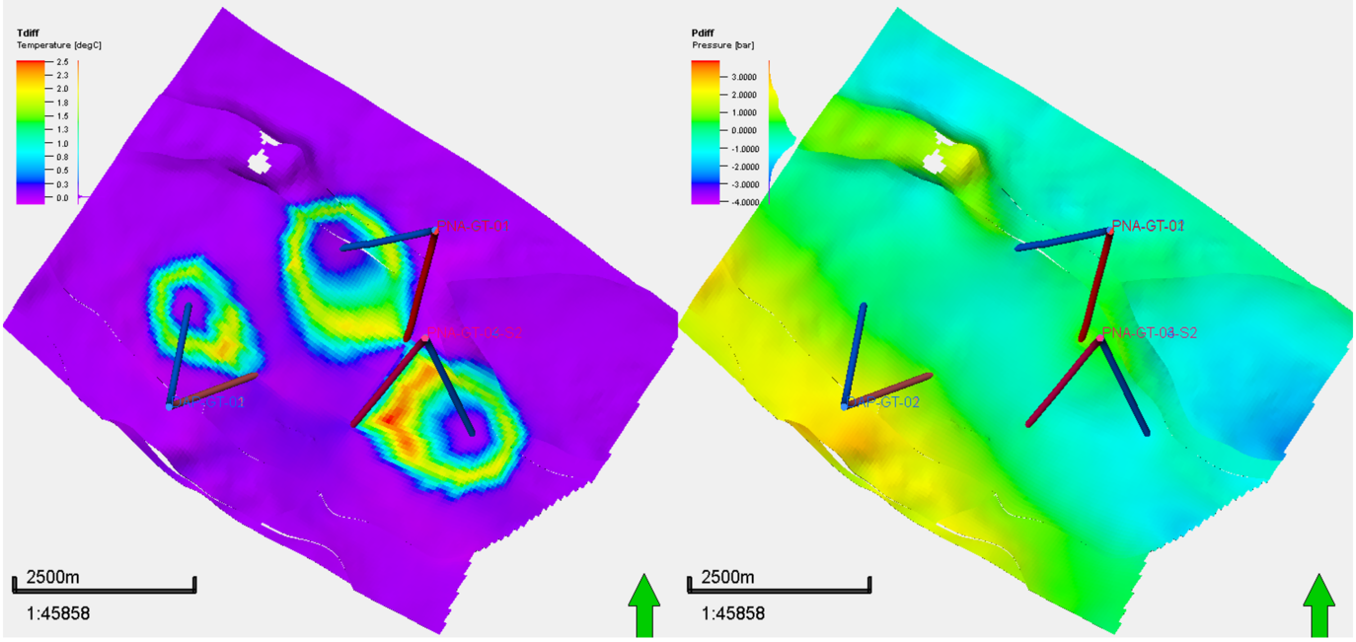

Figure F.2.1: Temperature (left) and pressure (right) difference between simulation with a fluid model with a salinity of 1 ppm and a formation water density of 999 kg/m^3 and a simulation with 106.406 ppm and 1076 kg/m^3.

F.3. Thermal Power Stand-Alone and Running All

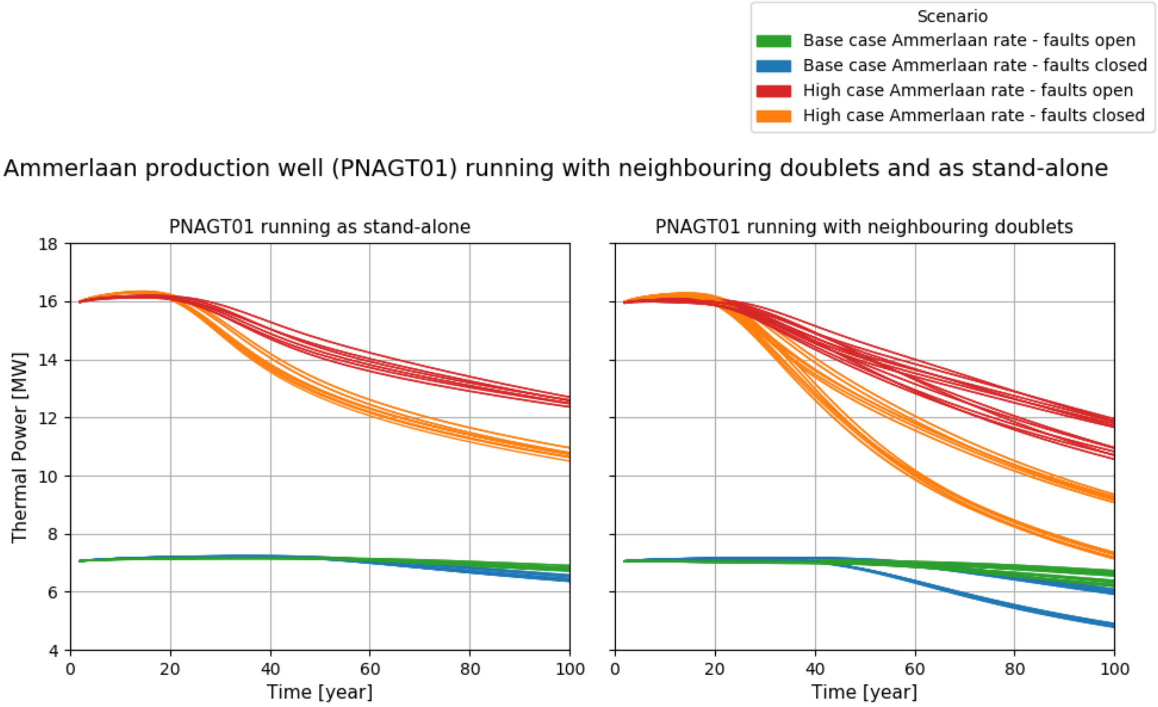

Figure F.3.1: Thermal power output of the Ammerlaan producer (PNAGT01) is plotted over time for four scenarios where PNAGT01 is producing with base case rates and high case rates and with open and sealing faults. Left: PNAGT01 is running in stand-alone configuration. Right: PNAGT01 is running while neighbouring doublets Duijvestijn and DAP are also producing.

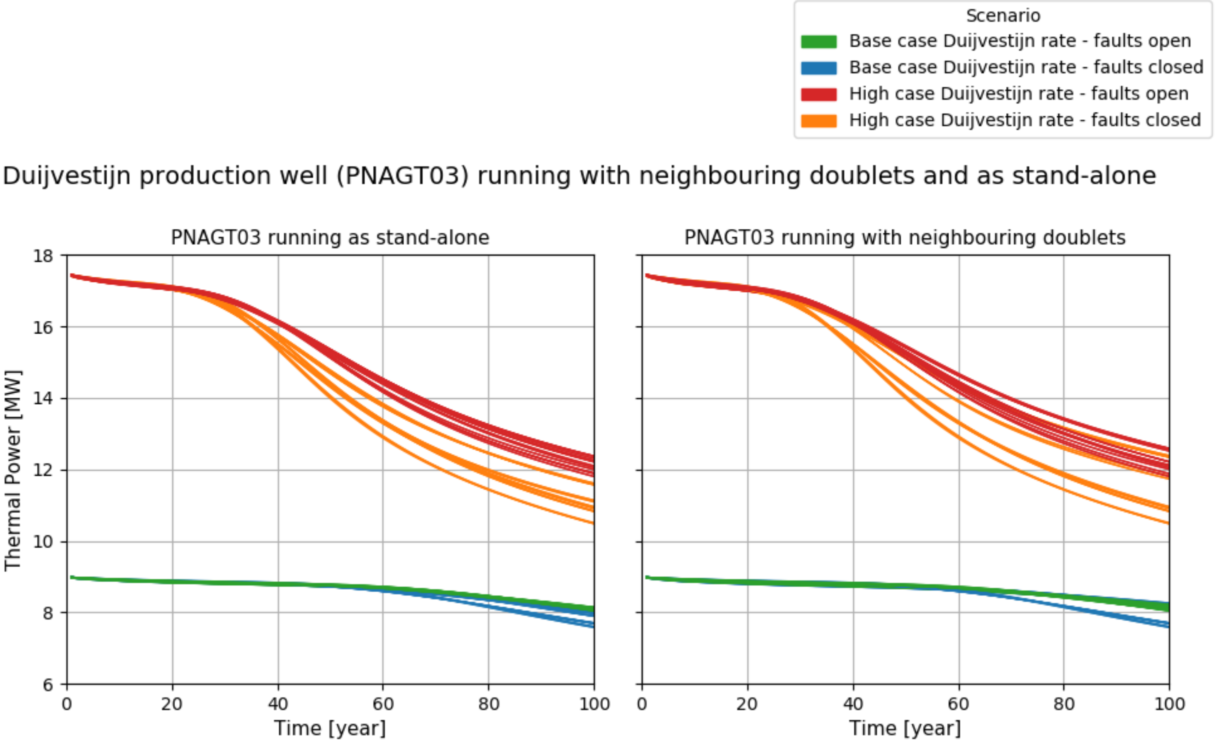

Figure F.3.2: Thermal power output of the Duijvestijn producer (PNAGT03) is plotted over time for four scenarios where PNAGT03 is producing with base case rates and high case rates and with open and sealing faults. Left: PNAGT03 is running in stand-alone configuration. Right: PNAGT03 is running while neighbouring doublets Ammerlaan and DAP are also producing.

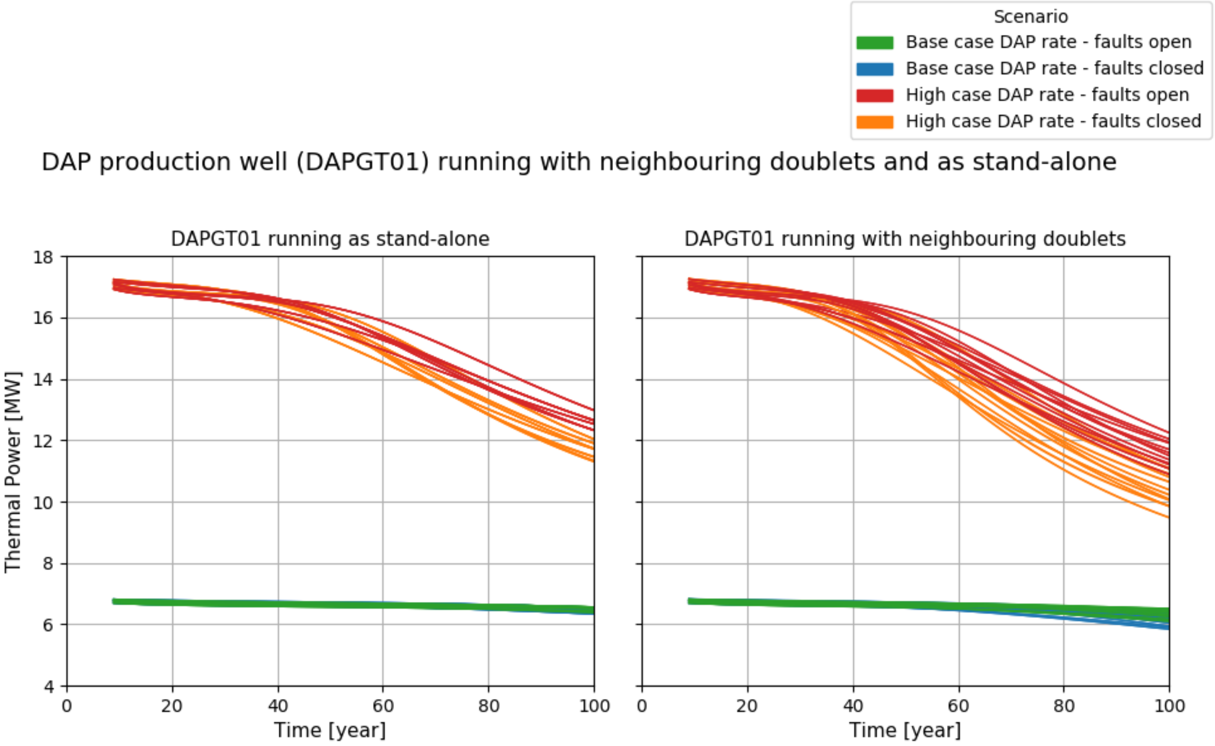

Figure F.3.3: Thermal power output of the DAP producer (DAPGT01) is plotted over time for four scenarios where DAPGT01 is producing with base case rates and high case rates and with open and sealing faults. Left: DAPGT01 is running in stand-alone configuration. Right: DAPGT01 is running while neighbouring doublets Ammerlaan and Duijvestijn are also producing.

G

Eclipse100 User Keywords

RUNSPEC Section

```
TEMP
```

Specified in the RUNSPEC section. This has no function but enables the computation of thermal properties.

```
NSTACK
75/
```

- Specified in the RUNSPEC section. Represents the size of the stack of previous search directions held by the linear solver. Is increased to mitigate linear solver convergence problems.

GRID Section

```
THCONR
```

- Specified in the GRID section. Specifies the combined rock and fluid thermal conductivities as a porosity weighted average of the phase and rock conductivities which will then be used to calculate the thermal conduction of heat in the reservoir.
- The conductivity of the rock is specified per grid cell in kJ/m/day/K. Repeat counts may be used for repeated values (for example 115*25: 115 cells are assigned a conductivity of 25 kJ/m/day/K).
- If nothing is inserted it will be automatically generated from the property. This method was used in this study.

PROPS Section

```
SPECROCK
20.0          2260
90.0          2410
/
```

- Specified in the PROPS section.
- Column 1: Temperature [°C]
- Column 2: Corresponding volume specific heat of rock [kJ/m^3/K]

```
SPECHEAT
10.0          0.5   3.66   0.5
50.0          0.5   3.70   0.5
100.0         0.5   3.73   0.5
/
```

- Specified in the PROPS section. The specific heat of a fluid is the amount of heat per unit mass required to raise the temperature by one degree Celsius. It is specified for oil, water and gas.
- Column 1: Temperature [°C]
- Column 2: Corresponding oil specific heat [kJ/kg/K]
- Column 3: Corresponding water specific heat [kJ/kg/K]
- Column 4: Corresponding gas specific heat [kJ/kg/K]

SOLUTION Section

```
RTEMVD
1          10
1000       41
3000       103 /
```

- Specified in the SOLUTION section.
- Column 1: Depth [m]
- Column 2: Corresponding initial reservoir temperature [°C] according to Section 6.3.2

SCHEDULE Section

```
WTEMP
WellName1   25.0 /
WellName2   25.0 /
WellName3   25.0 /
/
```

- Specified in the SCHEDULE section. Specifies the injection temperature
- Well nomenclature from WELSPECS should be used

```
TUNING
0.1        30   0.1 /
/
12         1    150   1*100 /
```

- Specified in the SCHEDULE section.

Bibliography

Abdulagatova, Z., Abdulagatov, I., and Emirov, V. (2009). Effect of temperature and pressure on the thermal conductivity of sandstone. *International Journal of Rock Mechanics and Mining Sciences*, 46(6):1055–1071.

Ahmed, T. (2018). *Reservoir engineering handbook*. Gulf Professional Publishing.

Ammiwala, H. (2018). Interference testing for Ammerlaan, Duijvestijn and DAPwell geothermal doublets. Unpublished report, Delft University of Technology.

Aramburo, D. (2017). Synergy between geothermal and stranded oil fields to add value to geothermal projects. Master's thesis, Applied Earth Sciences, Delft University of Technology.

Bonté, D., Van Wees, J.-D., and Verweij, J. (2012). Subsurface temperature of the onshore Netherlands: New temperature dataset and modelling. *Netherlands Journal of Geosciences*, 91(4):491–515.

Bridgwater, A. V. and Boocock, D. (2013). *Developments in Thermochemical Biomass Conversion: Volume 1*, volume 2. Springer Science & Business Media.

Cacace, M., Kaiser, B. O., Lewerenz, B., and Scheck-Wenderoth, M. (2010). Geothermal energy in sedimentary basins: What we can learn from regional numerical models. *Chemie der Erde-Geochemistry*, 70:33–46.

Dalfsen, W. v., van Gessel, S., and Doornenbal, J. (2007). Velmod-2. TNO report.

Daniilidis, A., Doddema, L., and Herber, R. (2016). Risk assessment of the Groningen geothermal potential: from seismic to reservoir uncertainty using a discrete parameter analysis. *Geothermics*, 64:271–288.

Daniilidis, A. and Herber, R. (2017). Salt intrusions providing a new geothermal exploration target for higher energy recovery at shallower depths. *Energy*, 118:658–670.

Davies, D., Williams, B., Vessell, R., et al. (1992). Models for meandering and braided fluvial reservoirs with examples from the Travis Peak Formation, East Texas. In *SPE Annual Technical Conference and Exhibition*. Society of Petroleum Engineers.

de Hoop, S. (2017). Determination of relevant spatial scale in reservoir simulation. Master's thesis, Applied Earth Sciences, Delft University of Technology.

Dehdari, V., Aminshahidy, B., Nejad, S., et al. (2008). Well spacing and recovery optimization of an Iranian Oil field by using streamline and reservoir simulation. In *SPE Western Regional and Pacific Section AAPG Joint Meeting*. Society of Petroleum Engineers.

Den Hartog Jager, D. (1996). Fluviomarine sequences in the Lower Cretaceous of the West Netherlands Basin: correlation and seismic expression. In *Geology of gas and oil under the Netherlands*, pages 229–241. Springer.

DeVault, B. and Jeremiah, J. (2002). Tectonostratigraphy of the Nieuwerkerk Formation (Delfland Subgroup), West Netherlands Basin. *AAPG bulletin*, 86(10).

Doddema, L. (2012). The influence of reservoir heterogeneities on geothermal doublet performance. *Training report, Master Programme Energy and Environmental Sciences, University of Groningen.*

Donselaar, M. E., Groenenberg, R. M., and Gilding, D. T. (2015). Reservoir geology and geothermal potential of the Delft Sandstone Member in the West Netherlands Basin. In *Proceedings World Geothermal Congress*.

Donselaar, M. E. and Overeem, I. (2008). Connectivity of fluvial point-bar deposits: An example from the Miocene Huesca fluvial fan, Ebro Basin, Spain. *AAPG bulletin*, 92(9):1109–1129.

Drost, G.I.A., K. M. (2009). Sediment-petrographical analysis of the Delft Sandstone. Master's thesis, Applied Earth Sciences, Delft University of Technology.

EBN (2019). *Hoe werkt aardwarmte.nl*. https://www.hoewerktaardwarmte.nl// [Accessed: 21-07-19].

Gilding, D. (2010). Heterogeneity determination of the Delft subsurface for heat flow modelling. Master's thesis, Applied Earth Sciences, Delft University of Technology.

Groot, J. (2014). The role of reservoir geology and reservoir architecture on geothermal doublet performance. Unpublished internship report, University of Utrecht.

Grunberg, L. (1970). Properties of sea water concentrations. *Third International Symposium on Fresh Water from the Sea*, 1:31–39.

Hamdhan, I. N. and Clarke, B. G. (2010). Determination of thermal conductivity of coarse and fine sand soils. In *Proceedings of World Geothermal Congress*.

Jansen, J. (2016). *Nodal analysis of oil and gas wells: System modeling and numerical implementation*. 4c. Delft University of Technology.

Jeremiah, J., Duxbury, S., and Rawson, P. (2010). Lower Cretaceous of the southern North Sea Basins: reservoir distribution within a sequence stratigraphic framework. *Netherlands Journal of Geosciences*, 89(3-4):203–237.

Kallweit, R. and Wood, L. (1982). The limits of resolution of zero-phase wavelets. *Geophysics*, 47(7):1035–1046.

Lake, L. and Society of Petroleum Engineers (1986). *Fundamentals of Enhanced Oil Recovery*. SPE continuing education. SPE.

Larue, D. K. and Hovadik, J. (2006). Connectivity of channelized reservoirs: a modelling approach. *Petroleum Geoscience*, 12(4):291–308.

Libecap, G. D. and Wiggins, S. N. (1985). The influence of private contractual failure on regulation: the case of oil field unitization. *Journal of Political Economy*, 93(4):690–714.

Loerakker, M. (2009). A core study to determine the heterogeneities in the Delft Sandstone Member in the Moerkapelle field. Master's thesis, Applied Earth Sciences, Delft University of Technology.

Matthews, J. D., Carter, J. N., Stephen, K. D., Zimmerman, R. W., Skorstad, A., Manzocchi, T., and Howell, J. A. (2008). Assessing the effect of geological uncertainty on recovery estimates in shallow-marine reservoirs: the application of reservoir engineering to the SAIGUP project. *Petroleum Geoscience*, 14(1):35–44.

Meehan, D. (1980a). A correlation for water compressibility. *Petroleum Engineer*, 56:125–126.

Meehan, D. (1980b). *A correlation for water viscosity*. Pet. Eng. 125-126.

Mijnlieff, H. and van Wees, J. (2009). Rapportage ruimtelijke ordening geothermie (F3). Unpublished report, TNO.

Ministry of Economic Affairs (2014). *The Mining Act*. https://wetten.overheid.nl/BWBR0014168/2019-04-10/#SlotformulierEnOndertekening [Accessed: 08-06-19].

Mueller, T. D., Witherspoon, P. A., et al. (1965). Pressure interference effects within reservoirs and aquifers. *Journal of Petroleum Technology*, 17(04):471–474.

Muntendam-Bos, A. (2008). Bergermeer seismicity study. *TNO Report*, 1:43.

NLOG (2014). *Oil, gas and geothermal resources in the Netherlands Applications for permits for exploration and production*. https://www.nlog.nl/sites/default/files/procedures_vergunning_web_1_uk.pdf [Accessed: 24-08-19].

Ondrak, R., Wenderoth, F., Scheck, M., and Bayer, U. (1998). Integrated geothermal modeling on different scales in the Northeast German basin. *Geologische Rundschau*, 87(1):32–42.

Poulsen, S., Balling, N., and Nielsen, S. (2015). A parametric study of the thermal recharge of low enthalpy geothermal reservoirs. *Geothermics*, 53:464–478.

Reith, D. (2018). Dynamic simulation of a carbonate reservoir. Master's thesis, Applied Earth Sciences, Delft University of Technology.

Robertson, E. (1988). Thermal properties of rocks (no. 88-441). *US Geological survey*.

Saeid, S., Al-Khoury, R., Nick, H. M., and Hicks, M. A. (2015). A prototype design model for deep low-enthalpy hydrothermal systems. *Renewable energy*, 77:408–422.

Schlumberger (2014). Eclipse technical description. Technical report, Version 2014.1.

Schoof, F., v. d. H. M. v. Z. J. v. H. J. (2018). Masterplan aardwarmte in Nederland. Technical report, Platform Geothermie, DAGO, Stichting Warmtenetwerk, EBN.

Shetty, S. (2018). Numerical strategy for uncertainty quantification in low enthalpy geothermal projects. Master's thesis, Applied Earth Sciences, Delft University of Technology.

Smits, P. (2008). Construction of an integrated reservoir model using the Moerkapelle field for geothermal development of the Delft sandstone. Master's thesis, Applied Earth Sciences, Delft University of Technology.

SoDM (2013). Protocol bepaling maximale injectiedrukken bij aardwarmtewinning. [Accessed: 04-02-19].

SodM (2017). Staat van de sector geothermie. https://www.sodm.nl/documenten/brieven/2017/07/13/brief-naar-minister-staat-van-de-sector-geothermie [Accessed: 20-08-19].

Spivey, J. P. and McCain Jr, W. (2003). Recommended correlations for fluid property estimation.

Staatscourant van het Koninkrijk der Nederlanden (2017a). Winningsvergunning aardwarmte Pijnacker-Nootdorp 4, Ministerie van Economische Zaken. https://zoek.officielebekendmakingen.nl/stcrt-2017-3132.html [Accessed: 20-08-19].

Staatscourant van het Koninkrijk der Nederlanden (2017b). Winningsvergunning aardwarmte Pijnacker-Nootdorp 5, Ministerie van Economische Zaken. https://zoek.officielebekendmakingen.nl/stcrt-2017-3136.html [Accessed: 20-08-19].

TNO (2019). *Nederlands Olie en Gas Portaal (NLOG)*. https://www.nlog.nl/ [Accessed: 26-01-19].

TNO-AGE (2014). *Overwegingen bij de berekening van de begrenzing van een winningsvergunning voor aardwarmte*. https://www.nlog.nl/sites/default/files/14-10.050%20ez%20%28hm%29%20bepaling%20begrenzing%20wv%20aw.pdf [Accessed: 05-09-19].

Van Adrichem Boogaert, H. and Kouwe, W. (1993). Stratigraphic nomenclature of the Netherlands, revision and update by Rijks Geologische Dienst (RGD) and Netherlands oil and gas exploration and production association (NOGEPA). *Mededelingen Rijks Geologische Dienst*, 50.

Vondrak, A., Donselaar, M., and Munsterman, D. (2018). Reservoir architecture model of the Nieuwerkerk Formation (Early Cretaceous, West Netherlands Basin): diachronous development of sand-prone fluvial deposits. *Geological Society, London, Special Publications*, 469:SP469–18.

Voskov, D. V. (2017). Operator-based linearization approach for modeling of multiphase multi-component flow in porous media. *Journal of Computational Physics*, 337:275–288.

Wang, Y., Khait, M., Voskov, D., Saeid, S., and Bruhn, D. (2019). Benchmark test and sensitivity analysis for geothermal applications in the Netherlands. In *44th Workshop on Geothermal Reservoir Engineering, Stanford, California.*

Watanabe, N., Wang, W., McDermott, C. I., Taniguchi, T., and Kolditz, O. (2010). Uncertainty analysis of thermo-hydro-mechanical coupled processes in heterogeneous porous media. *Computational Mechanics*, 45(4):263.

Weerd, A., B. U. (2016). Geology study for the Delft Geothermal Project (DAP). Unpublished Report prepared for Delft University of Technology.

Wiggers, C. (2009). The Delft Sandstone in the West Netherlands Basin. Master's thesis, Applied Earth Sciences, Delft University of Technology.

Willems, C., Nick, H., Weltje, G., and Bruhn, D. (2017a). An evaluation of interferences in heat production from low enthalpy geothermal doublets systems. *Energy*, 135.

Willems, C. J. (2012). Study of the Lower Cretaceous sands in the Van den Bosch Geothermal energy concession. Master's thesis, Applied Earth Sciences, Delft University of Technology.

Willems, C. J., Nick, H. M., Donselaar, M. E., Weltje, G. J., and Bruhn, D. F. (2017b). On the connectivity anisotropy in fluvial hot sedimentary aquifers and its influence on geothermal doublet performance. *Geothermics*, 65:222–233.

Willems, C. J., Vondrak, A., Munsterman, D. K., Donselaar, M. E., and Mijnlieff, H. F. (2017c). Regional geothermal aquifer architecture of the fluvial Lower Cretaceous Nieuwerkerk Formation - a palynological analysis. *Netherlands Journal of Geosciences*, 96(4):319–330.

Wong, T. E., Batjes, D. A., and de Jager, J. (2007). *Geology of the Netherlands*. Edita-the Publishing House of the Royal.

Wong, Z. Y., Horne, R., and Voskov, D. (2015). *A geothermal reservoir simulator in AD-GPRS*. PhD thesis, Stanford University.

Zigrang, D. and Sylvester, N. (1982). Explicit approximations to the solution of Colebrook's friction factor equation. *AIChE Journal*, 28(3):514–515.

Delft
University of
Technology

Challenge the future